THESE DE DOCTORAT

Présentée à

l'Université de Lille

Ecole Doctorale Régionale

Sciences Pour l'Ingénieur/Science de l'Ingénierie et des Systèmes

pour l'obtention du grade de

DOCTEUR en

Micro et Nanotechnologies, Acoustique et Télécommunications

par

Ngoc Kim Thanh BUI

Growth of earth abundant material based thin films by sputtering technique for photovoltaics

Elaboration de nouveaux matériaux en films minces par pulvérisation cathodique pour cellules solaires

Soutenue le 2 Décembre 2021

Mireille RICHARD	Rapporteur	Directeur de Recherche CNRS, Institut des Matériaux Jean Rouxel de Nantes
Philippe DANIEL	Rapporteur	Professeur, Le Mans Université, Institut des Molécules et Matériaux du Mans
Wilfried FAVRE	Examinateur	Ingénieur, Commissariat à l'énergie atomique et aux énergies, Institut National de l'Energie Solaire (Chambéry)
Christophe LETHIEN	Examinateur Président	Professeur, Université de Lille, Institut d'Electronique, de Microélectronique et de Nanotechnologie
Mathieu HALBWAX	Co-encadrant	Maître de Conférences, Université de Lille, Institut d'Electronique, de Microélectronique et de Nanotechnologie
Jean-Pierre VILCOT	Directeur de thèse	Directeur de Recherche CNRS, Institut d'Electronique, de Microélectronique et de Nanotechnologie

Acknowledgments

After 3 years of research, my thesis has been done at the Institut d'Electronique de Microélectronique et de Nanotechnologie – IEMN, it would not be complete without the help of many people. Now, this is the right time to send gratitude to everyone.

First of all, I would like to thank my supervisor Dr. Jean-Pierre VILCOT who has accepted me into his project, he also made my European dream come true. I not only learned from him knowledge about research and science but also many other things, such as optimism, communication, future plan and how to relieve stress. He gave me encouragement, enthusiastic help, the effective orientation to perform my thesis. At times, he looks busy and tired but the door of his office is always open and greets everyone with a welcoming smile.

I would like to thank Mathieu HALBWAX, Cathy SION, Boubakeur AYACHI for being my tutorials during my first days in IEMN. They had supported me with knowledge from theory to practice.

Thanks to Guillaume COCHEZ, Christophe BOYAVAL, Florent BLANCHARD, Marc DEWITTE, Isabelle ROCH-JEUNE, Pascal TILMANT, Francois VAURETTE, David GUERIN, Vanessa AVRAMOVIC and Etienne OKADA for their technical help.

I am very grateful to the collaborators in the OPERA project: Jean Lamour Institute (JLI), The Group of electrical engineering of Paris (GeePs) and The National Institute for Solar Energy (INES).

I would like to thank Nora BENBAHLOULI and Andy LEDENT who are always available and have helped me in all the administrative steps and procedures.

I would like to thank the committee members, Mireille RICHARD and Philippe DANIEL who reviewed my work as Wilfried FAVRE and Christophe LETHIEN who examinated it.

I would also like to thank all members of the Optoelectronic group: Siva GANESAN, Mohamed Taieb BAKOUCHE, Pierre-Vincent DUGUE, Khaoula FERCHICHI, Sophie MARICOT, Phuong DO. We shared happy moments, travels and parties with delicious food prepared by each of us.

Thank you to my Vietnamese friends, especially Phuong BUI, Thao NGUYEN, Quynh DUONG, Quan LE and Tan NGUYEN for all the time we have shared together, for their strong support in my personal and professional life.

I thank my aunt Thuy LE-TOAN and my uncle Duc BUI for supporting and loving me during my years in France.

Finally, to my parent and my brother, thank you for always supporting my decisions. I know that you were very worried when I quit my job to continue my academic career, but you still love, trust and encourage me. I love you more than I can say.

Table of contents

PREAMBLE

This work has been made in the framework of the ANR "OPERA" project. The goal of this project (10/2017 - 09/2021) was to assess the potentialities of the $ZnSnN_2$ material line as a potential candidate for an inorganic thin film for the fabrication of tandem cells. The project consortium comprised four partners:

- Institut Jean Lamour (IJL) in Nancy for material deposition and deep crystallography analyses,
- Institut d'Electronique, de Microélectronique et de Nanotechnologie (IEMN) in Lille for material deposition, photodetector fabrication and photoelectric properties assessment,
- Laboratoire de Génie Electrique de Paris (GeePs) for deep electrical and electrooptic measurements,
- Commissariat à l'Energie Atomique et aux Energies Alternatives - Laboratoire d'Innovation pour les Technologies des Energies nouvelles et les Nanomatériaux (CEA-LITEN), and more particularly Institut National de l'Energie Solaire (INES) in Chambéry for solar cell design and characterization.

Within my work, magnetron sputtering technique was used to deposit the $ZnSnN_2$ thin films. It was mainly targeted to determine the influence of the deposition parameters on the basic electrical and optical properties of the deposited materials. This parametric study that involved the fabrication of numerous samples is reported in Chapters II, III and IV.

In order to fabricate devices, transparent conductive oxides, either n or p-type shall be used. Chapter IV discusses the topic.

Photodetector structures, either photoconductor- or photodiode- like, were then fabricated using best promising $ZnSnN_2$ materials issued from the parametric study and the transparent conductive oxides of previous chapter. The fabrication and the characterization of those structures under solar illumination are reported in Chapter V.

The Chapter I will introduce the photovoltaics application field and the way research is going to the development of low-cost tandem cells. The particular research domain on $ZnSnN_2$ material will be introduced by the literature review of knowledge database about its properties that were available at project starting and that generated the interest for this study.

Chapter I: **INTRODUCTION**

I.1 State of the art

Along with the rapid development of science and technology, the basic human needs for live also enhance day by day. More and more energy is consumed to make life better and more comfortable. Besides the earth is being cooked and fossil energy resources are gradually running out. Today, renewable energy sources such as hydropower, bio-fuels, solar and wind are researched and developed. They play an important role as sustainable solutions for electricity supply as well as reducing greenhouse gas emissions that are a reason of climate change. In the Global Energy Review 2020 of the International Energy Agency (**Figure I. 1**), solar energy is represented as furnishing around 3% of global electricity generation. Depending on own feeling, this can be judged as a quite big leap compares to data in 2013 (around 1%) or a very modest step but, in any case, it is still a small part of overall electricity supply.

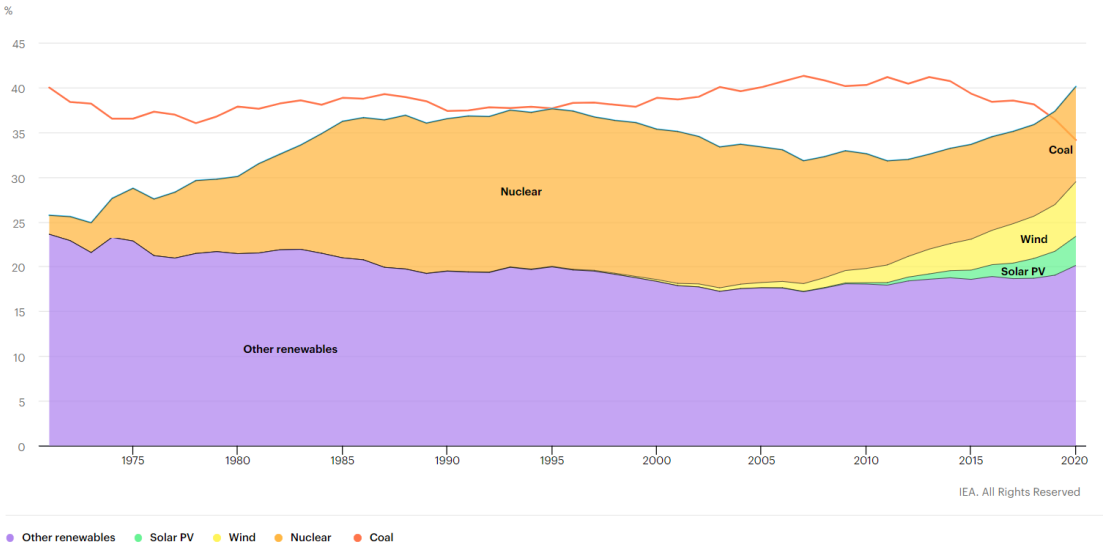

Figure I. 1: *Worldwide electricity generation shares between fossil (coal), nuclear and low-carbon sources* [1]

The solar resource is enormous and electricity issued from solar energy exhibits low greenhouse gas emissions (no emission during use, only during the fabrication of solar panels). There are two technologies to convert directly solar energy to electricity: photovoltaic (PV) and concentrated solar power (CSP). PV can be used either for individual

or large-scale (solar farms) photovoltaic generation units and CPV is mainly used for large-scale units.

Focusing on cell research, it is incessantly targeting cells with higher power conversion efficiencies, lower material usage and reduced manufacturing complexity and cost. **Figure I. 2** shows the well-known panorama of research photovoltaic cell efficiency record versus time made by the National Renewable Energy Laboratory (NREL).

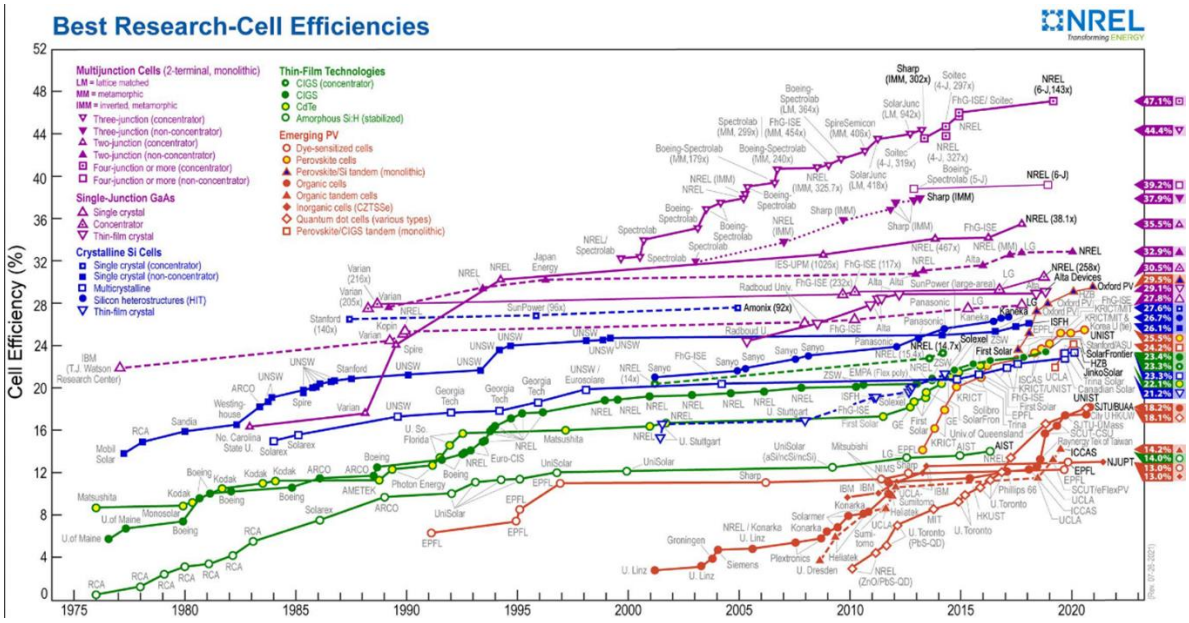

Figure I. 2: *Record Lab-Cell Power Conversion Efficiencies (from NREL)* [2]

Highest power conversion efficiencies are obtained by the use of III-V material compounds. Especially, 29.1% for single-junction gallium arsenide (GaAs) device announced by Alta Devices manufacturer [3] and using six-junction III-V solar cell, the efficiency grows up to 39.2% under 1 sun (PV) and 47.1% under 143 suns concentration (CPV) [4]. Nevertheless, the increase of efficiency by a factor, let us say, around 1.5, does not bear comparison with the increase in fabrication costs that are at least a decade higher making such a technology unrealistic for large scale terrestrial application.

The crystalline silicon solar cell, named as first-generation cell, has been studied and put into practical use long time ago: first genuine photovoltaic cell exhibiting roughly 6% efficiency was demonstrated in 1954 by researchers of Bell Laboratories. Since that time, its technology has continuously evolved, more specially this last decade, so that current

industrial panels can achieve around 25% efficiency together with a large decrease in fabrication cost (roughly a decade). Moreover, its base raw material is the second more abundant element on Earth. Then, it is not surprising that it dominates the current market share. According to the International Technology Roadmap for PhotoVoltaic (ITRPV) published in April 2020 [5], the market share of mono-crystalline silicon (c-Si) cells is close to 75 percent and multi-crystalline silicon (mc-Si) cells is around 20 percent. Those two last years, great efforts have been made in silicon purification processes that lead, today, to almost the vanishing of cell production using mc-Si. So, silicon based solar cells are decreasing in production costs and their conversion efficiency asymptotically tends towards the highest achievable value that has been theoretically evaluated to 29.43%: current [6] record values are 27.6% [7] and 26.7% [8] for homojunction cells (CPV configuration) and heterojunction cells (PV configuration), respectively.

Owing to the light absorption properties of thin -ranging from hundreds of nanometers to few microns- PV materials, thin-film PV cells, known as second generation cells, were seen as a solution decreasing raw material consumption and so the weight-per-unit-power figure of merit and ultimately the overall cost of solar cells. Amorphous Si was firstly used; it effectively led to a low-cost technology but also a low efficiency one, the highest efficiency value is 14.04% for triple-junction solar cell [9]. CdTe, and more recently copper indium gallium di-selenide (CIGS), materials were then used. The efficiency of cells based on such materials is now comparable to the one of crystalline Si cells. More specifically, Solar Frontier published their results on CIS with an efficiency of 23.35% [10] and First Solar reported 22.1% (cell efficiency) and 18.2% (module efficiency) on thin-film CdTe [11]. Nevertheless, due to the sharp concurrence of silicon technology as well as some process or material toxicities concerns (e.g. Cd for CdTe and Se for CIGS cells) and raw material possible shortage (i.e. In and Ga for CIGS), those technologies do not succeed to affect first generation market share supremacy. Their current fabrication cost is still slightly higher than that of Si cells and they really get inevitable in flexible cells where first-generation cells are definitely not usable.

The huge challenge for PV is how to maximize the conversion efficiency while minimizing the fabrication costs. The efficiency of single junction cells are limited by the Shockley-Queisser limit that was initially (in 1961) assessed to 33%. Since that time the model has

been revised and the limit is now evaluated around 29.5% as mentioned earlier. Even if silicon has not the optimum bandgap maximizing the efficiency -1.4 eV-, it allows approaching this limit very close. The way that is now unanimously recognized to outperform the Shockley-Queisser limit is to use tandem solar cells, i.e. two-junction cells (**Figure I.3**).

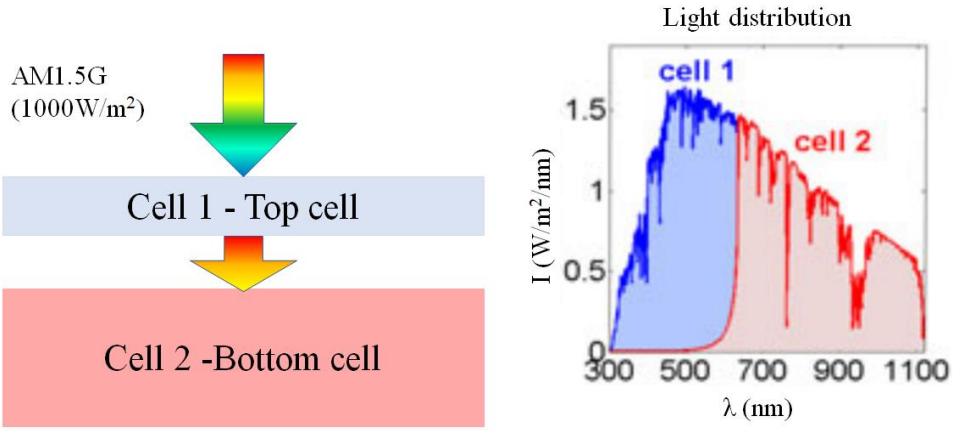

Figure I. 3: *Schematic of the tandem cell including two elementary cells using materials with different bandgap. Light with higher energies (lower wavelengths) is absorbed in the higher bandgap top cell. Light with lower energies goes through and is absorbed in the bottom cell (lower bandgap material).*

The studies that have been made on multi-junction cells have shown the limits of the approach, particularly in the materials and the fabrication cost issues. Although other materials could have been used, best way to achieve a sustainable tandem cell is to use a crystalline Si (c-Si) bottom cell since Si cell technology is already well handled, leads to high efficiency cells and Si is a sustainable material (as mentioned before, it is the second earth more abundant material after oxygen). According to Thomas P. White [12], tandem solar cells based on c-Si bottom cell and a thin-film top cell present a practical route toward low-cost cells with efficiencies above 30%. From his tandem cell model, the characteristics of the top cell can be derived. Following his results (**Figure I.4**), the higher the material bandgap is, the lower the requirement in efficiency is needed achieving a tandem cell with a given efficiency (η = 25%, 27.5% or 30%). The choice of top cell materials that have suitable bandgap is then more flexible.

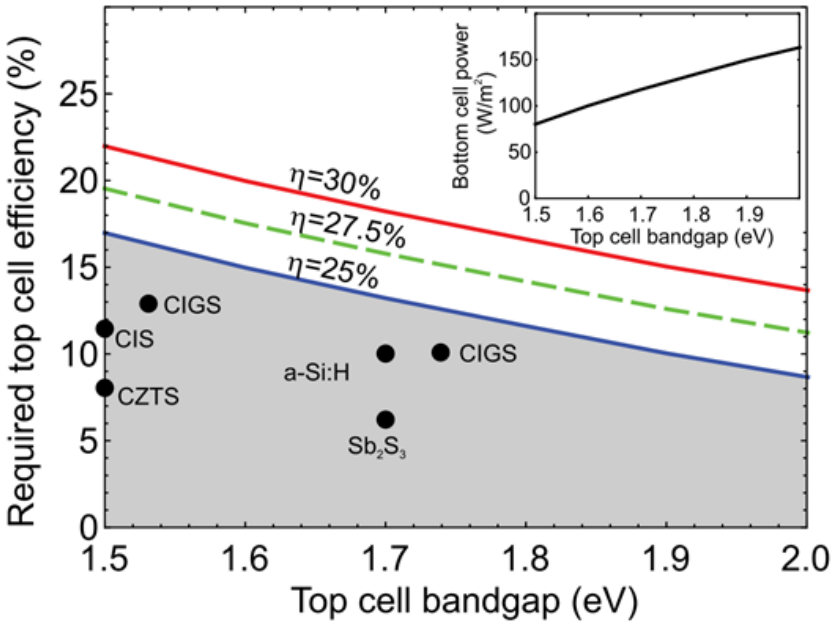

Figure I. 4: *Top cell conversion efficiency required for a c-Si bottom-cell based tandem cell to reach a conversion efficiency of η = 25% (blue solid curve), 27.5% (green dashed curve), and 30% (red solid curve). The shaded area indicates areas where η < 25%. Dots indicate experimental cell efficiencies reported for several high bandgap materials. Inset: output generated power of the bottom cell when the top cell absorbs all photons with energy above the bandgap* [12].

There is currently no technology achieving a sustainable and cost-efficient top cell. Therefore, the first step before designing such a tandem cell is to get a top cell material with adequate bandgap and low environmental footprint which technology can match the requirements of its integration, as a thin film, onto a c-Si cell. By experiment, tandem solar cells based on III-V semiconductors reach high efficiency; specially achieve 33.3% efficiency for triple-junction GaInP (E_g = 1.90 eV)/ GaAs (E_g = 1.43 eV)/ Si ((E_g = 1.12 eV) cell [13]. Besides, the experimental results of GaAs (E_g = 1.42 eV) single-junction solar under one-sun illumination record the conversion efficiency of 27.6% [14] and 29.3% [15]. In the case of perovskite, the conversion efficiency reaches 13.37% when the bandgap is 1.38 eV [16]. According B. Ehrler *et al.* [17], dual-junction tandem cells were made from combinations of III-V semiconductors, combinations of perovskite, perovskite/Si or perovskite/CIGS have the efficiency higher than 23.4%, the record efficiency and bandgap of the sub-cells are summarized in **Table I. 1**. We can conclude that semiconductors with bandgap between 1.4 and 2.0 eV can be used as top-cell of tandem cell.

Table I. 1: The efficiency of dual junction tandem cells and bandgap of sub-cells were recorded by B. Ehrler *et al.* [17]

Materials	Record efficiency (%)	Bandgap (eV)
GaInP/ GaAs	32.8	1.95/ 1.42
GaAsP/ Si	23.4	1.73/ 1.12
Perovskite/ Si	29.2	1.70/ 1.12
Perovskite/ Perovskite	24.2	1.82/ 1.27
Perovskite/ CIGS	24.2	1.70/ 1.13

Today, the energy conversion potentialities of a material are not the only focus, its sustainability, fabrication environmental footprint and lifetime properties added: that was not always the case in previous approaches. We will focus in this work on new inorganic materials using earth-abundant and non-toxic elements. Among them ternary zinc nitride semiconductors have been pointed out as potential candidates.

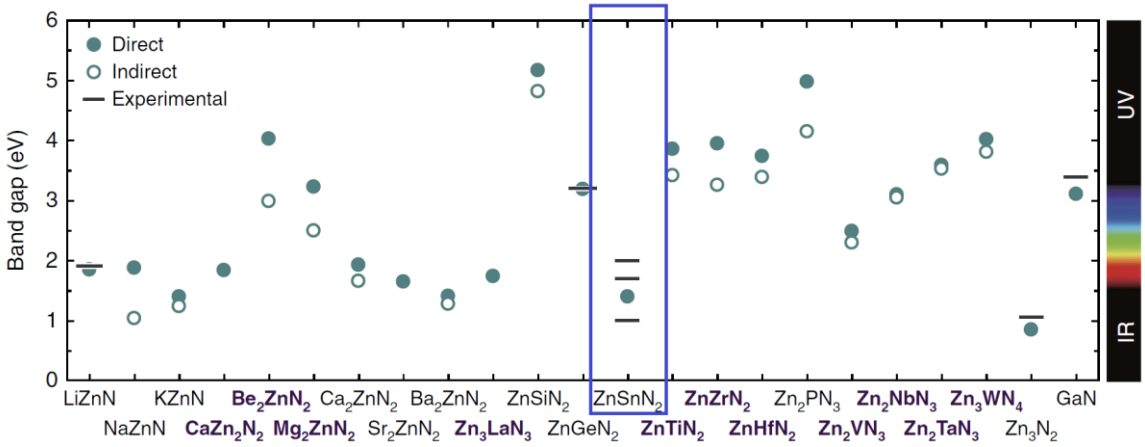

Figure I. 5: Theoretical and experimental bandgap of ternary zinc nitride [18]

Figure I. 5 shows the theoretical and experimental bandgap of those materials, summarized by Y.Hinuma *et al.* [18]. According to their research, the combination of zinc and IA (Li, Na, K), IIA (Be, Mg, Ca, Sr, Ba) elements and nitrogen produces materials with bandgap in the range from 1.5 to 2.0 eV approximately. They are so promising as to be used as top cell absorber material of tandem cell as an alternative to III-V and perovskite. However, in ambient condition, the IA and IIA react quickly with water and oxygen to create hydroxide

and oxide layers, this leads to difficult ternary material fabrication, as well as durability and stability. We focus hereby on the $ZnSnN_2$ material line, the material bandgap ranges from 1.0 to 2.0 eV based on reported computational and experimental results. It is so a potential candidate satisfying the criteria of the availability (earth-abundant) and low cost of used raw materials. Nevertheless, even if computational results are promising, few experimental data are available, it is then a fully innovative research way.

I.2 Zn-IV-N_2 semiconductors

The first-principle study of ternary Zn-IV-N_2 semiconductors, where IV = Si, Ge or Sn, was done in 2008 by Tula R. Paudel and Walter R. L. Lambrecht to show the ground-state and phonon related properties [19]. It indicates that the crystal structure of these compounds is wurtzite-derived-type orthorhombic as well as their ground-state structural properties and phonon related quantities look close to those of III-N compounds. Other properties have continued to be calculated, such as the elastic constants and compliances, the piezoelectric tensor and spontaneous polarization, the non-linear optical and linear electro-optic coefficients that are determined in the local density approximation (LDA) [20], [21].

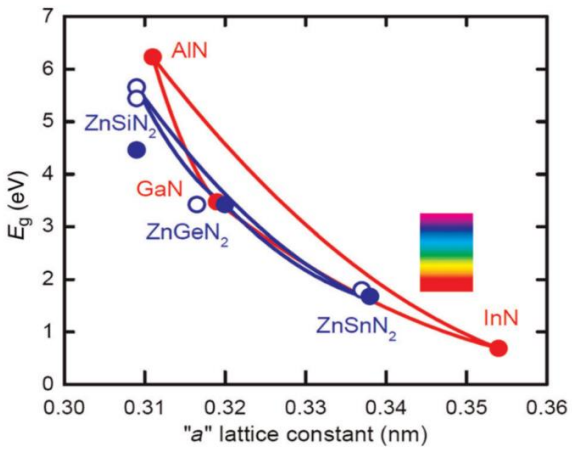

Figure I. 6: *The band gaps versus "a" lattice constant for III-nitrides and Zn–IV-nitrides* [22]

Furthermore, the crystal structure parameters of Zn-IV-N_2 semiconductors were calculated by using the full–potential linearized muffin-tin orbital (FP-LMTO) using both the local

density approximation (LDA) and the generalized gradient approximation (GGA)[21], [23]. **Figure I. 6** shows the relationship between bandgap and "a" lattice constants of Zn-IV-Nitrides compared to III-Nitrides; the same behaviour [22] can be observed.

The results of band structure elucidate $ZnSiN_2$ as an indirect band gap material, whereas $ZnSnN_2$ and $ZnGeN_2$ are determined as direct bandgap materials; the band gap energies are calculated by A.Punya *et al.* [20] by using LDA, GGA and quasiparticle self-consistent GW methods (QSGW), summarized in **Table I. 2**.

Table I. 2: Bandgap (eV) of Zn-IV-N2 semiconductors calculated by A.Punya et al. [23]

Compound		LDA	GGA	QSGW
$ZnSiN_2$	Indirect	3.60	3.23	6.01
	Direct	3.84	3.45	6.26
$ZnGeN_2$	Direct	1.66	1.57	3.99
$ZnSnN_2$	Direct	0.55	0.35	2.64

I.3 $ZnSnN_2$: From theory to experiment

I.3.1 Theory review

$ZnSnN_2$ is a member of ternary Zn-IV-N_2 semiconductors, the most stable structure of bulk $ZnSnN_2$ was given to be the orthorhombic $Pna2_1$ phase by calculating the total energy per unit cell, band structure and electronic density of states [24] (**Figure I. 7)**.

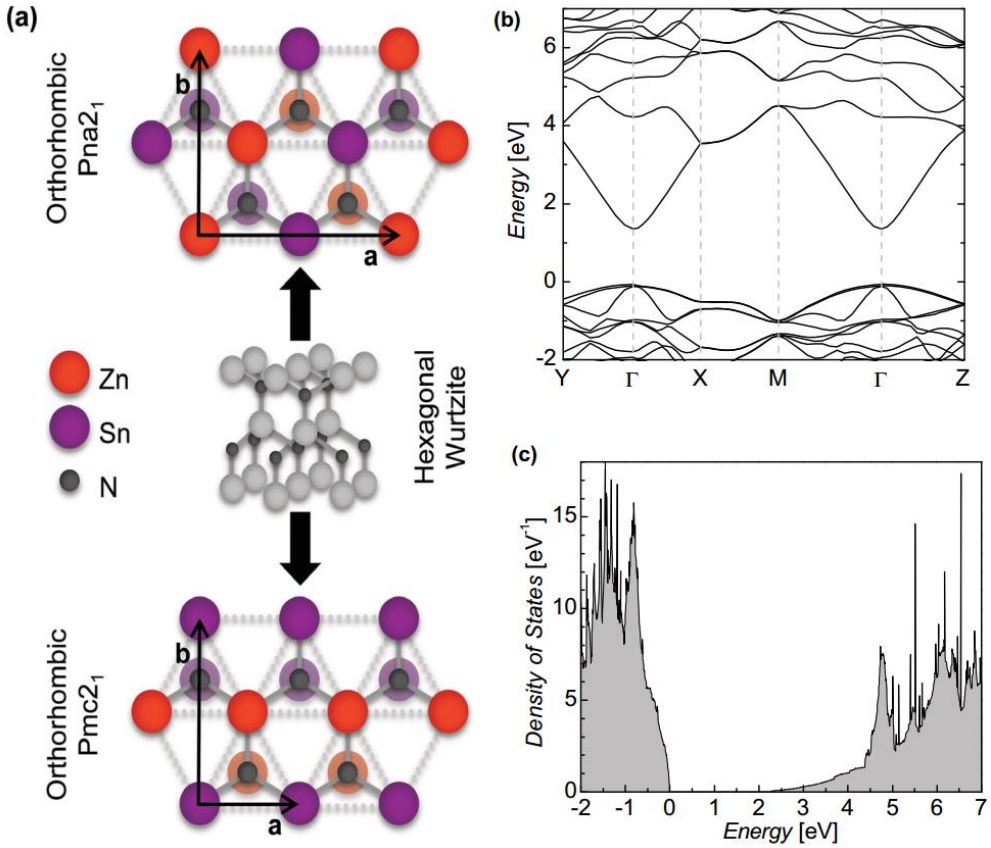

Figure I. 7: *(a) Schematic of the predicted wurtzite-derived structure of $ZnSnN_2$ including two possible orthorhombic structures, $Pmc2_1$ or $Pna2_1$, (b) Band structure and (c) electronic density of states of orthorhombic $Pna2_1$ $ZnSnN_2$* [24]

Paul C. Quayle *et al* [25] illuminated a wurtzite-like diffraction spectrum by described octet-rule-preserving arrangements of the atoms in hetero-valent ternary nitride structures. In addition, they used a pseudopotential plane wave method, LDA, GGA and FP-LMTO to calculate the lattice parameters, total energy, formation energies; and QSGW to calculate band structure of $ZnSnN_2$ and $ZnGeN_2$. Their results reveal the similarities between $Pna2_1$ and $Pmc2_1$ in band gap and lattice parameters of $ZnSnN_2$; and the difference in the formation energies between $Pna2_1$ and $Pmc2_1$ is only 16 meV/formula unit in LDA calculation. The formation energy of $ZnSnN_2$, which is defined by the enthalpy change of the following reaction,

$$Zn\ (hcp) + Sn\ (diamond) + N_2\ (gas) \rightarrow ZnSnN_2$$

where zinc is in hexagonal close-packed structure, tin is in diamond structure and nitrogen is at gas state. Based on FP-LMTO method [21], the calculated formation energies of $ZnSnN_2$ are -1.67 eV/formula unit (in LDA) and -2.32 eV/formula unit (in GGA). On the other hand, the results obtained by S. Chen *et al* [26] gave very small values, -0.17 eV/formula unit ($\alpha = 0.31$), -0.13 eV/formula unit ($\alpha = 0.25$) by using the hybrid functional calculation. Besides that, when they used the developed scheme proposed by V. Stevanovic et al [27], the energy of formation is equal to -0.14 eV/formula unit. In addition, six possible defects of $ZnSnN_2$ are given and explained. The challenge is achieving single-phase synthesis due to the very narrow window of equilibrium phase stability shown in **Figure I. 8** [26]**.**

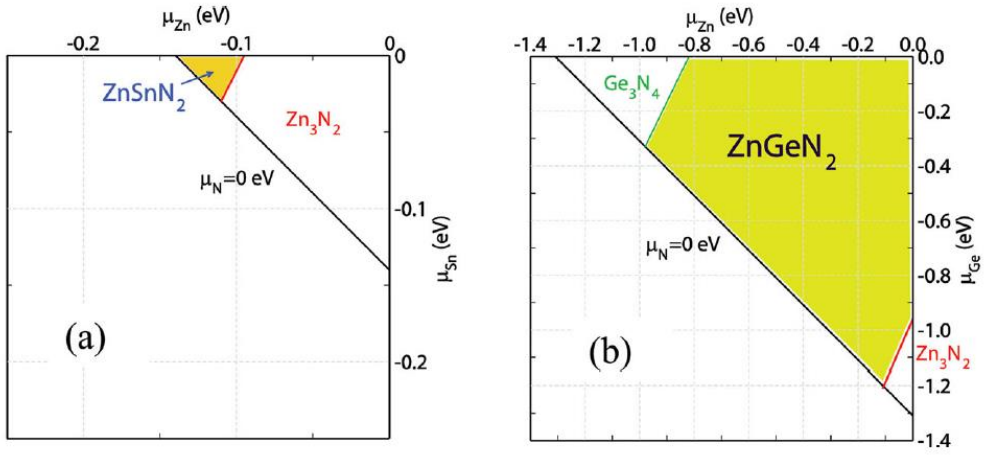

Figure I. 8: *The yellow regions provide stabilized single-phase $ZnSnN_2$ (a) and $ZnGeN_2$ (b), obtained by calculated chemical potentials of the component elements (μZn, μSn, μGe, μN)* [26].

The cation disorder degree plays an important role in crystallography, the predicted structures of $ZnSnN_2$ are ordered orthorhombic $Pna2_1$ and disordered wurtzite-like lattice structure [22], [25], [28]–[32]. The X-ray powder diffraction spectra calculation of L. Lahourcade *et al.* [24] are described in **Figure I. 9(a)**. Observably, the characteristic peak positions of $Pmc2_1$, $Pna2_1$ and average wurtzite structures are relatively similar, except $Pna2_1$ has 2 characteristic peaks at position $2\theta = 20 - 21°$. Furthermore, the fundamental band gap of $ZnSnN_2$ in the range 1 – 2 eV depend on degree of cation disorder and Burstein – Moss effect [24], [28], shown in **Figure I. 9(b)**.

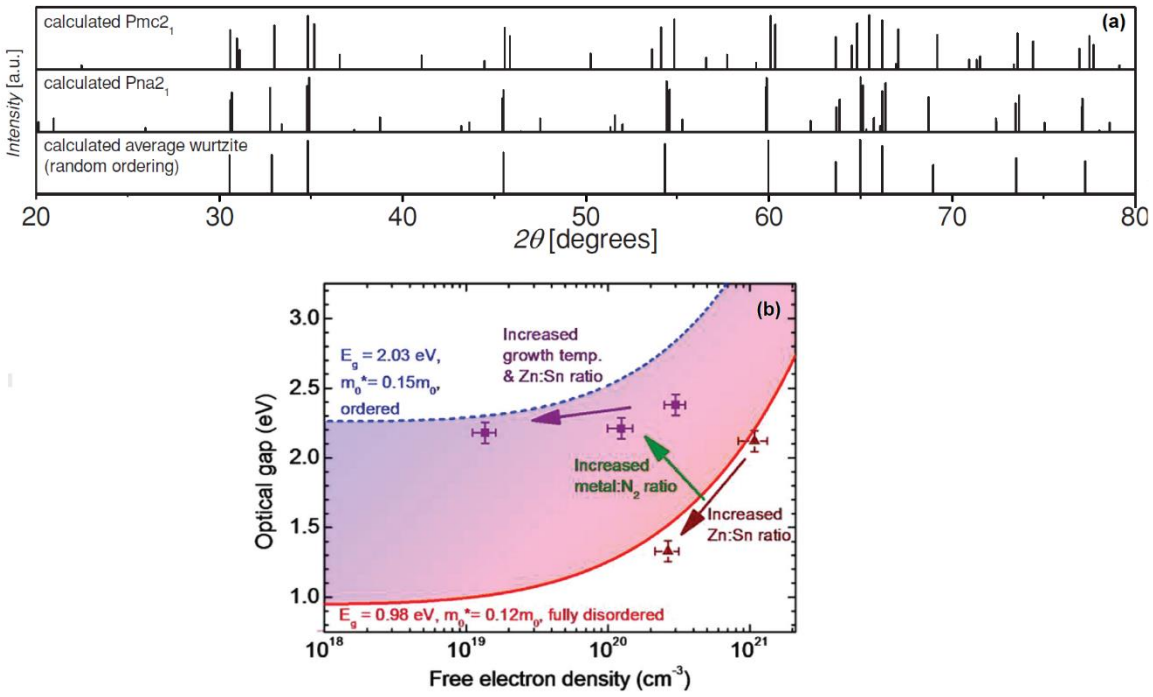

Figure I. 9: *(a) Simulated powder XRD patterns of $ZnSnN_2$* [24]*; (b) Bandgap versus free electron density of $ZnSnN_2$*[28]

Effective mass of $ZnSnN_2$ (m_e^*) is also a well-researched parameter, most of results give small m_e^* values, approx. $0.1m_0$ [23], [24], [28], [33] (where m_0 denotes the free electron mass). The relationship between effective mass and electron concentration is represented by the following equations (1), (2).

$$n_e = N_C \, exp\left(-\frac{E_C - E_F}{kT}\right) \tag{1}$$

$$N_C = 2\left(\frac{2\pi m_e^* kT}{h^2}\right)^{\frac{3}{2}} \tag{2}$$

where E_F is the Fermi level, E_C is the minimum energy of the conduction band, and N_C is a concentration coefficient that depends on temperature, k is Boltzmann's constant and h is Planck's constant.

The electron mobility is defined by the equation (3), (4):

$$\vec{v} = \mu\vec{E} \tag{3}$$

$$\mu = \frac{e\bar{\tau}}{m_e^*} \quad (4)$$

where e is the electron charge, $\bar{\tau}$ the average scattering time, and $\vec{E}$ the electric field.

According to these equals, small m_e^* values lead to the high electron mobility (μ) and the low carrier density (n).

The work function and valence-band onset were measured by using ultraviolet photoelectron spectroscopy (UPS) or X-ray photoelectron spectroscopy (XPS), approximately 4.0 eV and 1.2 eV below the vacuum level, respectively [34]. Additionally, the work function is described as proportional to the amount of oxygen contamination; the more oxygen content, the higher the work function is.

Up to now, $ZnSnN_2$ is still a new material and was only introduced in research in recent years, its first synthesis was published by Coronel et al [35] and Feldberg et al [36] in 2012. Currently, this material is being studied more extensively, the calculation results of the crystal structure, the electronic structure will help to evaluate and interpret the experimental results.

I.3.2 Preparation of $ZnSnN_2$

I.3.2.1 Plasma-assisted vapor-liquid-solid method

Quayle *et al.* synthesized polycrystalline $ZnSnN_2$ by using a plasma-assisted vapor-liquid-solid method [22], this experiment was carried out at high temperatures, 390°C and 525°C, and the Zn composition in the layers was 8 and 45%, respectively. Their X-ray diffraction (XRD) results show the diffraction peaks that are characteristic of Sn and Zn phases beside the $ZnSnN_2$ phase. In addition, the lattice parameters of the orthorhombic structure were a=6.75 Å, b=5.84 Å and c=5.42 Å. The optical bandgap was obtained by photoluminescence excitation (PLE) spectroscopy and was around 1.7eV.

I.3.2.2 Plasma-assisted molecular beam epitaxy (PAMBE)

$ZnSnN_2$ thin films were fabricated on yttrium-doped zirconia substrates by using PAMBE system [37], [38] in active nitrogen (10^{-5} torr) and 150 W of RF power. The effects of substrate temperature (300°C to 700°C) and Zn:Sn flux ratios (1:1 to 20:1) were analysed. The $ZnSnN_2$ thin films obtained by this method are high-purity and monocrystalline as well as highly textured and polycrystalline, all the films show a monoclinic structure of $ZnSnN_2$.

However, the subsequent publications by T. Veal *et al.* [28] and R. Makin *et al.* [29] demonstrate the existence of both wurtzite structure (cation disordered) and orthorhombic structure (cation order).

I.3.2.3 High-pressure metathesis reaction

F. Kawamura *et al.* show that a high-pressure metathesis reaction can be used to synthesize $ZnSnN_2$ crystals [31], $ZnSnN_2$ is synthesized by the following equation:

$$ZnF_2 + SnF_4 + 2Li_3N + 3LiF \rightarrow ZnSnN_2 + 9LiF$$

The temperature and pressure applied in this study ranged from room temperature to 1000ºC and from 2.5 to 7.7 GPa, respectively. Single-phase $ZnSnN_2$ crystals were synthesized by this method, and the bandgap was measured at 1.4 eV by using the diffuse reflection method.

I.3.2.4 Magnetron sputtering deposition:

The sputtering PVD-technique is one of the most commonly used methods for producing, tailoring and engineering materials to improve thin-film device performance. The primary advantages of using sputtering are high deposition rates, applicability to a large variety of materials, high-purity and adhesive films, ability to coat heat-sensitive substrates (glass substrates, plastic substrates) and automation capabilities [39].

In addition, the fabrication of $ZnSnN_2$ thin films by vapor-liquid-solid method, molecular beam epitaxy or high-pressure metathesis reaction are all done at high temperatures, up to 1000°C that, *in fine*, are not compatible with the targeted application. Therefore, the

sputtering method is used predominantly in the synthesis of $ZnSnN_2$, this makes sense in reducing production costs based on reduced power usage. **Table I. 2** summarizes the theoretical and experimental reported values of the electrical properties of $ZnSnN_2$: the band gap varies in range 0.58 to 2.62 eV, the highest carrier mobility equals to 24 cm/(V.s) [33] and the lowest carrier concentration equals to $4x10^{16}$ cm^{-3} [40]. **Table I. 3** reports the same kind of information for the lattice parameters of $ZnSnN_2$: a rather good agreement is obtained between calculation and experiment results for Orthorhombic $Pna2_1$ phase structure.

Table I. 3: Reported optical and electrical properties of $ZnSnN_2$ determined by computation and experiment

Methods	Bangap (eV)	n (cm^{-3})	μ ($cm.V^{-1}s^{-1}$)
Computation			
LDA [21]	0.58		
QSGW [21]	1.94		
0.8∑ approximation[21]	1.65		
HSE06 density functional [41]	1.40		
QSGW [41]	2.02		
PBE0 funcrional [42] – monolayer	2.39		
PBE0 funcrional [42] – bilayer	2.62		
Experiment			
Co-sputtering in RF mode [41]	2.10		
Vapor–liquid–solid method[22]	1.70		
Plasma-assisted MBE [36]	2.10		
Plasma-assisted MBE [37]	2.21 – 2.38	$3.0x10^{20}$ to $1.1x10^{21}$	10
Plasma-assisted MBE [28]	1.33 – 2.38	$1.4x10^{19}$ to $1.1x10^{21}$	
High-pressure metathesis reaction [31]	1.4		
RF Magnetron Sputtering [24]	1.9 – 2.2	$5.0x10^{19}$ to $1.0x10^{21}$	10
RF Magnetron Sputtering [43]	1.25 – 1.51	$2.8x10^{20}$ to $5.1x10^{20}$	
Co-sputtering in RF mode [44]	1.0 – 1.4	$1.8x10^{18}$ to $4.0x10^{20}$	0.5 – 11
Co-sputtering in RF mode [40]		$4.0x10^{16}$ to $1.96x10^{18}$	0.28 – 8.76

Co-sputtering in RF mode [34]	1.9	$3.6x10^{20}$	2.4
Co-sputtering in RF mode [45]	1.96 – 1.77	$4.99x10^{18}$	11.1 – 15.5
Co-sputtering in RF mode [46]		$3.97x10^{18}$ to $2.42x10^{18}$	14.5 – 11.1
DC Magnetron Sputtering [47]	1.9	$2.3x10^{17}$ to $1.6x10^{18}$	1.86 – 3.98
DC Magnetron Sputtering [48]	1.64 – 1.70	$2.77x10^{17}$ to $6.78x10^{17}$	0.37 – 2.07
DC Magnetron Sputtering [49]	1.67 – 1.73	$9.58x10^{17}$	3.79
Magnetron co-sputtering [50]	1.8	$1.0x10^{19}$	3.8
Co-sputtering RF_{Zn} – DC_{Sn} [33]	2.0	10^{21} -10^{19}	2 – 24
Co-sputtering RF_{Zn} – DC_{Sn} [51]	1.43	$9.92x10^{16}$ to $1.88x10^{19}$	22.7 – 4.93

Table I. 4: Comparison of calculated and experimental lattice parameters of $ZnSnN_2$

	Methods	a (Å)	b (Å)	c (Å)
Calculated				
Orthorhombic $Pna2_1$	ABINIT - LDA [19]	5.85	6.76	5.58
	FP-LMTO - LDA [23]	5.70	6.59	5.41
	FP-LMTO - GGA [23]	5.80	6.70	5.53
	Hydrid HSE06 [24]	5.84	6.72	5.46
	DFT code VASP [36]	5.846	6.755	5.534
Orthorhombic $Pmc2_1$	Hydrid HSE06 functional [24]	5.771	3.388	5.427
Experimental				
Orthorhombic $Pna2_1$	Vapor–liquid–solid method[22]	5.842	6.753	5.462
	Sputtering in DC mode [47]	5.853	6.741	5.498
	High-pressure metathesis reaction [31]	5.848	6.753	5.464
	Co-sputtering in RF mode [45]	5.60	6.74	5.42
		5.70	6.74	5.43
		5.79	6.74	5.59
	Co-sputtering in RF mode [46]	5.79	6.72	5.45
Monoclinic	Plasma-assisted molecular beam epitaxy (PAMBE)[36]	3.395	3.400	5.534

I.4 **Manuscript overview**

$ZnSnN_2$ has only been studied for about a decade; while the first calculation was done in 2008 [19], the synthesis of $ZnSnN_2$ started in 2013 [22], [24], [37]. The structure and basic properties of $ZnSnN_2$ are still being studied by varying parameters during fabrication. However, the relationship between the previous results and the applicability of $ZnSnN_2$ in the photovoltaics field is still unknown.

Based on the literature review of $ZnSnN_2$ material, my thesis will focus deeply on the study of the effect of the different parameters that support the sputtering process to elaborate $ZnSnN_2$ thin films. The effects of sputtering atmosphere and target biasing will be described in Chapter II. Other sputtering conditions such as sputtering pressure, substrate temperature and post deposition annealing (RTA) will be described in Chapter III. The difference of co-sputtering with two elemental targets and sputtering with compound target will be explained in Chapter IV. The fabrication of aluminum doped zinc oxide and p-type tin oxide that will be used to fabricate photodetector devices will be shown in Chapter V. An initial assessment of the photoelectric properties will be presented in Chapter VI.

Chapter II: **SPUTTERING ATMOSPHERE AND TARGET BIASING**

After a brief introduction to the sputtering process and the equipment that has been used all along this work, this chapter will focus on the effects of the sputtering atmosphere as well as of the target biasing on the properties of the $ZnSnN_2$ thin films.

Whatever the sputtering atmosphere is, two metallic targets of Zn and Sn are used in a reactive co-sputtering scheme. Target biasing can be made in a RF or DC mode. Sputtering atmosphere is then either a pure nitrogen, a nitrogen/argon mix, or a nitrogen/hydrogen/argon mix.

Physical properties of the deposited films are investigated by SEM, EDX and XRD. Their electrical and optical properties are determined from resistivity and Hall measurements and UV-Vis spectroscopy, respectively.

II.1 **Reactive sputtering**

Reactive sputter deposition is a process in which the reaction takes place between the atoms removed from the target and the gaseous species, such as oxygen or nitrogen (called "reactive gas"). Reactive gases can be present in either molecular or "activated" species, activation process can occur according to the following equations to form new fragments that are more chemically reactive and easier to absorb [52]:

- $N_2 + e^- \rightarrow 2N_o$ and $NH_3 + e^- \rightarrow N_o + 3H_o$
- $O_2 + e^- \rightarrow 2O_o$ then $O_o + O_2 \rightarrow O_3$

However, nitrogen and oxygen are light ions, with atomic masses 14 u (or Da)* and 16 u, respectively; they are unattractive in sputtering

. This is explained by the relationship between sputtering yield and energy transfer mass factor [53], described in following equations:

$$Y = (6.4 \times 10^{-3}) M_t \gamma^{5/3} E_i^{0.25} \left(1 - \frac{E_{th}}{E_i}\right)^{3.5} \quad (2.1)$$

where Y is the sputtering yield, M_t is the target particle mass (in atomic mass unit), E_i is the initial energy of the incident atom (in eV), E_{th} is the threshold energy for sputtering (in eV), γ is the energy transfer mass factor defined by:

$$\gamma = \frac{4 M_t M_i}{(M_t + M_i)^2} \quad (2.2)$$

with M_i the incident particle mass (in atomic mass unit).

In addition, the energy loss of the reflected particle is dependent on the atomic masses M_t, M_i and the angle of impact, θ , as depicted in **Figure II. 1**. According to the laws of

*1 u = 1 Da (Dalton) = 1.66053906660 x 10^{-27} kg.

conservation of energy and the conservation of momentum [54], the energy that is transferred by the physical collision between hard spheres, E_t, is given by Equation 2.3:

$$\frac{E_t}{E_i} = \frac{4M_tM_i}{(M_t+M_i)^2}\cos^2\theta \qquad (2.3)$$

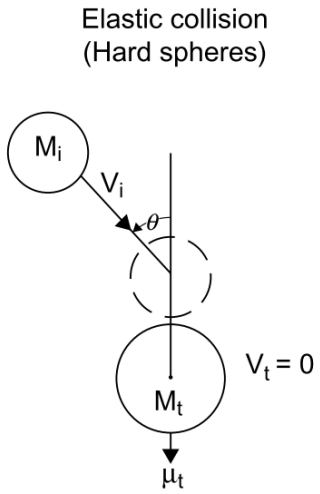

Figure II. 1: *Collision of incident particle (M_i) and target particle (M_t); after collision M_t moves along path connecting the center line of the sphere μ_t* [54].

As it can be deduced from the equation (2.3), the transferred energy is maximum when $\cos\theta = 1$ (θ = zero degree) and $M_t = M_i$, that means the atomic mass of the bombarding ion is important to the sputtering yield. For sputtering heavy elements, krypton (84 u), xenon (131 u), and mercury (201 u) are then favorably used, and light ions such as nitrogen (14 u) are unattractive and not effective in sputtering. Thus, to aid reactive sputtering, a heavy inert gas is used in conjunction with the reaction gas. Based on its cost and non-toxicity, argon (40 u) is widely used.

Thus, a sputtering environment formed by a mixture of argon and nitrogen has been used in most studies related to the fabrication of $ZnSnN_2$ thin films by the sputtering method [24], [33], [34], [43]–[46], [51]. Concerning the free carrier density that is the macroscopic property that is often considered as characteristic of the material potentialities, the lowest value ($4x10^{16}$ cm^{-3}) was obtained by using RF co-sputtering and post-annealing in 5%H_2 in

N_2 atmosphere [55], while the highest (22.7 $cm.V^{-1}s^{-1}$) was obtained using $Zn_{RF}Sn_{DC}$† co-sputtering in mixed N_2/Ar atmosphere [51]. However, literature results report on fixed sputtering gas composition, its parametric study has not been reported, yet.

II.2 Sputtering system and characterization methods

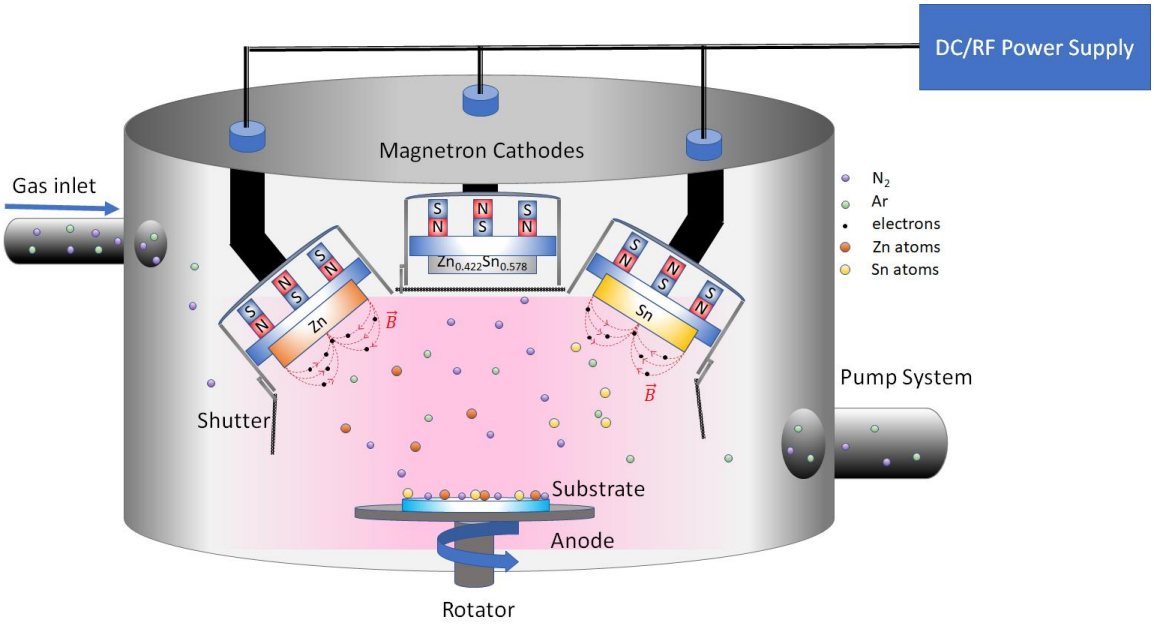

Figure II. 2: *Schematic of the magnetron-sputtering chamber of the Alliance Concept CT200 equipment.*

The deposition system that was used all along my work is an Alliance Concept CT200 equipment. This equipment has 3 separate deposition chambers, a transfer chamber and a loadlock. It is composed of three 2" target holders (cathodes) that are configured in a confocal arrangement, the distance between the targets and substrate holder is approximately 5 cm and the sputtering gun is inclined at 20°. All cathodes are magnetron equipped. The substrate is located on a rotating holder that improves the film uniformity. Different gas inlets are available; three of them have been used for Ar, N_2 and H_2/N_2 (5% H_2) gas inputs. A schematic of the sputtering chamber is shown in **Figure II.2**. Each target can be fed using either a DC or a RF generator. Metals are deposited using either the co-

† All along this manuscript, the following writing rule will be adopted concerning the way the films have been deposited: $Zn_{XX}Sn_{YY}$ where XX and YY are either DC or RF and correspond to the power supply that has been used on each target during deposition.

sputtering of two separate Zn (purity 99.99%) and Sn (purity 99.99%) targets or the sputtering of a single $Zn_{42.2}Sn_{57.8}$ target (purity 99.95%). A preliminary assessment shows that the plasma cannot be ignited and maintained when the gas flow is less than 10 sccm and the deposition pressure less than 0.01 mbar. In this work, the rotation speed of the substrate holder was set to 20 rpm and, except otherwise noted, the argon flow was fixed to 10 sccm and film deposition was made without intentional heating. The operating pressure in the chamber is 2.10^{-2} mbar (base pressure of 10^{-8} mbar). The effect of operating pressure will be discussed in Chapter III.

After the film deposition, the film thickness is measured using surface profilometry after a physical mark was made on the thin film (DektakXT stylus surface profiler).

The surface morphology of the $ZnSnN_2$ thin films is observed by using scanning electron microscopy SEM (field emission gun (FEG) equipment: Zeiss Ultra 55). The film composition is investigated by energy-dispersive X-ray spectroscopy (EDS Quanta 200 / Flash 4010 from Bruker inserted in the SEM). The composition in light elements (such as O and N) cannot be retrieved, only the Zn and Sn elements are measured after sensor calibration. $ZnSnN_2$ is considered stoichiometric when Zn/(Zn+Sn) is equal to 50%. When this ratio is higher than 50%, material is Zn-rich, otherwise it is Sn-rich.

Electrical characteristics, resistivity, carrier concentration and mobility, are determined from Van der Pauw resistivity measurement method and Hall voltage measurements made with a 4-probe system (Nanometrics HL 5500 PC).

The optical properties are determined from UV-Vis spectrometry (Perkin Elmer).

The crystal structure is analyzed by using X-ray diffraction equipment (Rigaku SMARTLAB) in Bragg-Brentano mode with Cu-Kα radiation.

Except otherwise noted, all samples have been deposited on Eagle XG substrates of 1"-square dimensions.

II.3 Investigation of sputtering rate in argon environment

II.3.1 Each metallic element separately

The purpose of this survey is the determination of the sputtering rate of each metallic target (Zn and Sn) under pure argon atmosphere. The deposition rate was evaluated by measuring the thickness of thin films obtained from a 10 minutes-long process. This experiment was performed on new targets to ensure the surface area of targets and so the power density. Effectively, as processes are going on, the magnetron sputtering process makes erosion of the target. Its effective surface area is then modified time running, as shown in **Figure II. 3**, and so might affect the power density (new targets are 6 mm thick). The sputtering rate of Zn and Sn is different, consequently, the erosion groove of each target is also different after the same period of use. It implies that the calibration of the deposition process shall be done regularly in order to amend the deposition rates.

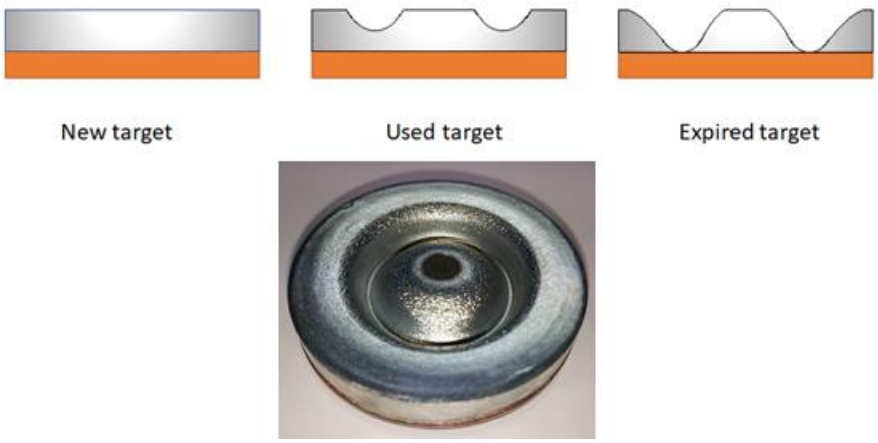

Figure II. 3: *Due to the magnetron sputtering process, a circular pattern of erosion is created on targets as they are used (example of Sn target).*

The thickness of the pure metallic thin films is shown in **Figure II. 4**. The deposition time was 10 minutes

The deposition rate of Sn is almost 2 times higher when using DC mode than using RF mode. Even if deposition conditions were different, such a ratio range in deposition rate values was observed for other metals as aluminum [56](1.86) and copper [57](1.89). In contrast, the sputtering rate of Zn is higher using RF mode than when using DC mode. This

is rather usual for poorly conductive materials but less common for metals. Nevertheless, the DC sputtering rate of Sn is almost double than that of Zn that is a rather common figure [58].

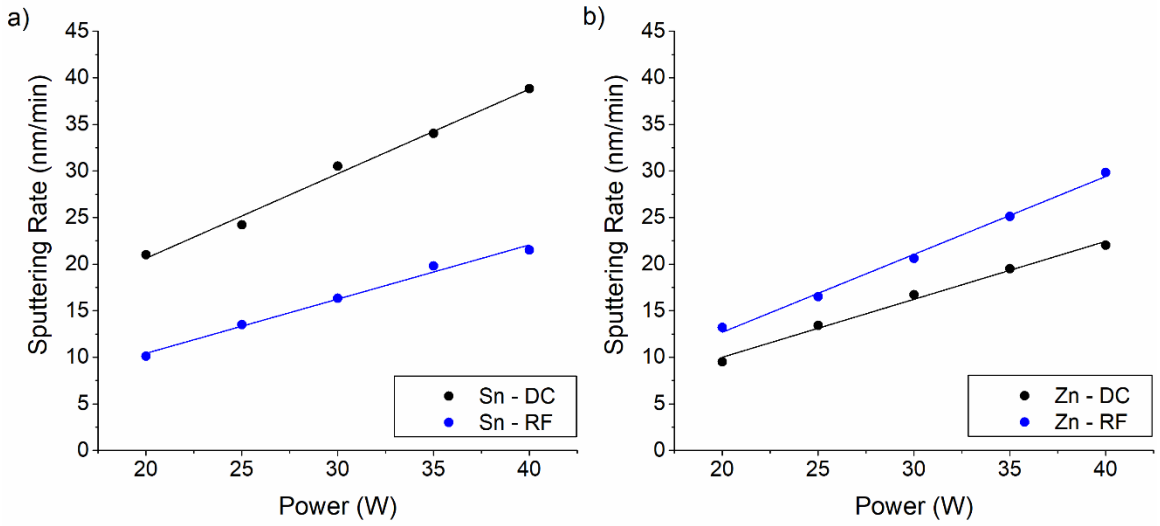

Figure II. 4: *Thickness and corresponding sputtering rate in DC and RF modes for: a) Sn and b) Zn (Ar flow rate was 10 sccm and deposition pressure 2.10^{-2} mbar).*

Based on the theoretical values of density and molecular weight for each metal and assuming that both targets have the same porosity, the predicted thickness ratio of Zn to Sn is given by Equation 2.5:

$$\frac{d_{Zn}}{d_{Sn}} = \frac{\rho_{Sn} M_{Zn}}{\rho_{Zn} M_{Sn}} = 0.588 \qquad (2.5)$$

where d is the thickness of corresponding films (nm), ρ_{Sn} and ρ_{Zn} are the density of Sn (7.625 g/cm^3) and Zn (7.14 g/cm^3), and M_{Sn} and M_{Zn} the atomic mass of Sn (118.71 u) and Zn (65.37 u), respectively.

The $Zn_xSn_{1-x}N_2$ thin film is considered as stoichiometric when the atomic percentage of Zn and Sn are equal (x=0.5). Combined with the sputtering yield rates derived from **Figure II. 4**, the stoichiometry for ZnSn could be achieved, for example, by those configurations:

- $Zn_{DC}Sn_{RF}$ configuration: 25 W DC applied to Zn; 40 W RF applied to Sn.
- $Zn_{RF}Sn_{DC}$ configuration: 25 W RF applied to Zn; 29 W DC applied to Sn.
- $Zn_{DC}Sn_{DC}$ configuration: 25 W DC applied to Zn; 22 W DC applied to Sn.
- $Zn_{RF}Sn_{RF}$ configuration: 25 W RF applied to Zn; 51 W RF applied to Sn

II.3.2 Compound Zn_xSn_{1-x} metallic thin films

Based on the results presented in Section II.3, first experiments to deposit stoichiometric metallic ZnSn layers used the $Zn_{DC}Sn_{RF}$ configuration with parameters mentioned in section II. 2, i.e. the Ar flow rate was 10 sccm and deposition pressure 2.10^{-2} mbar, 25W-DC‡ and 40W-RF power supplies applied to Zn and Sn target, respectively. After the deposition, the composition determined from EDS measurements was 47.8% Zn and 52.1% Sn so not exactly 1:1 but not so far. The RF power applied to Sn target was then decreased to 35 W and the zinc/tin ratio so obtained was practically 1:1, 50.09% Zn and 49.91% Sn from EDS measurements.

II.4 Sputtering in mixed nitrogen and argon environment

II.4.1 First tests of $Zn_xSn_{1-x}N_2$ thin films

Then, nitrogen was introduced into the deposition chamber together with the argon. The power supplies were then 25 W-DC and 35 W-RF, for Zn and Sn targets, respectively. The nitrogen gas flow rate was varied from 0 to 30 sccm with a 5 sccm step, the argon flux is fixed at 10 sccm (N_2/Ar ratio is then in the range 0 to 3) and the deposition pressure is kept as 2.10^{-2} mbar. Deposition process was carried out for 25 minutes to ensure sufficient thickness of the films for EDS measurements. The change in film composition and thickness are illustrated in **Figure II. 5**. The data at nitrogen flux =0 correspond to the metallic film of section II.4.1.

There is a significant change in the composition of the thin film with the nitrogen flux value. The film becomes zinc-rich as soon as nitrogen (5 sccm) is added in the sputtering atmosphere; the atomic percent of zinc increases then considerably from 50% to 65%. Then it increases slightly, to approximately 68%, for 10 sccm (N_2/Ar = 1) of nitrogen and exhibits less pronounced changes, remaining at values around approximately 70% for higher

‡ All along this manuscript, the following writing rule will be adopted concerning the way the power is applied on the different targets: XXW-YY where XX is the power applied and YY the sputtering mode, either DC or RF.

nitrogen fluxes. Besides that, the thickness of the layer exhibits a fast decrease, from 530 nm (pure argon atmosphere) down to 280 nm (for 30 sccm flow rate of nitrogen, (N_2/Ar = 3).

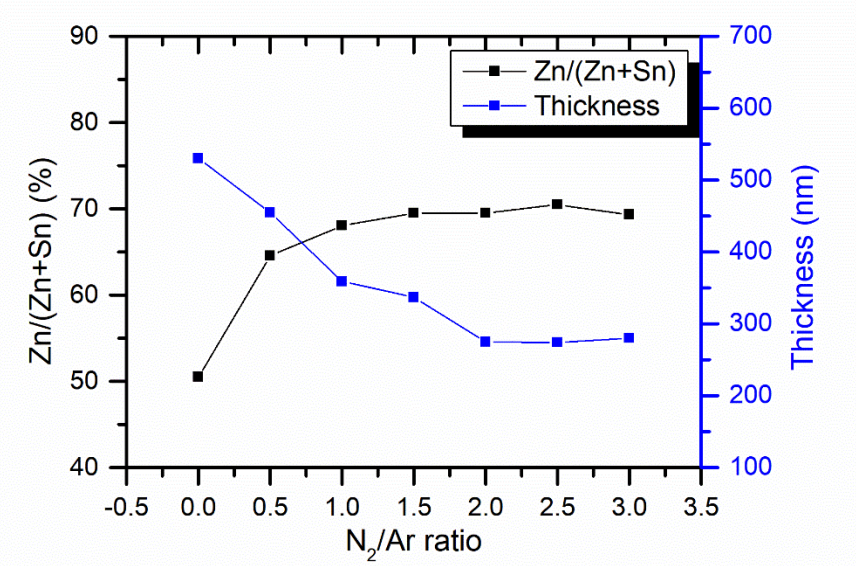

Figure II. 5: *Zn/(Zn+Sn) ratio and thickness of $ZnSnN_2$ ($Zn_{DC}Sn_{RF}$ series) thin films versus nitrogen flow rate (Ar flow rate:10 sccm, deposition pressure: 2.10^{-2} mbar, 25W-DC applied to Zn and 35W-RF applied to Sn targets).*

It can be concluded that nitrogen decisively modifies the sputtering process, especially having a strong effect in the Sn composition of the films because they become Zn-rich as soon as nitrogen is added. Several origins may be put forward:

(i) The addition of nitrogen increases the gas density in the reaction chamber, reducing the probability of a collision between the gas and the target surface.

(ii) The change in mass of the gas mixture and the different effect of each gas (argon and nitrogen) affecting the sputtering efficiency of both metals.

Since the atomic mass of Sn (118.71 u) is high, it is more efficiently sputtered by argon ions (65.37 u) than nitrogen ions (14 u). The combined effect of above two reasons might explain that Zn-rich compounds are mainly linked to a lower Sn incorporation than a higher Zn one.

(iii) The targets can react with nitrogen to form compounds on their surface, like SnN_2 (146.72 u) or ZnN_2 (93.39 u) that have higher atomic mass than elementary elements (respectively 118.71 u and 65.38 u for Sn and Zn) slowing the sputtering process.

II.4.2 The effect of N_2/Ar ratio on $Zn_xSn_{1-x}N_2$ thin films

In this section, 2 series of films have been produced depending how DC and RF generators were applied to sputtering targets: $Zn_{DC}Sn_{RF}$ and $Zn_{RF}Sn_{DC}$. The nitrogen gas flux was varied from 5 to 40 sccm with a 5 sccm step, argon flux is fixed at 10 sccm. The operating pressure in the chamber is 2.10^{-2} mbar (base pressure is 10^{-8} mbar).

II.4.2.1 $ZnSnN_2$ thin film - $Zn_{DC}Sn_{RF}$ series

As shown on **Figure II. 5**, the value of nitrogen flux modifies the Zn/(Zn+Sn) ratio as well as the deposition rate. Then, the target applied powers were adjusted to stabilize the Zn/(Zn+Sn) ratio around 50% and the sputtering time was tuned to get a film thickness close to 400 nm whatever the nitrogen flux was. The performed experiences are summarized in **Table II. 1**. It has to be noticed that the effect of nitrogen flux on film composition and deposition rate is no more really perceptible for values equal or higher than 25 sccm (N_2/Ar = 2.5): so, the power of generators and process time have been kept constant for those values of nitrogen flux.

Table II. 1: Process parameters for different N_2/Ar flux ratios of sputtering atmosphere. (Power of generators and processing time have been adjusted to get 50/50 Zn/Sn composition and 400nm thick films. (Common parameters are 10 sccm argon flux and $2x10^{-2}$ mbar process pressure)

N_2/Ar flux ratio	DC – Zn (W)	RF – Sn (W)	Zn (at. %)	Sn (at. %)	Time (min)	Thickness (nm)
0.5	25	50	52.2	47.8	19	448
1	25	60	49.8	50.2	20	392
1.5	25	65	49.6	50.4	21	364
2.0	25	67	49.5	50.5	23	366
2.5	25	70	50.8	49.2	25	341
3	25	70	51.0	49.0	25	403
3.5	25	70	50.5	49.5	25	401
4	25	70	50.5	49.5	25	412

Scanning electron microscopy (SEM) was employed to investigate the surface morphology of the $ZnSnN_2$ films, views are shown in **Figure II. 6.**

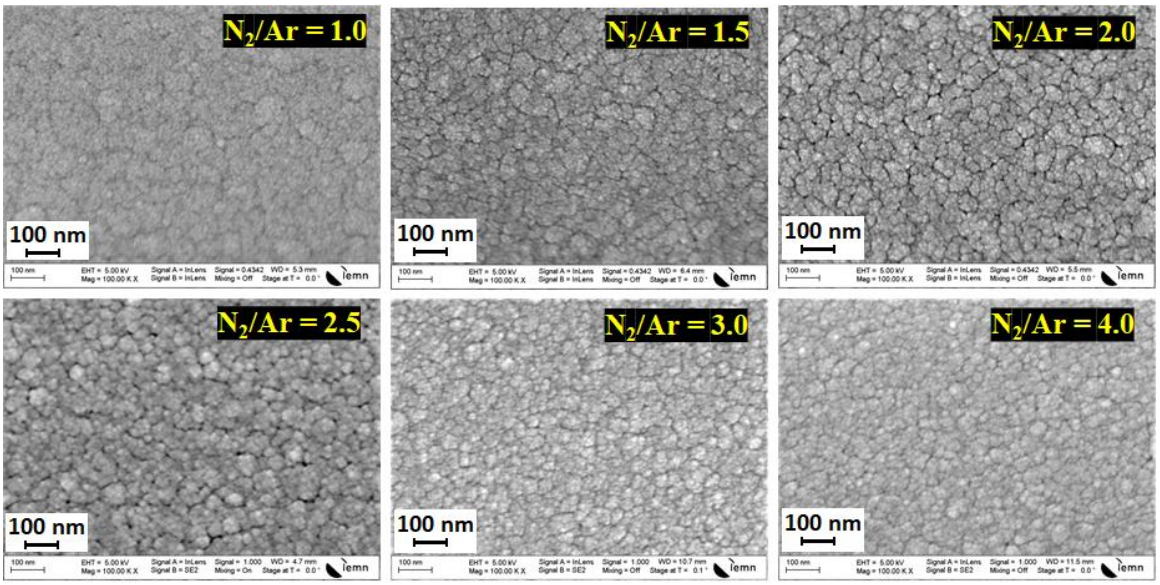

Figure II. 6: *Top surface views of $Zn_{DC}Sn_{RF}$ series under different N_2/Ar ratio deposition atmospheres.*

When the nitrogen content is equal to or less than the amount of argon used (10 sccm, N_2/Ar <= 1), it is difficult to identify grain boundaries, the surface is similar to granular background, the average grain size after deposition is small and the structure tightly arranged. As N_2/Ar ratio is in the range 1.5 to 2.5, the difference of surface morphology is difficult to assess and much more cauliflower-like, interstitial voids can be perceived. At higher N_2/Ar, the grain size is "visually" smaller and the voids become ambiguous.

XRD patterns are presented on **Figure II. 7**. As N_2/Ar ratio is lower than 1.0, the spectra do not exhibit particular peak and the films are rather of amorphous nature. This is consistent with the surface views of **Figure II. 6**. At higher N_2/Ar ratios, XRD data match all the characteristic peaks of crystalline $ZnSnN_2$, particularly, up to seven peaks can be distinguished; they are located at 2θ angles: 30.1°, 32.4°, 34.3°, 45.0°, 53.6°and 59.2° and 65.3° corresponding to (200), (002), (121), (122), (320), (123) and (322) directions [59] [§].

[§] In the following of the manuscript, these seven particular peaks will be referred as the seven characteristic peaks of $ZnSnN_2$.

Although the most stable crystal structure of $ZnSnN_2$ is predicted to be orthorhombic [24], the two characteristic peaks, corresponding to 110 and 011 reflections, at respectively $2\theta = 20°$ and 22° cannot be pointed out on the XRD results (perhaps an occurrence for $N_2/Ar = 3$).

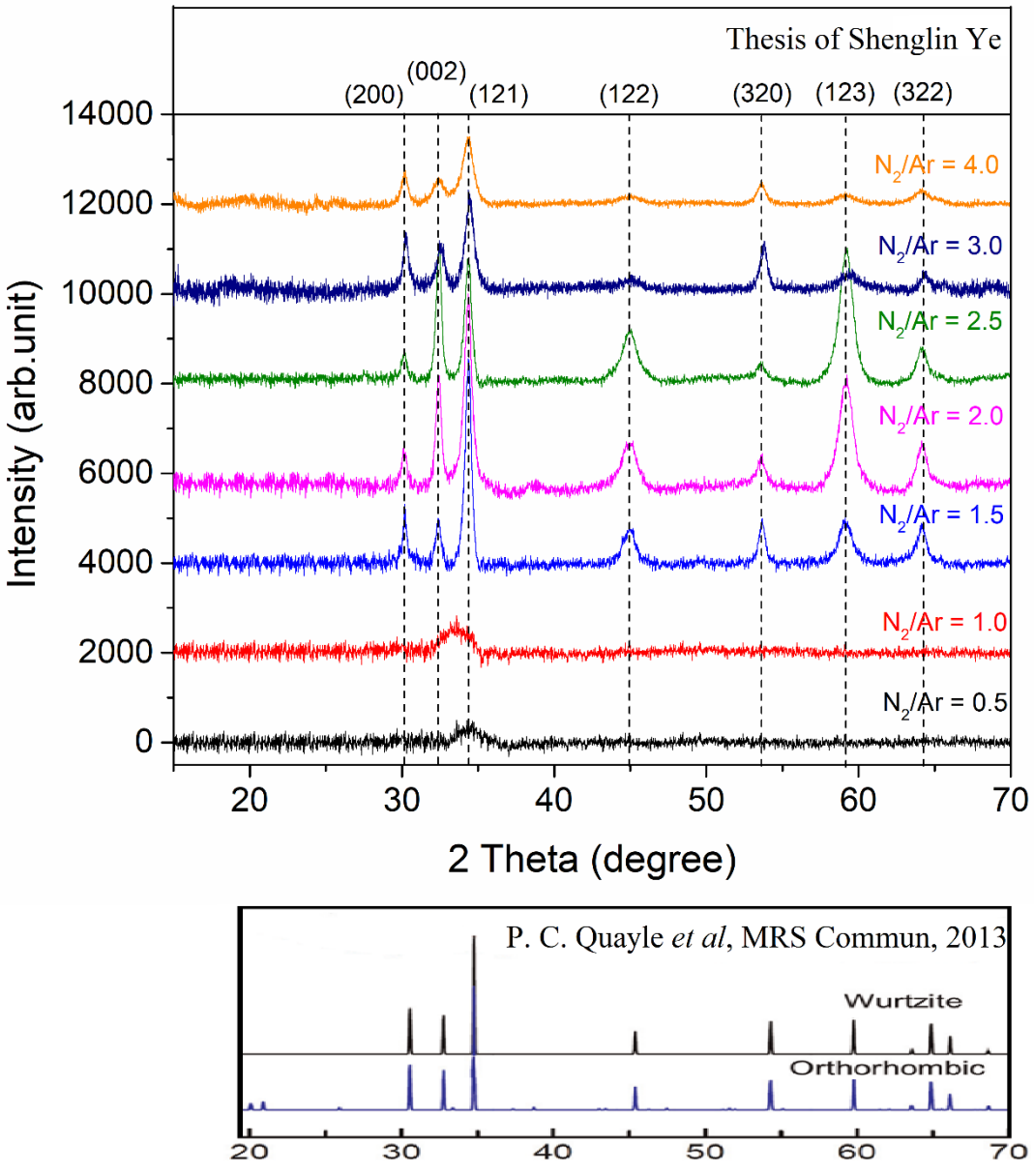

Figure II. 7: *XRD diffractograms of the $ZnSnN_2$ films ($Zn_{DC}Sn_{RF}$ series) deposited under different N_2/Ar ratios, compared to experiment result* [59] *and simulation result* [22].

The explanation may be that the intensity of these peaks is too weak and the baseline noise overlaps. Furthermore, another, even smaller, peak that is predicted around $2\theta = 38.5°$ can

be observed on the N_2/Ar = 2 deposited sample. Another hypothesis is that $ZnSnN_2$ has a wurtzite-like crystal structure [22], [24], [25], based on the random distribution of the Zn and Sn atoms. Even if we tried to get the same sample thickness for all experiments, it should be noted that it is not practically the case; care shall be taken comparing the peak intensities between all samples. Based on the presence and the shape (narrow and sharp) of the peak corresponding to (121) plane ($2\theta = 34.3°$) for gas ratios greater than 1.0, it has been used as a reference. There is no particular explanation for the change of peak intensity when increasing N_2/Ar ratio that is seen in (002), (122) and (123) planes: their intensity increases as increasing N_2/Ar ratio, then decreases at high N_2/Ar ratio (≥ 3.0).

The average crystallite size (D) has been evaluated from the (002) peak width using the Scherrer formula [60] (2.6),

$$D = \frac{K\lambda}{\beta\cos\theta} \tag{2.6}$$

where K is the shape factor (~ 0.93) [60], λ the wavelength of CuKα radiation (0.15406 nm) and β the full half width maximum (FHWM).

It shows that when the N_2/Ar ratio increases from 1.5 to 4.0, the crystallite size decreases from 19.0 to 6.2 nm. These values are higher than A. Shing *et al*. [61] and R. Quin et al [48] reports, but smaller than K. Chinnakutti *et al*. [45]. Those results are consistent with the visual evaluation from SEM images (**Figure II. 6**).

Assuming that the crystal structure of $ZnSnN_2$ is orthorhombic, the lattice parameters determined from our measurements are compared to predicted and experimental reported values in **Table II.2**. The lattice parameters of $ZnSnN_2$ are not significantly changed by the N_2/Ar ratio used during deposition.

Table II. 2: Lattice parameters and crystallite size for $Zn_{DC}Sn_{RF}$ series deposited at different N_2/Ar ratios, determined from XRD measurements. Values are compared to literature results for orthorhombic phase structure of $ZnSnN_2$.

N_2/Ar ratio or literature	a (Å)	b (Å)	c (Å)	D (nm)
LDA [23]	5.70	6.59	5.41	
GGA [23]	5.80	6.70	5.53	
Hydrid HSE06 [24]	5.84	6.72	5.46	
Experimental by VLS [22]	5.84	6.75	5.462	
Experimental by sputtering [46]	5.79	6.74	5.59	
N_2/Ar = 1.5	5.92	6.83	5.52	19.0
N_2/Ar = 2.0	5.93	6.84	5.52	17.3
N_2/Ar = 2.5	5.93	6.84	5.52	17.9
N_2/Ar = 3.0	5.90	6.82	5.50	10.9
N_2/Ar = 4.0	5.92	6.85	5.51	6.2

Carrier concentration and mobility were characterized by Van der Pauw resistivity measurement method and Hall voltage measurements. In order carrying out these characterizations, samples are cut into 1cm×1cm pieces and indium balls are used as electrodes. They are deposited at the four corners of those pieces and annealed at 200°C in 5%H_2/N_2 atmosphere during 4 minutes (see **Figure II. 8** right).

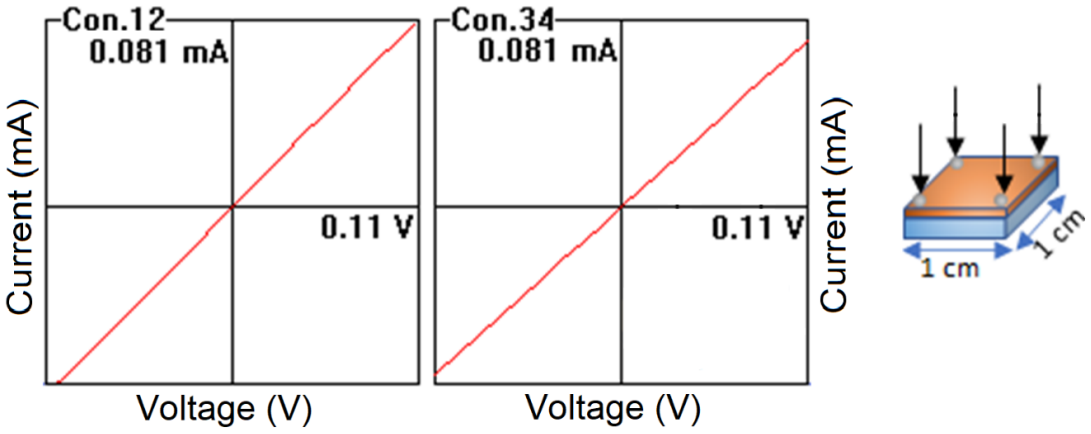

Figure II. 8: *I-V curves obtained from Van Der Pauw resistivity measurements of sample N_2/Ar = 2.5 (insert shows the way contacts are taken).*

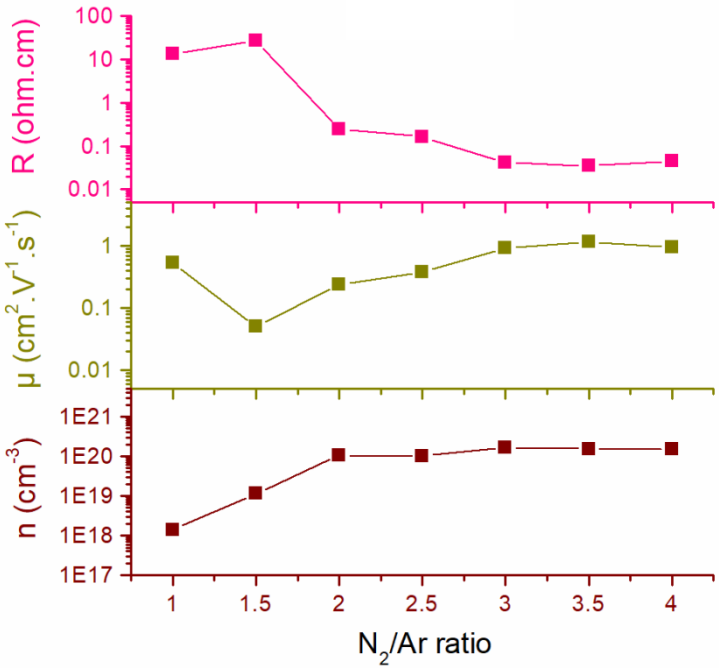

Figure II. 9: *Resistivity (R), carrier mobility (μ) and carrier density (n) of $Zn_{DC}Sn_{RF}$ series (determined from Hall effect measurements) versus N_2/Ar ratio.*

Figure II.8 shows typical results of I-V measurements where the ohmicity of contacts can be noticed. The results are shown in **Figure II. 9**. The resistivity of $ZnSnN_2$ decreases by two decades as the nitrogen content increases (ranging from 27.47 down to 0.16 Ω.cm). The carrier mobility illustrates low values from 0.05 to 0.53 $cm^2V^{-1}s^{-1}$. All the samples exhibit n-type semiconductor polarity. The lower nitrogen content is, the lower carrier density is. It increases by 2 decades, from $1x10^{18}$ to $1x10^{20}$ cm^{-3}, when the N_2/Ar ratio rises from 1 to 2 and stays almost constant afterwards.

The UV-Vis spectra represented in **Figure II.10a** show a shift of the transmittance cut-off towards lower wavelengths (blue shift) as the N_2/Ar ratio increases.

The optical bandgap was evaluated using using Tauc's relation (2.7):

$$\alpha h\nu = \beta\left(h\nu - E_g^{opt}\right)^n \qquad (2.7)$$

where hν represents the photon energy, β is a fixed constant, E_g^{opt} is the optical bandgap energy, and n is the allowed direct band with a value of 1/2.

The absorption coefficient (α) is determined by the following equation:

$$\alpha = \frac{1}{d} \ln \frac{(1-R_1)(1-R_2)(1-R_3)}{T} \tag{2.8}$$

where T represents the film transmittance, R is the reflection and d its thickness.

In this study, the reflection of $ZnSnN_2$ has not measure yet, the Fresnel equation can be used to calculate the reflection:

$$R_1 = \left(\frac{n_{air} - n_{ZnSnN_2}}{n_{air} + n_{ZnSnN_2}}\right)^2 \tag{2.9}$$

$$R_2 = \left(\frac{n_{ZnSnN_2} - n_{glass}}{n_{ZnSnN_2} + n_{glass}}\right)^2 \tag{2.10}$$

$$R_3 = \left(\frac{n_{glass} - n_{air}}{n_{glass} + n_{air}}\right)^2 \tag{2.11}$$

where:

n_{air}: refractive index of air, equals to 1.0

n_{glass}: refractive index of glass, equals to 1.5

n_{ZnSnN2}: refractive index of $ZnSnN_2$, equals to 2.4 according calculated result of A. Virfeu *et al* [62]

Equation (2.8) becomes:

$$\alpha = \frac{1}{d} \ln \frac{1}{T} - \frac{0.28}{d} \tag{2.12}$$

$$\alpha^* = \frac{1}{d} \ln \frac{1}{T} \tag{2.13}$$

As assuming no reflection, we obtain $\alpha < \alpha^*$, α^* will be used to calculate the optical bandgap in next measurements.

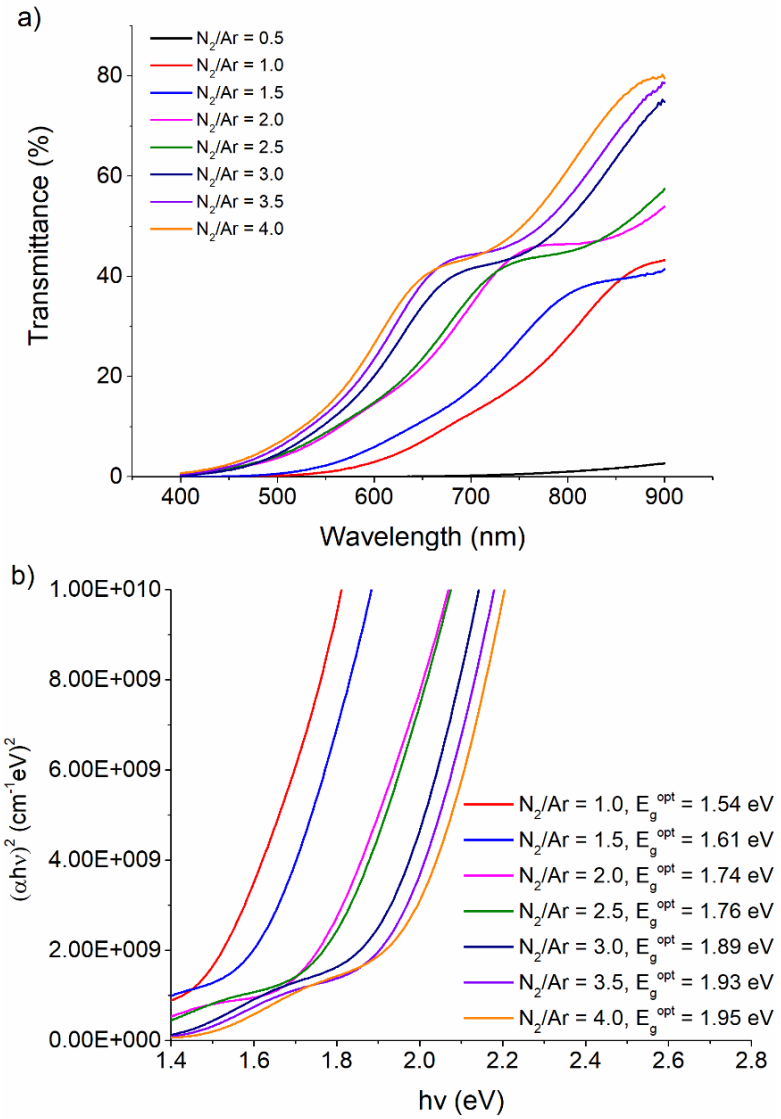

Figure II. 10: *a) Transmittance vs. wavelength spectra (UV-Vis spectroscopy) for $Zn_{DC}Sn_{RF}$ samples deposited under varied N_2/Ar ratios, b) Corresponding optical bandgap values calculated using Tauc's relation.*

The optical bandgap increases from 1.54 eV to 1.95 eV when N_2/Ar ratio increases from 1.0 to 4.0 (**Figure II.10b**). Comparing the carrier concentration (**Figure II.9**) and the optical bandgap (**Figure II.10b**), it is perceptible that higher the concentration is, larger the gap is. This relationship is explained by the Burstein-Moss effect, which has been mentioned in previous studies [24], [28], [63]. The relationship of carrier concentration (ne) and optical bandgap (E_g^{opt}) is expressed by the following equation [33], [43]:

$$E_g^{opt} = E_g + \Delta E_g^{BM} - (\Delta E_{ee} + \Delta E_{ei}) \quad (2.9)$$

where E_g is the intrinsic bandgap energy; ΔE_{ee} and ΔE_{ei} are the bandgap narrowing based on electron-electron and electron-impurity interactions, respectively; ΔE_g^{BM} is the band gap widening induced by the Burstein-Moss effect, described as:

$$\Delta E_g^{BM} = \frac{\hbar^2}{2m_{VC}^*}(3\pi^2 n_e)^{\frac{2}{3}} \quad (2.10)$$

where $\hbar$ is the Plank constant and m_{vc}^* is the reduced effective mass given by:

$$m_{VC}^* = \left(\frac{1}{m_v^*} + \frac{1}{m_c^*}\right)^{-1} \quad (2.11)$$

where m_c^*, m_v^* denote the conduction-band and valence-band effective mass, respectively.

II.4.2.2 $ZnSnN_2$ thin film – $Zn_{RF}Sn_{DC}$ series

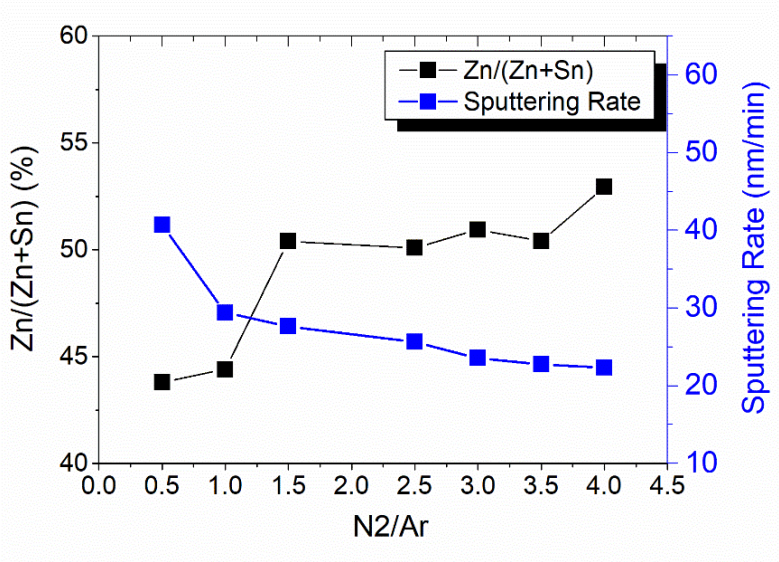

Figure II. 11: *Zn/(Zn+Sn) ratio and sputtering rate of $ZnSnN_2$ ($Zn_{RF}Sn_{DC}$ series) thin films versus nitrogen flow rate (Ar flow rate:10 sccm, deposition pressure: 2.10^{-2} mbar, 35W-RF applied to Zn and 50W-DC applied to Sn targets).*

In this series and contrary to the previous series, all sputtering parameters were fixed, except for nitrogen flux (i.e. no tunings were made either on target applied power or sputtering time). 30W-RF and 50W-DC powers were applied to Zn and Sn targets, respectively. The operating pressure in the chamber was fixed at 2.10^{-2} mbar, the argon

flux was 10 sccm, and the sputtering time was 11.5 minutes for all samples. The effects of nitrogen on thin film composition and sputtering rate are described in **Figure II. 11**.

A rather similar behavior that observed on the $Zn_{DC}Sn_{RF}$ series has to be noticed (see Table II. 1), i.e. the effect of nitrogen flux on film composition is no more really perceptible after a certain N_2/Ar ratio; here the switchover is around a ratio N_2/Ar between 1 and 1.5 (it was 2.5 for the $Zn_{DC}Sn_{RF}$ series). The sputtering rate shows also the same trend, i.e. decreases rapidly, from 40.7 to 25.7 nm/min, at low N_2/Ar ratios (below 1), then reduces continuously as N_2/Ar ratio grows up to 4.0.

The SEM images that are shown in **Figure II.12** illustrate the change in surface morphology of the $Zn_{RF}Sn_{DC}$ series of $ZnSnN_2$ thin films. For N_2/Ar ratio of 0.5, the interstitial voids are clearly perceived and they look like cracks in the surface; the shape of grains is random. At higher N_2/Ar ratios, the difference in surface morphologies is difficult to assess, the grain size is visually smaller as N_2/Ar ratio increases.

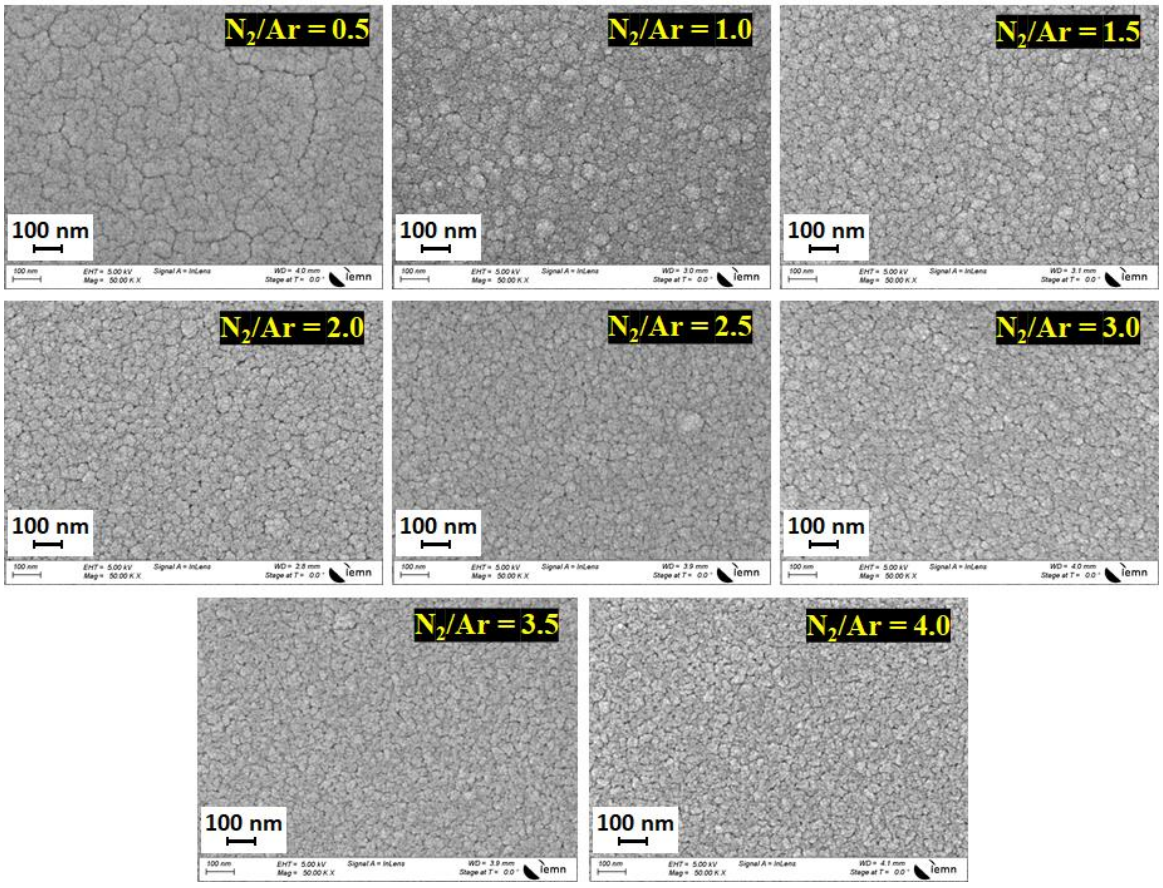

Figure II. 12: *Top view of $Zn_{RF}Sn_{DC}$ series deposited at different N_2/Ar ratios.*

The XRD data (**Figure II. 13**) show the change in the preferential orientation of crystal. As N_2/Ar equals 0.5, the $ZnSnN_2$ thin film is of amorphous nature. At N_2/Ar ratio of 1.0, there are only 2 peaks corresponding to (200) and (320) planes. They are located at of 30.1° and 53.6° respectively, both of them are sharp and narrow. When N_2/Ar ratio is equal or higher than 1.5, the peak of (121) plane appears at 2θ equal to 34.2°. At higher N_2/Ar ratios, other peaks appear at 32.4°, 45.0°, 59.2° and 65.3°, corresponding to (002), (122), (123) and (322) directions [59], respectively. The seven characteristics peaks of $ZnSnN_2$ phase are present as N_2/Ar ratio is equal or higher than 3.0. Although those results are similar to the results of $Zn_{DC}Sn_{RF}$ series (**Figure II. 7**), peaks are here less clearly defined. The average crystal size (D), evaluated from the (200) peak width using the Scherrer formula (2.6), decreases from 22.5 to 13.1 nm when the N_2/Ar ratio increases. These results are consistent with visual evaluation from SEM images above (**Figure II. 12**). The lattice parameters are described in **Table II. 3**, the c value declines slightly by the increase of N_2/Ar. The dispersion in values is lower than that of $Zn_{DC}Sn_{RF}$ series (**Table II. 2**)

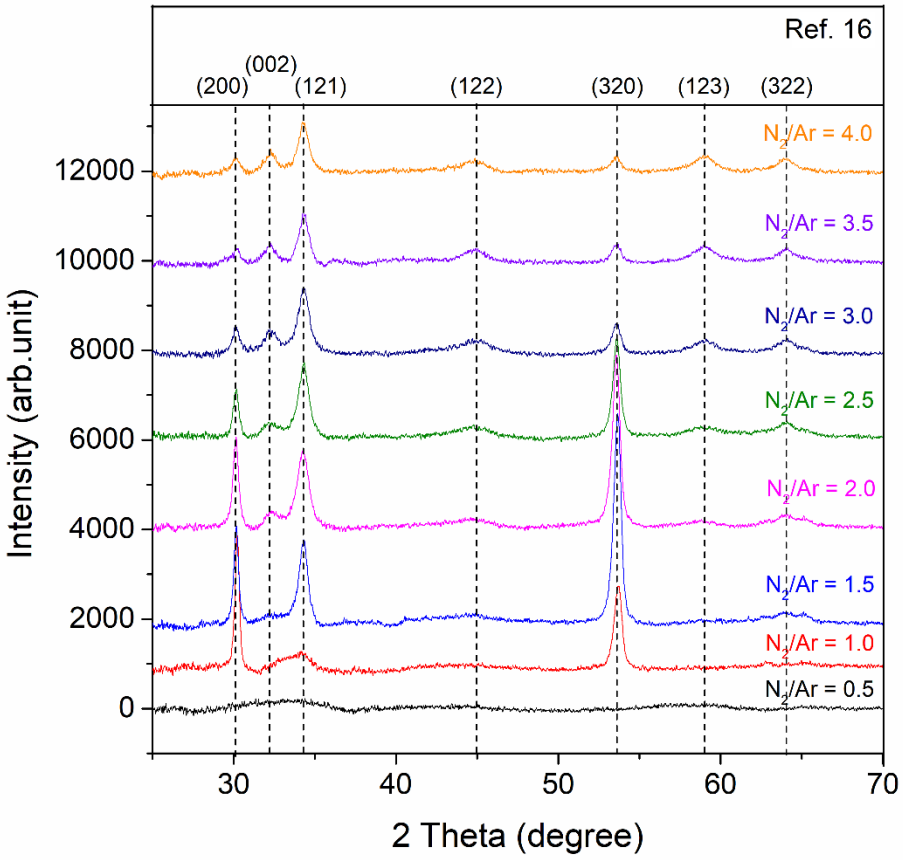

Figure II. 13: *XRD diffractograms of $Zn_{RF}Sn_{DC}$ series versus N_2/Ar ratio.*

Table II. 3: Lattice parameters and crystallite size for $Zn_{RF}Sn_{DC}$ series for different N_2/Ar ratios, determined from XRD.

N_2/Ar ratio	a (Å)	b (Å)	c (Å)	D (nm)
1.5	5.92	6.80	5.63	22.5
2.0	5.93	6.82	5.61	18.8
2.5	5.92	6.82	5.58	13.1
3.0	5.92	6.84	5.53	13.7
3.5	5.92	6.83	5.55	13.1
4.0	5.93	6.84	5.54	13.1

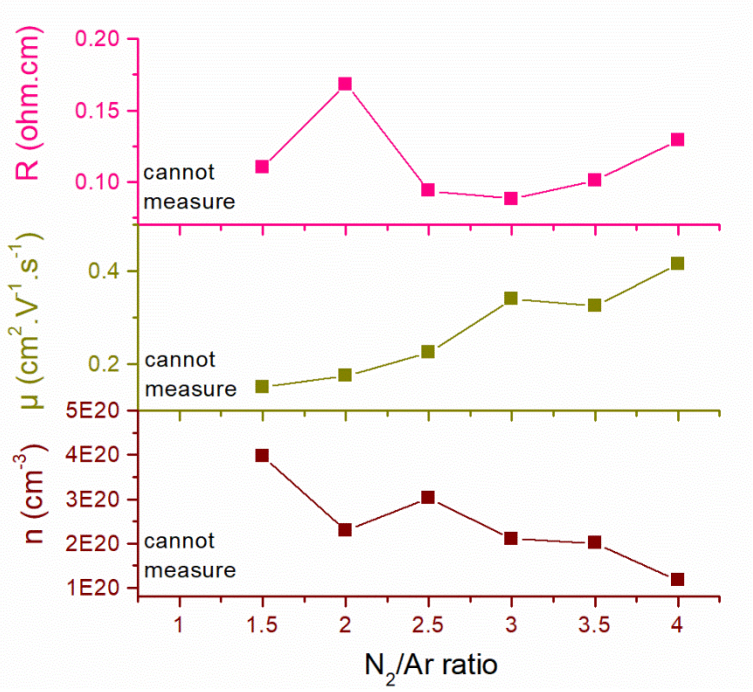

Figure II. 14: *Resistivity (R), carrier mobility (μ) and carrier density (n) of $Zn_{RF}Sn_{DC}$ series (determined from Hall effect measurements) versus N_2/Ar ratio.*

Electrical characteristics are reported in **Figure II. 14**, contrary to what was observed for the $Zn_{DC}Sn_{RF}$ series (see **Figure II. 9**), there is little change of properties with the N_2/Ar ratio. In particular, the resistivity of $ZnSnN_2$ remains around 0.1 Ω.cm. The carrier mobility also illustrates low variation, ranging from 0.15 to 0.42 $cm^2V^{-1}s^{-1}$ as well as the carrier

density that ranges from $4.0x10^{20}$ to $1.1x10^{20}$ cm^{-3}. All the samples exhibit n-type semiconductor characteristics.

Figure II.15a shows a shift of the cut-off in transmittance towards lower wavelengths (blue shift) as the nitrogen flux increases, the optical bandgap is calculated using Tauc's relation (2.7) (**Figure II.15b**). It increases from 1.59 eV to 1.95 eV when N_2/Ar ratio increases from 1.0 to 4.0. So even with a slight variation (decrease) of carrier density, a rather large increase of optical bandgap is observed that is moreover shifting the other way it should have done if the Burstein-Moss effect was its origin.

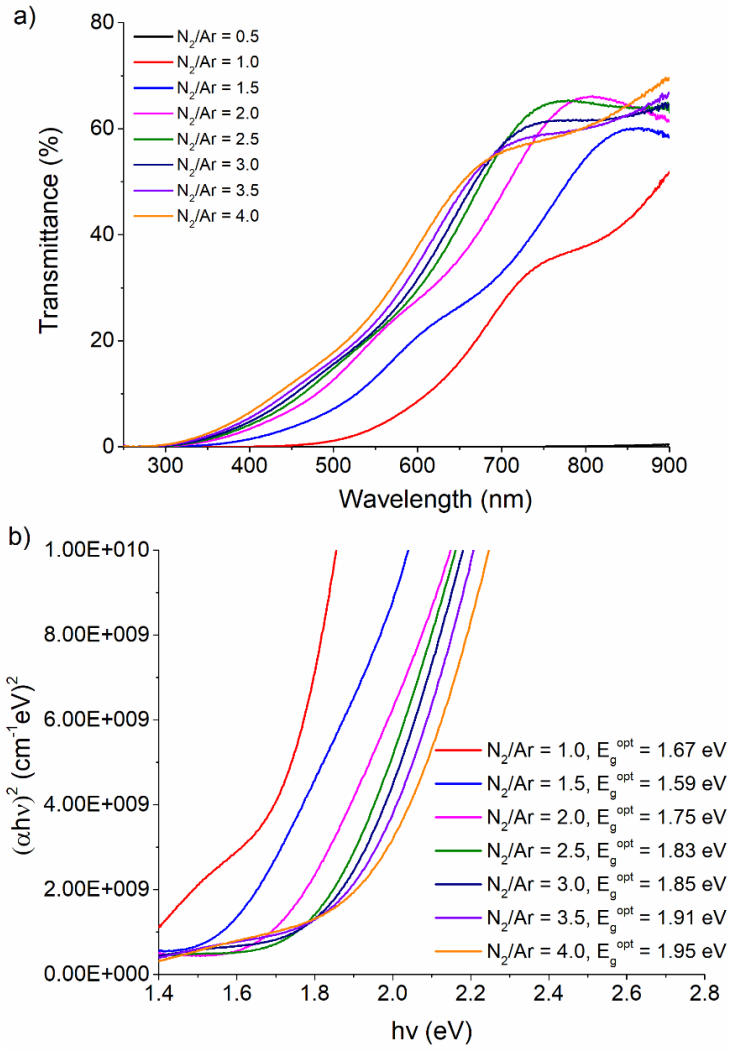

Figure II. 15: *a) Transmittance vs. wavelength spectra (UV-Vis spectroscopy) for $Zn_{RF}Sn_{DC}$ samples deposited under varied N_2/Ar ratios , b) Corresponding optical bandgap values calculated using Tauc's equation.*

II.5 Sputtering in 5%H_2/N_2 mixed Ar environment:

Hydrogen plays an important role in the optical and electrical properties of semiconductors. According to S.J. Pearton [64], [65], the nitride semiconductors with nitrogen vacancy, V_N, defects are not stable and may decompose and oxidize during storage in the ambient air. Furthermore, hydrogen can be used to passivate the electrical activity, by combining with dangling and defective bonds, as it used, for example, in amorphous silicon. Hydrogen has also be pointed out as decreasing the carrier density in $ZnSnN_2$ material [40].

In this section, 5%H_2/N_2 (0.05HN) gas was used instead of pure nitrogen. The gas flux was varied from 5 to 35 sccm with a 5 sccm step, the argon flux was fixed at 10 sccm. A 25W-DC feeding was used for Zn and a 40W-RF for Sn (it is then a $Zn_{DC}Sn_{RF}$ series like in section II.4.2.1). It can be noticed that a lower Sn power was used than that used in section II.4.2.1 (it was 60 to 70 W for achieving a stoichiometric composition (**Table II. 1**)) so a Zn rich material is awaited. The operating pressure in the chamber is unchanged and fixed at 2.10^{-2} mbar.

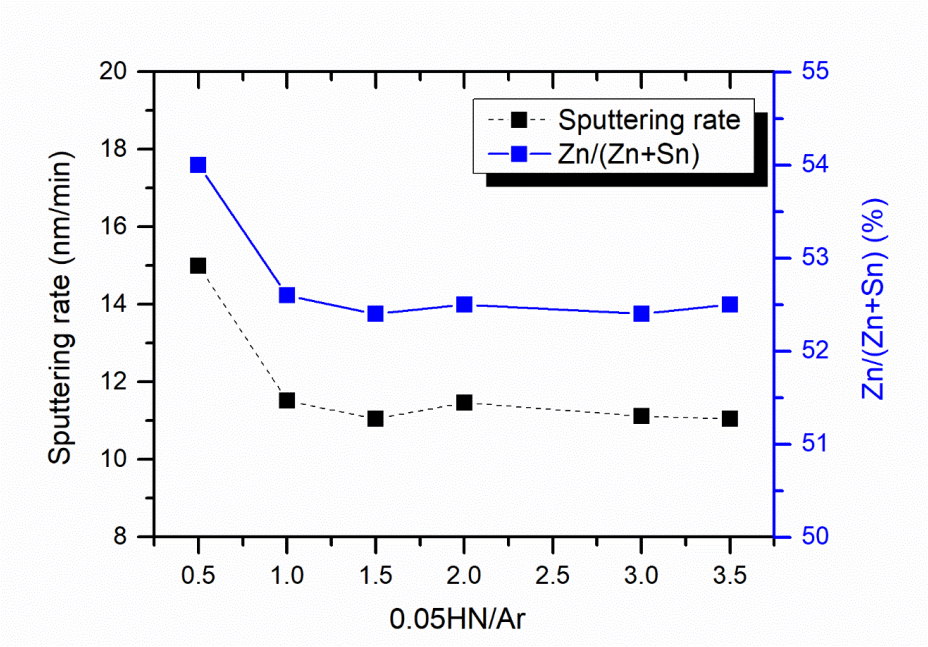

Figure II. 16: *Sputtering rate and Zn/(Zn+Sn) ratio versus 0.05HN/Ar ratio.*

The sputtering rate and Zn composition obtained for different 0.05HN/Ar ratios is shown in **Figure II. 16**. When the 0.05HN/Ar ratio is higher than 1.0, it does not affect, or slightly,

the deposition rate and the Zn/(Zn+Sn) ratio (nearly 52.5%). This behavior is similar to the one obtained for deposition without hydrogen (see **Table II. 1**) except in that later case, the switchover was around a 0.05HN/Ar ratio of 2-2.5. As awaited, material is Zn rich.

The surface morphology is illustrated in **Figure II.17**. When 0.05HN/Ar ratio is equal to 0.5, the shape is much more cauliflower-like. However, the morphology changes to long granular grains for ratios between 1.0 and 2.0; then it seems returning to a cauliflower-like structure. This behavior is different from the one obtained without hydrogen (see **Figure II. 6**) by the granular structure obtained for middle range of N_2/Ar ratios. Moreover, for those ratios, the density of voids appears much less than on the pure nitrogen case.

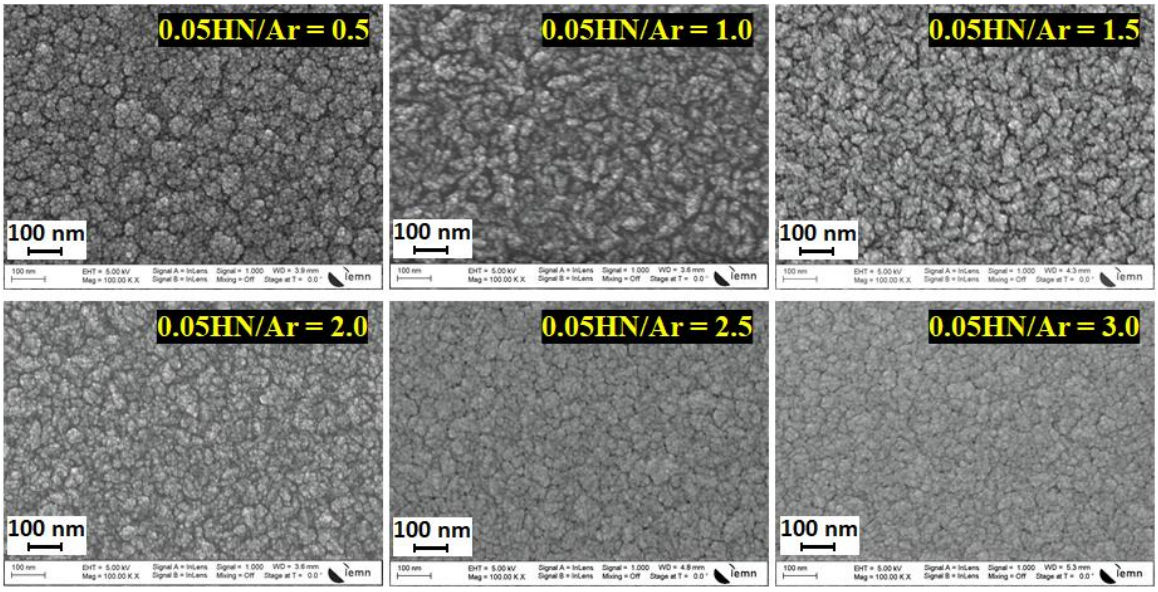

Figure II. 17: *Top surface SEM images of $Zn_{DC}Sn_{RF}$ series deposited in different mixed 0.05HN/Ar environments.*

The electrical properties are shown in **Figure II.18**. The resistivity increases as the 0.05HN/Ar ratio increases, ranging from 1.7 to 10 Ω.cm over the full range. Even if it could appear as a singular point, the highest mobility is 6.0 $cm^2V^{-1}s^{-1}$ that is a decade higher than when sputtering in N2/Ar atmosphere (see **Figure II. 9**). This value corresponds to that (5.8 $cm^2V^{-1}s^{-1)}$ reported by A. Fioretti *et al.* [55] when incorporating hydrogen in the sputtering atmosphere. Contrary to previous cases, the material polarity when 0.05HN/Ar ratio is higher than 1.5 is ambiguous since both polarities can be returned. Nevertheless, up to a two-decades decrease in carrier concentration can be noted over the full range .Such

an amphoteric behavior has been reported by Coronel *et al.* for $ZnSn_xGe_{1-x}N_2$ [63], the reason for this phenomenon is still unclear. Besides that, the change in electrical properties of $ZnSnN_2$ are preferably explained by the defects inside the crystal [26], [66]. In n-doped $ZnSnN_2$, the carrier density lowering is caused by the complexation between excess Zn (**Figure II. 16** shows all samples are Zn-rich) and hydrogen, activating the Zn_{Sn} acceptor. This situation hinders the formation of donor defects, such as nitrogen vacancies V_N and unintentional O_N impurities. Such a behavior is consistent with the analysis of Fioretti *et al.* [55].

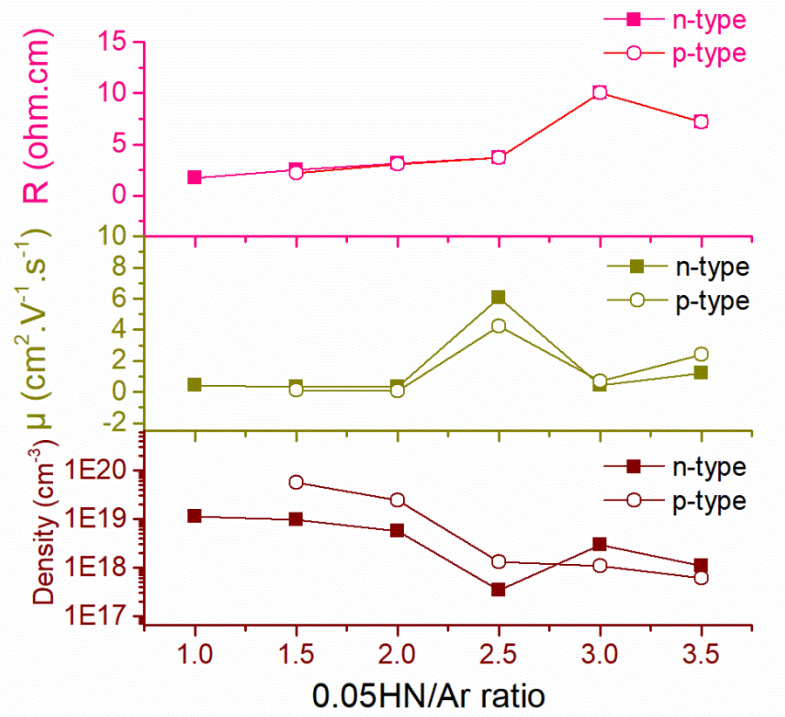

Figure II. 18: *Resistivity (R), carrier mobility (μ) and carrier density of $ZnSnN_2$ films (determined from Hall effect measurements) versus 0.05HN/Ar ratio.*

The UV-Vis spectroscopy measurements show a blue shift as the 0.05HN/Ar ratio increases (**Figure II.19a**). The optical bandgap increases from 1.87 to 2.21 eV as the carrier density decreases from 10^{-19} to 10^{-18} cm^{-3}. If the increase in bandgap value was previously allotted to the Burstein-Moss effect, the behavior, here, does not reflect such a phenomenon since the bandgap value slightly increases when the carrier density decreases by one decade.

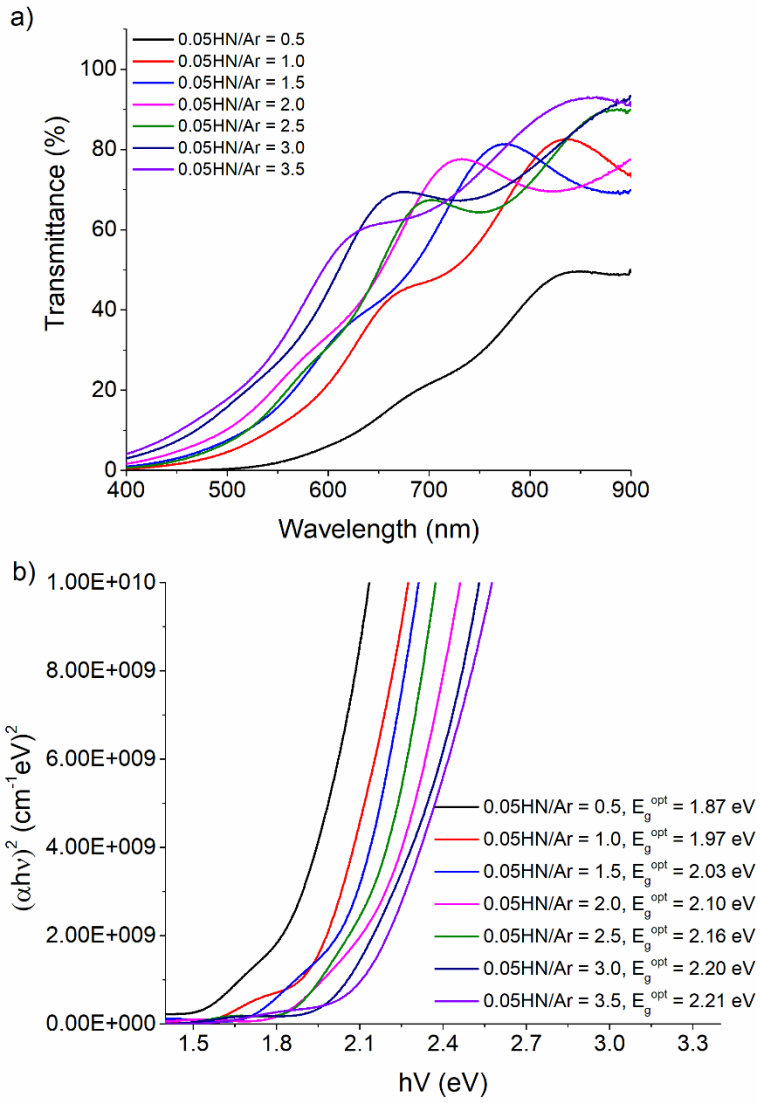

Figure II. 19: *a) Transmittance vs. wavelength spectra (UV-Vis spectroscopy) for $Zn_{DC}Sn_{RF}$ samples deposited under varied 0.05HN/Ar ratios, b) Corresponding optical bandgap values calculated using Tauc's equation.*

II.6 Sputtering in H_2 mixed N_2 environment:

Following the results presented in section II.5 that point out a decrease of the carrier concentration when the hydrogen is added to the sputtering atmosphere, another sample series was fabricated in a H_2/N_2 sputtering environment.

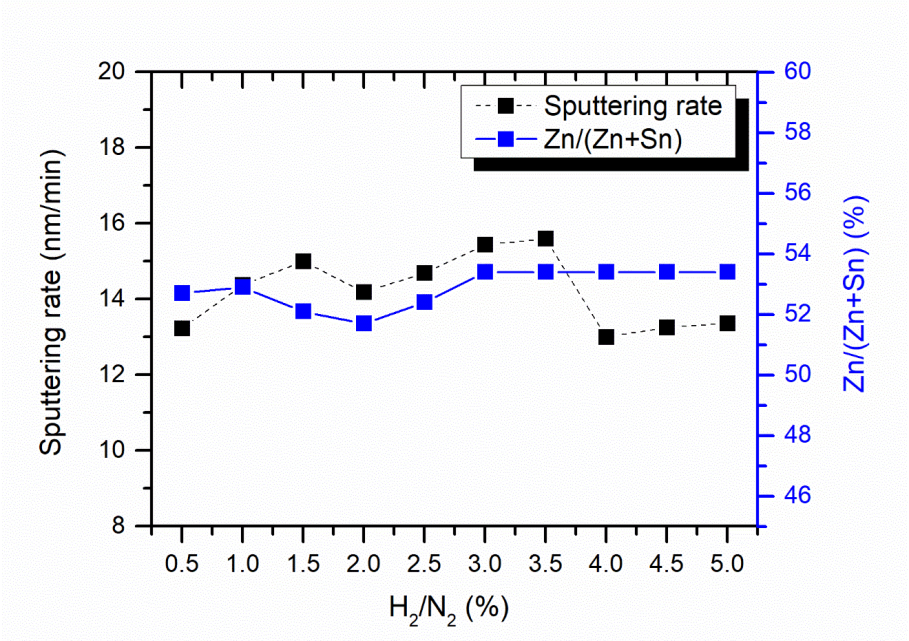

Figure II. 20: *Sputtering rate and Zn/(Zn+Sn) ratio versus H_2/N_2 ratio.*

The total gas flux was fixed at 40 sccm, the partial flux of nitrogen and hydrogen is calculated in such a way the percentage of hydrogen is between 0.5 and 5%. The target power biasing is the same as for previous series, i.e. a 25W-DC feeding was used for Zn and a 40W-RF for Sn. Other parameters were also kept identical. The sputtering rate and Zn composition obtained under different H_2/N_2 ratios are shown in **Figure II.20**. All the samples are Zn-rich, that is awaited from the power supply values used as in the previous case. The Zn/(Zn+Sn) ratio varies from 52 to 53% so also rather the same values that using a gas mix with Ar (cf. **Figure II.16**). The sputtering rate is between 13 to 15 nm/min so roughly 25% faster than when using a gas mix with Ar. So, no particular effect of hydrogen concentration can be observed either on sputtering rate or material composition.

The surface morphology is shown in **Figure II.21**. In all cases, the aspect is much more cauliflower-like. For the lower (0.5%) and higher ($\geq$ 4%) H_2/N_2 ratios, the morphology is rather similar with apparent bigger grain size.

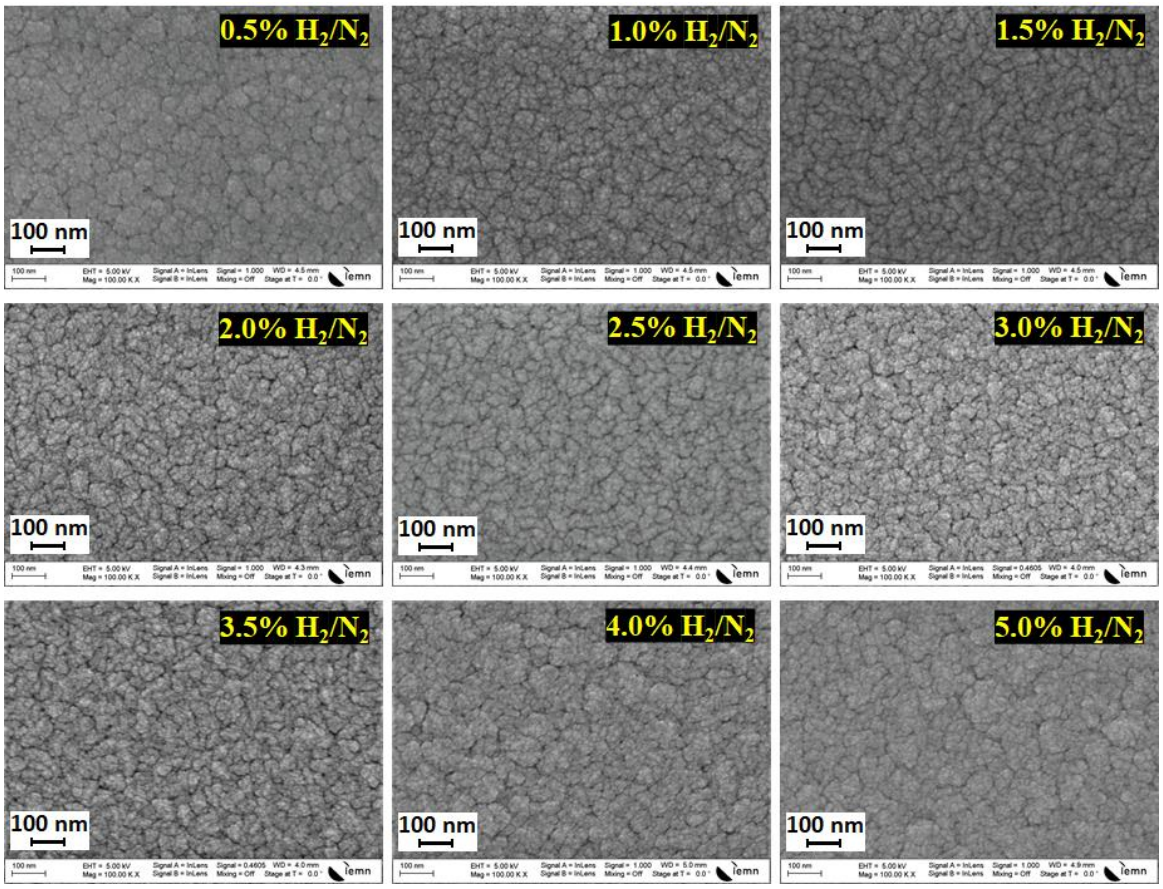

Figure II. 21: *Top surface SEM images of $Zn_{DC}Sn_{RF}$ series deposited using different H_2/N_2 ratios.*

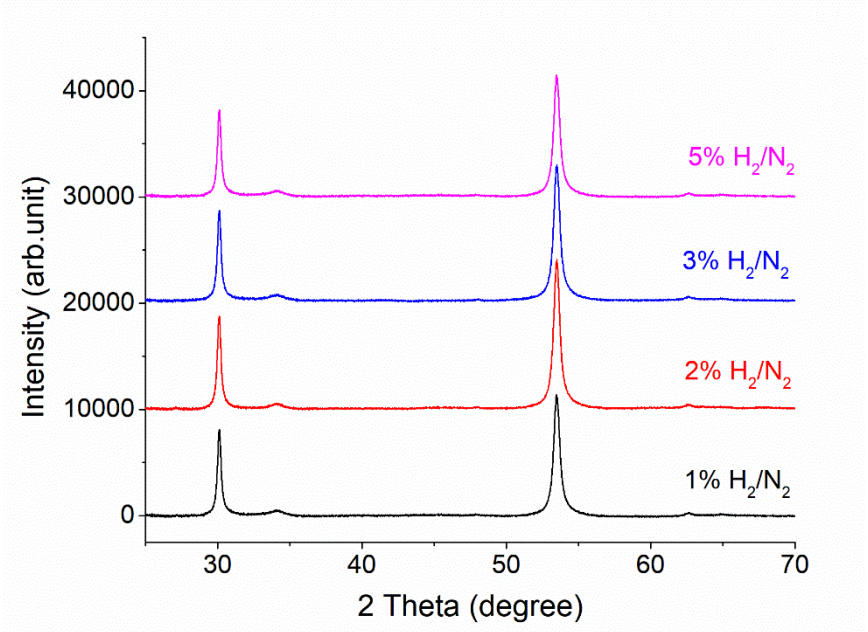

Figure II. 22: *XRD patterns of the $ZnSnN_2$ films deposited in different percentage of hydrogen*

XRD diffractograms do not point out any change in crystal structure of $ZnSnN_2$ versus the increase of hydrogen content (**Figure II.22**). All samples show only four peaks located at 2θ equal to 30.1°, 34.0°, 53.4° and 62.6°, corresponding to (200), (121), (320) and (322) plane respectively. The average crystal size (D), evaluated from the (200) peak width using the Scherrer formula (2.6), is approximately 22 nm for all samples that antagonizes the observations that were made from the SEM images for the extreme H_2/N_2 ratios.

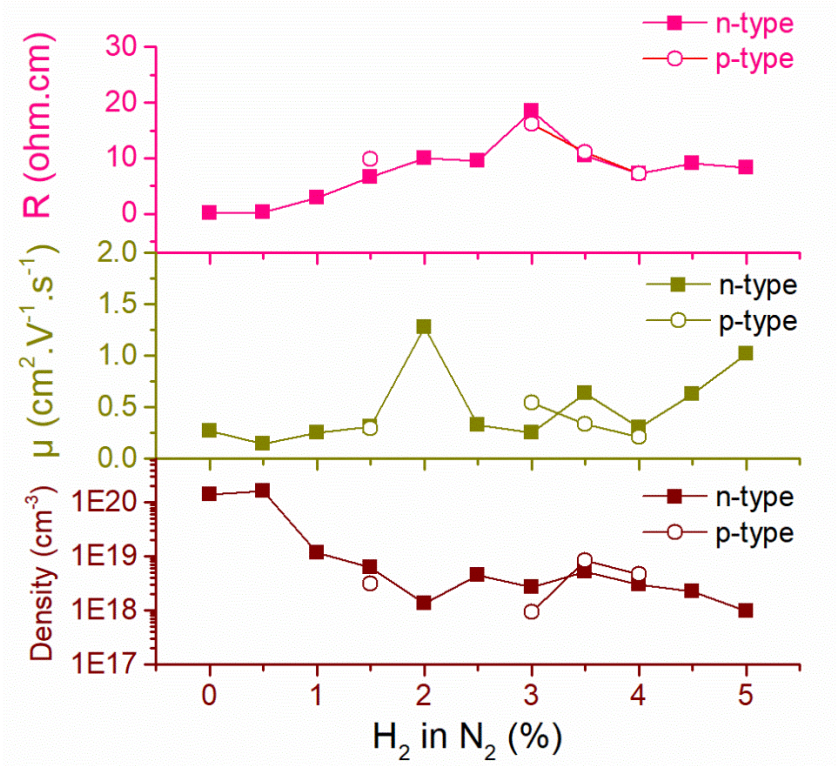

Figure II. 23: *Resistivity (R), carrier mobility (μ) and carrier density of $Zn_{DC}Sn_{RF}$ series (determined from Hall effect measurements) versus H_2/N_2 ratio.*

Figure II.23 shows the electrical properties. The resistivity increases with the hydrogen concentration and a higher value is also observed at 3% concentration as observed for the previous case, i.e. with a mix hydrogen, nitrogen, argon atmosphere. This similarity could indicate that it could be rather a trend than a singular experimental point. The mobility varies from 0.1 to 1.3 $cm^2V^{-1}s^{-1}$, the highest value obtained at 2% H_2/N_2. The electron density decreases 2 orders of magnitude as the hydrogen concentration increases as observed in the previous case. At 0.5% H_2/N_2, electron density is not significantly different from that of samples deposited in pure nitrogen. But at hydrogen ratio of 1%, the carrier

density reduces a decade compared to the 0.5% H_2/N_2 sample reaching 10^{19} cm^{-3} that is the same value as with argon (see **Figure II. 18**). The lowering of carrier density can be explained similar as in Section II. 5 by the hindering of the process of formation of donor defects (V_N or O_N). Also, same as for the previous case (see **Figure II.18**), the reason for the appearance of hole carrier in some samples is still ambiguous, but the value of density obtained for both polarities does not differ considerably.

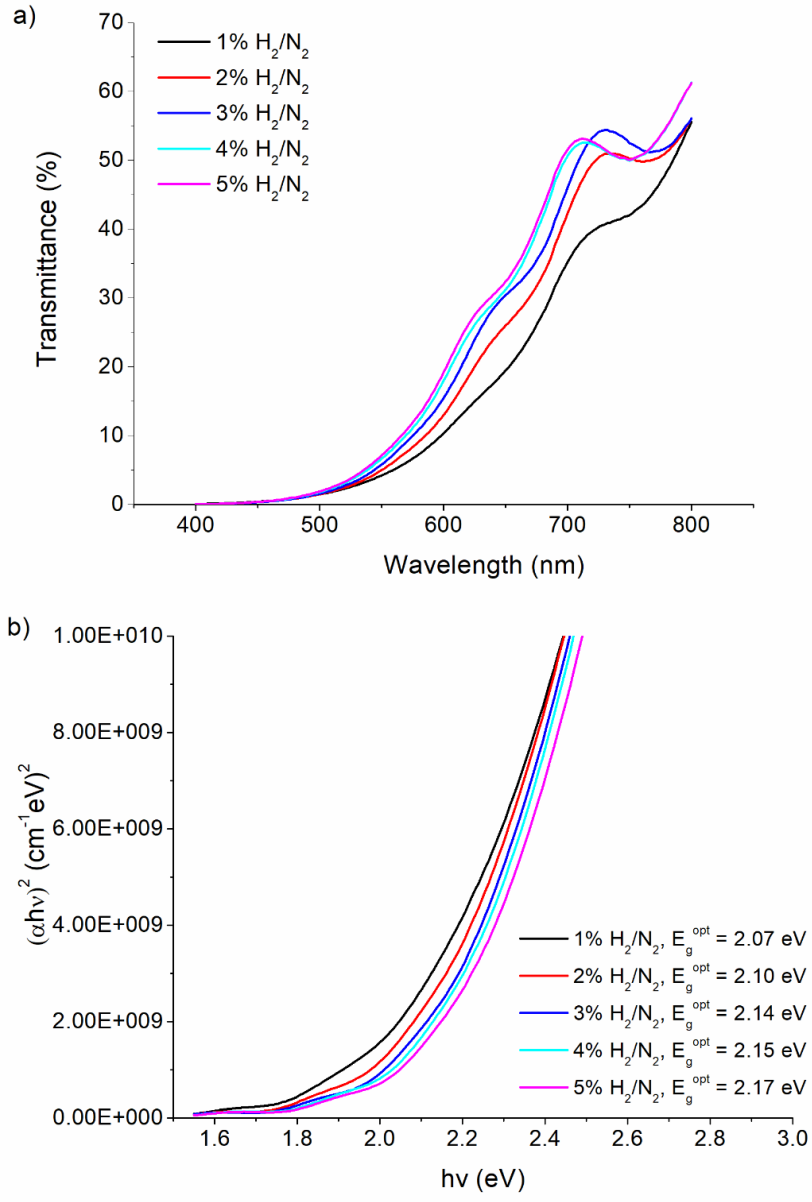

Figure II. 24: *a) Transmittance vs. wavelength spectra (UV-Vis spectroscopy) for $Zn_{DC}Sn_{RF}$ samples deposited under varied H_2/N_2 ratios sputtering atmospheres, b) Corresponding optical bandgap values calculated using Tauc's equation.*

A progressive shift of the cut-off of the transmittance value towards lower wavelengths (blue shift) is observed when the H_2/N_2 ratio increases (**Figure II.24a**). The optical bandgap, illustrated in **Figure II.24b**, rises gradually from 2.07 to 2.17 eV. Here too, the Burstein-Moss effect cannot be directly pointed out since, even with a decrease of two decades in the carrier concentration with the H_2/N_2 ratio, no drastic change in the bandgap value can be observed.

II.7 Comparison of sputtering in different environments

In order easier comparing the effects of each environment, three samples were fabricated in the same period and under the same sputtering conditions ($Zn_{DC}Sn_{RF}$ series), except for varying the deposition environment (**Table II. 4**). Compared to previous experiments, the pure nitrogen sputtering atmosphere was a new case and the mix H_2/N_2/Ar environment (Section II. 5) is not represented. The power supplies were 25W-DC and 70 W-RF for Zn and Sn, respectively. The operating pressure in the chamber was fixed at 2.10^{-2} mbar and the overall gas flow rate is 40 sccm.

Table II. 4 : Sputtering gas composition (gas flow rates in sccm) used for the fabrication of the different types (N, NA and NH) of samples.

Gas \ Sample name	NA	NH	N
Ar	10	0	0
N_2	30	24	40
5%H_2 in N_2 (0.05HN)	0	16	0

The sputtering rate and Zn composition is shown in **Figure II. 25**. The fastest sputtering rate is in the presence of argon (NA), the sputtering rate in the pure nitrogen (N) environment is slightly greater than that of mixed of hydrogen and nitrogen (HN). In addition, the Zn/(Zn+Sn) ratio is the highest for the HN sample and the smallest for the NA sample. It means that argon supports the sputtering process of tin, due to high atomic mass (40 u). Hydrogen is very light (1 u) and not effective in sputtering.

Scanning electron microscopy (SEM) and atomic force microscopy (AFM) were employed to investigate the surface morphology and surface topography of $ZnSnN_2$ films (**Figure II. 26**). The difference of surface morphologies is difficult to assess between NA and NH samples and their roughness is almost similar. In pure N_2, the grain size is "visually" bigger

and morphology looks like pyramidal shape, corresponding roughness is also larger than for the other samples.

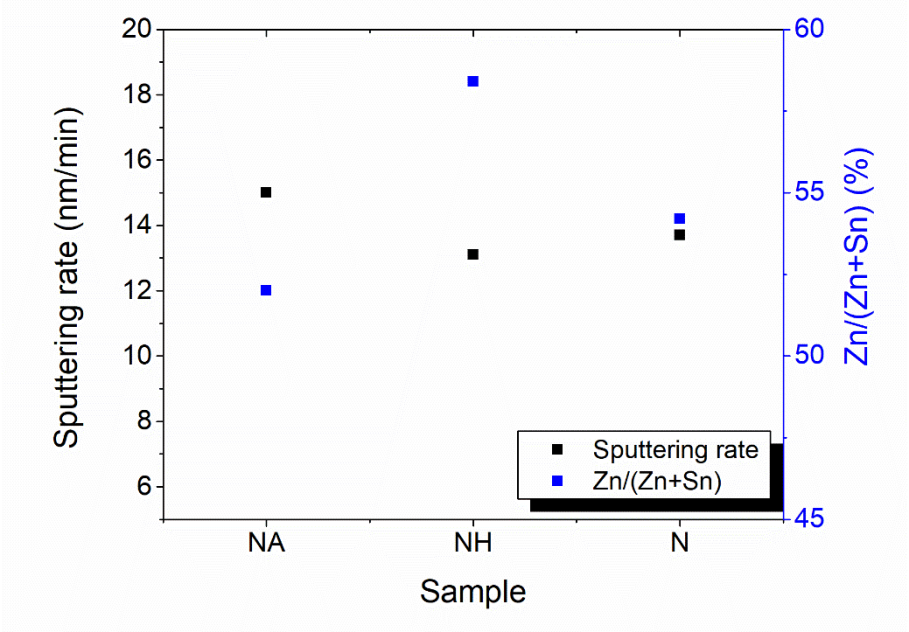

Figure II. 25: *Comparison of sputtering rate and Zn/(Zn+Sn) ratio of $ZnSnN_2$ samples deposited in different environments.*

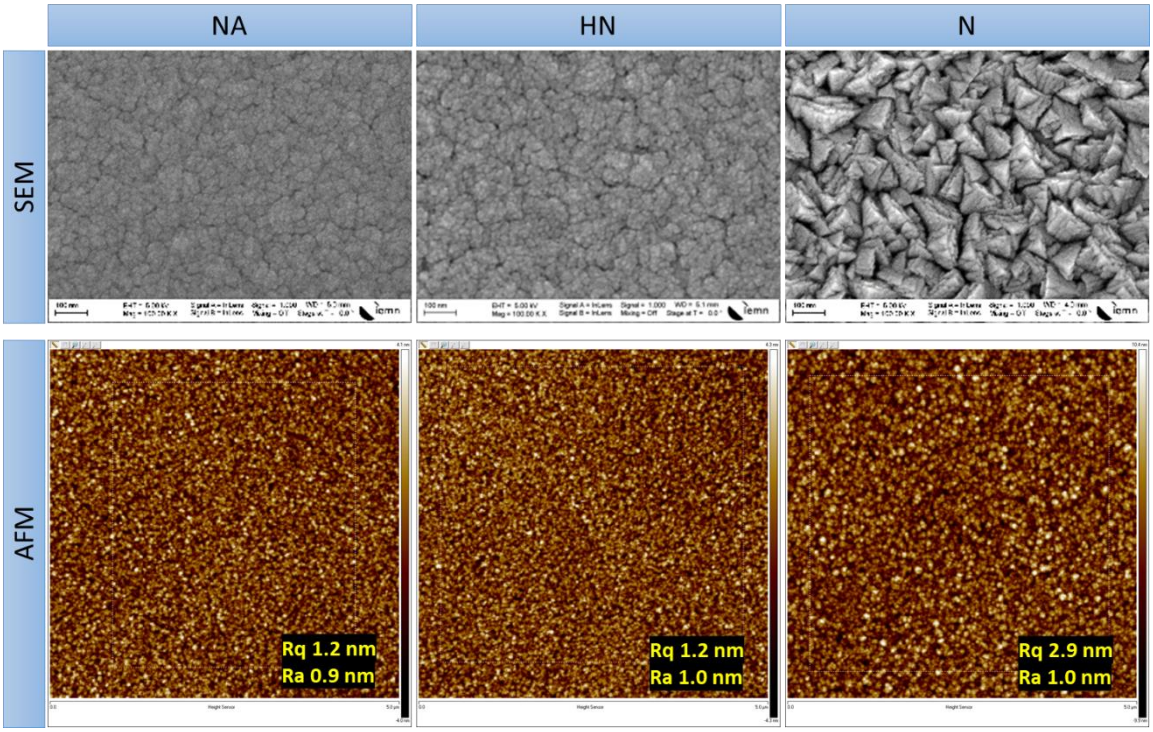

Figure II. 26: *SEM (top) and AFM (bottom) images of $ZnSnN_2$ films for NA, NH and N samples.*

Figure II. 27 shows the change in crystallinity states of the different series. For NH samples, XRD data show only four peaks located at 2θ equal to 30.1°, 34.0°, 53.4° and 62.6°, corresponding to (200), (121), (320) and (322) planes, respectively. Meanwhile, N samples have five peaks located at 2θ equal to 32.4°, 34.3°, 53.6°, 59.2° and 65.3° corresponding to (002), (121), (122), (123) and (322). Only NA samples exhibited all characteristic peaks of $ZnSnN_2$, located at 30.1°, 32.4°, 34.3°, 45.0°, 53.6°, 59.2° and 65.3° corresponding to (200), (002), (121), (122), (320), (123) and (322). Furthermore, all samples were recorded the same thickness, approximately 1 µm. The peak of (200) and (320) planes of HN sample and those of (121) and (322) planes of N sample are narrower and sharper than those of NA samples.

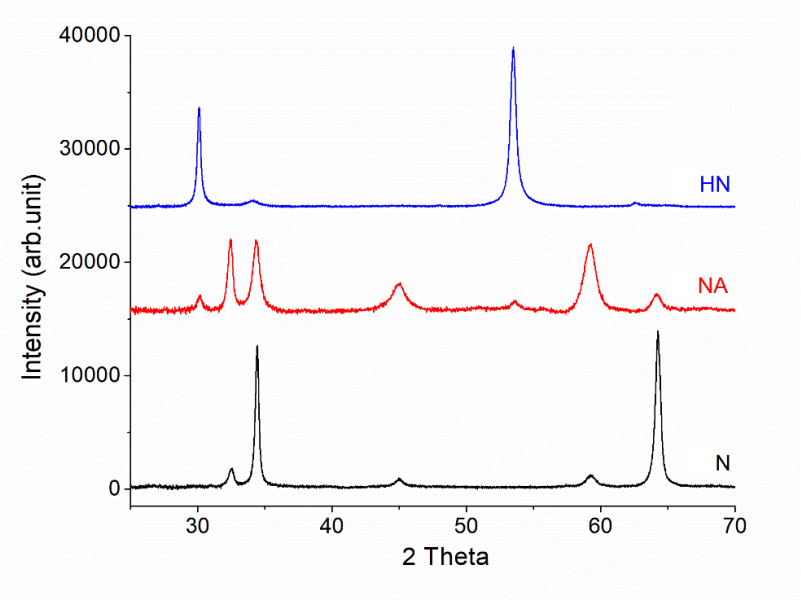

Figure II. 27: *Comparison of XRD diffractograms of the $ZnSnN_2$ films deposited in different sputtering environments.*

All samples exhibit n-type semiconductor characteristics under Hall effect measurements (**Figure II.28**). The carrier density and carrier mobility values behave mostly inverse, the higher density lower mobility. The lowest density and highest mobility, 2.5 x 10^{17} cm^{-3} and 2.0 $cm^2V^{-1}s^{-1}$ respectively, are obtained for the samples deposited in 2%H_2 in N_2 environment jointly with a high resistivity value, around 13 Ω.cm.

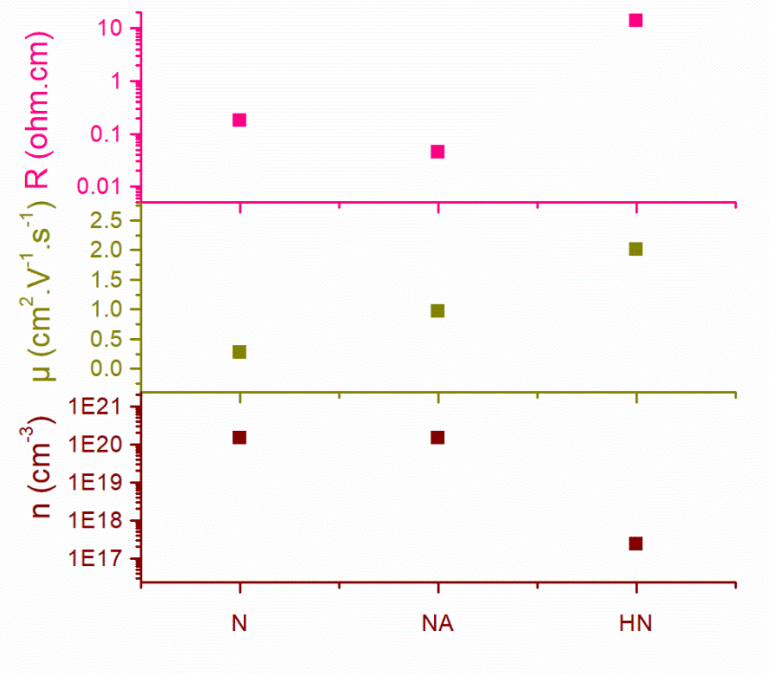

Figure II. 28: *Resistivity (R), carrier mobility (μ) and carrier density of $ZnSnN_2$ films (determined from Hall effect measurements) depending on their sputtering environment.*

Figure II. 29 shows the UV-Vis spectra of the different samples and the deduced optical bandgap using Tauc's relation (2.7). This bandgap is 1.94, 2.04 and 2.19 eV corresponding to N, NA and HN series, respectively. Without hydrogen, bandgap values are rather similar.

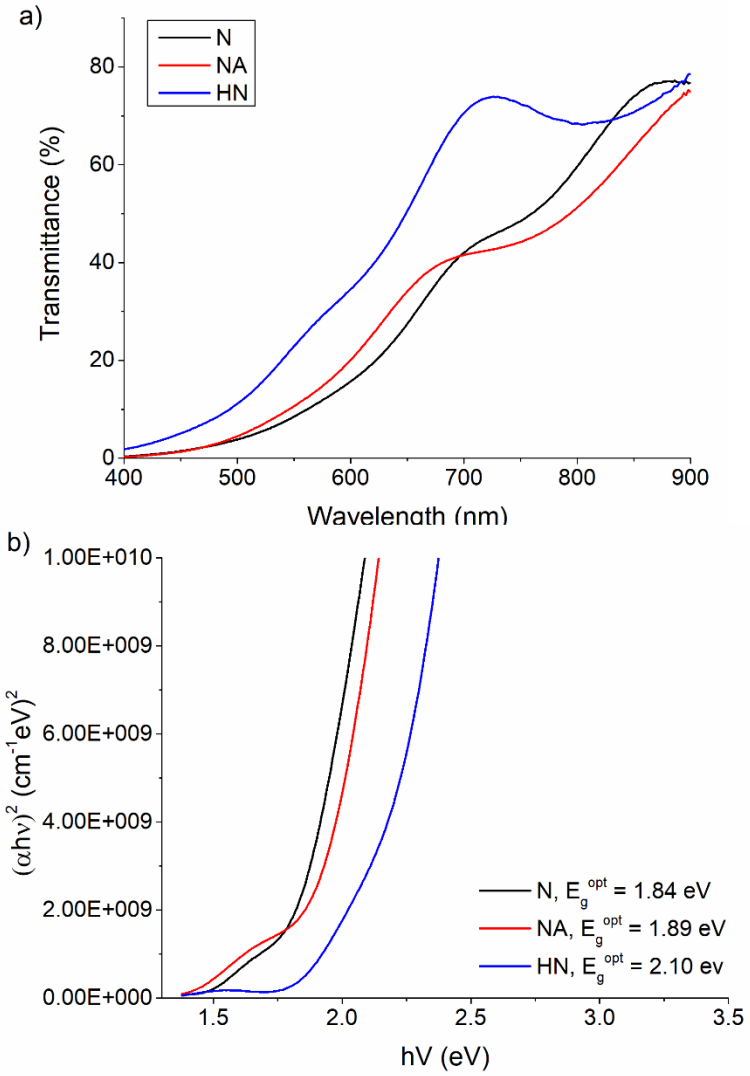

Figure II. 29: *a) Transmittance vs. wavelength spectra (UV-Vis spectroscopy) for $Zn_{DC}Sn_{RF}$ series deposited under varied sputtering atmospheres, b) Corresponding optical bandgap values calculated using Tauc's equation.*

II.8 Discussions and partial conclusions

The deposition of $ZnSnN_2$ was made using two metallic (Zn and Sn) targets in a confocal arrangement. Starting from the deposition rate of the metallic targets that were obtained in a pure argon atmosphere, the power supply of each target was determined in order achieving a stoichiometric compound. Nevertheless, as soon as nitrogen is inserted in the sputtering atmosphere, the deposited films shift to a Zn-rich composition. So, the calibration of the film composition can get a guess by the deposition of each elementary metal but the real calibration needs to be done using a nitrogen atmosphere. This Zn-rich characteristic has been attributed to a lower incorporation of Sn than to a higher one of Zn due to the respective mass of metallic and sputtering gas species (see section II. 4.2).

For all sputtering atmospheres containing argon (see **Figures II. 5, II. 11** and **II. 16**), the deposition rate decreases as the nitrogen concentration (from 0 up to some percents) increases. This could be linked to the formation of SnN_2 or ZnN_2 compounds at target surface that are heavier species to sputter than pure metallic ions. When no argon is involved (H_2/N_2 atmosphere, **Figure II. 20**), the deposition rate is almost constant whatever the H_2/N_2 ratio is (in the 0.5-5% range that is been studied). Following the same argumentation than above, i.e. taking into account the respective mass of the species that are present inside the sputtering atmosphere, the lighter mass of hydrogen (1 u) does not modify the sputtering process that is govern by the nitrogen ions.

Using a mixed N_2/Ar sputtering atmosphere, whatever the power biasing of targets is, Zn concentration of films increases as nitrogen concentration increases (see **Figures II. 5** and **II. 11**). The N_2 flux shall at least be the same that the Ar flux ($N_2/Ar > 1$) in order the film not to ne amorphous (see **Figures II.7** and **II. 13**). However, after a switchover point in the composition of the mixed N_2/Ar atmosphere that depends on power biasing conditions, the Zn concentration of films tends to stabilize.

From the XRD measurements, it is rather impossible to discern the crystal structure of the material, orthorhombic or wurtzite, since both of them exhibit an almost identical spectrum (see **Figure II. 7**). Since the orthorhombic structure is reported as the most stable one, we, as many authors, assume that it was the case here. All samples fabricated in an argon containing atmosphere show the characteristics peaks of $ZnSnN_2$ (see **Figures II. 7** and **II.**

13). The lattice parameters (see **Tables II. 1** and **II. 2**) are not really impacted by the N_2/Ar ratio or the target bias arrangement. Without argon, only 2 main diffraction peaks are observed as it has been reported also for materials fabricated under pure nitrogen atmosphere.

Top views of films show a cauliflower-like structure for almost all cases (**see Figure II. 6, II. 12, II. 17, II. 21**). Only sputtering in pure N_2 atmosphere exhibits a completely different structure (see **Figure II. 26**).

Table II. 5 attempts to summarize the main effects of those actions, modifying either the sputtering atmosphere or the biasing mode of the metallic targets.

Table II. 5: Main effects of the tuning of sputtering parameters on the film properties.

Action	Film composition	Deposition rate	Crystallography
Increasing N_2 concentration in a mix N_2/Ar sputtering atmosphere.	Quick increase (between 10 and 20%) of Zn concentration with a tendency to stabilize.	Monotonous decrease (by a factor 2) with a tendency to stabilize.	No significant change. Crystallite size in the order of 10 to 20 nm.
Adding H_2 in the sputtering atmosphere.	Little (N_2/Ar) or no (N_2) change.	Little (N_2/Ar) or no (N_2) change	No significant change.
Removing Ar from sputtering atmosphere	Increase in Zn concentration: some percents (N_2) to 10% (N_2/H_2).	Slight decrease.	No more cauliflower-like aspect (N_2). Only 2 main peaks in XRD diffractograms.
Changing biasing mode of targets.	Can be adjusted by power tuning of each power supply.	Higher in $Zn_{RF}Sn_{DC}$ mode.	No significant change.

Concerning the electrical characteristics of the materials, without hydrogen into the sputtering atmosphere (either within a N_2 or a N_2/Ar atmosphere), films are almost

degenerate with very high electron density, around some 10^{20} cm^{-3} (see **Figures II. 9** and **II. 14**). Adding hydrogen (either within a N_2 or a N_2/Ar atmosphere) to a ratio H_2/N_2 of 2-3% leads to decrease the carrier concentration by at least two decades, some 10^{17} cm^{-3} can then be achieved (see **Figures II. 18** and **II. 28**). This effect is jointly obtained with an amphoteric behavior since n-type or p-type material is retrieved from Hall measurements (see Figures **II. 9, II. 14, II. 18, II. 23** and **II. 28**). The carrier mobility is very low of some $cm^2.V^{-1}.s^{-1}$ or even less (see **Figures II. 18** and **II. 28**). Hence, the resistivity is low, in the order of 0.1-1 Ω.cm for materials deposited without hydrogen in the sputtering atmosphere. One or even two orders of magnitude can be gained adding hydrogen, reaching then around 10 Ω.cm.

The optical bandgap deduced from UV-Vis spectroscopy measurements show a very huge large range, from 1.6 eV up to 2.2 eV depending on the different sputtering conditions. In all cases, the transmittance spectrum does not exhibit an abrupt transition. Even if the Burstein-Moss effect has been suspected for the first case that was made, i.e the $Zn_{DC}Sn_{RF}$ one (see **Figures II. 9** and **II. 10**), all other subsequent experiments do not support this. Same range of variation of bandgap has been obtained for the $Zn_{RF}Sn_{DC}$ (see **Figures II. 14** and **II. 15**) where the carrier concentration is slightly changing but the reverse way of the bandgap variation if the Burstein-Moss effect was applying. Nevertheless, except the points corresponding to the first investigated N_2/Ar ratios of the $Zn_{DC}Sn_{RF}$ configuration and the measurement accuracy, a huge bangap variation (from 1.6 to 2 eV) should have been linked to a small carrier concentration modification (from 1 to 5 10^{20} cm^{-3}).

Thinks get shaky when hydrogen is added since with a decrease of carrier concentration by two decades (see **Figures II. 18** and **II. 19** or **Figures II. 23** and **II. 24**), the optical bandgap increases or remains almost stable. Same trend is also observed on the small comparative series depicted in section II. 7 where the optical bandgap value varies inversely to the carrier concentration (see **Figures II. 28** and **II. 29**).

Right now, no clear conclusion can be made on the link between carrier concentration and optical bandgap.

Chapter III: **PRESSURE, TEMPERATURE AND RAPID THERMAL ANNEALING**

In this chapter, we will firstly mention the effect of sputtering pressure on properties of $ZnSnN_2$ thin films.

Secondly, we will report on the effect of temperature on the film properties. Temperature has been applied either during or after deposition. The in-situ heating is achieved owing to the in-built substrate heater within the deposition chamber. The post-annealing is made using rapid Thermal Annealing (RTA) in a chamber that is under N_2 atmosphere.

The in-situ heating extends greatly the processing time since several hours are needed for temperature to be reached and the same time for system to cool down before sample extraction.

III.1 **Effect of sputtering pressure:**

According to Wasa [67], the deposition process under low vacuum pressure can influence the morphology of the deposited thin films, especially their porosity, leading to poor adhesion. The adhesion between the material and the substrate is dependent on the stored energy at unit area (u_s) of the deposited film, expressed by equation (3.1) [67]:

$$u_s = u_v d = \frac{\sigma^2 d}{2Y} \left(J/m^2 \right) \tag{3.1}$$

where u_v indicates the elastic energy, d is the thickness of thin the film, σ is the internal stress, and Y is the Young's modulus.

The thin film is removed from the substrate when the thickness exceeds the critical thickness or the stored energy at unit area is larger than the adhesive energy. It is possible to minimize the u_s by minimizing the stress σ. The thermal expansion coefficient and the lattice structure of the substrate should be suitable with deposited material. The internal stress, σ, is given by equation (3.2)

$$\sigma = \frac{\varepsilon Y}{2\nu} \tag{3.2}$$

where ε indicates the strain and ν indicates the Poisson's ratio of the films.

Additionally, the pressure in the sputtering chamber is also an important parameter in preventing the undesirable contamination of oxygen [33]. Although oxygen is not introduced into the sputtering chamber, unintentionally oxygen doped $ZnSnN_2$ films are mentioned in previous literature reports [33], [43], [44], [50], [51], [68]. Its origin may issue from two options that are not necessarily exclusive: from oxygen impurities in Ar and N_2 gas (≤ 5ppm) during deposition, and adsorbed oxygen during air exposure after deposition.

The base pressure was 10^{-8} mbar, the sputtering pressure was varied from 0.01 to 0.05 mbar, and other parameters were fixed. A 30W-RF and 50W-DC powers were supplied to Zn and Sn targets, respectively. Argon flux was 10 sccm, nitrogen flux was 20 sccm (N_2/Ar

ratio = 2), sputtering time was 11.5 minutes. All the samples were deposited on Eagle XG substrate.

The effects of pressure on thin film composition and sputtering rate are shown in **Figure III.1**. At lowest pressure (0.01 mbar), the material is Zn-rich (54% of Zn). When the pressure increases, the films become Sn-rich, Zn/(Zn+Sn) is in range 48% to 49%. Whereas the composition does not change significantly while pressure increases from 0.02 to 0.05 mbar, the sputtering rate decreases by nearly 2 times.

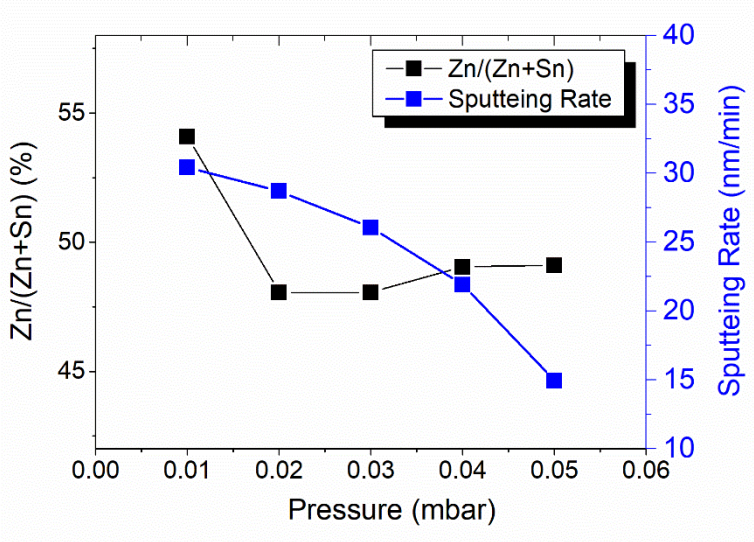

Figure III. 1: *Zn/(Zn+Sn) ratio and sputtering rate via sputtering pressure ($Zn_{RF}Sn_{DC}$ series).*

The scanning electron microscopy (SEM) was employed to investigate the top and cross-sectional views of films (**Figure III. 2**). SEM imaging of 0.01 mbar sample was difficult to perform, the obtained image was not clear, the grain boundaries are tough to assess even if large voids seem present. At higher pressure, it is difficult to identify the difference in surface morphology that is much more cauliflower-like; interstitial voids can be observed in all cases and their size seems to expand with increasing pressure. Large voids may be the cause of the increase of the amount of oxygen adsorbed on the surface and reducing the adhesion between thin film and substrate. The SEM cross-section image shows the microstructure is columnar. This result is consistent with the explanation of John A. Thornton [69], [70]. The grain size becomes "visually" smaller by increasing sputtering pressure.

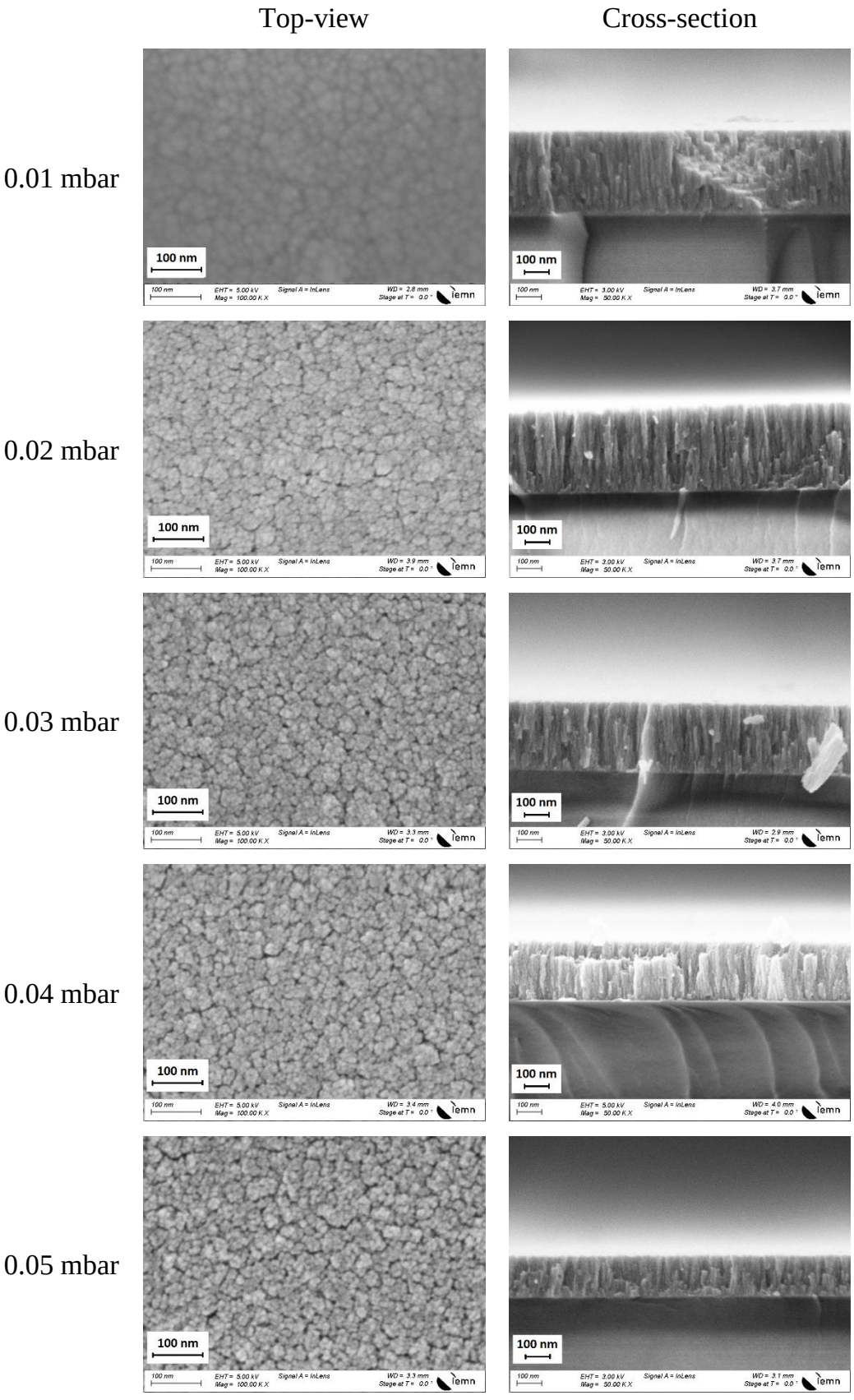

Figure III. 2: *SEM images, top-views (on the left hand side) and cross-sections (on the right hand side) of $ZnSnN_2$ thin films ($Zn_{RF}Sn_{DC}$ series) deposited at pressure of 0.01 to 0.05 mbar.*

The effect of the sputtering pressure on the crystal structure is showed on **Figure III.3**. At 0.01 mbar, XRD data match all the characteristic peaks of $ZnSnN_2$. As sputtering pressure increase, the (200) (121) and (320) become predominant, and the other peak intensities decrease, although the difference in thickness prevents the full comparison of peak intensity between samples. It is has to be noted that for a pressure range of 0.02 to 0.05 mbar, the sputtering rate decreases by 2 times while the intensities of (200), (121) and (320) peaks decrease by approximately 7, 4 and 14 times, respectively.

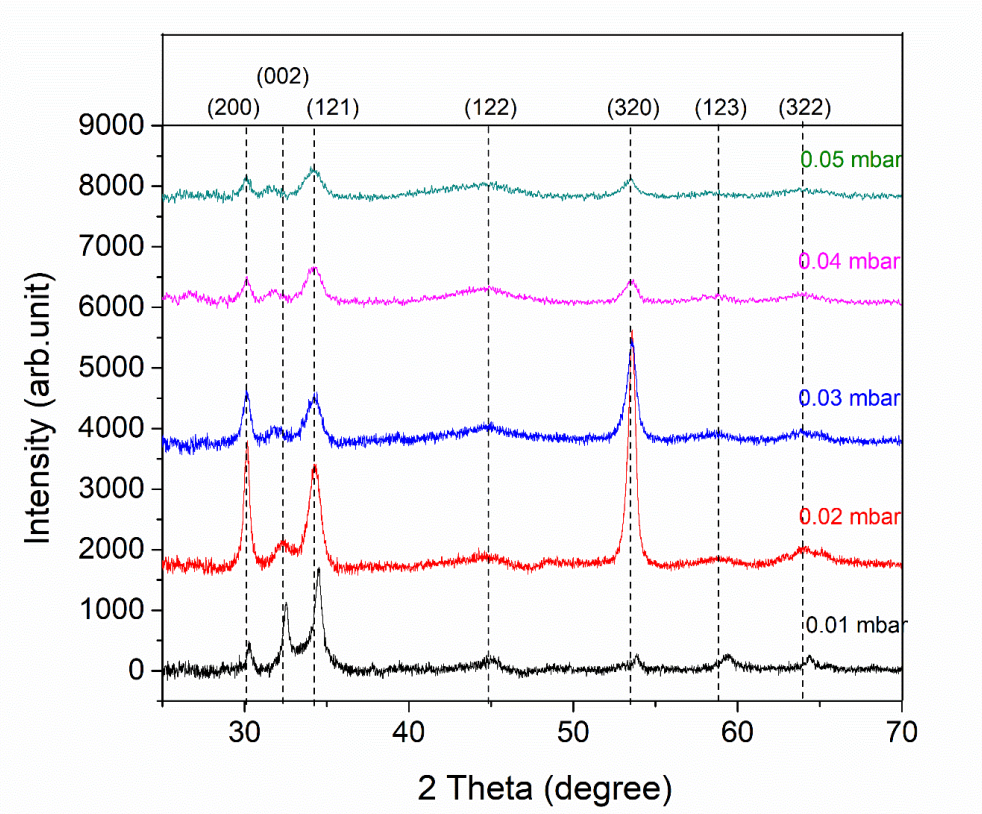

Figure III. 3: *XRD diffractograms of $ZnSnN_2$ films ($Zn_{RF}Sn_{DC}$ series) deposited at different sputtering pressure.*

As in previous chapter, assuming that the crystal structure of $ZnSnN_2$ is orthorhombic, the lattice parameters determined from XRD data are reported in **Table III. 1**. While increasing the sputtering pressure, b value slightly increases. The a and c values remain rather constant within experimental determination error. We can notice that those values are consistent with that obtained in another fabrication run of samples (**Table II.3**, N_2/Ar ratio = 2).

Table III. 1: Lattice parameters calculated from XRD data for $ZnSnN_2$ thin films ($Zn_{RF}Sn_{DC}$ series) deposited at different pressure.

Pressure (mbar)	a (Å)	b (Å)	c (Å)	D (nm)
0.01	5.90	6.79	5.57	21.7
0.02	5.93	6.82	5.60	18.1
0.03	5.93	6.82	5.65	15.3
0.04	5.93	6.84	5.61	12.4
0.05	5.93	6.86	5.59	12.4

The average crystal size (D), evaluated from the (200) peak width using the Scherrer formula (2.6), shows that the crystal size decreases from 22 to 12 nm when the pressure increases from 0.01 to 0.05 mbar; that is consistent with SEM top view images of **Figure III. 2**.

The strain of thin film can be measured determined from XRD data by using Williamson-Hall plot method [71]:

$$\beta_{tot} = \beta_D + \beta_\varepsilon \tag{3.3}$$

where β_{tot} is the total broadening, β_D is the broadening (determined at full width at half maximum (FWHM)) due to crystalline size and β_ε is the broadening due to strain.

$$\beta_D = \frac{K\lambda}{D\cos\theta} \tag{3.4}$$

$$\beta_\varepsilon = 4\varepsilon\tan\theta \tag{3.5}$$

where K is the shape factor (~ 0.93), λ the wavelength (0.15406 nm), θ is the peak position in radians, D is the average crystal size and ε the strain.

Combining equations (3.3), (3.4) and (3.5), we obtain:

$$\beta_{tot}\cos\theta = \frac{K\lambda}{D} + 4\varepsilon\sin\theta \tag{3.6}$$

Using a graphical representation, ε is the slope of the $\beta_{tot}\cos\theta = f(4\sin\theta)$ linear curve.

The so obtained strain value of $ZnSnN_2$ thin films is shown in **Figure III. 4**. When pressure increases from 0.01 to 0.05 mbar, the strain value increases by one order of magnitude, from $2.8x10^{-3}$ to $2.3x10^{-2}$. From equation (3.2) it can be predicted that the internal stress of the film increases with sputtering pressure.

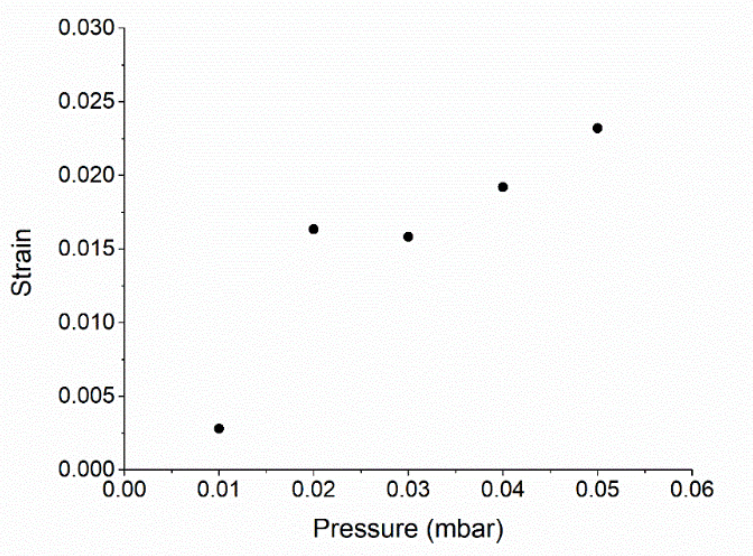

Figure III. 4: *Calculated strain,ε, of $ZnSnN_2$ films ($Zn_{RF}Sn_{DC}$ series) deposited on Eagle XG substrate via versus the sputtering pressure (N_2/Ar =2).*

The UV-Vis spectra represented in **Figure III. 5a** show a shift of the cut-off in transmittance towards lower wavelengths (blue shift) as the pressure increase. The optical bandgap can be calculated using Tauc's relation (2.7) (**Figure III. 5b**). It increases from 1.47 eV to 2.04 eV when pressure increases from 0.01 to 0.04 mbar, then it decreases to 1.93 eV at 0.05 mbar.

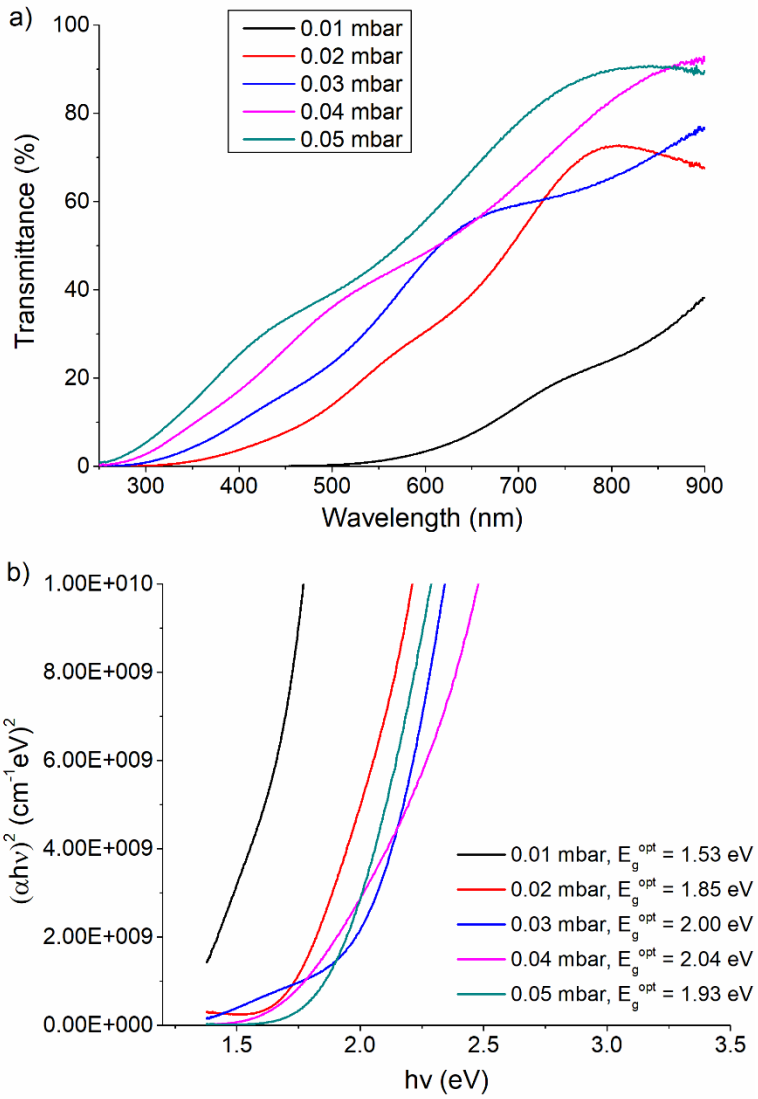

Figure III. 5: *a) Transmittance vs. wavelength spectra (UV-Vis spectroscopy) for $Zn_{RF}Sn_{DC}$ samples deposited under varied deposition pressures (N_2/Ar = 2), b) Corresponding optical bandgap values calculated using Tauc's equation.*

The results of Hall measurements are shown in **Figure III. 6**. The measurement of 0.01 mbar sample cannot be made. The resistivity does not significantly vary; it ranges from 0.12 to 0.18 Ω.cm. Nevertheless, as the sputtering pressure increases, the mobility increases from 0.16 to 2.74 $cm^2V^{-1}s^{-1}$ whereas the carrier density decreases by one order of magnitude from $2.3x10^{20}$ to $1.2x10^{19}$ cm^{-3}. All the samples exhibit n-type polarity. The Hall measurement results obtained are similar to those reported by Cai *et al.* [72], the increase in sputtering pressure reduces the concentration of oxygen contaminating the $ZnSnN_2$ during sputtering, and increases the nitrogen content. It means the concentration

of the donor effect O_N (oxygen substituting nitrogen) and V_N (nitrogen vacancy) are reduced, leading to decrease the carrier density.

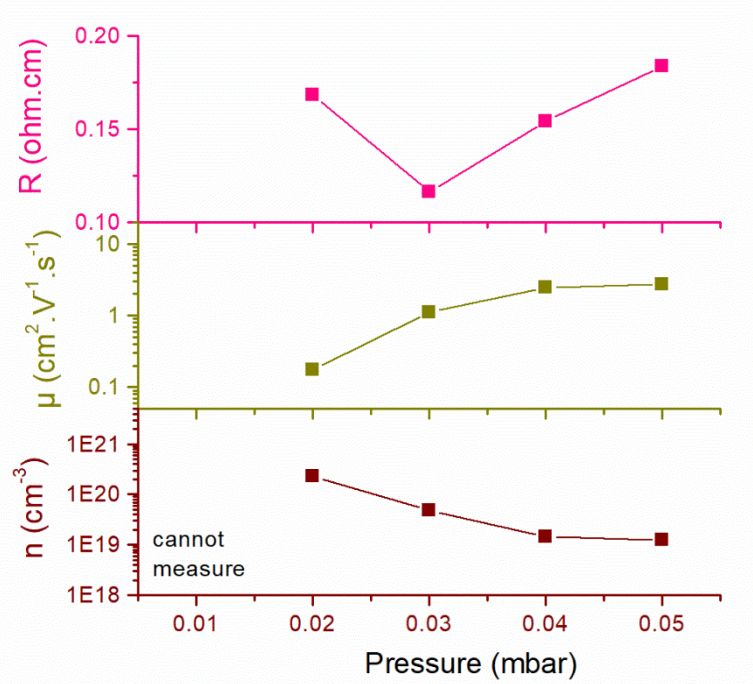

Figure III. 6: *Resistivity (R), carrier mobility (μ) and carrier density (n) of $Zn_{RF}Sn_{DC}$ series (determined from Hall measurements) versus deposition pressure.*

Since the carrier concentration is decreasing when increasing the sputtering pressure whereas the optical bandgap value increases, a relationship between those two involving Burstein-Moss effect cannot be clearly established.

III.2 Effect of substrate temperature

In Chapter II, the $ZnSnN_2$ thin films were deposited at room temperature, or more precisely without any intentional heating (the substrate holder is cooled during deposition). Small crystal sizes were obtained. Specially, the XRD data of $Zn_{RF}Sn_{DC}$ (Section II.4.2.2) do not show all the characteristic peaks of $ZnSnN_2$ when deposition was made at low nitrogen flux. In addition, the increase in nitrogen flux reduced the crystal size. To improve the microstructure of thin film, kinetics of growth is a factor that should be concerned. At high substrate temperature, the kinetic energy of incident species increases leading to an increase in the grain size [67]. The change in microstructure, optical and electrical properties based

on substrate temperature were reported at for ITO [73], ZnO [74], and NiO [75]. So far, most of the published results on $ZnSnN_2$ fabrication refer to deposition at substrate temperatures between 100°C and 450°C [33], [34], [43]–[46], [51], [76]. Furthermore, here, $ZnSnN_2$ is deposited on glass substrates that are stable in this temperature range in order to limit the diffusion of oxygen into the material during the sputtering process [51].

In this section, the substrate temperature was varied from room temperature (i.e. non intentionally heated, approximately 25°C) to 400°C. The limit in temperature is governed by technical aspects linked to the rotating substrate holder and its related vacuum joint. 30W-RF and 50W-DC power supplies were applied to Zn and Sn targets, respectively. Argon flux and nitrogen flux were fixed at 10 sccm and 20 sccm, respectively. The sputtering pressure was 0.02 mbar, and rotation speed was 20 rpm. All samples films were deposited on Eagle XG substrates and the process time was 11.5 minutes.

The variations of thin film composition and sputtering rate versus the sputtering temperature are shown in **Figure III.7**. At room temperature, the obtained $ZnSnN_2$ is almost stoichiometric (50% of Zn). When the substrate temperature is increased, the films become Zn-rich, Zn/(Zn+Sn) is in range 52% to 53%. This result shows the same behavior as reported by Fioretti *et al* [44]. Moreover, the deposition rate curve exhibits a rather U-shape behavior with a minimum at 200°C. Its variation is somewhat limited with a sputtering rate value of 27.8 ± 0.8 nm/min over the full temperature range.

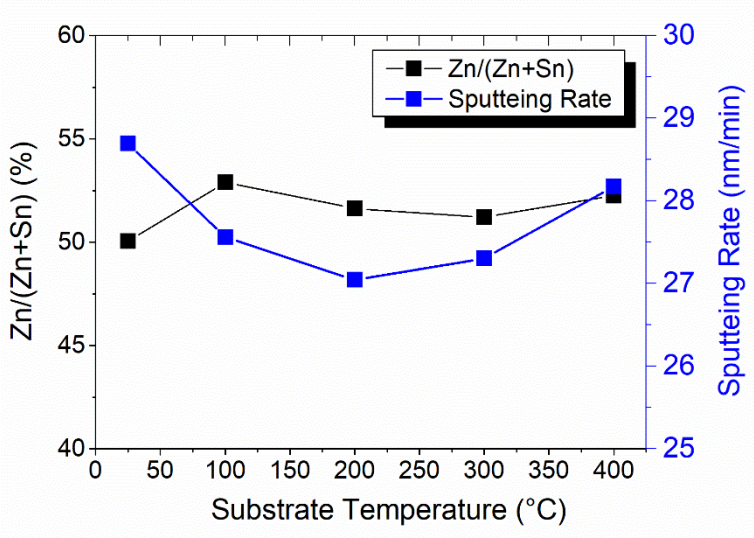

Figure III. 7: *Zn/(Zn+Sn) ratio and sputtering rate via sputtering pressure.*

Top and cross-sectional SEM views of $ZnSnN_2$ films are illustrated in **Figure III.8**. It is difficult to identify the difference in surface morphology that is much more cauliflower-like for all samples. The SEM cross-section image shows the microstructure is columnar. The grain size and column become "visually" bigger by increasing substrate temperature.

25°C

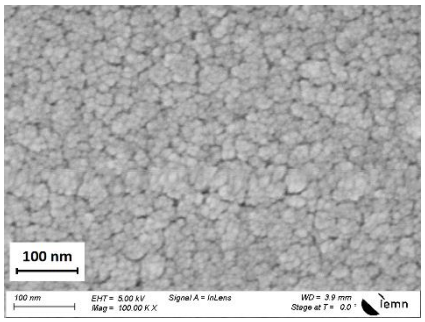

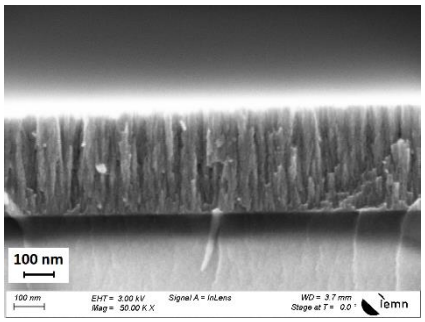

100°C

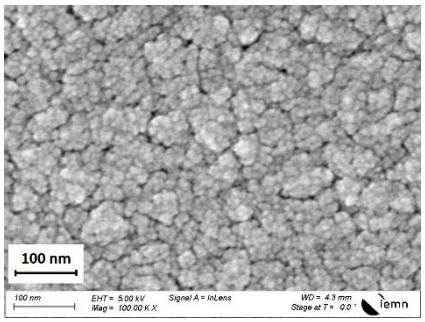

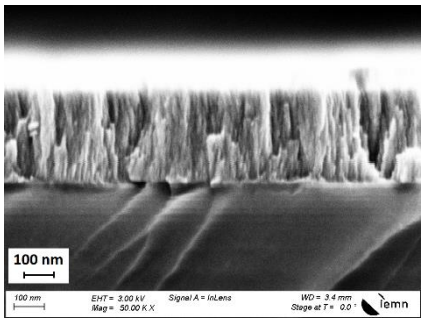

200°C

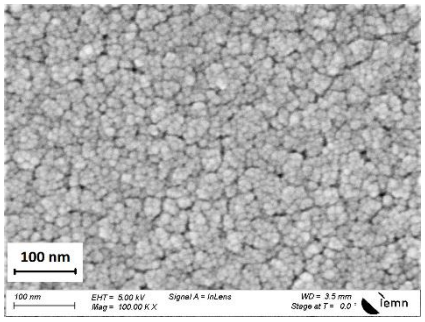

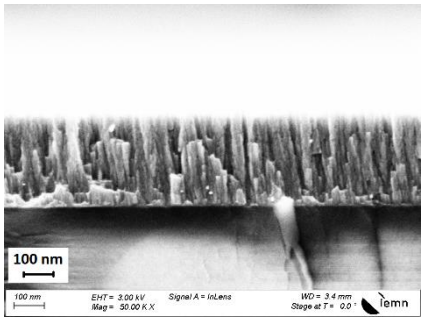

300°C

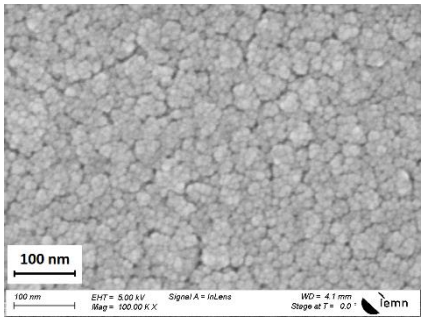

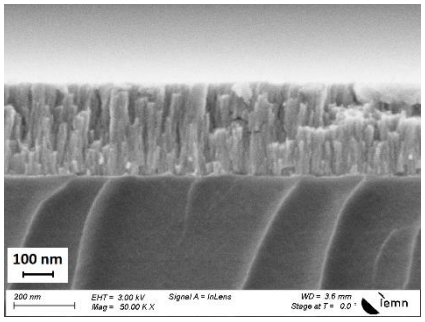

400°C

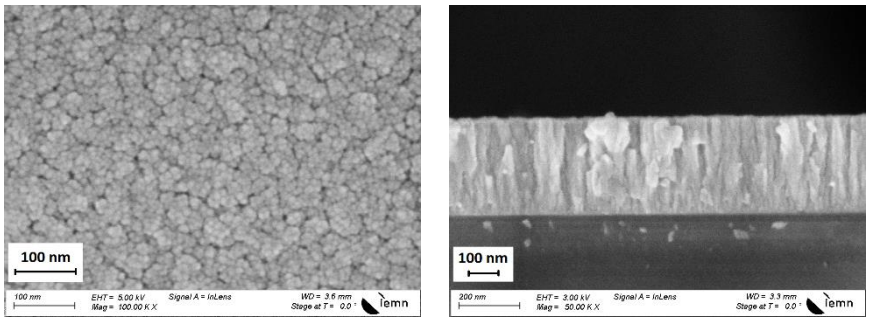

Figure III. 8: *SEM images, top-views (on the left hand side) and cross-sections (on the right hand side) of $ZnSnN_2$ thin films deposited at different temperatures, from room temperature up to 400°C.*

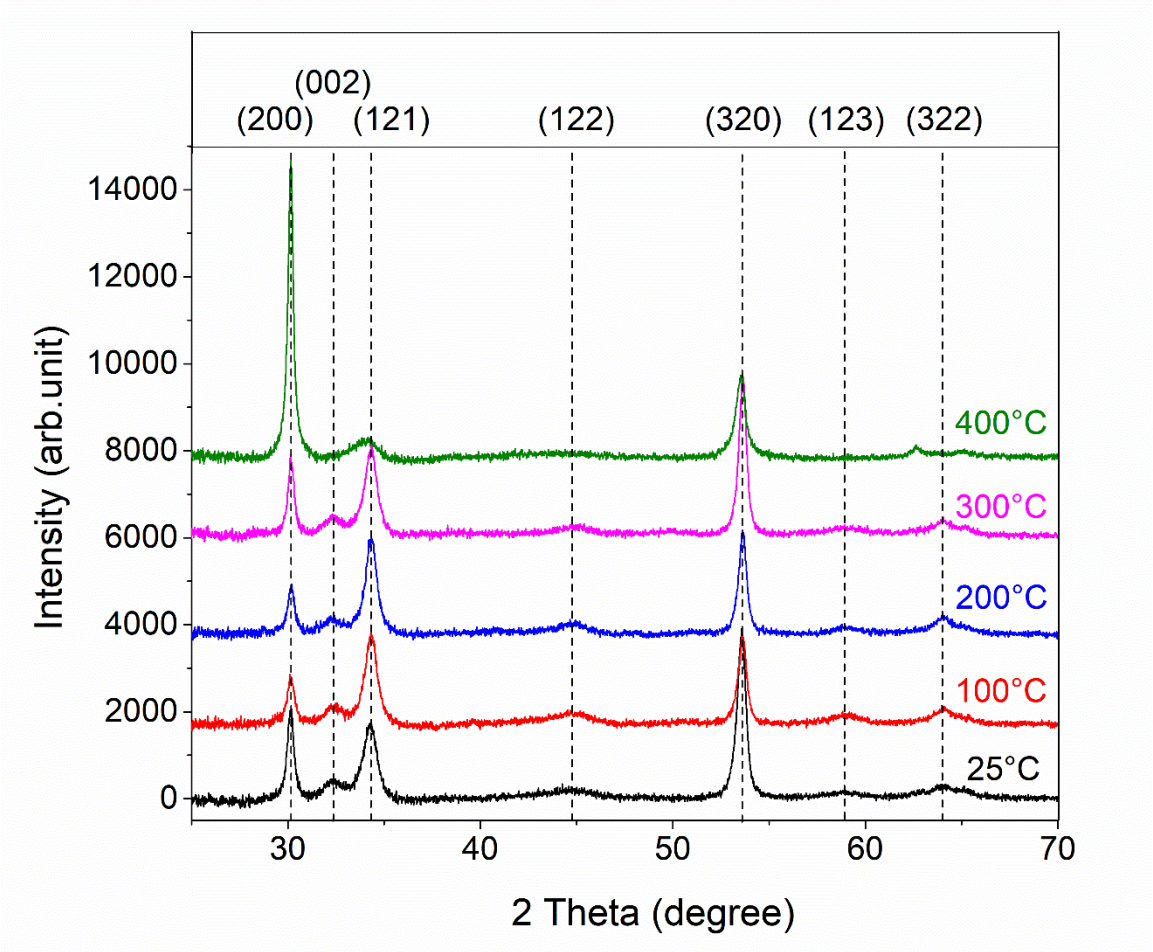

Figure III. 9: *XRD diffractograms of the $ZnSnN_2$ films deposited at different temperatures, from 25°C to 400°C (Note: the 25°C curve corresponds to the N_2/Ar curve of* ***Figure II.13****).*

The corresponding XRD data is presented in **Figure III. 9**. While the substrate temperature is lower than 400°C, the seven characteristic peaks [59] of $ZnSnN_2$ can be distinguished

even if some are weak. Only (200), (121) and (320) planes are dominant with high intensity, narrow and sharp peaks. At 400°C, the sputtering rate is almost equal to sample deposited on 25°C substrate, but the intensity of (200) peak increases dramatically by 3 times while some others completely disappear and even newer one (around 63°) appears. The average crystal size (D), evaluated from the (200) peak width using the Scherrer formula (2.6), increases from 17 to 21 nm when the substrate temperature increases. These results are consistent with visual evaluation from SEM images above (**Figure III. 8**). The lattice parameters are described in **Table III.2**, the c value increases slightly with the increase of substrate temperature.

Table III. 2: Lattice parameters and crystallite size determined from XRD data for $ZnSnN_2$ thin films deposited at different substrate temperature.

Temperature (°C)	a (Å)	b (Å)	c (Å)	D (nm)
25	5.93	6.82	5.60	17.0
100	5.92	6.81	5.59	16.6
200	5.92	6.81	5.58	17.7
300	5.92	6.81	5.60	19.3
400	5.93	6.85	5.76	21.0

The substrate temperature does not significantly affect the electrical properties of the material (**Figure III. 10**). The resistivity is in the range 0.08 - 0.25 Ω.cm, the mobility in the 0.17 to 0.30 $cm^2V^{-1}s^{-1}$ range and the carrier density in the $1.4x10^{20}$ to $3.8x10^{20}$ cm^{-3}. All the samples exhibit n-type polarity.

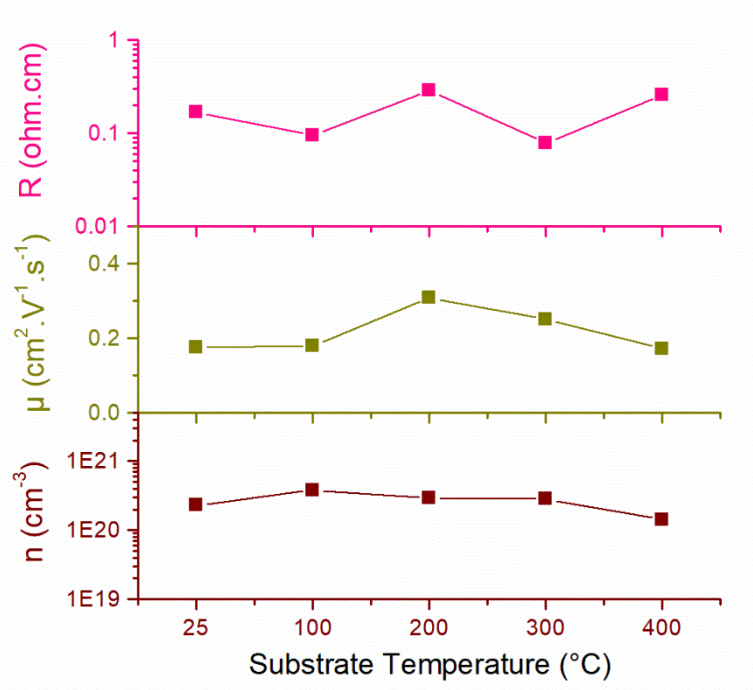

Figure III. 10: *Resistivity (R), carrier mobility (μ) and carrier density (n) of $Zn_{RF}Sn_{DC}$ series (determined from Hall measurements) versus substrate temperature.*

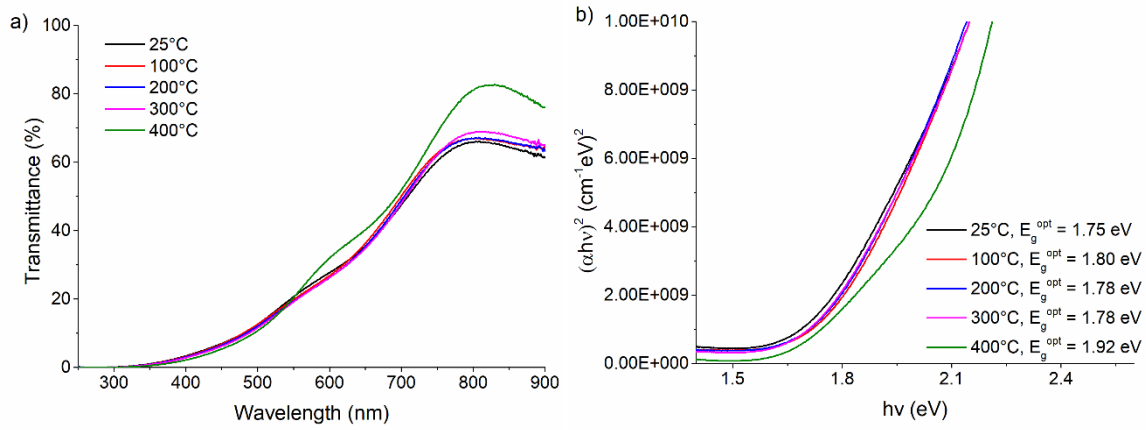

Figure III. 11: *a) Transmittance vs. wavelength spectra (UV-Vis spectroscopy) for $Zn_{RF}Sn_{DC}$ samples deposited at different substrate temperature, b) Corresponding optical bandgap values calculated using Tauc's equation.*

The UV-Vis spectra and optical band gap are described in **Figure III. 11**. No particular effect of temperature is seen on the optical properties of $ZnSnN_2$. This is quite in good agreement with the stability of carrier concentration that has been observed.

III.3 **Effect of rapid thermal annealing (RTA)**

As we saw in the previous paragraph, the substrate temperature during deposition does not affect significantly the electrical and optical properties of $ZnSnN_2$. Besides, the heating and cooling processes take long time. The second way applying temperature to the samples is using post-deposition annealing. Rapid thermal annealing (RTA) is a practical way doing so, control of heating and cooling gradients, easy temperature control and even some possibilities to choose the annealing atmosphere. It also makes sense in reducing production costs. Furthermore, the RTA step is an easy upscalable process that is used widely in the preparation of thin films in the semiconductor industry. The annealing treatment may relief strain due to lattice mismatch and also modify the surface morphology, increasing the grain size and crystalline quality [67].

III.3.1 RTA in $Zn_{DC}Sn_{RF}$ mode and under N_2/Ar atmosphere ($Zn_{DC}Sn_{RF}$ - NA)

III.3.1.1 Deposition of $Zn_{DC}Sn_{RF}$-NA thin films on Eagle XG Substrates

In this section, 25W-DC and 70W-RF supplies were applied to Zn and Sn targets, respectively. The operating pressure in the chamber was fixed at to 2.10^{-2} mbar, the argon flux to 10 sccm, and the nitrogen flux to 20 sccm. This is the same set of process parameters that has been used in section II.4.2.1 with N_2/Ar value of 2. The process time was 25 minutes. The as-deposited $ZnSnN_2$ thin film obtained nearly stoichiometry (approximately 49.8% Zn/(Zn+Sn) ratio) and its thickness was 440 nm. For the post-deposition annealing step, the temperature has been varied from 100°C to 550°C with a 50°C step in pure N_2 atmosphere (300 sccm). The annealing time was 15 minutes and the heating-up/cooling-down rate was 100°C/min. The change in the composition of the films was recorded using EDX and its thickness was measured (**Figure III. 12**). Below 500°C, the Zn/(Zn+Sn) ratio decreases monotonously in the range 49.8% down to 48.1% but increases drastically up to 64.7% at 550°C. Such a trend has not been recorded on the thickness that is rather stable, taking into account the measurement uncertainties, in the 420 to 440 nm range.

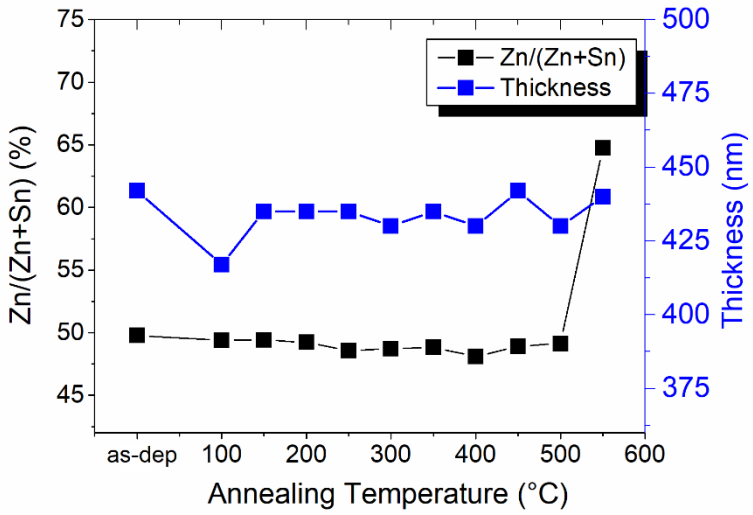

Figure III. 12: *Zn/(Zn+Sn) ratio and thickness of $Zn_{DC}Sn_{RF}$-NA samples deposited on Eagle XG substrate versus post-deposition annealing temperature.*

The effect of annealing process at different temperatures on thin film morphology is shown in **Figure III. 13**. Up to 300°C, the cross-section images show columnar microstructure for all samples with no significant changes in the morphology and grain size. At 400°C and 500°C, columnar structure appears slightly slanted with the degradation of surface flatness as well the apparition of vertical voids. At 550°C, the columnar structure has totally shifted towards a granular structure with large voids. From top views, cracks appear starting at 200°C whose size increases with increasing temperature. At 550°C, the granular aspect observed on cross-sectional views is also observed on top views. The cracks that appear for annealing temperatures equal or above 200°C are attributed to the stress state of the annealed thin films. The reason is that films deposited onto substrates of different material often develop in-plane tensile or compressive stress. When treated at high temperature then cooled, films will then develop biaxial in-plane tensile stresses if the thermal expansion coefficient of the film exceeds that of the substrate [77], it is also called thermal stress. This assumption is verified by comparing the thermal expansion coefficient (TEC) value of the $ZnSnN_2$ thin film and of the substrate. According to Atwater *et al.* [78], $ZnSnN_2$ thin films present TEC's of $\alpha_a \sim 3.5x10^{-5}$ K^{-1}, $\alpha_b \sim 5x10^{-5}$ K^{-1}, and $\alpha_c \sim 2.7x10^{-5}$ K^{-1} while Eagle XG substrate presents a TECs of $\alpha \sim 3.5x10^{-6}$ C^{-1} (data from the Certificate of Analysis), i.e. one order of magnitude below. The increase of the density and length/size of cracks when increasing the annealing temperature can then be correlated. The 550°C case is obviously

different since the columnar structure fully breaks down into a granular one. Some more or less spherical forms are observed at its surface (bottom left picture of **Figure III. 13**).

As-Dep

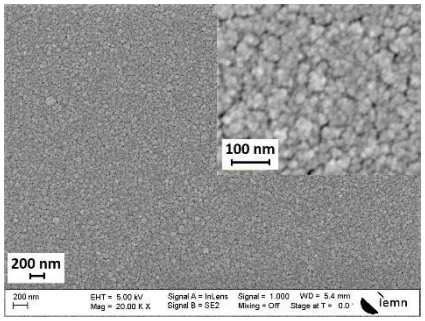

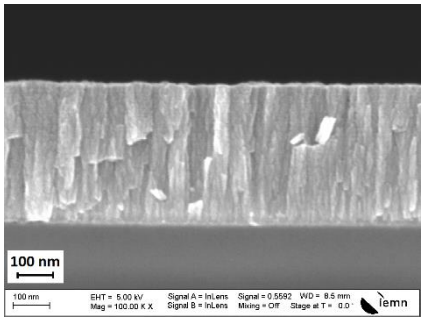

RTA
100°C

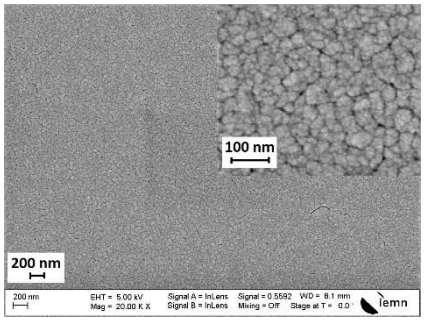

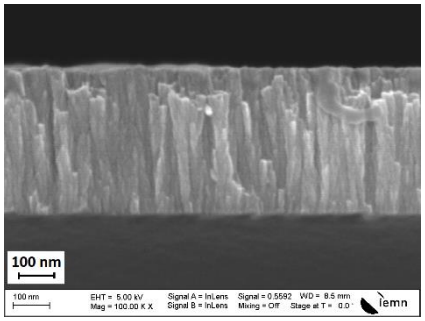

RTA
200°C

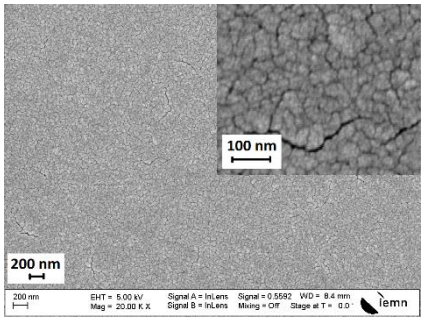

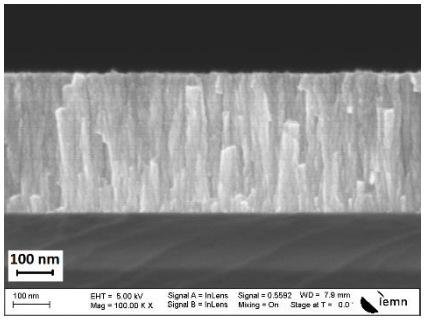

RTA
300°C

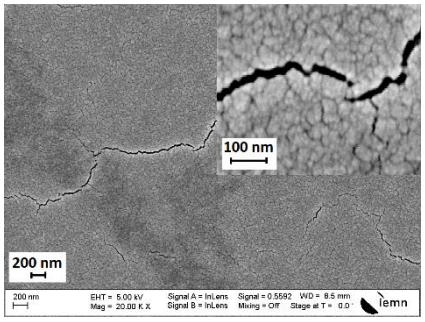

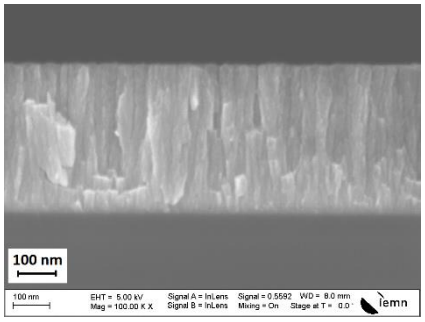

RTA
400°C

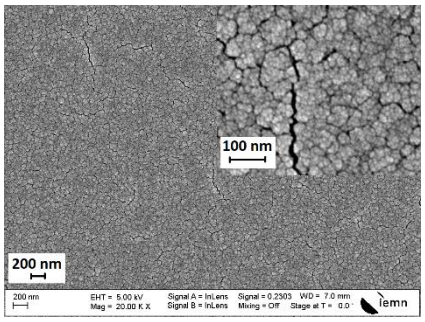

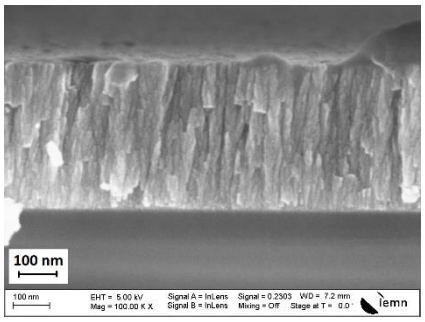

RTA
500°C

RTA
550°C

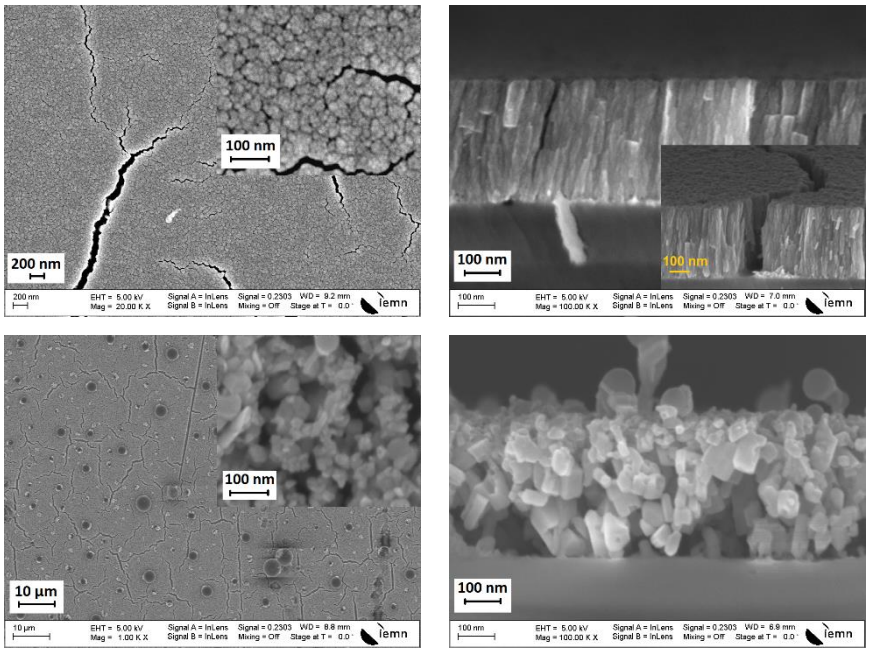

Figure III. 13: *SEM images, top-views (on the left hand side. To be noted that the zoom on the 550°C sample is 20 times greater compare to others) and cross-sections (on the right hand side) of $Zn_{DC}Sn_{RF}$-NA series thin films deposited at room temperature with different post-deposition rapid thermal anneals from 100°C up to 550°C.*

The $Zn_{DC}Sn_{RF}$-NA thin film that was post- annealed at 550°C was again observed by EDX mapping to identify what those spheres consist of (**Figure III. 14**). It revealed phase decomposition with the diffusion and crystallization of tin on the surface and a background layer that is mostly constituted of zinc. This is also demonstrated by XRD data, depicted in the **Figure III. 15b**.

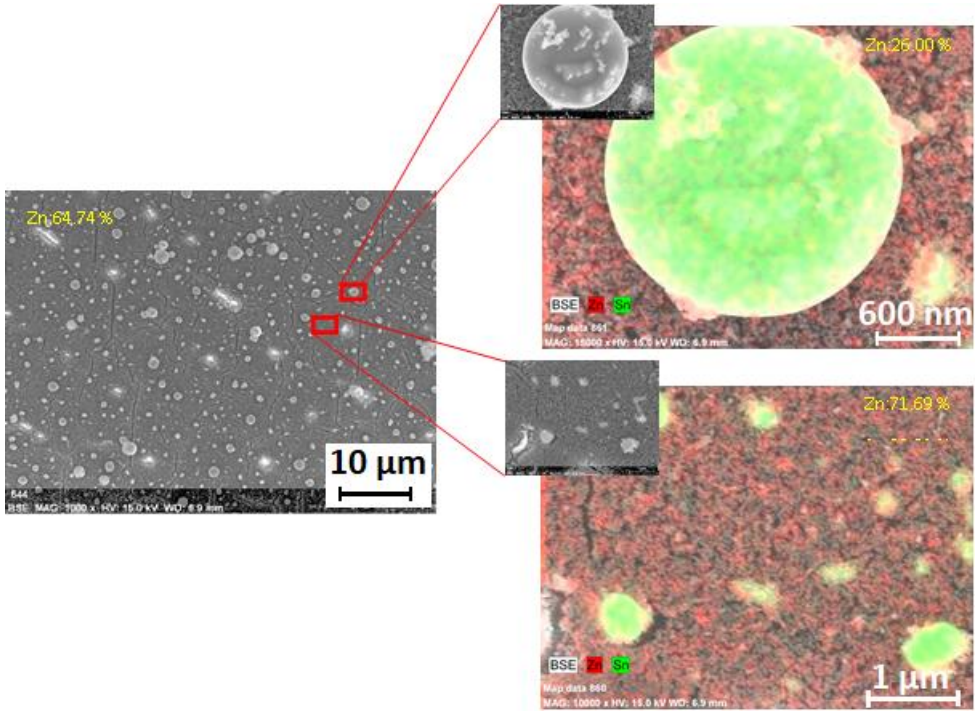

Figure III. 14: *SEM view (left hand side) and EDX mapping (right hand side) of* $Zn_{DC}Sn_{RF}$*-NA thin film on glass post-annealed at 550°C.*

The effect of post-annealing temperature on crystalline quality and orientation of the thin films is shown on **Figure III. 15**. For the annealing temperature range between 100°C and 500°C, all the characteristic peaks of $ZnSnN_2$ [59] can be retrieved. Their progressive shift towards higher diffraction angles could mean an increase of the inter-plane distance. The trend of preferred orientation is difficult to mention. For the 550°C case (**Figure III. 15b**), XRD data clearly show phase separation: the characteristic peaks of pure Sn (JCPDS #65-0296) [79] can be distinguished. Nevertheless, pure Zn XRD pattern (JCPDS #87-0713) [80] cannot be clearly pointed out. On the contrary, ZnO pattern (JCPDS #79-0206) [80] especially via the shallow peaks on both sides of 35° and around 47° could be discerned. Bottom right picture presented in **Figure III. 13** could effectively suggest the formation of ZnO particles.

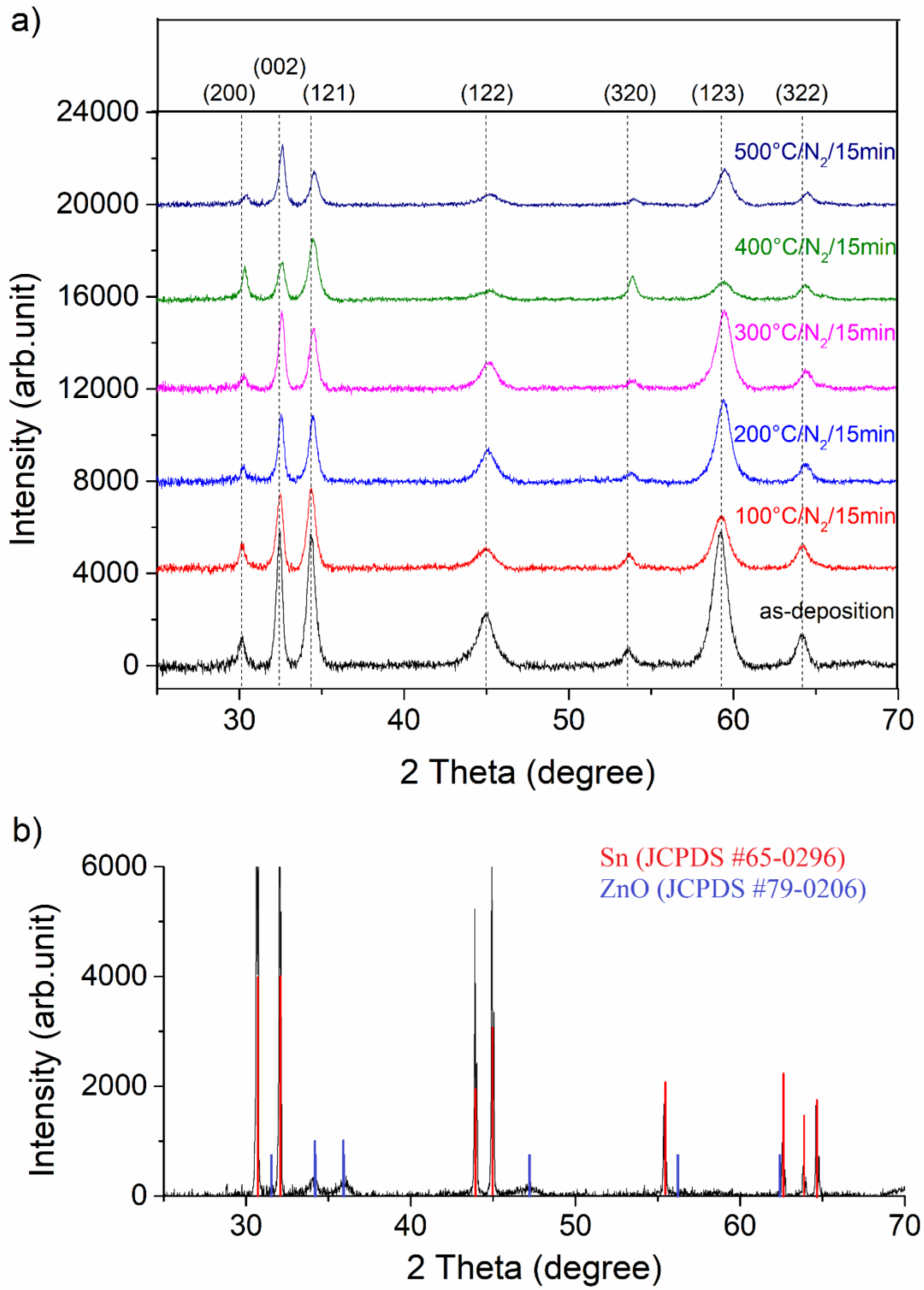

Figure III. 15: *XRD diffractograms of $Zn_{DC}Sn_{RF}$-NA series thin films on glass for different post-annealing temperatures: a) from 100°C to 500°C, b) 550°C sample data spectrum compared to XRD data of Sn on red peaks and ZnO on blue peaks*

The lattice parameters are described in **Table III. 3**; a very slight decrease of a, b and c values could be observed with temperature increase, whether this is really significant since it shall be within the experimental determination error..

Table III. 3: Lattice parameters calculated from XRD data of $Zn_{DC}Sn_{RF}$-NA thin films deposited on glass and post-annealed at 100°C to 500°C in N_2 atmosphere during 15 min.

Temp. (°C)	a (Å)	b (Å)	c (Å)
As-dep	5.93	6.83	5.52
100	5.92	6.83	5.51
150	5.91	6.82	5.51
200	5.90	6.81	5.50
250	5.91	6.81	5.50
300	5.90	6.81	5.50
350	5.90	6.81	5.50
400	5.89	6.81	5.50
450	5.89	6.81	5.51
500	5.88	6.80	5.49

Figure III. 16 shows the strain of $Zn_{DC}Sn_{RF}$-NA thin films deposited on glass calculated from XRD data and equation (3.6). The strain of as-deposited sample is $5.3x10^{-3}$, it increases to $7.0x10^{-3}$ as annealing temperature rises 100°C. At higher, the strain that should intuitively have been increased due to the difference in TEC value of $ZnSnN_2$ and glass does not exhibit a clear trend. The apparition of cracks in the films that can be observed on SEM pictures of **Figure III. 13** shall so have a stress-relief effect. The average crystal size (D), evaluated from the (200) peak width using the Scherrer formula (2.6), is in range 14.5 to 21.3 nm, so in the same order of values than on previous experiments (cf. section III. 1).

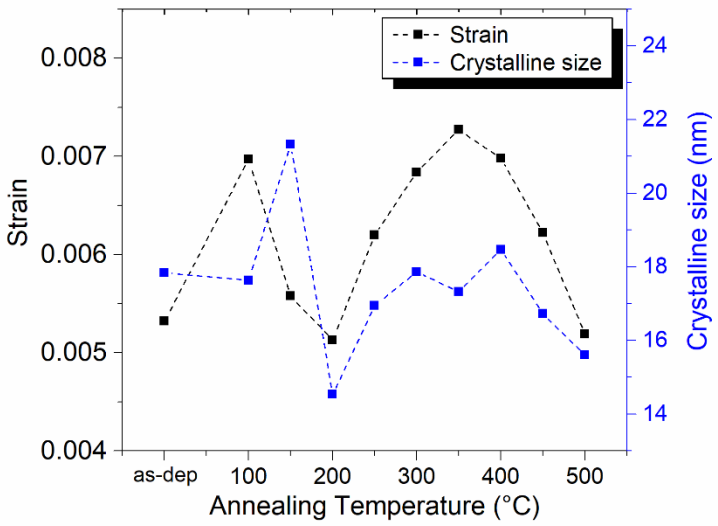

Figure III. 16: *Strain and crystal size of $Zn_{DC}Sn_{RF}$-NA series thin films deposited on glass and post-annealed from 100°C to 500°C.*

The UV-Vis spectra and optical band gap of $Zn_{DC}Sn_{RF}$-NA thin films on glass after annealing from 100°C to 550°C are shown in **Figure III. 17**. The optical gap increases slowly from 1.77 to 1.99 eV as the annealed temperature grows up to 500°C. Such an increase in optical bandgap by after annealing treatment has also been reported by some authors [45]–[47], [49]. The large increase to 2.26 eV observed at 550°C is obviously due to the film de-structuring as shown in **Figure III. 13**. Nevertheless, this value is far away the one of ZnO that is almost around 3.2 eV.

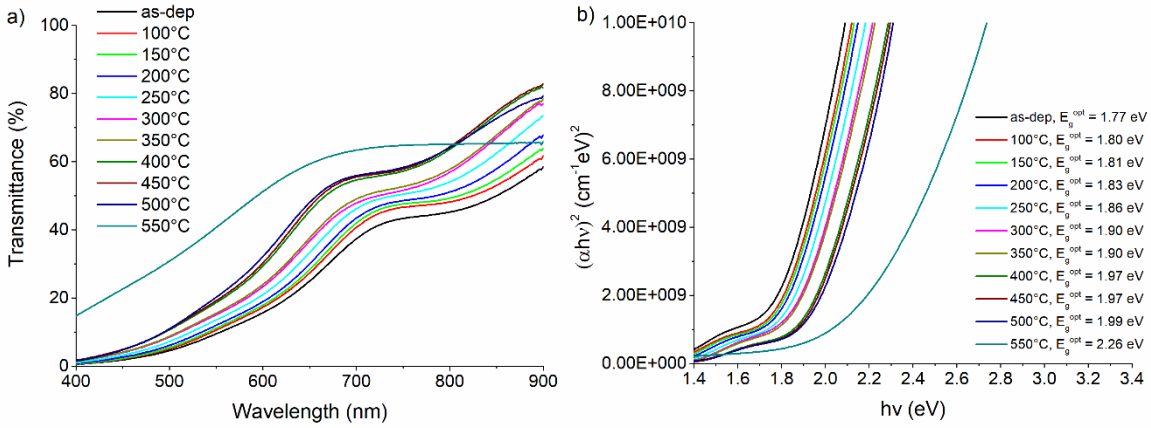

Figure III. 17: *a) Transmittance vs. wavelength spectra (UV-Vis spectroscopy) for $Zn_{DC}Sn_{RF}$-NA series deposited on glass at room temperature and post-annealed at different temperature, b) Corresponding optical bandgap values calculated using Tauc's equation.*

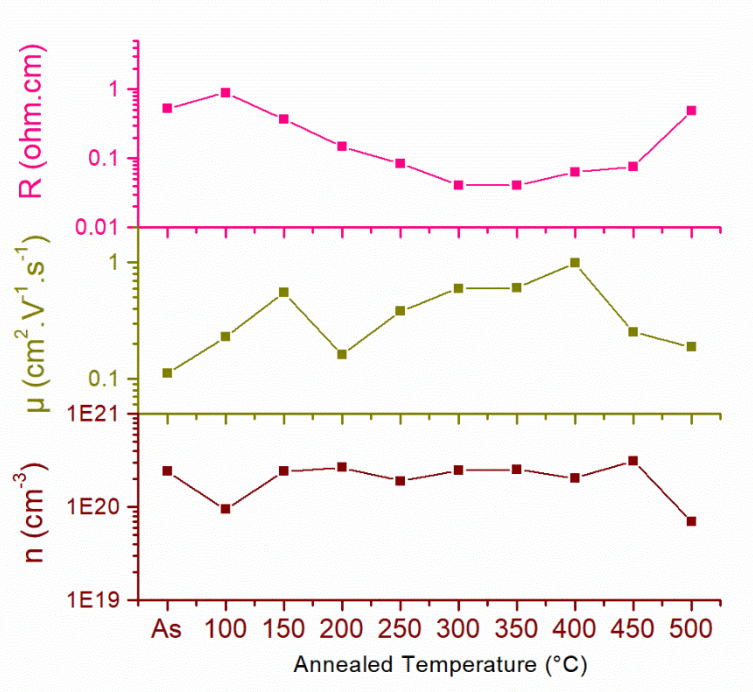

Figure III. 18: *Resistivity (R), carrier mobility (μ) and carrier density of $ZnSnN_2$ films (determined from Hall effect measurements) depending on the post-annealing temperatures.*

The annealing temperature does not significantly affect the electrical properties of the material, as illustrated in **Figure III. 18**. The resistivity is in range 0.04 to 0.90 Ω.cm, the mobility varies from 0.11 to 0.98 $cm^2V^{-1}s^{-1}$, and all the samples exhibit n-type polarity, with a carrier density ranging from $2.4x10^{20}$ to $7.0x10^{19}$ cm^{-3}.

III.3.1.2 Deposition of $Zn_{DC}Sn_{RF}$-NA thin film on Si (100)

To state on the origins of the cracks obtained in Section III.3.1.1, a lower TEC substrate, e.g. a silicon substrate [81] ($\alpha \sim 2.6.10^{-6}$ C^{-1}), was used instead of Eagle XG substrate.

The effect of annealing process at different temperatures on surface morphology of $Zn_{DC}Sn_{RF}$-NA thin films deposited on Si (100) substrates is shown in **Figure III.19**. In contrast to the deposition on Eagle XG substrate, the obtained thin films are almost crack-free after the annealing process as its temperature is raised to 400°C even if the density of interstitial voids increases. Larger cracks appeared at temperatures larger than of 400°C, and spherical Sn balls were also recorded. At 500°C, the surface of the thin film is also degraded.

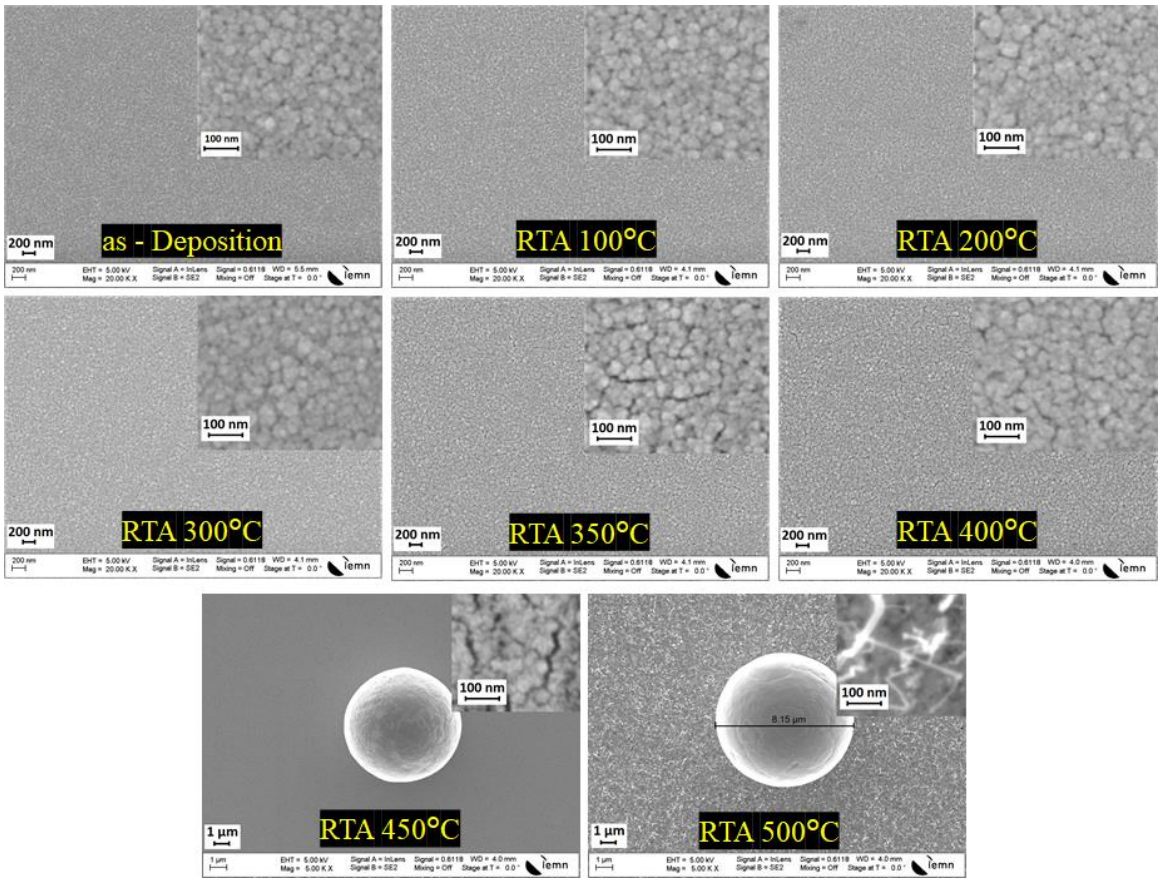

Figure III. 19: *SEM images of $Zn_{DC}Sn_{RF}$-NA thin films on Si (100) after RTA treatment (the scale of 450° and 500°C sample images is 4 times greater compared to others).*

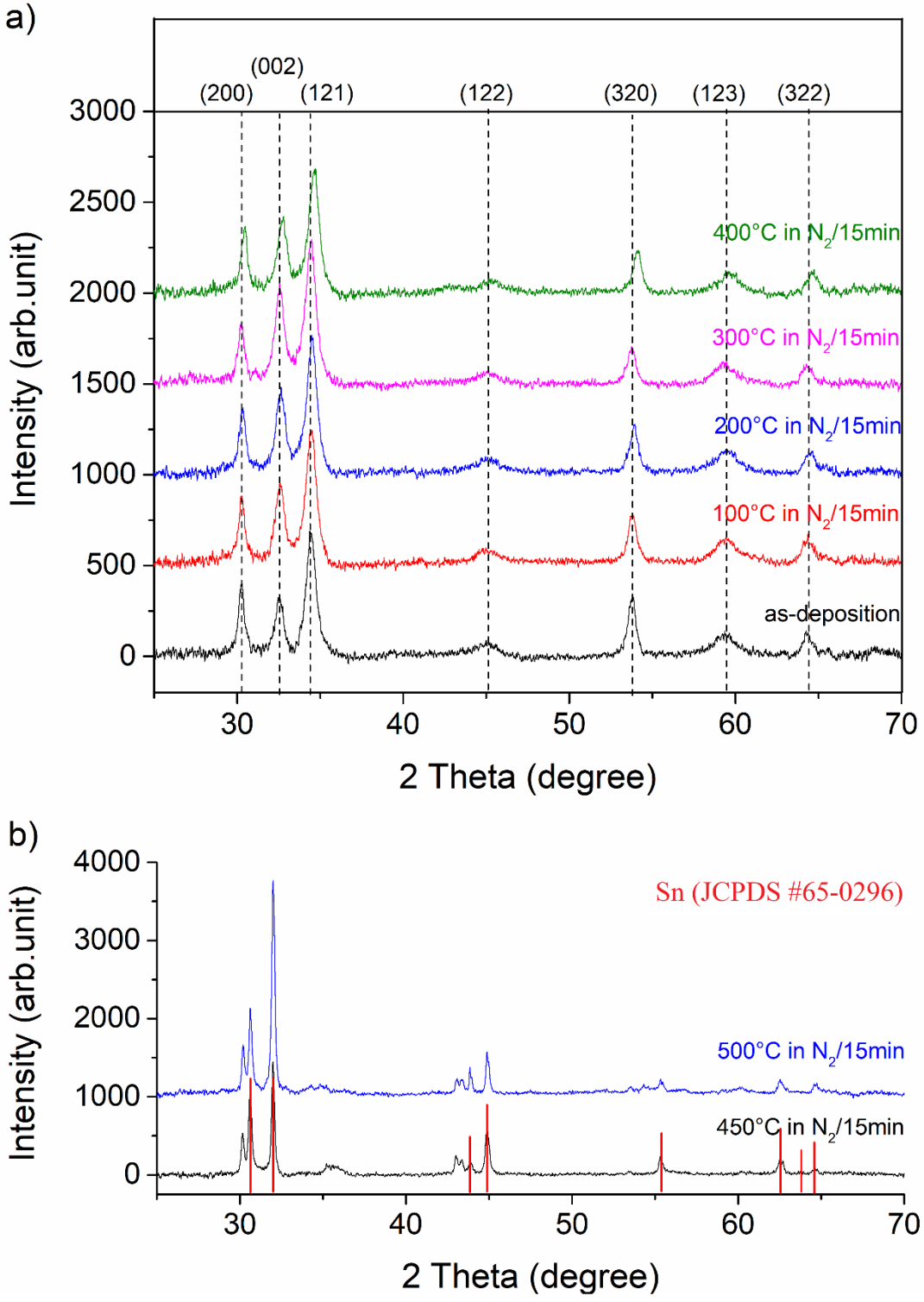

Figure III. 20: *XRD diffractograms of $Zn_{DC}Sn_{RF}$-NA thin films on Si (100) for different post-annealing temperatures: a) from 100°C to 400°C, b) 450°C and 500° data compared to XRD data of Sn on red peaks.*

The corresponding XRD diffractograms are shown on **Figure III. 20**. Up to annealing temperature of 400°C, XRD data match all the characteristic peaks of $ZnSnN_2$ [59] with a rather good reproducibility compared to other experiments. Then, any change in preferred orientation cannot really been perceived and the post-annealing of films deposited on Si (100) wafers does not seem to affect the crystal structure. As observed with a more progressive manner in the previous experiment (cf. **Figure III. 15**), a shift of diffraction peaks towards higher diffraction angles is observed at 400°C. As the temperature is higher than 400°C, XRD data match the characteristic peaks of pure Sn (**Figure III. 20b**).

The lattice parameters are described in **Table III. 4**. The same behavior as reported when deposited on Eagle XG is obtained, i.e. a, b and c values decrease slightly when the annealing temperature is increased.

Table III. 4: Lattice parameters calculated from XRD data of $Zn_{DC}Sn_{RF}$-NA thin films deposited on Si (100) and post-annealed at 100°C to 400°C in N_2 atmosphere during 15 min.

Temp. (°C)	a (Å)	b (Å)	c (Å)
As-dep	5.90	6.82	5.50
100	5.90	6.83	5.49
150	5.90	6.83	5.49
200	5.89	6.82	5.48
250	5.89	6.82	5.48
300	5.91	6.83	5.49
350	5.88	6.81	5.47
400	5.87	6.79	5.47

Figure III. 21 shows the strain of $Zn_{DC}Sn_{RF}$-NA thin films on Si (100) calculated from XRD data and equation (3.6). The strain value and particularly the average crystallite size, evaluated from the (200) peak width using the Scherrer formula (2.6), exhibit less variation than on glass substrate.

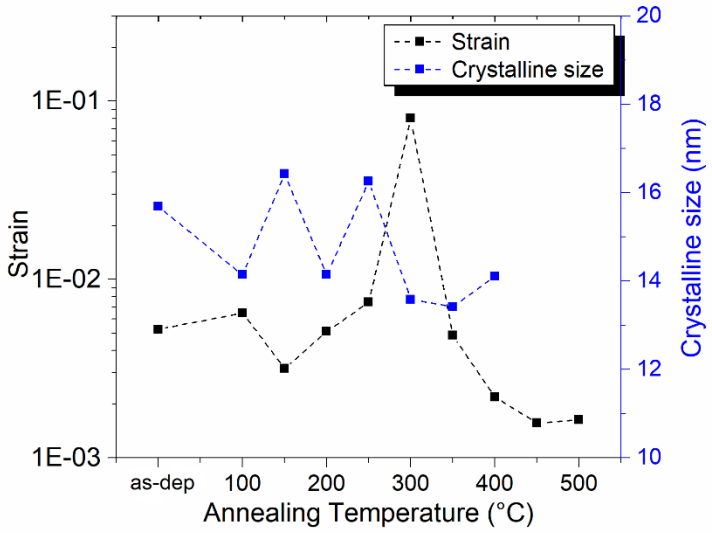

Figure III. 21: *Strain and crystal size of $Zn_{DC}Sn_{RF}$-NA series thin films deposited on Si(100) and post-annealed from 100°C to 500°C.*

III.3.2 RTA on $Zn_{DC}Sn_{RF}$ mode and under 2%H_2/N_2 ($Zn_{DC}Sn_{RF}$ -HN)

As reported by Atwater *et al.* [78], the TEC of $ZnSnN_2$ can explain to the appearance of cracks in the films. In their experiments and as in previous experiments (Section III.3.1), $ZnSnN_2$ thin films were deposited in N_2 mixed Ar environment [78]. As it has been seen in section II.7, the use of a H_2 mixed N_2 atmosphere during deposition can drastically reduce the free carrier concentration. In this section, the effect of using such an atmosphere on the morphology and crystal structure of $ZnSnN_2$ thin film after annealing treatment is studied: will the TEC value be modified by the sputtering conditions?

III.3.2.1 Deposition of $Zn_{DC}Sn_{RF}$-HN thin film on Eagle XG substrate:

The power feeding of targets is the same as in the previous experiments, i.e., 25W-DC and 70W-RF supplies were applied to Zn and Sn targets, respectively. The operating pressure in the chamber was still fixed at 2.10^{-2} mbar, the nitrogen flux was 24 sccm, the 5%H_2/N_2 flux was 16 sccm (overall H_2/N_2 is then 2%), and the sputtering process took time was 25 minutes.

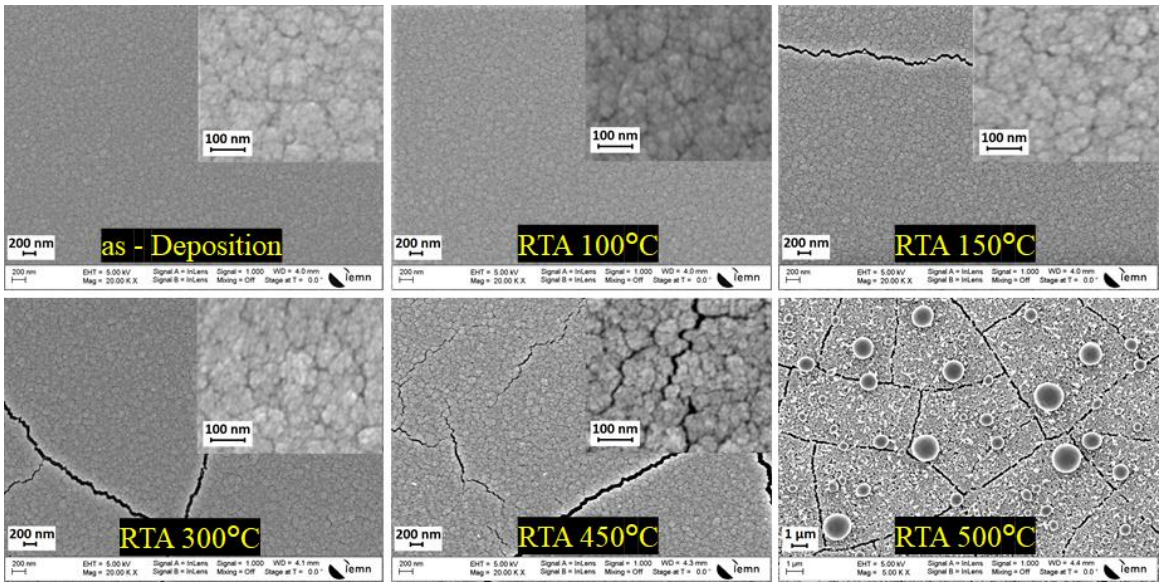

Figure III. 22: *SEM images of $DC_{Zn}RF_{Sn}$-HN thin films on Eagle XG after RTA treatment (note: magnification of 500°C sample is 4-time smaller compared to others)*

The effect of annealing process at different temperatures on surface morphology is shown in **Figure III. 22**. No significant changes in the morphology and grain size are observed for annealing temperature below 450°C but cracks begin to appear at 150°C. The density of cracks increases with the increase in annealing temperature and Sn balls appears at 500°C. Cracks appear for lower annealing temperatures than for the $Zn_{DC}Sn_{RF}$-NA series (cf. **Figure III. 13**). So, the presence of hydrogen in the sputtering atmosphere may lead to increase the difference of TEC value between the $ZnSnN_2$ thin film and the Eagle XG substrate. At 500°C, the crystal spheres of Sn appear on the surface.

There is no change in crystal structure when annealing from 100°C to 400°C (**Figure III. 23**). In addition, XRD data of all samples show only four peaks located at 2θ equal to 30.1°, 34.0°, 53.4° and 62.6°, corresponding to (200), (121), (320) and (322) planes respectively. Nevertheless, only two of them are well marked, corresponding to (200) and (320) planes. The peak intensity of (320) plane reduces as increasing the annealing temperature. As the temperature is equal to 500°C, XRD data match the characteristic peaks of pure Sn, as shown on **Figure III. 23b**.

The lattice parameters are described in **Table III. 5**; a, b and c value decrease slightly by the increase of annealed temperature.

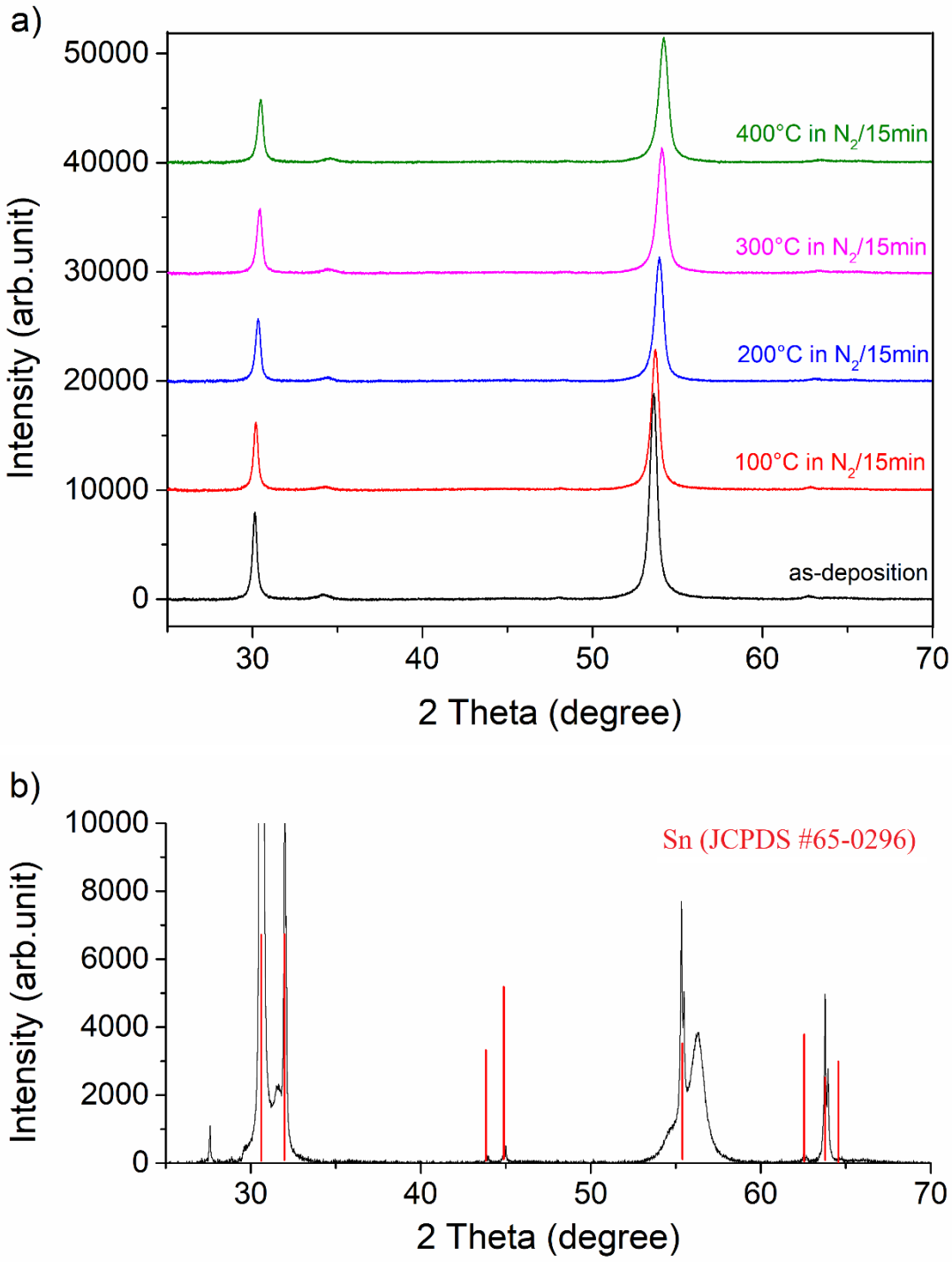

Figure III. 23: *XRD diffractograms of $Zn_{DC}Sn_{RF}$-HN thin films on Eagle XG substrate for different annealing temperatures: a) from 100°C to 400°C, b) 500°C data compared to XRD data of Sn on red peaks.*

The average crystal size (D), evaluated from the (200) peak width using the Scherrer formula (2.6), is showed on **Figure III. 24**. The crystal size is range in 18.9 to 22.6 nm; the maximum crystal size is obtained at 250°C.

Table III. 5: Lattice parameters calculated from XRD data of $Zn_{DC}Sn_{RF}$-HN thin films on Eagle XG substrate, annealed at 100°C to 450°C during N_2 in 15 min.

RTA Temp. (°C)	a (Å)	b (Å)	c (Å)
As-dep	5.93	6.81	5.71
100°C	5.92	6.80	5.69
150°C	5.90	6.79	5.67
200°C	5.89	6.78	5.66
250°C	5.93	6.81	5.68
300°C	5.87	6.77	5.63
350°C	5.87	6.76	5.60
400°C	5.86	6.76	5.60
450°C	5.85	6.75	5.57

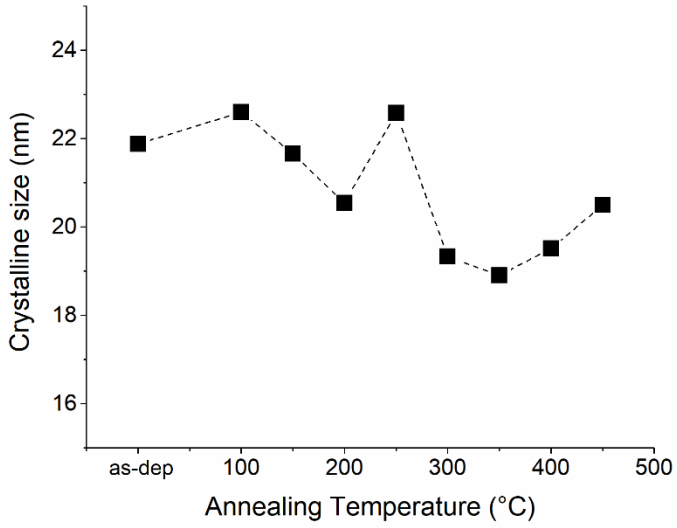

Figure III. 24: *Crystal size $Zn_{DC}Sn_{RF}$-HN thin films on Eagle XG Substrate after annealing from 100°C to 450°C*

III.3.2.2 Deposition of $Zn_{DC}Sn_{RF}$-HN thin film on Si (100)

In this section, all sputtering conditions are kept similar to section III.3.2.1, only a Si (100) substrate was used replacing Eagle XG substrate.

The effect of the annealing process at different temperatures on the surface morphology is shown in **Figure III. 25**. No significant changes in the morphology and grain size are observed for annealing temperatures below 350°C except, perhaps, some increase of voids. Above 350°C, the thin film becomes degraded and cracks appear on the surface. This phenomenon was not observed for the $Zn_{DC}Sn_{RF}$-NA on Si (100) at the same temperature. This tends to confirm the previous remark stating that deposition under mix hydrogen-nitrogen atmosphere increases the TEC value of the material. At 500°C, crystal balls of Sn are present on the surface as in the previous cases.

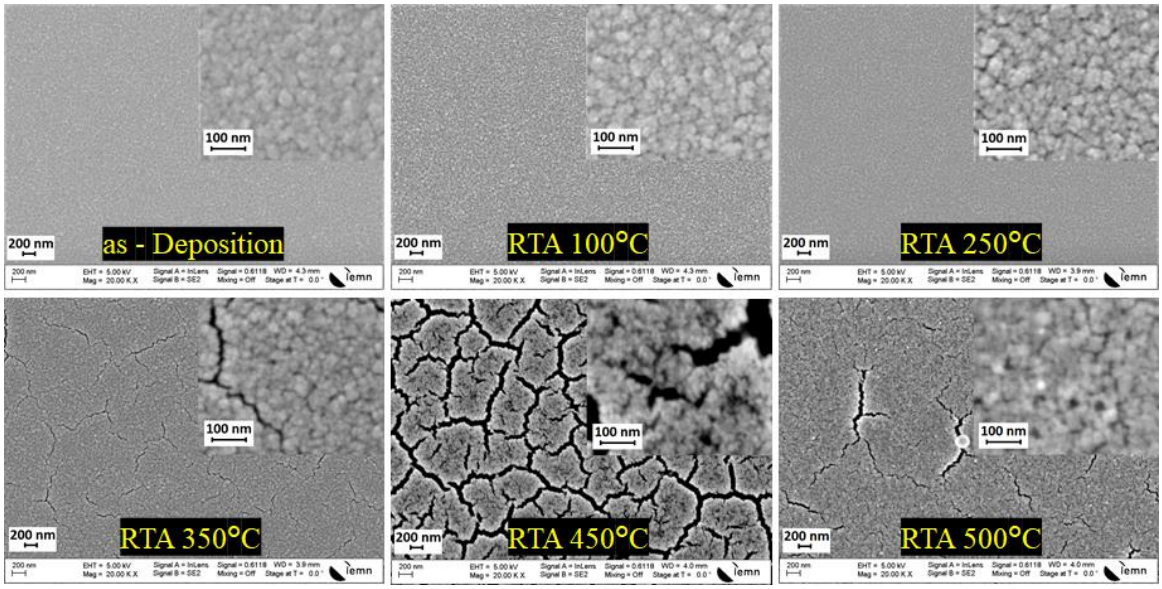

Figure III. 25: *SEM images of $Zn_{DC}Sn_{RF}$-HN thin films on Si (100) after RTA treatment from 100°C to 500°C*

There is no change in crystal structure of $ZnSnN_2$ when annealing from 100°C to 400°C, (**Figure III. 26a**). XRD data of all samples show only four peaks located at 2θ equal to 30.1°, 34.0°, 53.4° and 62.6°, corresponding to (200), (121), (320) and (322) planes respectively, and (200) plane is dominant. In contrast to deposition on Eagle XG substrate, the peak intensity of (320) plane is weaker and its amplitude does not change by with

annealing temperature. Although, the Sn balls are not clearly observed on SEM image at 450°C, XRD data match the characteristic peaks of pure Sn, as noticed on **Figure III. 26b**.

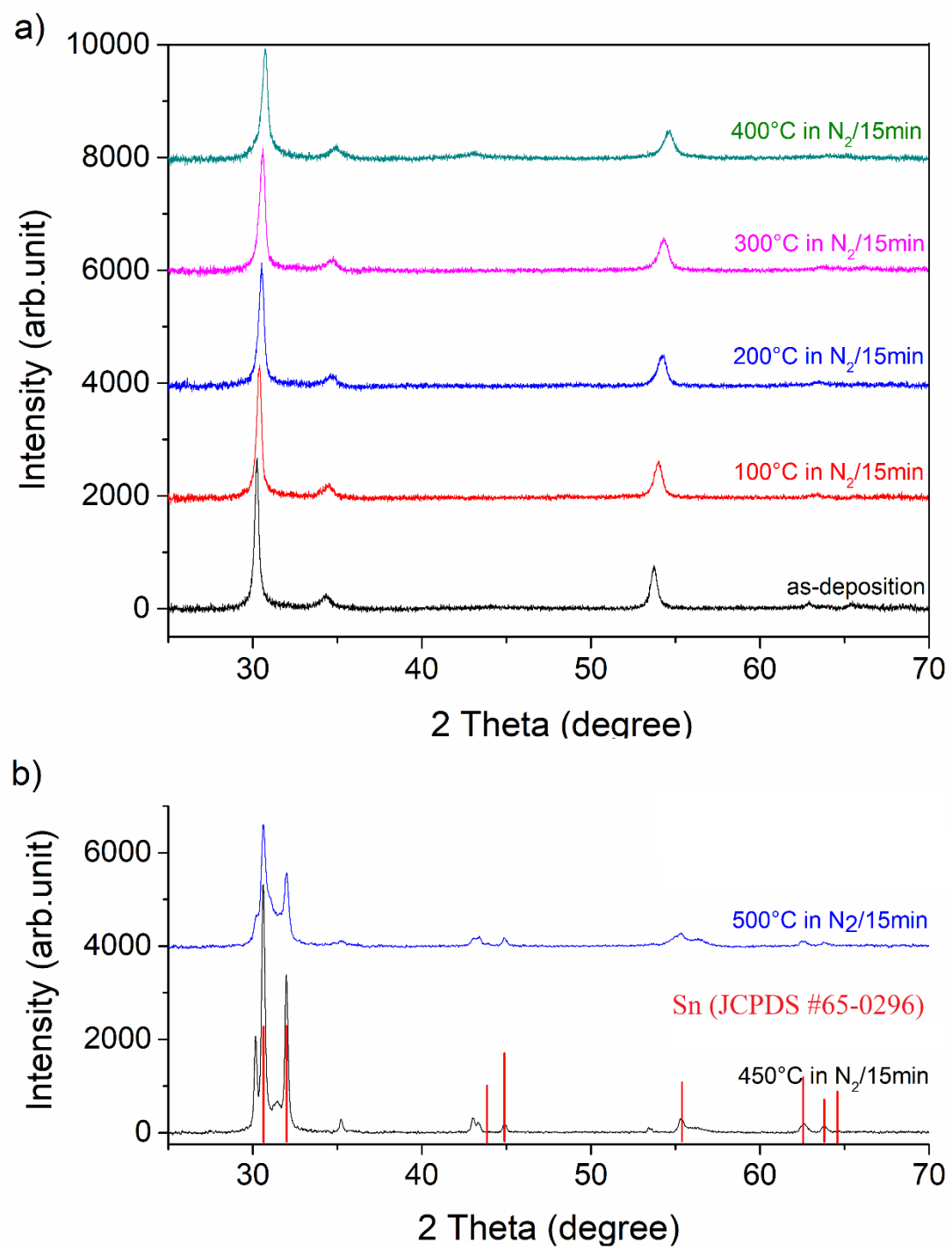

Figure III. 26 : *XRD diffractograms of* $Zn_{DC}Sn_{RF}$*-HN* thin films *on Si (100) substrate for different annealing temperatures: a) from 100°C to 400°C, b) 500°C data compared to XRD data of Sn on red peak).*

The lattice parameters are described in **Table III. 6**; a, b and c value decrease slightly by the increase of annealed temperature.

Table III. 6: Lattice parameters calculated from XRD data of $Zn_{DC}Sn_{RF}$-HN thin films on Si (100), annealed at 100°C to 450°C in N_2 during 15 minutes.

Temp. (°C)	a (Å)	b (Å)	c (Å)
As-dep	5.91	6.81	5.64
100°C	5.88	6.79	5.62
150°C	5.87	6.77	5.60
200°C	5.86	6.77	5.57
250°C	5.91	6.81	5.66
300°C	5.85	6.76	5.56
350°C	5.83	6.74	5.55
400°C	5.82	6.72	5.48

The average crystal size (D), evaluated from the (200) peak width using the Scherrer formula (2.6), is in the range 15.4 to 22.8 nm and decreases with the increase of the annealing temperature (**Figure III. 27**).

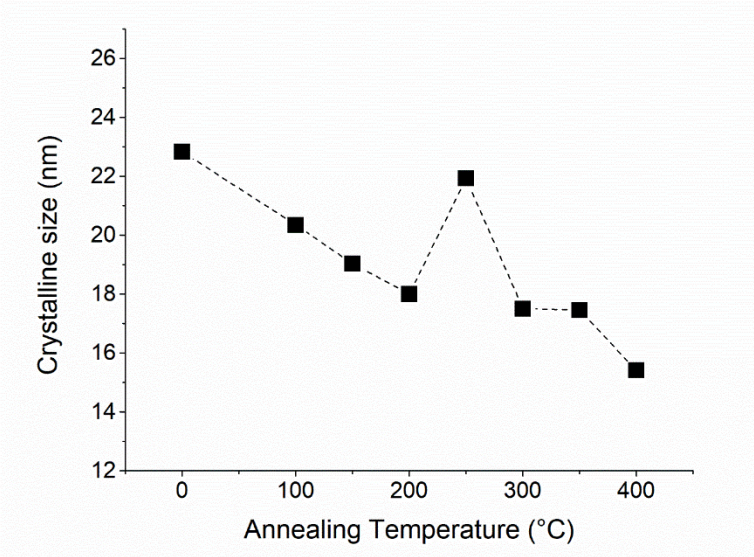

Figure III. 27 : *Crystal size of (200) plane of $DC_{Zn}RF_{Sn}$-HN thin films on Eagle XG Substrate after annealing from 100°C to 450°C*

III.3.3 RTA on $Zn_{RF}Sn_{DC}$ series under N_2/Ar atmosphere ($Zn_{RF}Sn_{DC}$-NA)

In this section, all sputtering conditions are kept similar as in section III.3.1.1 except the target power supplies. This will allow to compare with the results obtained on $Zn_{DC}Sn_{RF}$ series.

After their deposition, the films are annealed in pure N_2 (300 sccm) and in a temperature range from 100°C to 500°C with a 100°C step. The annealing time was 15 minutes and the heating-up/cooling-down rate was 100°C/min.

The change in the composition of the films (EDX) and their thickness are reported in **Figure III. 28**. This figure has to be compared with **Figure III. 12**. The Zn/(Zn+Sn) ratio is rather stable, in the range 48.1% to 49.8%. The deposition rate shows a small trend increasing with the increase in temperature. So, no significant variation is observed on those two parameters when changing the post-anneal temperature.

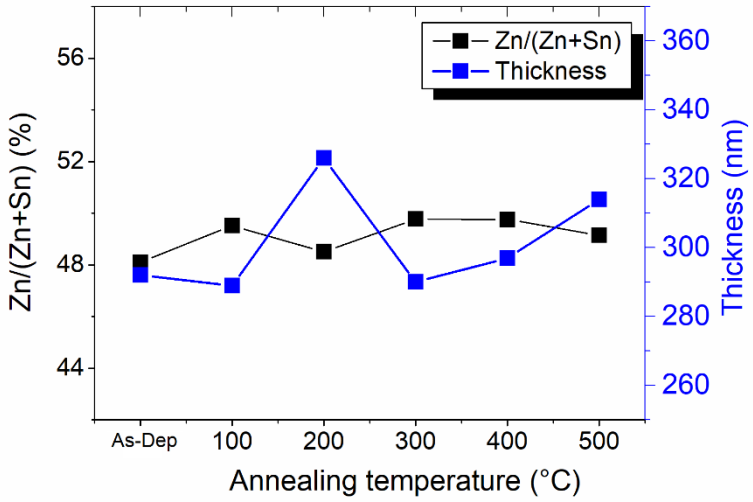

Figure III. 28: *Zn/(Zn+Sn) ratio and thickness of $Zn_{RF}Sn_{DC}$-NA samples deposited on Eagle XG glass versus post-deposition annealing temperature (N_2 atmosphere).*

The effect of the annealing process temperature on surface morphology is shown in **Figure III. 29**. Up to 500°C, the rapid thermal annealing does not affect the morphology of the films; the SEM cross-section images show columnar microstructure for all samples. No

cracks are observed on the surface of all samples. At 500°C, the surface of thin film is degraded and the columnar structure is no clearer.

As- dep

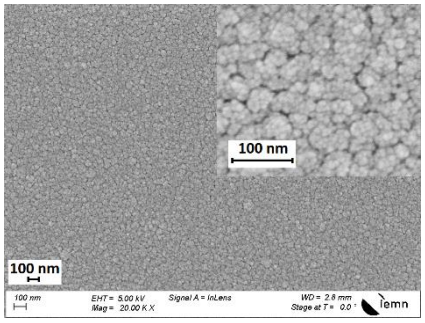

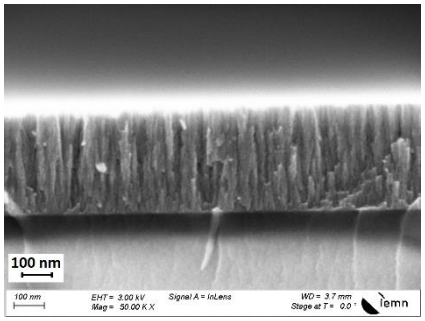

RTA
100°C

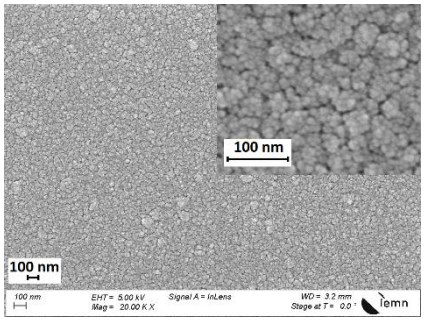

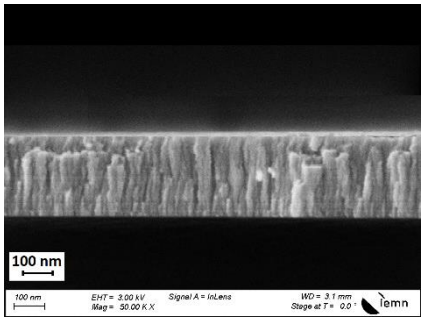

RTA
200°C

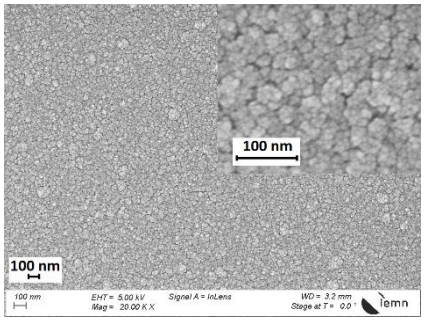

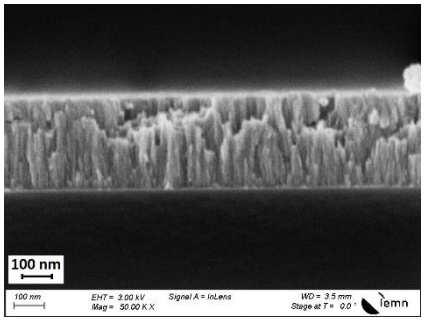

RTA
300°C

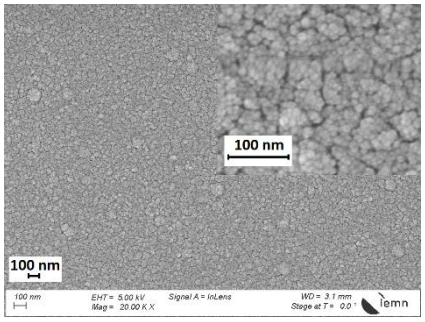

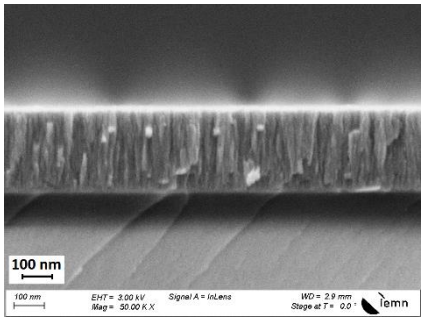

RTA
400°C

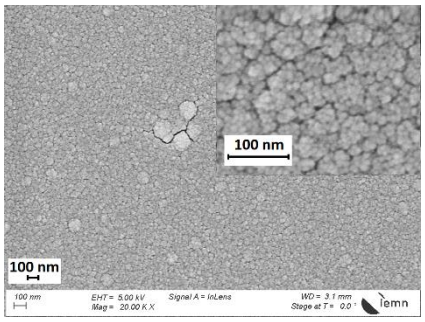

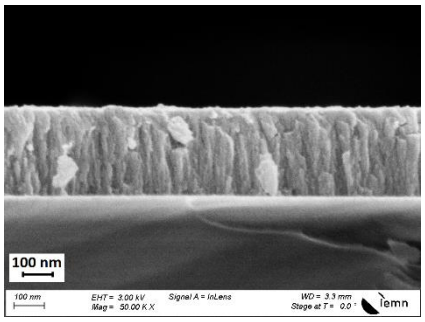

RTA
500°C

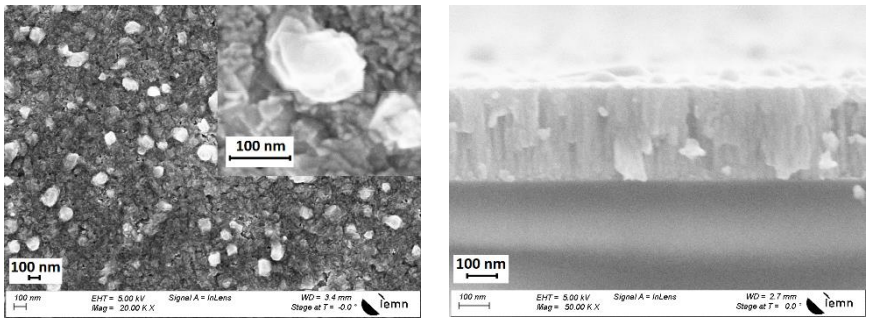

Figure III. 29: *SEM images, top-views (on the left hand side) and cross-sections SEM (on the right hand side) of $Zn_{RF}Sn_{DC}$-NA series deposited on Eagle XG glass after RTA treatment from 100°C to 500°C.*

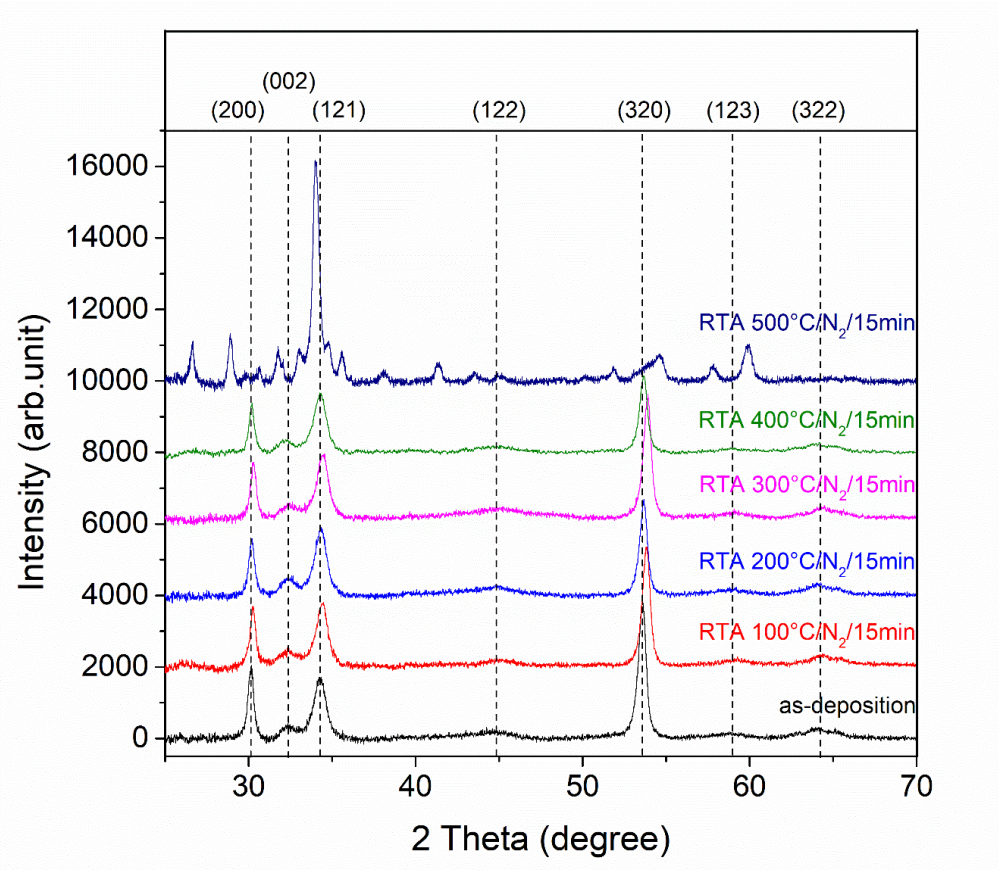

Figure III. 30: *XRD diffractograms of $Zn_{RF}Sn_{DC}$-NA thin films on Eagle XG substrate for different annealing temperatures, from 100°C to 500°C.*

The corresponding XRD data is shown in **Figure III. 30**. Up to 500°C, XRD data are rather invariant and match all the characteristic seven peaks of $ZnSnN_2$. Though, only (200), (121) and (320) planes are dominant with high intensity, narrow and sharp peaks. At 500°C, XRD

diffractogram is no more representative a $ZnSnN_2$ material and no clear material representation can be retrieved.

Table III. 7: Lattice parameters calculated from XRD data of $Zn_{RF}Sn_{DC}$-NA thin films on Eagle XG substrate, annealed from 100°C to 400°C in N_2 during 15 minutes.

Temp. (°C)	a (Å)	b (Å)	c (Å)
As-dep	5.93	6.82	5.60
100	5.90	6.78	5.60
200	5.92	6.82	5.58
300	5.90	6.78	5.60
400	5.92	6.82	5.61

The values of lattice parameters are described in **Table III.7** and do not show any significant change under the temperature of the annealing treatment.

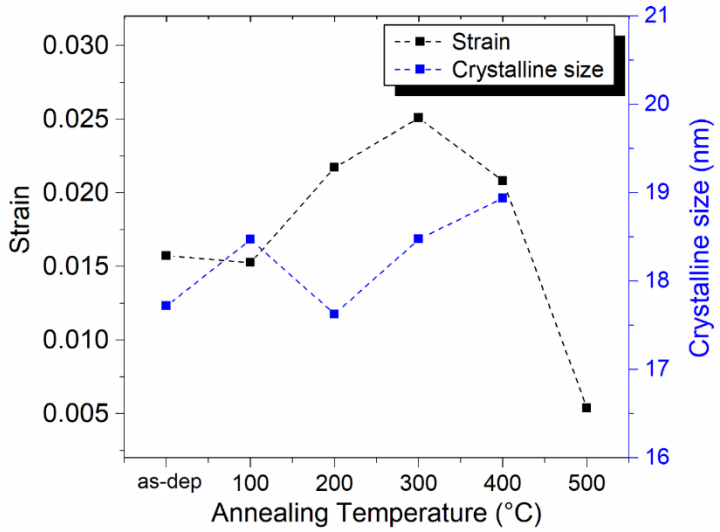

Figure III. 31 : *Strain and crystal size of (200) plane of $Zn_{RF}Sn_{DC}RF_{Zn}DC_{Sn}$-NA thin films on Eagle XG substrate after annealing from 100°C to 500°C.*

Figure III. 31 shows the strain of $Zn_{RF}Sn_{DC}$-NA thin films on Eagle XG substrate calculated from XRD data and equation (3.6). The rise in the annealing process temperature

from 100°C to 300°C leads to increase the strain from $1.5x10^{-2}$ to $2.5x10^{-2}$. At 400°C, the strain decreases; this can be linked to the appearance of cracks on the surface (cf. F**igure III. 29**). The strain value is three times higher than for $Zn_{DC}Sn_{RF}$-NA case (cf. **Figure III. 16**) by order of magnitude. The average crystal size (D), evaluated from the (200) peak width using the Scherrer formula (2.6), is in the range 17.6 to 18.9 nm, so rather the same value than in the $Zn_{DC}Sn_{RF}$-NA case (cf. **Figure III. 16**).

The UV-Vis spectra and optical bandgap of $Zn_{RF}Sn_{DC}$-NA thin films on glass after annealing from 100°C to 550°C are reported in **Figure III. 32**. As the temperature is in the range in 100°C to 300°C, the anneal does not affect at all the optical properties of the material. The optical bandgap is equal to 1.70 eV. At 400°C, this value increases to 1.83 eV.

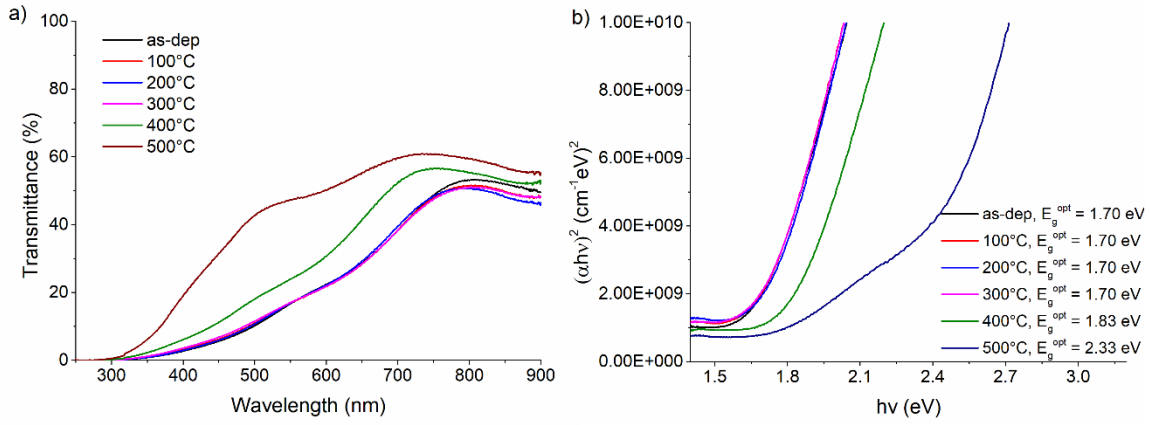

Figure III. 32: *a) Transmittance vs. wavelength spectra (UV-Vis spectroscopy) for $Zn_{RF}Sn_{DC}$-NA series deposited on glass at room temperature and post-annealed at different temperature, b) Corresponding optical bandgap values calculated using Tauc's equation.*

The Hall measurement results are shown in **Figure III. 33**. Except for the particular case of 500°C annealing temperature, values are slightly changing. All the samples exhibit n-type polarity with a carrier density in the order of some 10^{20} cm^{-3}.

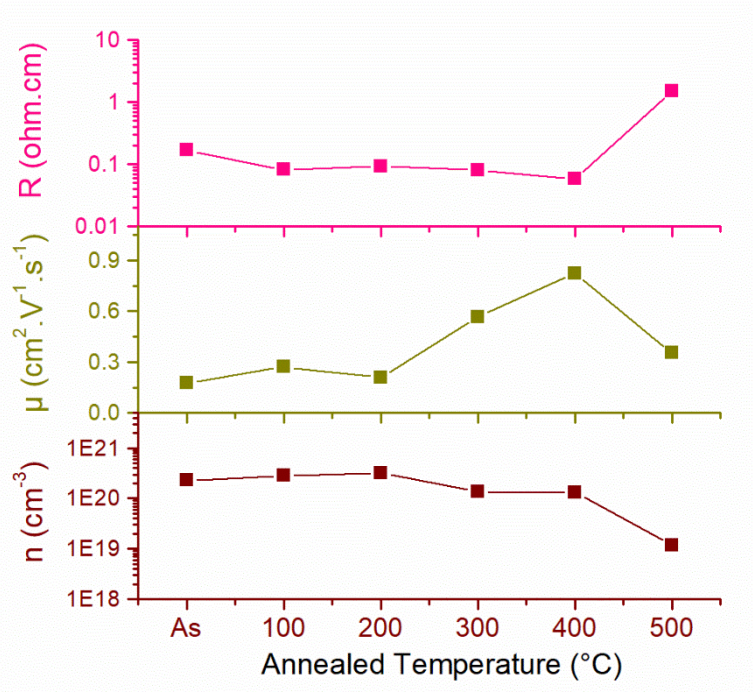

Figure III. 33: *Resistivity (R), carrier mobility (μ) and carrier density of $Zn_{RF}Sn_{DC}$-NA series (determined from Hall effect measurements) depending on the post-annealing temperature.*

III.4 **Discussions and partial conclusions**

At the lowest deposition pressure films tend to be Zn-rich and become quickly Sn-rich as pressure increases. Nevertheless, this tendency is weak and can be easily counterbalanced tuning the power bias of targets. By contrast, the sputtering rate is clearly divided by two when the pressure increases from 10^{-2} up to $5x10^{-2}$ mbar (see **Figure III. 1**). The number and size of voids increase with the increase in deposition pressure as well as the strain of the films (see **Figures III. 2** and **III. 4**).

Heating the substrate during deposition does not really impact sputtering rate as well as film composition (see **Figure III. 7**). Crystallite size is also not really modified. However, the number and size of voids increase with the increase of temperature (see **Figure III. 8**).

The use of a post-anneal under N_2 atmosphere and up to 400°C does not really change drastically the XRD diffractograms of samples whatever the power configuration of targets, the substrate used or the deposition atmosphere are (see **Figures III. 15, III. 20, III. 23, III. 26** and **III. 29**). Above 400°C, the films disaggregate and Sn balls can be observed at surface of the films (see **Figure III. 14**). When deposited on glass, cracks in the films appear approximately at 300°C whatever the power configuration of targets (see **Figures III. 13** and **III. 29**). Those cracks do not appear when deposited on silicon substrate (see **Figure III. 19**). Even if some slight decrease (maximum around 10%) of crystallite size can be observed with the increase in temperature, (see Figures **III. 16, III. 21, III. 24, III. 27**, and **III. 30**), this cannot be seen as a rule. When using a hydrogenated argon-free deposition atmosphere, cracks appear on both substrates, glass and silicon but at higher temperatures (300°C) on Si than on glass (150 °C). As already observed in Chapter II, when using an argon-free deposition, only two main peaks are observed on the XRD patterns of films.

Table III. 8 attempts to summarize the main effects of pressure or temperature on the physical properties of films.

Table III. 8: Main effects of process pressure and temperature, either during or post deposition, s on the film properties.

Action	Film composition	Deposition rate	Crystallography
Increasing deposition pressure	Slight variation	Monotonous decrease (by a factor 2) when pressure raises from 10^{-2} to $5x10^{-2}$ mbar.	Increase the number and size of voids.
Increasing process temperature (during deposition, < 400°C)	No significant change.	No significant change.	Increase the number and size of voids
Increasing post-deposition annealing temperature	No significant change.	-	Cracks appears at temperature switchover points depending on substrate
Using a N_2/H_2 deposition atmosphere		Higher in $Zn_{RF}Sn_{DC}$ mode.	Higher film stress: cracks appear at lower temperature than using an argon-based atmosphere.

The increase in sputtering pressure leads to increase the optical bandgap (see **Figure III. 5**), the carrier mobility and decreasing the carrier density; the latter two by two orders of magnitude (see **Figure III. 6**). As observed in Chapter II, this is contrary to a Burstein-Moss effect.

No significant effect on electrical and optical properties of $ZnSnN_2$ thin film were recorded under the different deposition or annealing conditions that have been used.

Chapter IV: **TUNING THE COMPOSITION**

In this chapter, we will investigate how the change in $ZnSnN_2$ thin film composition affects the microstructure, the electrical and the optical properties of the material. To do so, the power of the generators feeding the targets will be tuned. In the preceding chapters, the film composition was kept stoichiometric, or we tried to get it as close as possible. Besides that, the effect of generators used to apply power for the target is also clarified.

IV.1 $Zn_xSn_{1-x}N_2$: Co-sputtering with two elemental targets

IV.1.1 $Zn_{DC}Sn_{RF}$ series

$Zn_{DC}Sn_{RF}$ series was deposited on Eagle XG substrate at room temperature and in a mixed N_2/Ar atmosphere (so, same configuration as in section II.4.2.1). The N_2/Ar ratio was fixed at 2.0 and the sputtering chamber pressure at 0.02 mbar. The different samples of this series were not fabricated at the same period; Zn-rich to stoichiometric samples were done 6 months sooner than Sn-Rich samples. As mentioned in Chapter II, due to target erosion, same power density will request more power over time. So, no relationship between applied power and film composition could have been drawn on this series. The thickness of the different films is in the 400 to 500 nm range. The power applied to Zn and Sn targets were varied to get the zinc concentration, x, in the 0.27 - 0.74 range.

Up to x = 0.5, i.e. Sn-rich films, the surface aspect is more cauliflower-like (**Figure IV.1**). For $0.54 \leq x \leq 0.60$, i.e. Zn-rich films, surface aspect changes to elongated grains with huge interstitial voids. For higher x values, the surface aspect changes back to a cauliflower-like structure. The grain size "visually" increases as increasing the Zn composition.

The corresponding XRD patterns are reported in **Figure IV. 2**. As $0.27 \leq x \leq 0.34$, there are only 3 peaks corresponding to (200), (121) and (320) planes and located at 30.1°, 34.3° and 53.6°, respectively. At x = 0.42, small peak locates at position 32.2°, indicating the (002) plane is recorded. For $0.46 \leq x \leq 0.50$, XRD data match all the seven characteristic peaks of $ZnSnN_2$: this corresponds to the case recorder in section II.4.2.1 were stoichiometry was rather sought for. The change in grain shape observed on SEM images (see **Figure IV. 1**) for $0.54 \leq x \leq 0.60$ connects to the disappearing of (200) and (320) peaks in XRD patterns. When x value increases up to 0.67, XRD data illustrate the seven characteristic peaks of $ZnSnN_2$, but the crystalline quality degrades with an enlarging of peaks. At x = 0.74, no particular order appears and the $ZnSnN_2$ thin film reports as of amorphous nature.

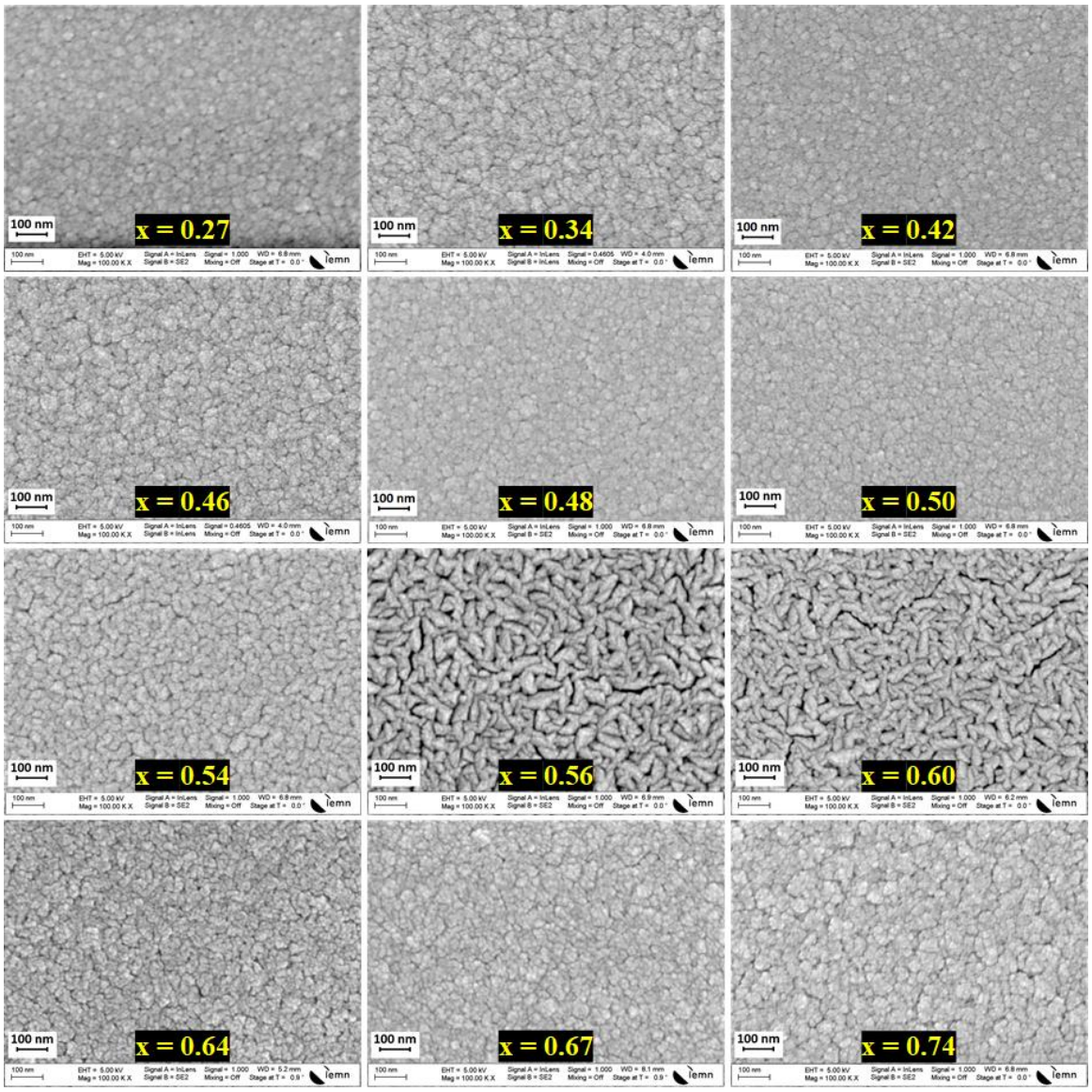

Figure IV. 1: *SEM surface images of the $Zn_xSn_{1-x}N2$ ($Zn_{DC}Sn_{RF}$ series) thin films with $0.27 \leq x \leq 0.74$.*

Lattice parameters calculated from XRD data are reported on **Figure IV. 3a**. As Zn composition increases, a progressive shift of the diffraction peaks towards higher diffraction angles can be observed (see **Figure IV. 2**). This shift indicates that the dimensions of the elementary cell decrease. Taking into account that Zn atoms occupy Sn sites, so creating Zn_{Sn} defects, and that the atomic radius of Zn (134 pm) is smaller than that of Sn (140pm), this substitution of Sn atoms by Zn atoms shall effectively lead to reduce the cell lattice.

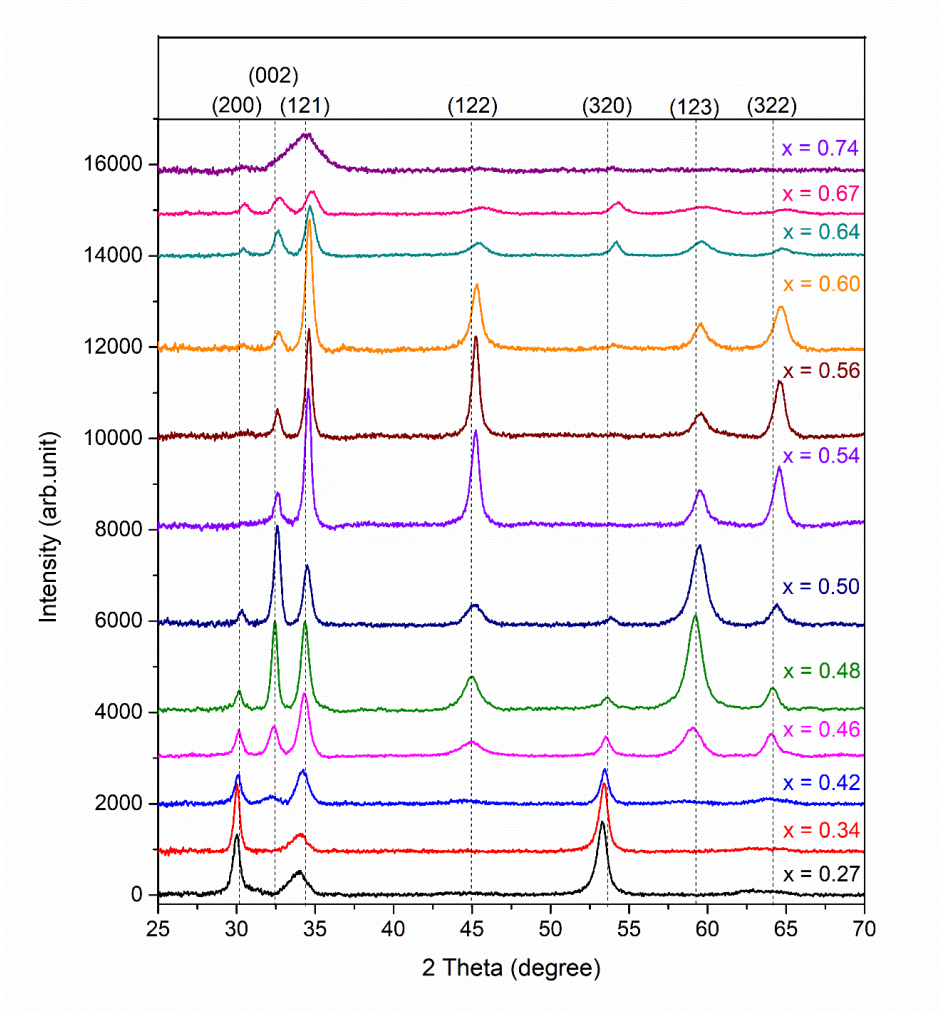

Figure IV. 2: *XRD diffractograms of $Zn_xSn_{1-x}N_2$ ($Zn_{DC}Sn_{RF}$ series) thin film with $0.27 \leq x \leq 0.74$.*

The average crystal size (D), evaluated from the (121) peak width using the Scherrer formula (2.6), is illustrated in **Figure IV. 3b**. When Zn composition increases from 0.27 to 0.56, the crystal size grows from 4.2 nm to 17.0 nm, and then goes back to 11.5 nm at higher Zn composition. These results are consistent with visual evaluation from SEM images above (see **Figure IV. 1**). It has also to be noticed that, even with a time difference of 6 months between the experiments of section II.4.2.1 and those ones, the XRD diffractograms (see **Figures II. 7** and **IV. 2**) and the lattice parameters (see **Table II.2** and **Figure IV. 3**) are consistent (comparison to be made with $N_2/Ar = 2$ in Chapter II and x = 0.5 in this Chapter).

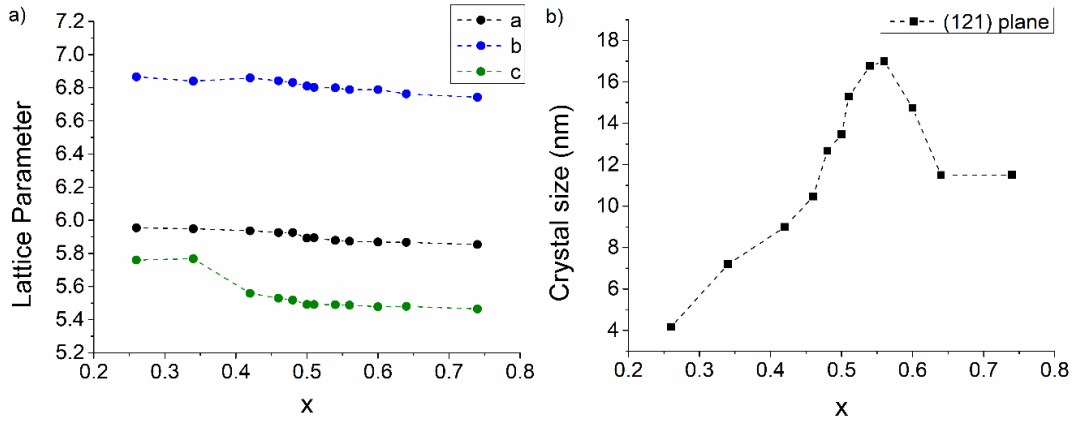

Figure IV. 3: *a) Lattice parameters and b) crystal size of (121) plane calculated from XRD data of $Zn_xSn_{1-x}N_2$ thin film with $0.27 \leq x \leq 0.74$ ($Zn_{DC}Sn_{RF}$ series).*

The resistivity is between 0.03 and 0.77 Ω.cm, lowest values being obtained around stoichiometry (**Figure IV. 4**).

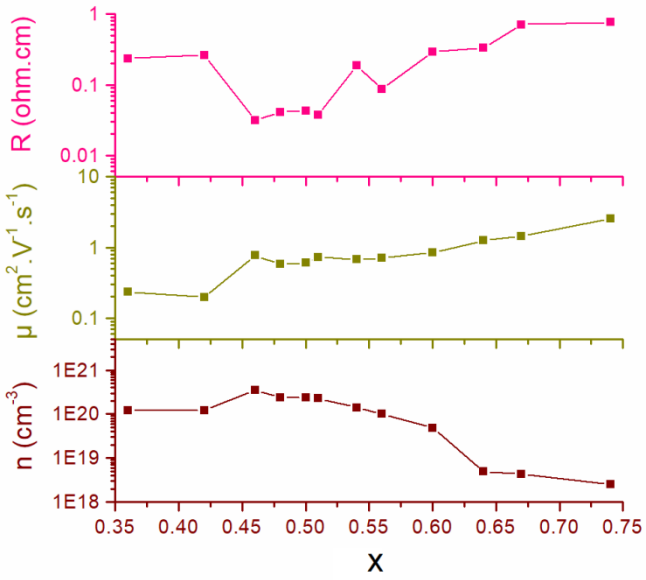

Figure IV. 4: *Resistivity (R), carrier mobility (μ) and carrier density (n) of $Zn_xSn_{1-x}N_2$ ($Zn_{DC}Sn_{RF}$ series) thin film with $0.27 \leq x \leq 0.74$.*

When Zn composition increases, the carrier mobility gains roughly one decade, from 0.20 to 2.56 $cm^2V^{-1}s^{-1}$ and the carrier concentration reduces dramatically, the lowest value is equal to 2.5 x 10^{18} cm^{-3} for $Zn_{0.74}Sn_{0.26}N_2$. All the samples demonstrated n-type polarity. For Sn-rich up to stoichiometric compositions, there is no major difference in the carrier

density that ranges in the 10^{20} cm^{-3} and more precisely between 1.2 x 10^{20} and 3.5 x 10^{20} cm^{-3}. The decrease of carrier concentration versus the increasing in Zn composition matches previous reports [26], [40], [44] that mention the ZnSn defects as acceptor defects, counterbalancing the inherent high n-type behaviour of the material.

Figure IV. 5a shows a shift of the cut-off in transmittance towards higher wavelengths (red shift) as the Zn composition increases. Correspondingly, the optical bandgap (**Figure IV. 5b**) is primarily reducing, from 2.06 eV to 1.77 eV.

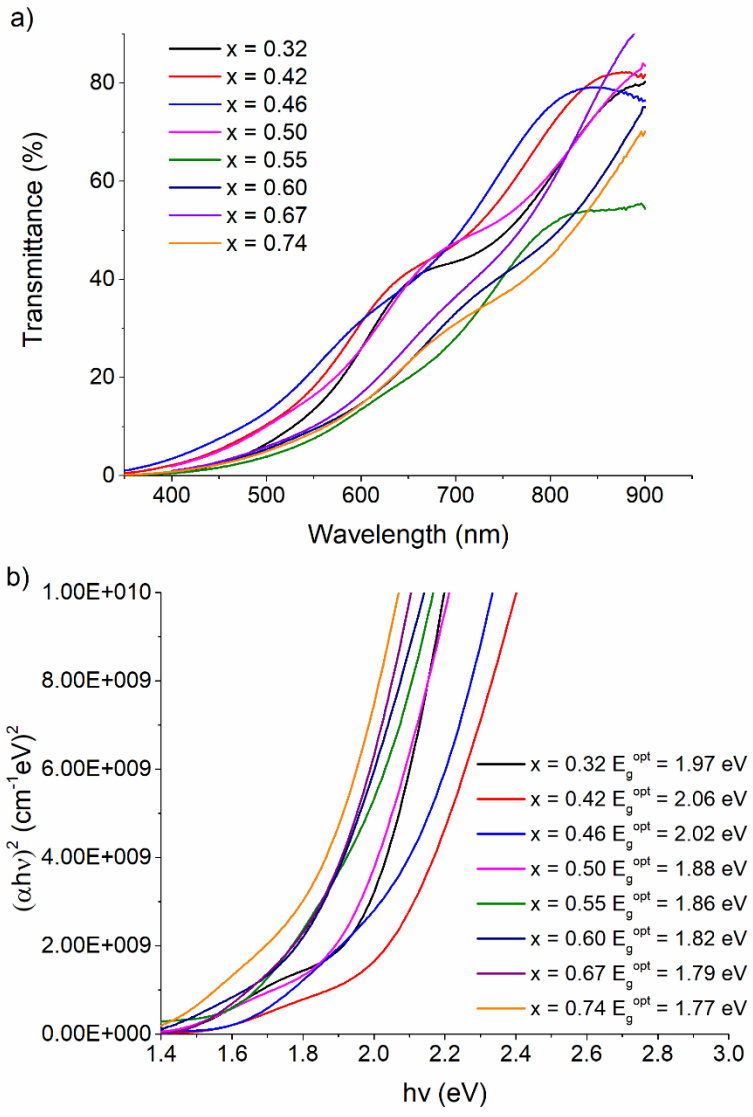

Figure IV. 5: *a) Transmittance vs. wavelength and b) Optical bandgap of $Zn_xSn_{1-x}N_2$ thin film with $0.27 \leq x \leq 0.74$, fabricated in $Zn_{DC}Sn_{RF}$ mode.*

By combining with electrical results presented in **Figure IV. 4** and contrary to almost all observations of previous chapters, the decrease of optical bandgap value with the decrease of carrier density when the Zn composition increases could be related to a Burstein-Moss effect.

IV.1.2 $Zn_{RF}Sn_{DC}$ series

$Zn_{RF}Sn_{DC}$ series was fabricated on the same time slot than the previous series. The deposition parameters were kept identical, i.e. deposition on Eagle XG substrate, at room temperature and in a mixed N_2/Ar of 2.0 with a sputtering chamber pressure at 0.02 mbar (so, same configuration as in section II.4.2.2). Power feeding was 30W-RF and 30W to 59W-DC for Zn and Sn targets, respectively. **Figure IV. 6** shows the Zn composition and the sputtering rate versus the DC power applied to the Sn target. The sputtering time was optimized to get the thickness of films approximately to 300 nm, whatever the bias conditions were.

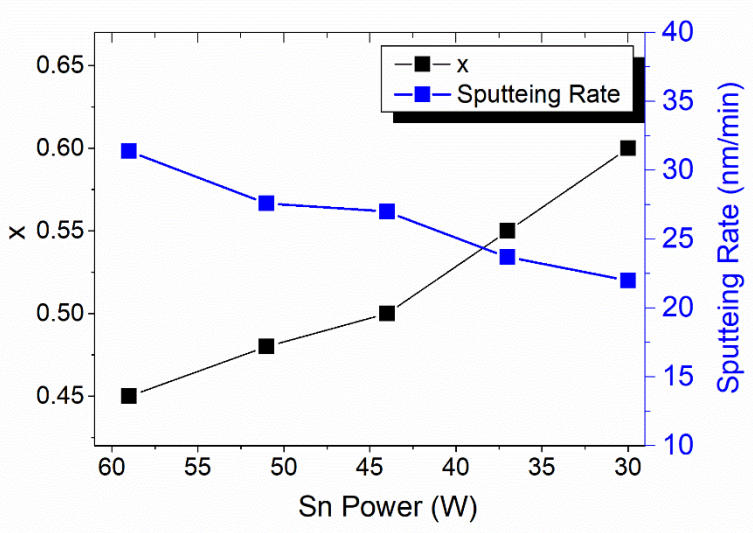

Figure IV. 6: *Composition and sputtering rate via DC power bias of Sn of $Zn_xSn_{1-x}N_2$ ($Zn_{RF}Sn_{DC}$ series) thin film (attention: x axis is reversed).*

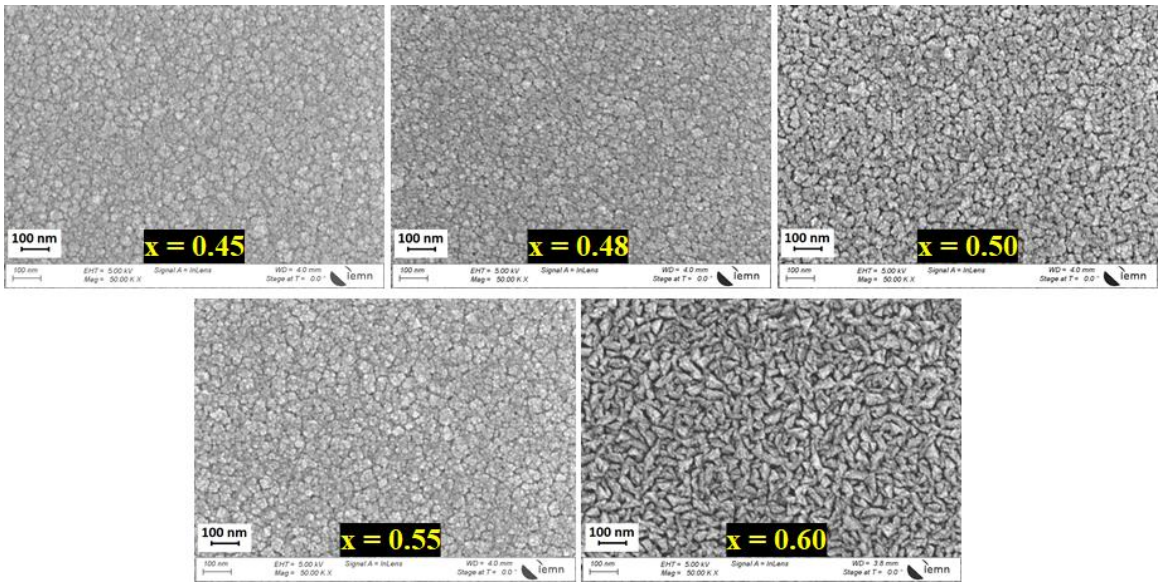

Figure IV. 7: *Top-view images of the $Zn_xSn_{1-x}N_2$ thin films with $0.45 \leq x \leq 0.60$ ($Zn_{RF}Sn_{DC}$ series).*

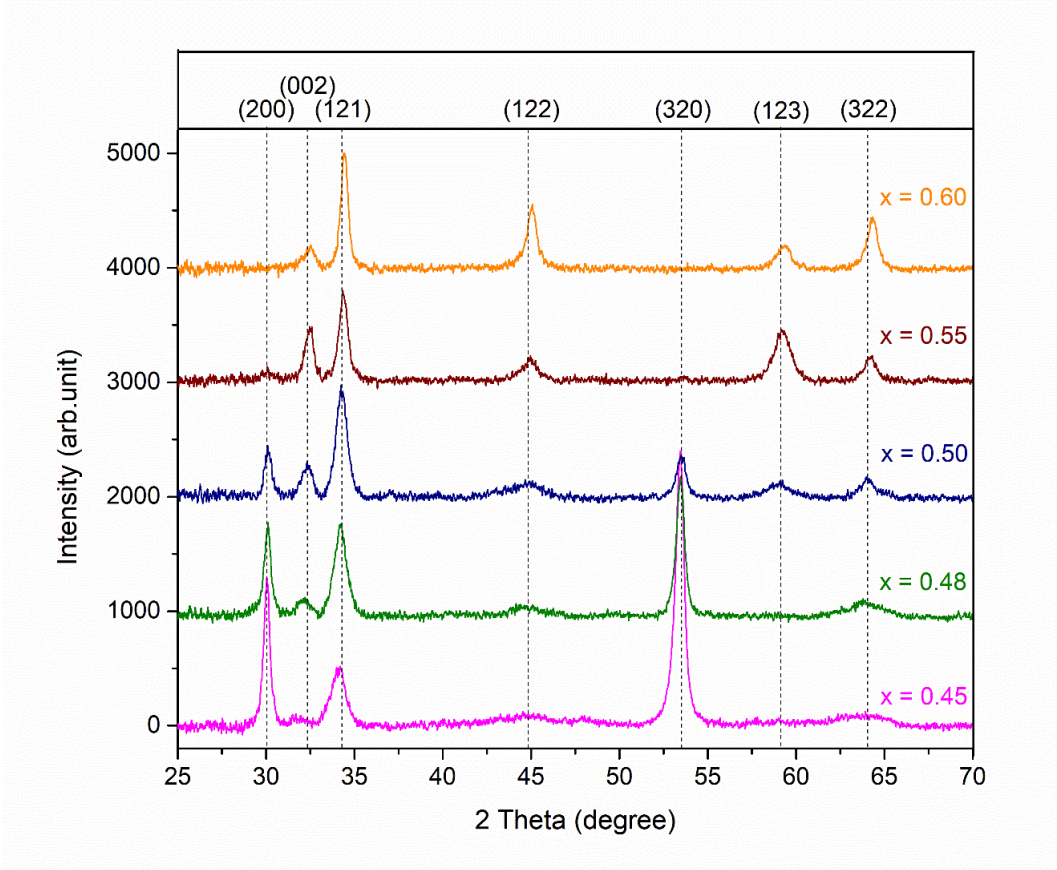

Figure IV. 8: *XRD diffractograms of $Zn_xSn_{1-x}N_2$ thin film with $0.45 \leq x \leq 0.60$, fabricated in $Zn_{RF}Sn_{DC}$ mode.*

The reducing of Sn target power leads to changes in the surface morphology of the films (**Figure IV. 7)**. At x ≤ 0.55, the difference of surface morphologies is difficult to assess and they present a cauliflower-like surface. When x is equal to 0.60, the elongated grains jointly with interstitial voids structure that was observed in the $Zn_{DC}Sn_{RF}$ series for 0.54 < x < 0.60 (see **Figure IV. 1**) is again obtained. Also as observed on the previous series, in that case, (200) and (320) peaks are absent from XRD diffractograms (**Figure IV. 8**). So, for high Zn contents, rather the same result is obtained whatever the biasing of the target is.

The XRD results, reported in **Figure IV. 8**, exhibit rather the same trend that in the $Zn_{DC}Sn_{RF}$ series for the presence of peaks related to the film composition. Besides, the shift of diffraction peaks towards higher diffraction angles when increasing the Zn composition is also observed. The lattice parameters (**Figure IV. 9a)** behave also the same as in $Zn_{DC}Sn_{RF}$ series, i.e. the higher Zn composition is, the smaller the c parameters is. The average crystal size, evaluated from the (121) peak, is illustrated in **Figure IV. 9b** and is in the same range than in $Zn_{DC}Sn_{RF}$ series.

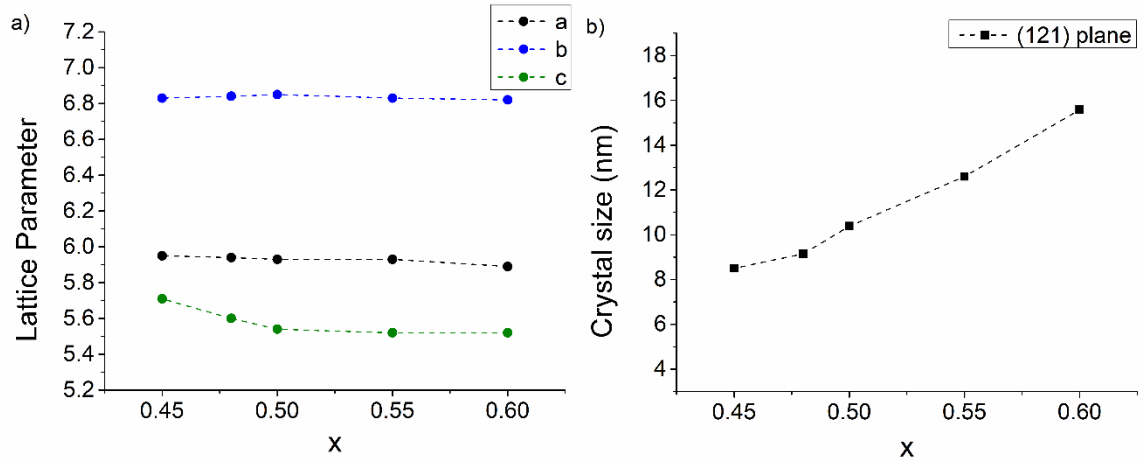

Figure IV. 9: *a) Lattice parameter and b) crystal size of (121) plane calculated by XRD data of $Zn_xSn_{1-x}N_2$ thin film with 0.45 ≤ x ≤ 0.65, fabricated in $Zn_{DC}Sn_{RF}$ mode.*

The electrical properties, represented in **Figure IV. 10**, do not drastically differentiate from that of $Zn_{DC}Sn_{RF}$ series.

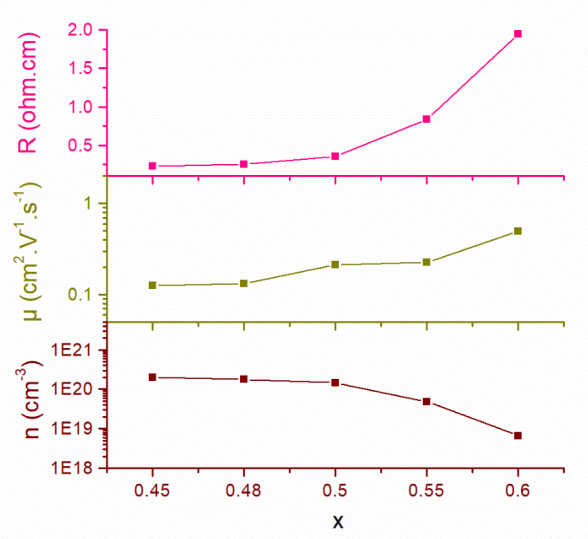

Figure IV. 10: *Resistivity (R), carrier mobility (μ) and carrier density (n) of $Zn_xSn_{1-x}N_2$ thin film with $0.45 \leq x \leq 0.60$, fabricated in $Zn_{RF}Sn_{DC}$ mode.*

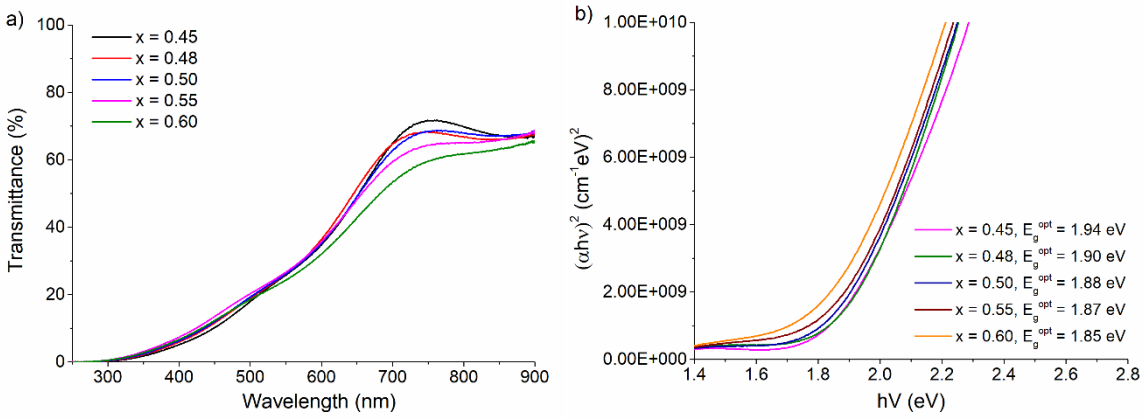

Figure IV. 11: *a) Transmittance vs. wavelength and b) Optical gap of $Zn_xSn_{1-x}N_2$ thin film with $0.45 \leq x \leq 0.60$, fabricated in $Zn_{RF}Sn_{DC}$ mode*

Figure IV. 11a shows a shift of the cut-off in transmittance towards higher wavelengths (red shift) as the Zn composition increases. Correspondingly, the optical bandgap (**Figure IV. 11b**) is primarily reducing from 1.94 eV to 1.85 eV while x value increase from 0.45 to 0.60. A Burstein-Moss effect could also be suspected in this series. Nevertheless, the correlation between carrier concentration and bandgap does not match since, in this case, a lower bandgap variation is obtained for rather the same variation of carrier concentration.

IV.1.3 $Zn_{DC}Sn_{DC}$ series

All along this thesis, the possibilities of the sputtering equipment evolve and particularly, the possibility feeding both targets in DC mode was set lately. Always keeping the same sputtering atmosphere, 20W-DC and 17W to 37W-DC was used for Zn target and Sn targets, respectively. **Figure IV. 12** shows the Zn composition and the sputtering rate versus the DC power applied to the Sn target. Here too, the sputtering time was optimized to get a film thickness of approximately 300 nm.

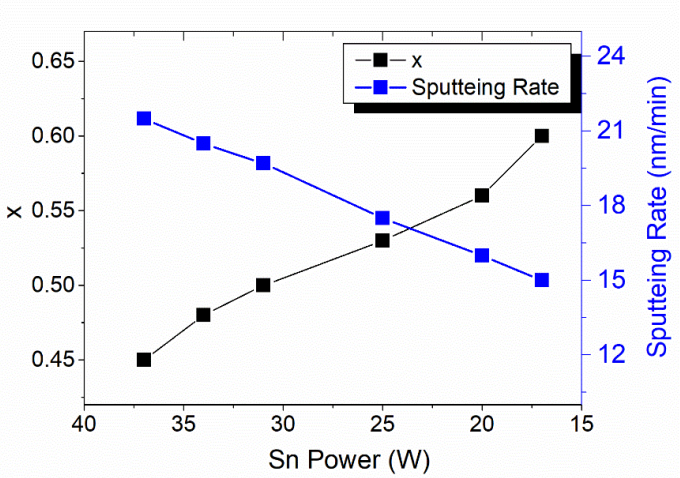

Figure IV. 12: *Composition and sputtering rate via Sn power of $Zn_xSn_{1-x}N_2$ ($Zn_{DC}Sn_{DC}$ series) thin films.*

Figure IV. 13 illustrates the surface morphology of $Zn_xS_{n1-x}N_2$ thin films, fabricated in $Zn_{DC}Sn_{DC}$ mode. For $x \leq 0.53$, the difference of surface morphologies is difficult to assess and presents a cauliflower-like surface. For x = 0.60, the surface morphology changes to elongated grains with voids as observed in the previous cases for such x values. For x = 0.55, surface morphology appears as a kind of transition between cauliflower-like structure and elongated grains. For Sn-rich samples (x< 0,5), the XRD diffractograms (**Figure IV. 14**) shows three dominant peaks located at 30.2°, 34.2° and 53.6°, related to (200), (121) and (320) planes, as rather observed on previous deposition modes. For stoichiometric samples, the seven characteristic peaks of $ZnSnN_2$ [59] are recorded. For Zn-rich samples, the disappearing of (200) and (320) planes rather follow previous observations and can be clearly correlated to the change in surface morphology that are observed by SEM (see **Figure IV. 13**).

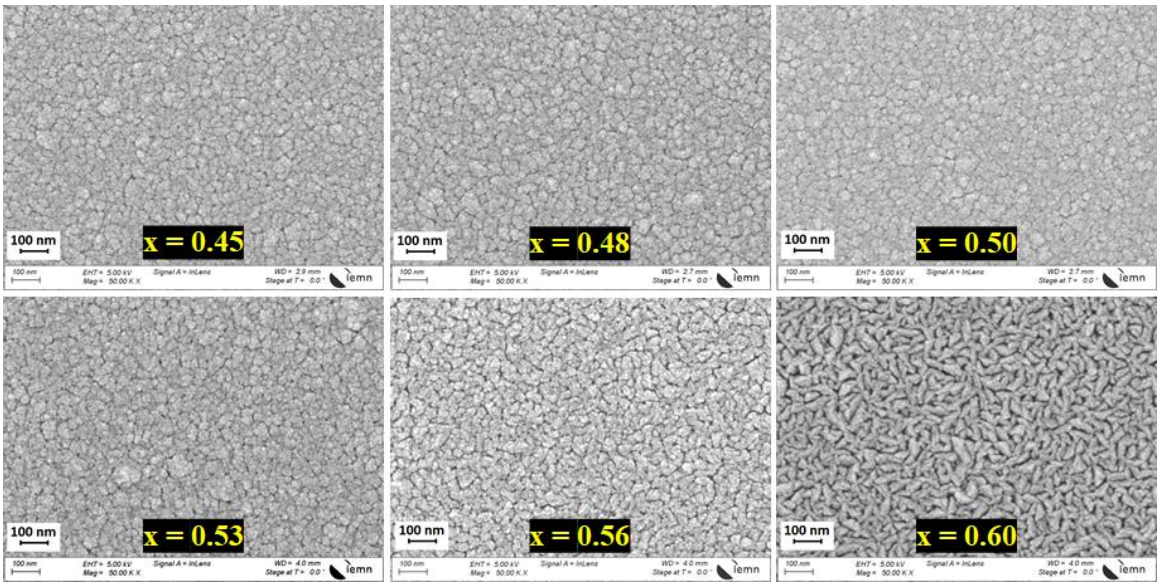

Figure IV. 13: *Top-view SEM images of $Zn_xSn_{1-x}N_2$ thin films ($Zn_{DC}Sn_{DC}$ series) with $0.45 \leq x \leq 0.60$.*

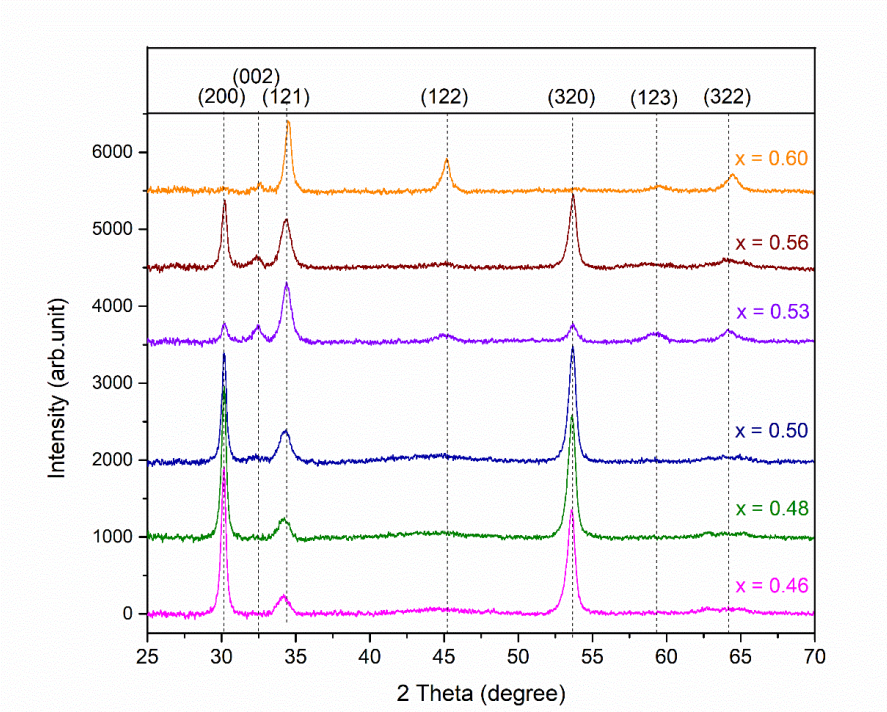

Figure IV. 14: *XRD diffractograms of $Zn_xSn_{1-x}N_2$ thin films ($Zn_{DC}Sn_{DC}$ series) with $0.45 \leq x \leq 0.60$.*

The lattice parameters and crystal size determined from (121) plane peak are reported in **Figure IV. 15** and show the same trend than above reported, i.e. mainly the c parameter

that decreases when the Zn composition increases. The crystal size is close to 10 ± 0.5 nm as $0.45 \leq x \leq 0.58$. For the highest Zn composition tested here, a larger crytallite size is obtained that is coherent with the SEM observations.

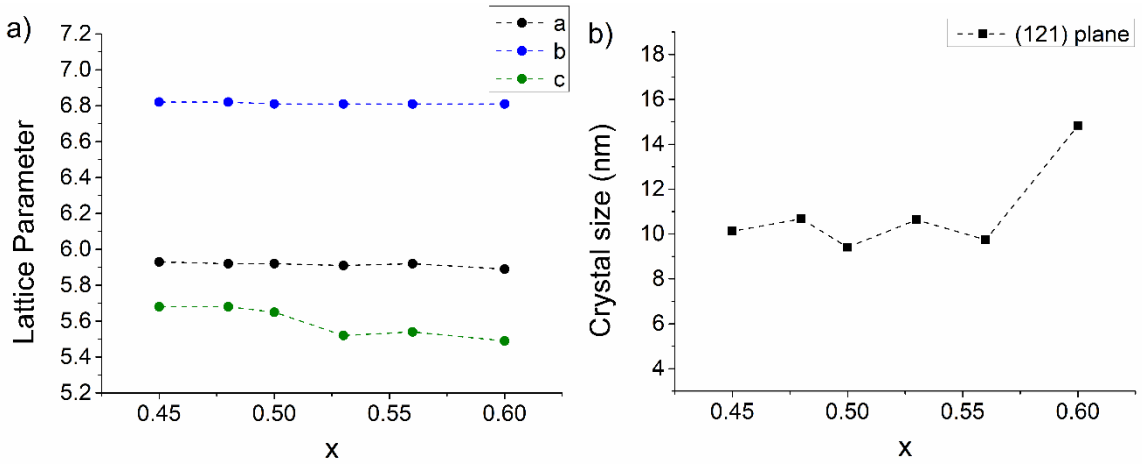

Figure IV. 15: *a) Lattice parameter and b) crystallite size calculated from XRD data ((121) plane for crystallite size) of $Zn_xSn_{1-x}N_2$ thin films ($Zn_{DC}Sn_{DC}$ series) with $0.45 \leq x \leq 0.65$.*

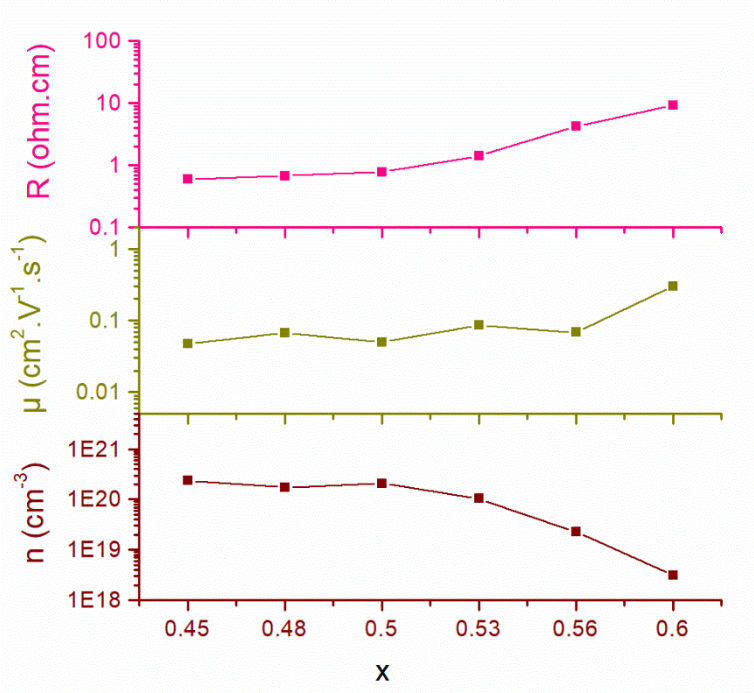

Figure IV. 16: *Resistivity (R), carrier mobility (μ) and carrier density (n) of $Zn_xSn_{1-x}N_2$ thin films ($Zn_{DC}Sn_{DC}$ series) with $0.45 \leq x \leq 0.60$.*

All samples exhibit n-type polarity **(Figure IV. 16)**. The carrier density and carrier mobility values behave mainly as observed on previous cases, too As the Zn composition increases, the resistivity increases up to approximately 10 Ω.cm that can be considered as the highest resistivity compared to that of other series. However, the mobility and carrier density do not exhibit huge variation compared to other series and display the same behavior.

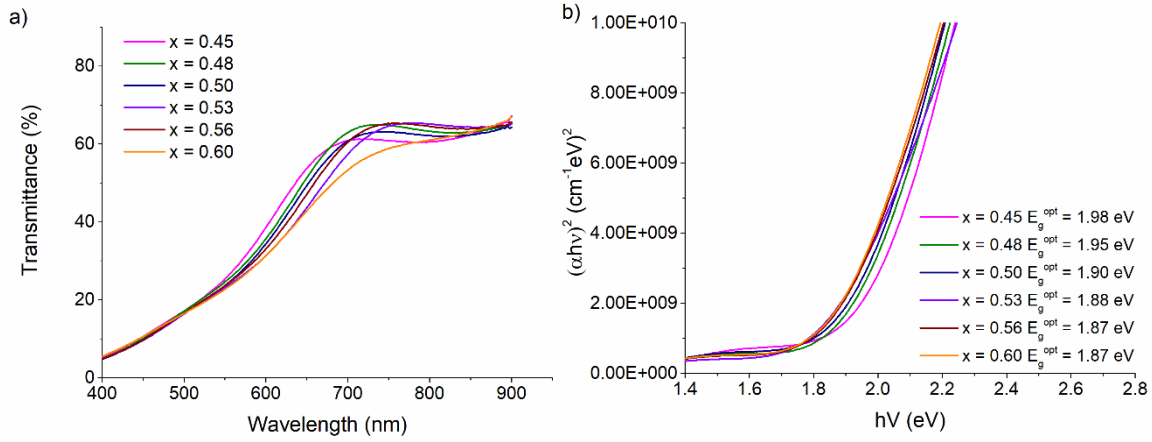

Figure IV. 17: *a) Transmittance vs. wavelength and b) Optical bandgap of $Zn_xSn_{1-x}N_2$ thin films ($Zn_{DC}Sn_{DC}$ series)with $0.45 \leq x \leq 0.60$.*

In a predictable manner according to previous results, a progressive shift of the cut-off wavelength in transmittance towards higher values (red shift) is observed as the Zn composition increases (**Figure IV. 17**) with so the same comments.

IV.2 **$ZnSnN_2$: Sputtering with compound-target $Zn_{42.2}Sn_{57.8}$**

IV.2.1 $ZnSn_{DC}$ mode:

A compound target ($Zn_{42.2}Sn_{57.8}$) has been sputtered in pure DC on an Eagle XG glass, the applied power was varied from 30 W to 100 W and the atmosphere was N_2/Ar. Other parameters are the same (i.e. deposition at room temperature, N_2/Ar ratio fixed to 2.0, and sputtering chamber pressure to 0.02 mbar). The change in film composition and sputtering rate are illustrated in **Figure IV. 18**, the composition does not change significantly as supply power is smaller than 60 W, x value is in range 0.40 to 0.41 and rather corresponds to the target composition. When the power increases above this switchover point, the x

ratio increases. Reason of that has not been clearly pointed out. Rather predictably, the sputtering rate shifts linearly versus power.

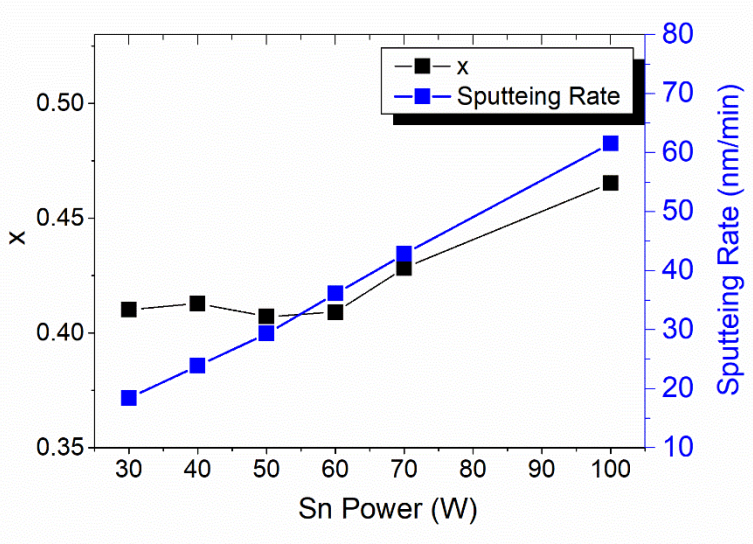

Figure IV. 18: *Composition and sputtering rate via DC power of $Zn_xSn_{1-x}N_2$ thin films, ($ZnSn_{DC}$ series).*

As depicted in **Figure IV. 19**, a cauliflower-like structure is obtained whatever the power is. Similarly, the crystal structure of $ZnSnN_2$ obtained from XRD diffractograms (**Figure IV. 20**) showed no significant difference and only three peaks are observed (located at 30.2°, 34.2° and 53.6° related to (200), (121) and (320) plane).

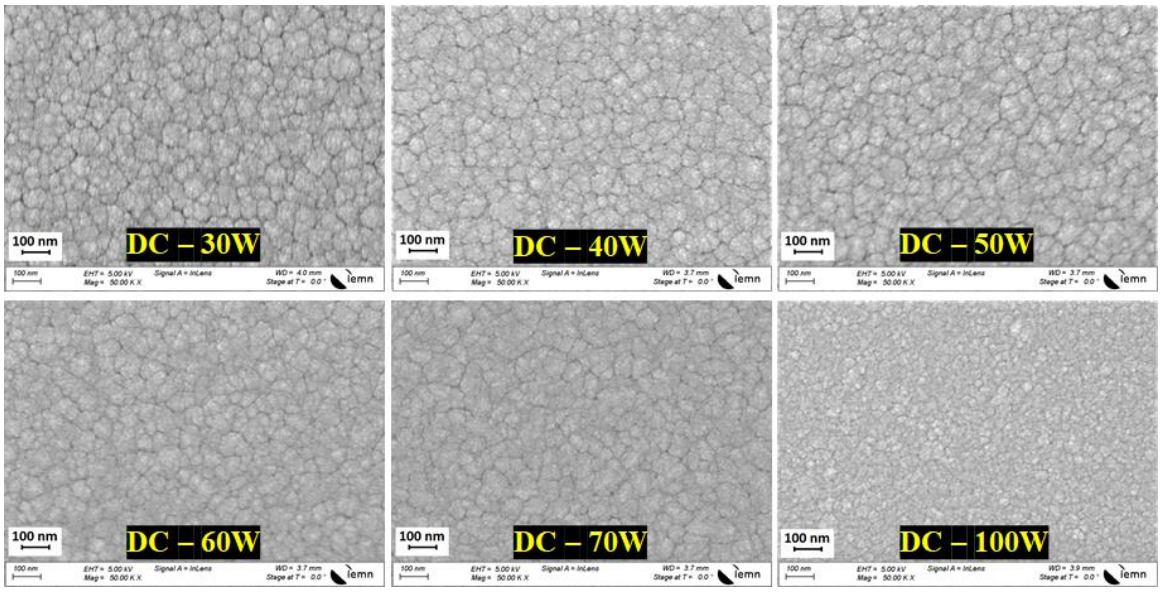

Figure IV. 19: *Top-view SEM images of the $Zn_xSn_{1-x}N_2$ ($ZnSn_{DC}$ series).*

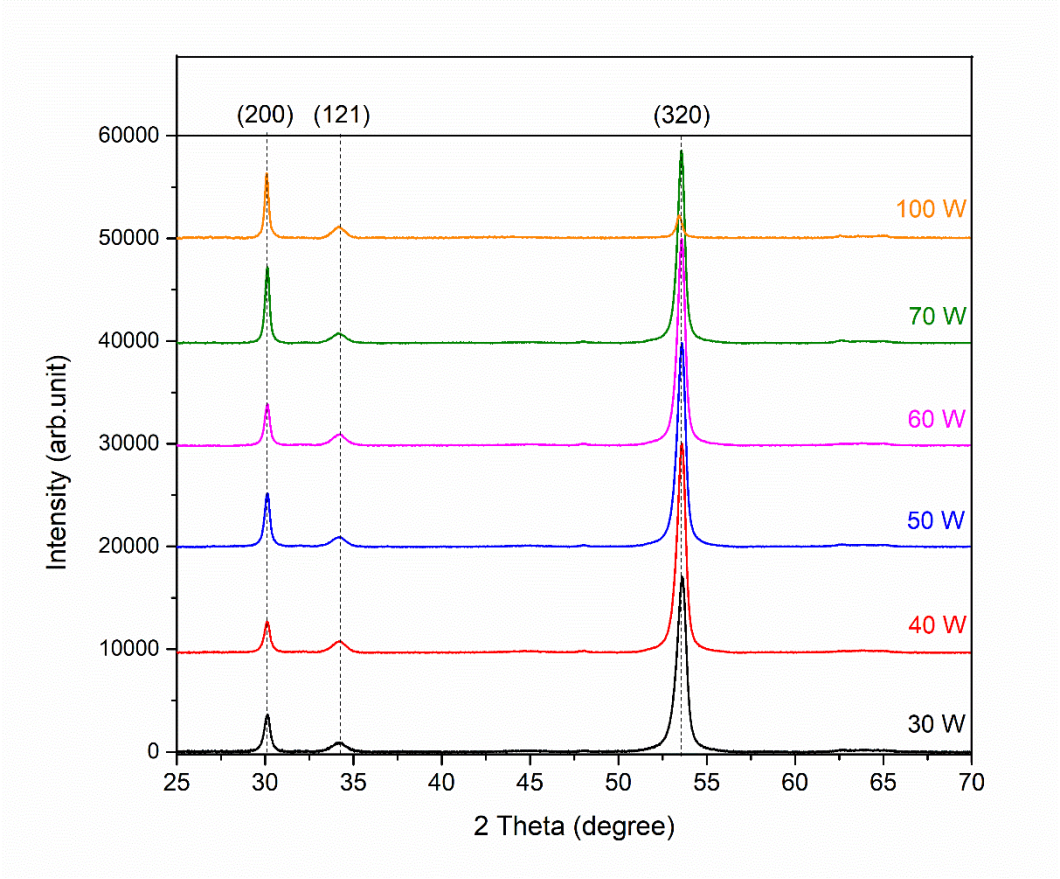

Figure IV. 20: *XRD diffractograms of $Zn_xSn_{1-x}N_2$ thin films ($ZnSn_{DC}$ series)via DC power.*

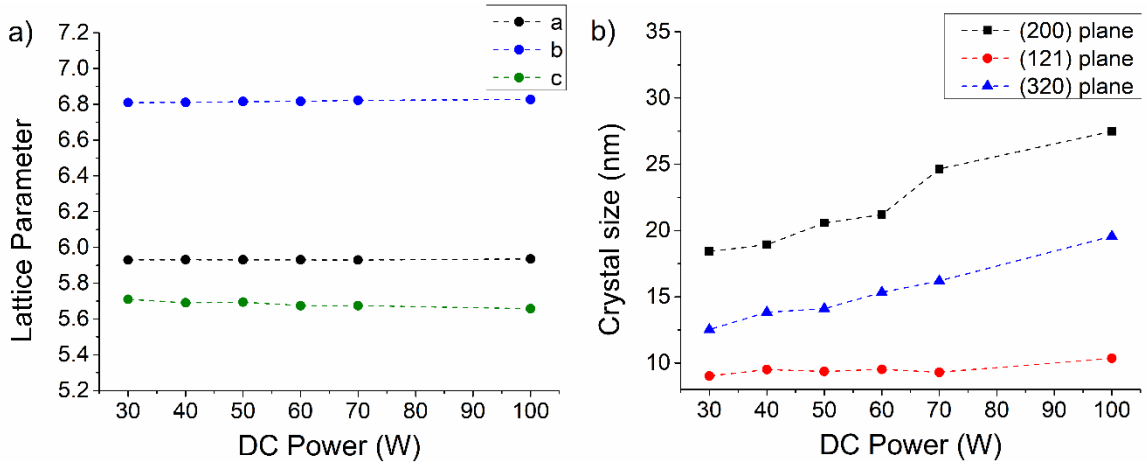

Figure IV. 21: *a) Lattice parameter and b) crystallite size calculated from XRD data ((121) plane for crystallite size) of $Zn_xSn_{1-x}N_2$ thin films ($ZnSn_{DC}$ series).*

The lattice parameters (**Figure IV. 21a)** do not change by the apply power. However, the crystal size evaluated from (200), (121) and (320) plane increase as increasing the power.

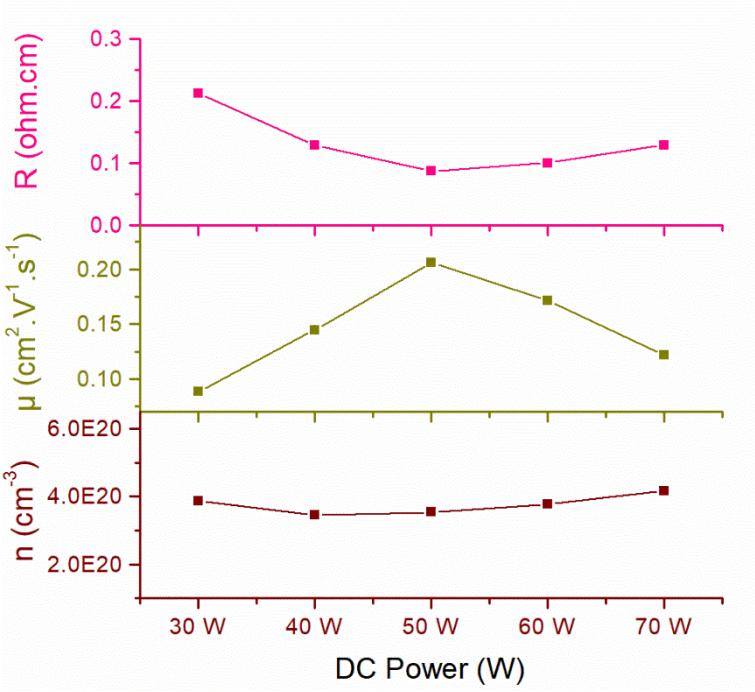

Figure IV. 22: *Resistivity (R), carrier mobility (μ) and carrier density (n) of $Zn_xSn_{1-x}N_2$ thin films ($ZnSn_{DC}$ series) via DC power*

When the applied power increases from 30 W to 70 W, there is no significant effect on electrical properties (**Figure IV. 22)**. The resistivity is in range between 0.09 and 0.21

Ω.cm, the carrier varies from 0.09 to 0.17 $cm^2V^{-1}s^{-1}$. the carrier concentration is always close to 4 x 10^{20} cm^{-3}.

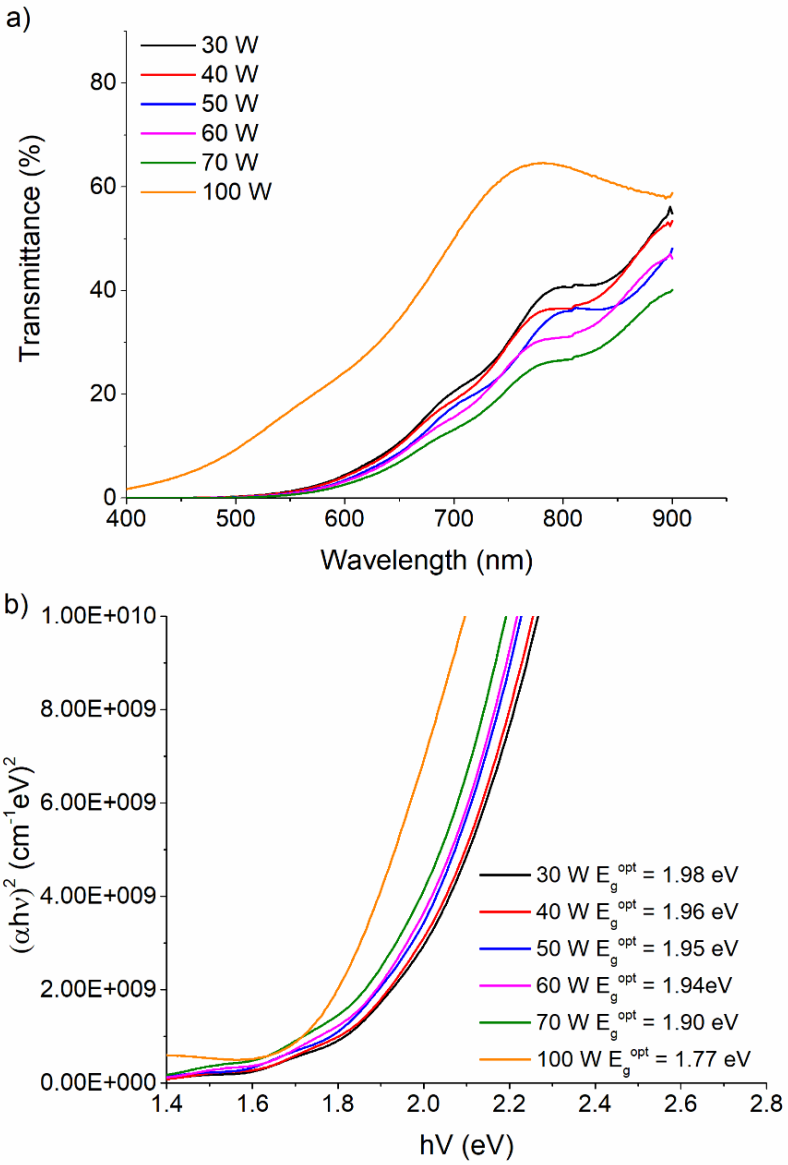

Figure IV. 23: *a) Transmittance vs. wavelength and b) Optical bandgap of $Zn_xSn_{1-x}N_2$ thin films ($ZnSn_{DC}$ series) via DC power*

The UV-Vis spectra do not exhibit a great change (**Figure IV. 23a**), except for the highest applied power where a shift of the cut-off in transmittance towards higher wavelengths (red shift) as the applied power increases. The optical bandgap can be calculated using (**Figure IV. 23b**), reduces from 1.98 eV to 1.77 eV.

IV.2.2 Comparision of $ZnSn_{RF}$ mode and $ZnSn_{DC}$ mode

In this section RF supply is used instead of DC for the compound target. All other parameters have been kept identical as in section IV.2.1. For low applied powers of 30 W, the sputtering rate is very slow, approximately 1nm/min. Reversely, sputtering at high RF powers cannot be done due to high level of reflected power that cannot be decreased. As a result, a RF power of 100 W is selected, the x value equals to 0.44. The sputtering rate is then of 32 nm/min that is smaller than 61 nm/min obtained in DC mode but a predictable behavior. The material surface (**Figure IV. 24)** is, a cauliflower-like and no particular difference is observed with the result obtained in DC mode.

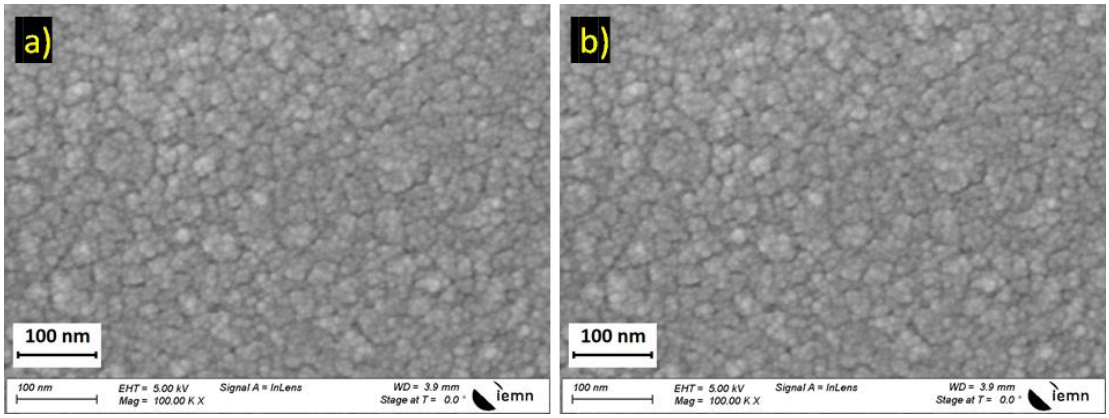

Figure IV. 24: *SEM image of $ZnSnN_2$ film deposited in (a) 100W-DC mode ($ZnSn_{DC}$ sample) and (b) 100W-RF mode ($ZnSn_{RF}$ sample) from a compound target.*

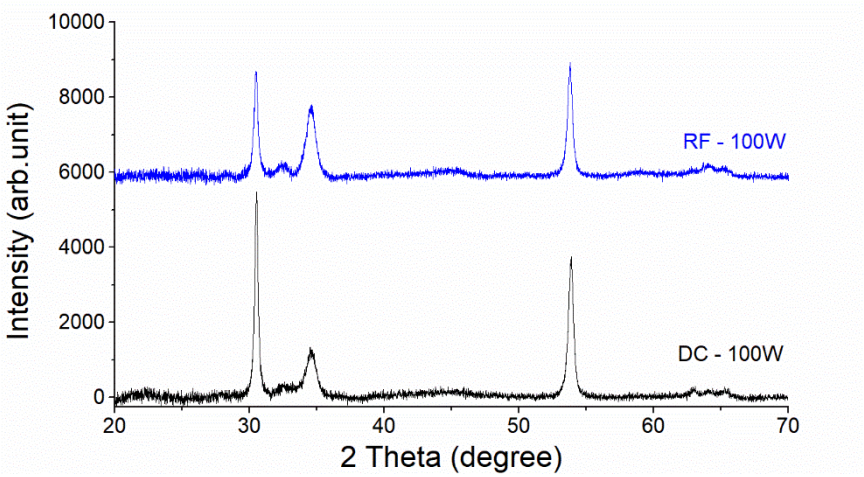

Figure IV. 25: *XRD diffractograms of $ZnSnN_2$ deposited in DC mode ($ZnSn_{DC}$ sample) and RF mode ($ZnSn_{RF}$ sample) from a compound target.*

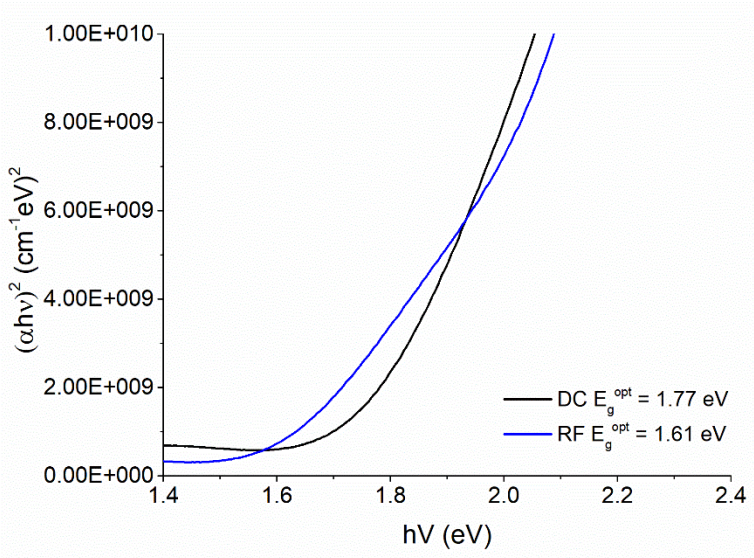

Figure IV. 26: *Optical bandgap of the $ZnSnN_2$ films deposited in DC mode ($ZnSn_{DC}$ sample) and RF mode ($ZnSn_{RF}$ sample) from a compound target.*

Optical and electrical properties also differ; the optical bandgaps obtained for the same compound composition are lower than in case using two elementary targets, 1.61 eV with RF and 1.77 eV with DC (**Figure IV. 26**). Besides that, Hall measurements show a very high carrier mobility of 23.7 $cm^2V^{-1}s^{-1}$ and a low carrier density of 1.60 x1 0^{18} cm^{-3} in RF mode. In DC mode, these values change to 3.02 $cm^2V^{-1}s^{-1}$ and 8.30 x 10^{18} cm^{-3}, respectively.

IV.3 **Discussions and partial conclusions**

In this chapter, we compared the properties of $Zn_xSn_{1-x}N_2$ films versus their composition (x parameter). As reported in previous chapters, owing to the co-sputtering technique, several configurations exist that are linked to the DC or RF power that is applied to each target. All configurations have been tested except a dual RF mode since only one RF generator is available. A compound ZnSn target has also been used in both deposition modes.

Focusing on the co-sputtering experiments, the characteristics XRD peaks of $ZnSnN_2$ are rather always observed (see **Figures IV. 2, IV. 8** and **IV. 14**) for near stoichiometric or moderately Zn rich material ($0.45 < x < 0.6$). Highly Zn rich films seem amorphous (e.g. $x = 0.74$ in **Figure IV. 2**) and moderately to highly Sn rich films do not show all peaks (e.g. $x < 0.45$ in **Figure IV. 2**). The lattice parameters and the crystallite size versus composition show almost the same behavior whatever the target bias configuration is. a and b parameters are unchanged whatever the x value is, c parameter decreases by roughly 10% as film starts becoming Zn rich. The crystallite size mainly increases with Zn composition with a mean value around 10 nm (see **Figures IV. 3, IV. 9** and **IV. 15**). The electrical parameters exhibit also almost the same behavior versus the Zn composition whatever the deposition mode is (see **Figures IV. 4, IV. 10** and **IV. 16**). Electron concentration decreases by two order of magnitude, from 10^{20} down to 10^{18} cm^{-3} when Zn concentration increases. Particularly, Sn rich films always exhibit high carrier concentration around 10^{20} cm^{-3} and a switchover point seems to exist at stoichiometric ratio: the two-decade decrease is so mainly observed for x values between 0.5 and 0.6. For $0.45 < x < 0.6$, the optical bandgap is decreasing from roughly 2eV down to 1.85 eV, whatever the deposition mode is (see **Figures IV. 5, IV. 11** and **IV. 17**).

Using a compound target ($Zn_{42.2}Sn_{57.8}$), experiments have been limited since problems due to reflected power in RF mode have been encountered. In DC mode, the obtained films are always Sn-rich. Below a switchover point around $3W/cm^2$ (60W on a 2" target), composition is rather stable and reflects that of target. Above this point, Sn concentration decreases and films tend to become stoichiometric. Nevertheless, they are always more or less Sn-rich and the carrier concentration is around some 10^{20} cm^{-3} as observed in the previous series.

Chapter V: **FABRICATION OF ALUMINUM DOPED ZINC OXIDE AND TIN OXIDE**

Since the beginning of the studies on $ZnSnN_2$ semiconductor, a decade ago, the scientific reports focused mainly on the structure and electrical properties of the material. Although, the computational and experimental results (discussed in Chapter I) are promising for this material to be used in photovoltaics, few data on photoelectric properties have been recorded, yet. Even if simulation results of p-$CuCrO_2$/n-$ZnSnN_2$ device display more than 20% of power conversion efficiency [32], [82], experimental results are in sharp contrast since only 0.37 % [49] and 1.54% [83] of conversion efficiency were obtained on p-SnO/n-$ZnSnN_2$ structures. Besides, the solar structure based on p-Si and n-$ZnSnN_2$ [48] was investigated, and no data of conversion efficiency was reported.

In this chapter, I will focus on the fabrication (always by using PVD, and especially, the sputtering technique) of complementary materials aiming building a cell structure. First, I will report on a rather usual n-type transparent conductive oxide that is aluminum-doped zinc oxide (AZO). AZO has been preferred to ITO since it is in the same spirit of sustainable development that $ZnSnN_2$ material although ITO use is controversial due to its indium content (exhibiting nevertheless slightly better electrical properties). As p-type material that can also acts as a transparent window, I will report on tin oxide (SnO). Both will be used trying making a cell in next chapter.

V.1 **Aluminum doped zinc oxide (AZO)**

V.1.1 State of the art

V.1.1.1 Structural

ZnO is a member of binary II-VI semiconductors, its crystal structure is either cubic zinc-blende or hexagonal wurtzite. Its characteristics peaks exhibit at (100), (002) and (101) planes [84]. By calculating the total energy per unit cell [85], [86], the most energetically stable ZnO structure is hexagonal wurtzite; hence, it is obtained in almost all reports on AZO, with a dominant orientation along the (002) direction, having c-axis perpendicular to the substrate [87], [88], [97]–[105], [89]–[96].

Besides, group III atoms such as Al, Ga, In acting as dopants were found not modifying the crystal structure, as most dopants. Due to difference in the ionic radius of doping materials and Zn^{2+} (74 pm), a shift of diffraction peaks was observed if they substitute Zn^{+2} in the lattice. In Al doped ZnO, the ionic radius of Al^{+3} is 53 pm, smaller than Zn^{2+}, the diffraction peak of (002) plane shifts toward higher angle [94], [103], [106]–[109].

In this study, we design a structure of $ZnSnN_2$/AZO because of their lattice mismatch is smaller than 5% [110]–[112]. It is possible to restricting the strain in interface and the degradation of device.

V.1.1.2 Electrical and optical properties of AZO

In most studies on AZO, the resistivity has been reported as low value, ranges in the order of 10^{-4} Ω.cm to the order of 10^{-2} Ω.cm. A post-annealing treatment contributes to the reduction of resistivity [87], [95], but no effect of substrate temperature was mentioned [96], [107]. Additionally, in sputtering method, the higher working pressure is, the higher resistivity is obtained [93].

It is largely agreed that AZO is a n-type semiconductor with high electron density, ranging between 10^{18} cm-3 and 10^{21} cm^{-3}, depending on deposition techniques and parameters [87], [88], [114]–[119], [89], [90], [95], [98]–[101], [113]. When the doping level of Al increases, the carrier density increases [89], due to Al_{Zn} donor defect (Al substitutes Zn).

The carrier mobility varies from 0.6 $cm^2V^{-1}s^{-1}$ [101] to 60 $cm^2V^{-1}s^{-1}$ [118]. The highest mobility is obtained when using DC magnetron sputtering.

In the visible region (400 to 800 nm), the optical transmittance is very high (≥ 75%). It is associated with an optical bandgap value between 3.15 eV [119] and 3.9 eV [120].

V.1.1.3 Deposition techniques of AZO thin film

There are several deposition techniques to fabricate AZO thin films, such as atomic layer deposition (ALD) [109], [121], [122], chemical bath deposition (CBD) [103], electrochemical deposition (ECD) [100], [108], electron beam evaporation [123], electro-spraying method [124], mist chemical vapor deposition [98], [105], plasma-enhanced metalorganic chemical vapor deposition [125], pulsed laser deposition [107], [126], [127], sol-gel coating [97], [102], [104], [106], [114], [128], spray pyrolysis [117], [129], [130], thermal evaporation [114], and finally sputtering (ion beam, DC or RF mode) [92]–[96], [131]. Sputtering is obviously the most popular method, owing to its advantages mentioned in Section I.3.2.4. In addition, the deposition of AZO thin films by sputtering will be more convenient in a full process making a device.

V.1.1.4 Application of AZO thin films

According to its electrical and optical properties, AZO thin films are used as transparent conductive oxide (TCO) for solar cells, mainly of 2nd generation. The experimental conversion efficiencies of CdTe, perovskite and Si solar cells using AZO films are summarized in **Table V.1**

Table V. 1: Comparison of the application of AZO as conductive electrode in of CdTe, perovskite and Si solar cell

	AZO fabrication	Voc (mV)	Jsc (mA/cm^2)	FF (%)	Efficiency (%)	Ref
CdTe Solar cell	RF sputtering	763	20.3	55.7	8.6	A. N. Tiwari *et al* [132]
	RF sputtering	814	23.6	73.2	14	A. Gupta *et al* [133]

	RF sputtering	834	24.7	75.9	15.6	J. Perrenoud *et al* [134]
	Spray pyrolysis	845	20.2	70.8	12.1	A. Crossay *et al* [117]
perovskite solar cells	Electro-Spraying	1045	15.1	76	12	K. Mahmood *et al* [124]
	RF sputtering	990	17.9	53.4	9.5	S. Ghosh *et al* [101]
	ALD	1080	18.6	70.8	14.2	H. Yang *et al* [122]
Si Solar cell	RF sputtering	411	30	66.7	8.2	D. Song *et al* [93]
	DC sputtering	1413	11.4	70.5	11.4	S. Neubert *et al* [118]

V.1.2 Fabrication of AZO by DC-sputtering

The deposition system is the same than for the $ZnSnN_2$, i.e. the Alliance Concept CT200 equipment. Here a 4-inch diameter 3%Al doped ZnO (purity 99.99) is used in a planar configuration. The distance between the target and substrate holder is approximately 5 cm. A DC generator was used and 80W were applied to the target. The rotation speed of substrate holder was 20rpm and the operating pressure in the chamber was 7.10^{-3} mbar (base pressure of 10^{-8} mbar), the Ar gas flow was fixed at 10 sccm. During the deposition, the substrate is not heated, or least not intentionally heated. After deposition on Eagle XG substrate in 9 min, the film thickness was measured using surface profilometry and has been recorded approximately to 270nm. **Figure V. 1** shows the top and cross-sectional views of AZO films. The shape of grain is random and the size is smaller than 100 nm. The cross-section image shows the microstructure is columnar.

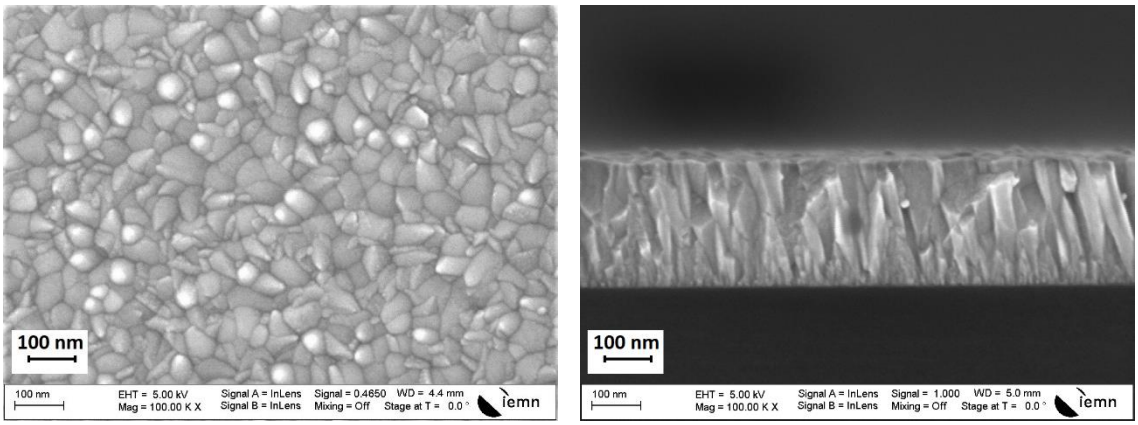

Figure V. 1 : *SEM top (on the left) and cross-sectional (on the right) views of AZO thin films.*

XRD pattern is presented on **Figure V. 2**. XRD data match all the characteristic peaks of hexagonal AZO, with peaks located at 2θ angles: 31.0°, 34.4°, 36.3°, 47.5°, 62.6°and 72.1° corresponding to (100), (002), (101), (102), (103) and (004) directions [94]. The orientation is more preferentially along the (002) direction. The average crystal size (D) is equal to 27 nm, evaluated from the (200) peak width using the Scherrer formula (2.6). The full width at half maximum is equal to 0.30316, the a and c parameters are equal to 3.26 Å and 5.20 Å respectively, in good agreement with other reports [105], [106], [123], [129].

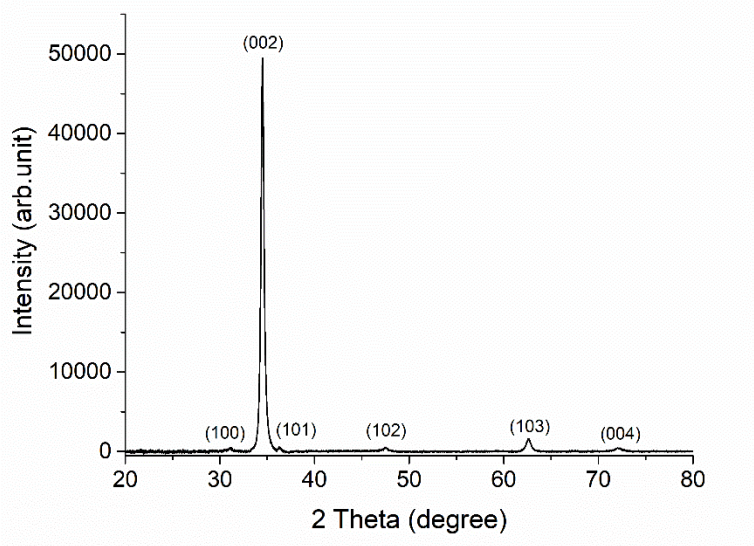

Figure V. 2 : *XRD pattern of AZO thin films on Eagle XG substrate.*

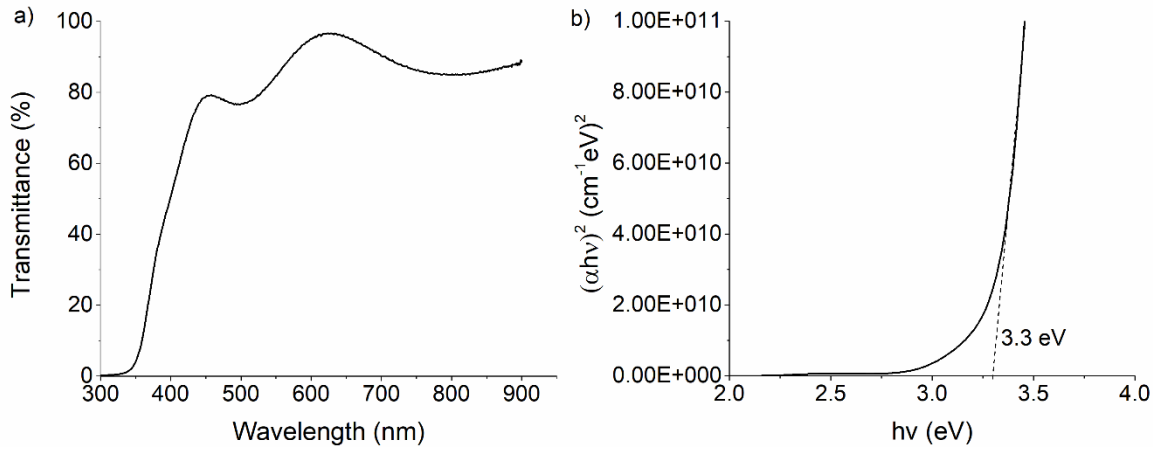

Figure V. 3 : *UV-Vis result of AZO thin film: a) Transmittance vs. wavelength spectra, b) Optical band gap calculated using Tauc's equation (2.7).*

The **Figure V. 3a** shows the optical transmittance of AZO thin film; at 630 nm the transmittance reaches 97% (for a thickness value that is here of 270 nm). The optical bandgap can be calculated using Tauc's relation (2.7) (**Figure V. 3b**) and is equal to 3.3 eV. This result is similar to the optical band gap of intrinsic ZnO [89], [105], and close to the result of AZO deposited by EDC [100] and sol gel spin coating [104]. Optical bandgap of AZO deposited by sputtering in previous study gave the value higher 3.4 eV [93], [94], [101], [115], [135].

The electrical properties of AZO were measured by using Hall system. The resistivity is equal to 2.82×10^{-3} Ωcm, the carrier density is equal to 1.84×10^{20} cm^{-3} and the mobility is equal to 12 $cm^2V^{-1}s^{-1}$, in excellent agreement with the result of Grilli *et al*. [99]. Our electrical results of AZO are approx. the value AZO thin film that was fabricated by A. Crossay *et al.* [117] and applied for TCO of CdTe solar cell.

V.2 **p-SnO thin film**

V.2.1 State of the art:

V.2.1.1 Structural

According to E. *Leja et al* [136], [137], α-SnO and SnO_2 are two stable compounds obtained from the combination of tin and oxygen, and both of them exhibit a tetragonal structure. In addition, α-SnO is a thermodynamically unstable phase; as temperature is higher than 300°C, it easily decomposes and recombines into SnO_2 by the following reaction (5.1).

$$2\ \alpha\text{-SnO} \rightarrow SnO_2 + \beta\text{-Sn} \qquad (5.1)$$

The formation of a stable α-SnO phase is limited to a narrow window. Specially in reactive sputtering technique, the oxygen partial pressure should be lower than 4.5% (working pressure ~ $7x10^{-3}$ mbar)[138] or lower than 9.5% (working pressure ~ $2.4x10^{-3}$ mbar)[139]. The post deposition annealing treatment will help to improve the crystalline quality, but it should not be higher than 200°C to avoid the appearance of a second phase SnO_2 [137], [138], [140].

Although most studies agree that SnO exists in the form of tetragonal crystals [139]–[144] with *P*4/*nmm* space group [143], [145]–[147], a metastable orthorhombic form was mentioned by S. Lin *et al* [140], the type of space group was not discussed.

V.2.1.2 Electrical and optical properties of SnO

A. Togo *et al.* [148] have calculated and suggested native defects in SnO: they are the O interstitial (O_i), the O vacancy (V_O), the Sn interstitial (Sn_i), the Sn vacancy (V_{Sn}). The formation energy of V_{sn}, V_O and O_i defects were recorded the similar order of magnitude. When the SnO obtained Sn-rich nature, the V_O defect is dominating, whereas O_i and V_{Sn} defects dominate. Depending on these defects are acceptor like or donor like, the charge state obtained is negative or positive, respectively. Additionally, the O_i defect does not

contribute to electric conductivity and Sn_i defect shows both positive- and negative-charge states near the valence band maximum (VBM) and conduction band minimum (CBM), respectively. The acceptor defect V_{sn} is the origin of p-type conductivity of SnO.

Besides, the electrical properties of SnO are greatly influenced by the fabrication conditions and the post-anneal treatment, as mentioned in Section V.2.1.1. When the transformation of SnO into SnO_2 occurs, it leads to change the type of charge carrier from p-type to n-type [137]–[140], [149].

For sputtered films, their optical bandgap increases as the working pressure [140] and oxygen partial pressure [139], [150] increase. The post-anneal treatment also leads to expand the optical bandgap [140], [151]. The optical band gap is between 2 eV and 3.5 eV [140], smaller than optical bandgap of SnO_2 [150].

V.2.1.3 Deposition techniques of SnO thin films

The p-type SnO thin films can be deposited by atomic layer deposition [152], electron beam evaporation [146], [147], pulsed laser deposition [149], [153], [154] and sputtering [137], [155]–[159].Here, sputtering is used in order to get compatibility between the different deposition technique and, *in fine*, to be able to grow deposit all the layers without exposing the samples to air.

V.2.2 Fabrication of SnO by magnetron sputtering

The deposition system arrangement is the same than used for AZO (see section V.1.2) except the Ar gas flow that was here fixed at 50 sccm and the process pressure to 2.10^{-2} mbar. A SnO (purity 99.99%) target is used. Both DC and RF mode were tested.

V.2.2.1 SnO deposition in RF mode

The power density was close to 1.2 W/cm^2, the sputtering rate obtained was close to 28 nm/min. After deposition, the SnO thin film was characterized by XRD and Hall effect measurements. The XRD data showed an amorphous nature and electrical properties could not be recorded. So, SnO thin films were fabricated again and post-annealed in nitrogen atmosphere at different temperatures, from 100°C to 400°C with a 50°C step. The

annealing time was 15 minutes and the heating-up/cooling-down rate was 100°C/min. It has to be noted that all the deposited samples were made in a single batch; their thickness is close to 250 nm.

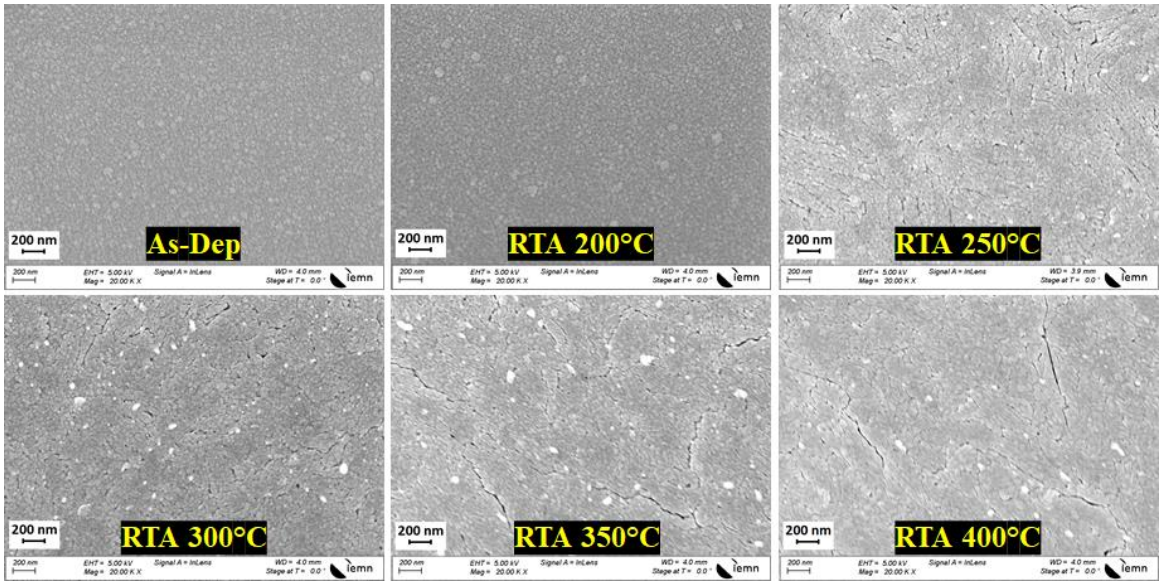

Figure V. 4 : *SEM images of SnO thin films deposited in RF mode after post-annealing treatment at different temperatures.*

The effect of annealing process at different temperature on surface morphology of SnO thin films is shown in **Figure V. 4**. As the temperature is lower than 200°C, rapid thermal annealing process does not affect the surface morphology of the films. At higher temperature, cracks appear on the surface and the SnO films are degraded and no longer homogeneous. Because tin has a relatively low melting point (approx. 232°C), the appearance of white pieces on the SnO surfaces that were annealed at temperature equal or above 250°C is predicted to be the crystallization of tin, as we also observed for $ZnSnN_2$ (see for example **Figure III. 14**). However, XRD diffractograms (showed in **Figure V. 5**) confirm the pure SnO phase, no diffraction peaks characteristic of secondary phases, neither β-Sn nor Sn_xO_y (SnO_2, Sn_3O_4…). There are two possible hypotheses: 1) the concentration of secondary phases is very small compared to that of SnO, the intensity of their characteristics peaks is too low to be observed, 2) the secondary phases do not exist in a crystalline form when the annealing temperature is below 400°C, and are so not clearly distinguishable by XRD.

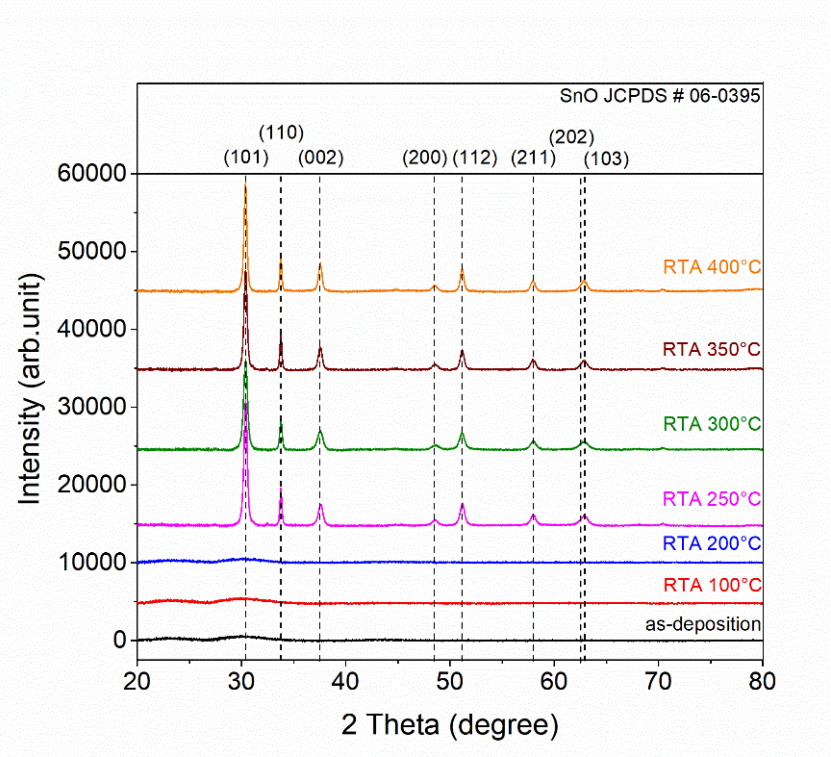

Figure V. 5: *XRD diffractograms of SnO thin films deposited in RF mode versus post-annealing temperature.*

The effect of post-annealing temperature on crystalline quality and orientation of SnO thin films is shown on **Figure V. 5**. The as-deposited and the annealed samples (temperature smaller than 250°C) have shown an amorphous nature. When the annealing temperature is equal or higher than 250°C, XRD data match all the characteristic peaks of a tetragonal structure of SnO, according to JCPDS # 06-0395. They are located at 2θ angles: 30.4°, 33.8°, 37.5°, 48.6°, 51.2°and 58.0° and 62.8° corresponding to (101), (110), (002), (200), (112), (211) and overlap of (202) and (103) directions. As the annealing temperature is ranging from 250°C to 400°C, there is no change in microstructure and orientation of SnO thin films, the (101) peak was the most dominant for all samples.

The lattice parameter of SnO tetragonal structure determined from the XRD measurements are compared to experimental reported values in **Table V. 2**. The a and c parameter do not change by increasing the annealing temperature and are close to the literature result.

Table V. 2: Comparison of lattice parameters issued from literature results and from here fabricated SnO thin films versus annealing temperature (determined from XRD measurements, (101) plane).

	a (Å)	c (Å)
F. Izumi [160]	3.80	4.84
A. Togo *et al* [148]	3.88	4.98
S. Lee *et al* [141]	3.80	4.84
A. Garzon-Fontecha *et al* [139]	3.80	4.84
SnO-RF-RTA250°C	3.75	4.78
SnO-RF-RTA300°C	3.74	4.79
SnO-RF-RTA350°C	3.74	4.79
SnO-RF-RTA400°C	3.75	4.79

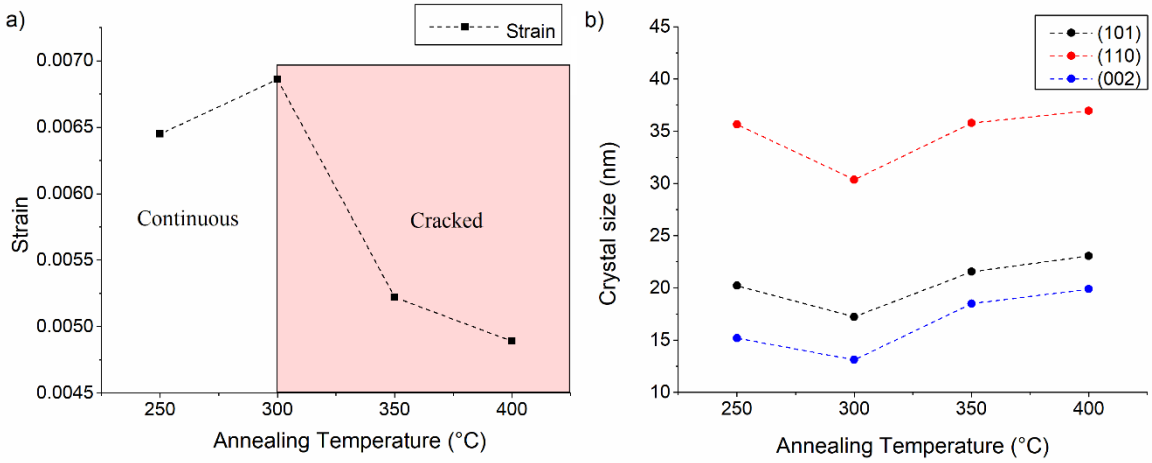

Figure V. 6 : *a) Calculated strain (ε) from XRD data and b) crystal size of (101), (110) and (002) plane of SnO fabricated on RF mode after annealing from 250°C to 400°C.*

Figure V. 6a shows the strain of SnO thin films on glass calculated by XRD data and equation (3.6). The strain increases slightly from $6.4x10^{-3}$ to $6.9x10^{-3}$ when the temperature is ranging between 250°C and 300°C. At higher temperatures, the strain reduces around $5x10^{-3}$ that can be explained by the increase of the density of cracks causing then stress-relief. The crystallite size (D), evaluated from the (101), (110), (002) peak width using the Scherrer formula (2.6), is reported in **Figure V. 6b**. The result obtained using (002) peak

gives a higher value than that reported by C. Jeong *et al* [161] and J. Caraveo-Frescas *et al* (the orientation plane used to calculate was not mentioned) [162].

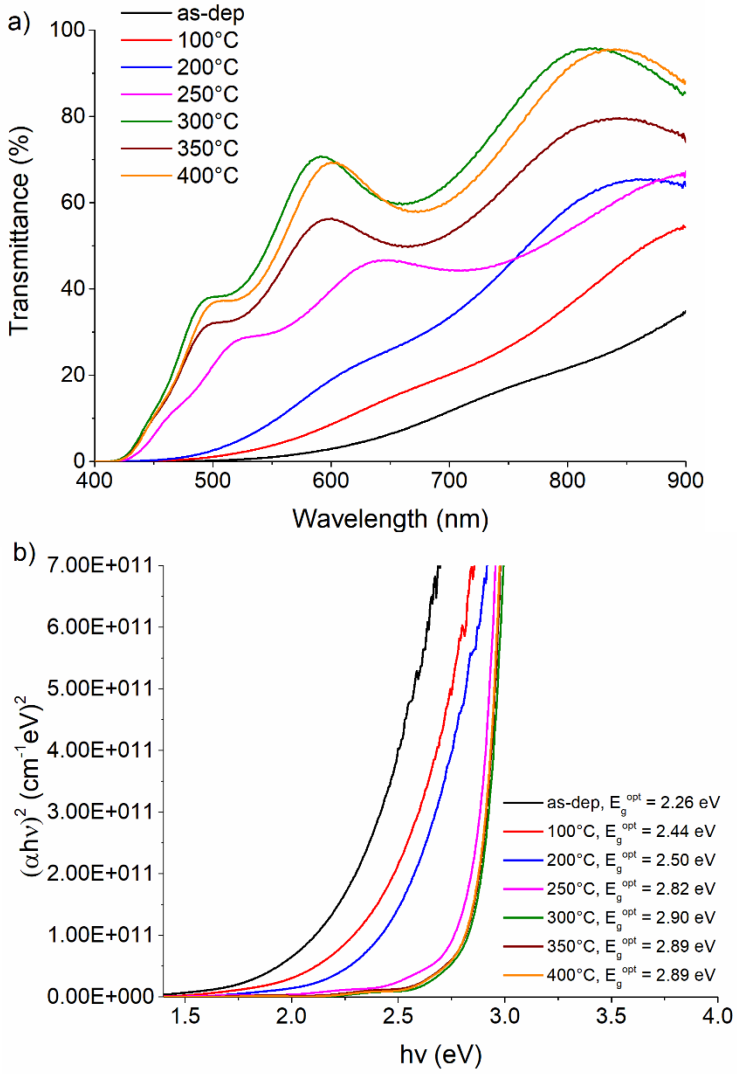

Figure V. 7 : *a) Transmittance vs. wavelength spectra (UV-Vis spectroscopy) for SnO films fabricated using RF mode, as-deposited and after annealing from 100°C to 400°C:, b) Corresponding optical bandgap calculated using Tauc's equation.*

Figure V. 7a shows the optical transmittance data of SnO films fabricated using RF mode and after annealing from 100°C to 400°C. Please, remind that all the samples have the same thickness (approx. 250 nm), the transmittance increase as increasing the annealing temperature. The highest one obtained in sample that annealing at 300°C, the maximum transmittance reaches 71% in visible light region (400 – 800 nm), and approaches 96% at wavelength equals to 820 nm. A progressive shift of the cut-off of the transmittance value

towards lower wavelengths (blue shift) is observed when the annealing temperature increases; the corresponding optical bandgap varies from 2.26 eV to 2.90 eV. Those values are lower than that reported by S. Lin *et al* [140] for SnO thin films that were deposited by RF magnetron sputtering at working pressures from 5.10^{-3} to 3.10^{-2} mbar (here, we are at 2.10^{-2} mbar) that were all determined as above 2.9 eV.

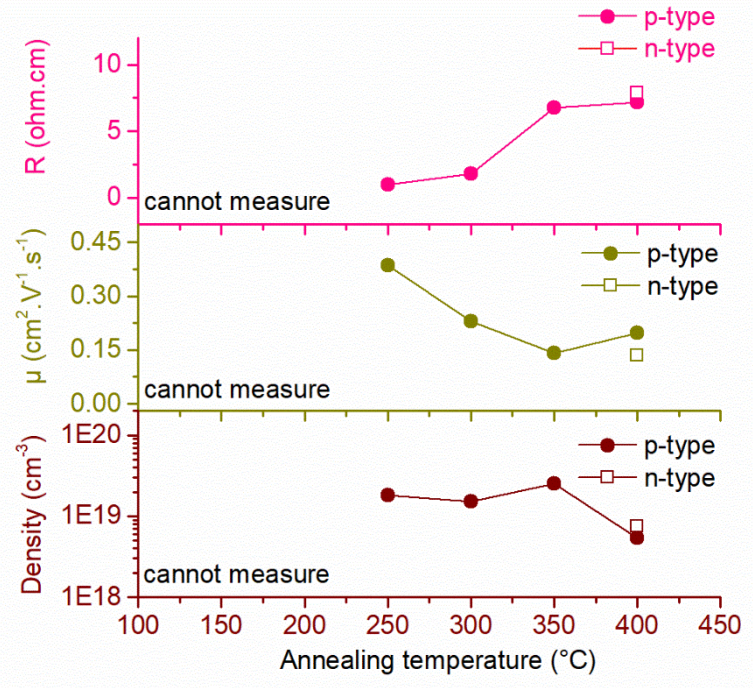

Figure V. 8 : *Resistivity (R), carrier mobility (μ) and carrier density of SnO films fabricated under RF mode versus annealing temperature.*

Figure V. 8 shows the electrical properties of SnO thin films. The resistivity increases from 0.97 Ω.cm to 7.16 Ω.cm. The mobility decreases from 0.39 to 0.14 $cm^2V^{-1}s^{-1}$ as annealing temperature varies from 250°C to 350°C, then grows slightly up to 0.20 $cm^2V^{-1}s^{-1}$ at 400°C. When SnO thin films were annealed at temperature below 400°C, p-polarity is observed, hole concentration is in the range $1.5x10^{19}$ - $2.5x10^{19}$ cm^{-3}. At 400°C, the polarity is uncertain with approximately the same concentration ($5x10^{18}$ cm^{-3}). This change in type of polarity under temperature has been explained in previous reports [137], [141], [151], [155], [163]. At low annealing temperatures, the main defects that are present are O_i and V_{Sn} that act as acceptors. Because SnO is less thermodynamically stable than SnO_2, at higher temperature (400°C here), SnO is easily transformed to SnO_2. However, XRD data in **Figure V. 5** does not record the presence of crystalline SnO_2 phase, with the

characteristic (110) peak located at 26.0°, according to JCPDS # 77-0452 [139]. At 400°C, SnO_2 cannot be completely converted or it does not exist in a crystalline form. According to XPS result of J. Huo *et al* [163], Sn^{+4} was present on the surface of the thin film after annealing at 400°C, the intensity of O-Sn^{+4} and O-Sn^{+2} are almost equal, their result is in good agreement with this study.

V.2.2.2 SnO deposition in DC mode

The DC power density was close to 0.6 W/cm^2 and the achieved sputtering rate was approximately 28 nm/min. Comparing to RF mode (see Section V.2.2.1), the sputtering rate in DC mode is twice than in RF mode. As-deposited SnO has an amorphous nature and electrical properties could not be recorded, recording so identically to the RF mode. SnO thin films was fabricated again and post-annealed at different temperatures from 100°C to 400°C with a 50°C step in nitrogen atmosphere. The annealing time was 15min and the heating-up/cooling-down rate was 100°C/min. It has to be noted that all the samples were made in a single batch, and their thickness is approximately 250 nm. Ultimately, the same fabrication process has been used for both modes!

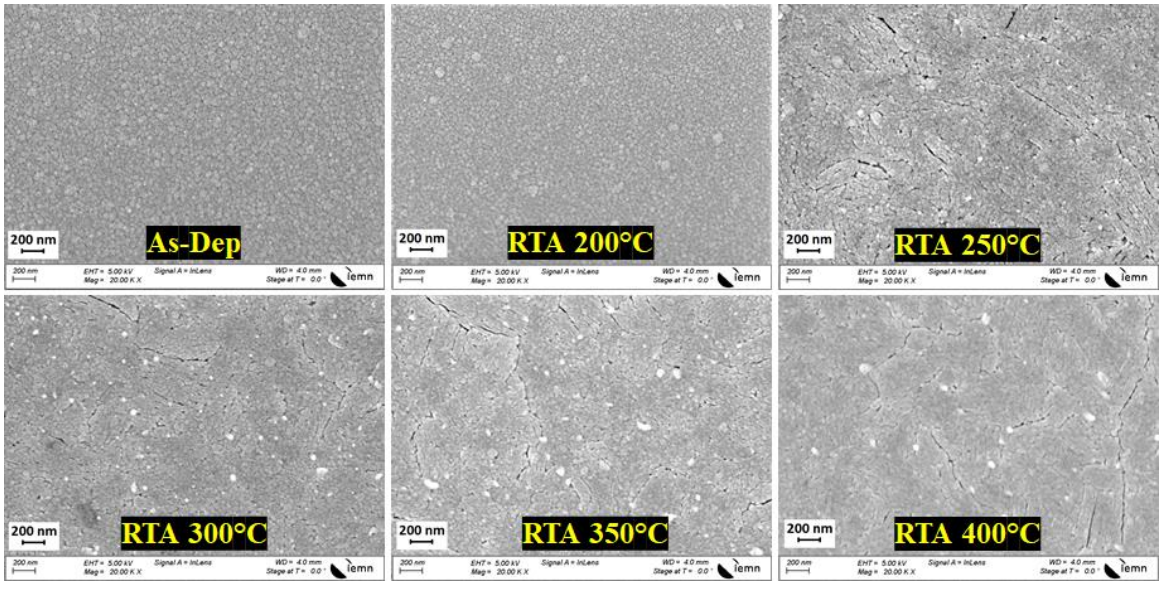

Figure V. 9 : *SEM images of SnO thin films deposited in DC mode after post-annealing treatment at different temperatures.*

Figure V. 9 illustrates the effect of the annealing process on surface morphology of the SnO thin films fabricated in DC mode. There is no significant difference between samples deposited in RF and DC mode.

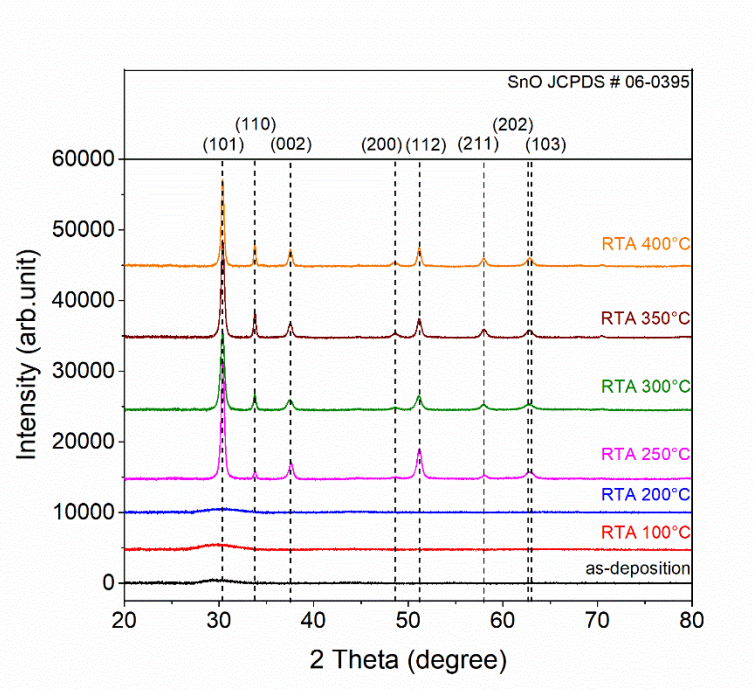

Figure V. 10 : *XRD diffractograms of SnO thin films deposited in DC mode versus post-annealing temperature.*

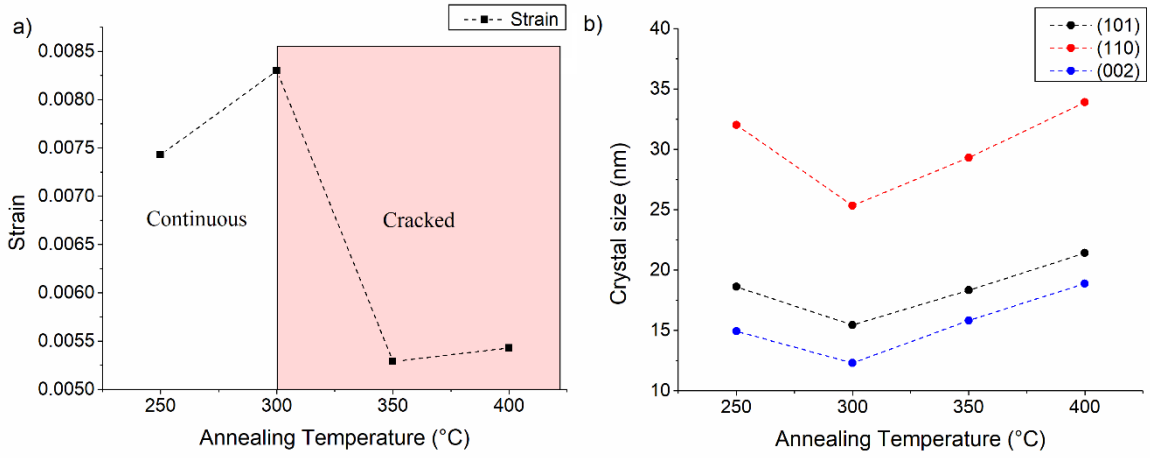

Figure V. 11 : *a) Calculated strain (ε) from XRD data and b) crystal size of (101), (110) and (002) plane of SnO fabricated on RF mode after annealing from 250°C to 400°C.*

The XRD diffractograms of **Figure V. 10** are almost the copy-paste of those obtained in RF mode presented in **Figure V. 5** and same conclusions can be drawn. Consequently, the strain and lattice parameters (**Figure V. 11**) show also the same trend than in RF mode with perhaps some very slight lower values.

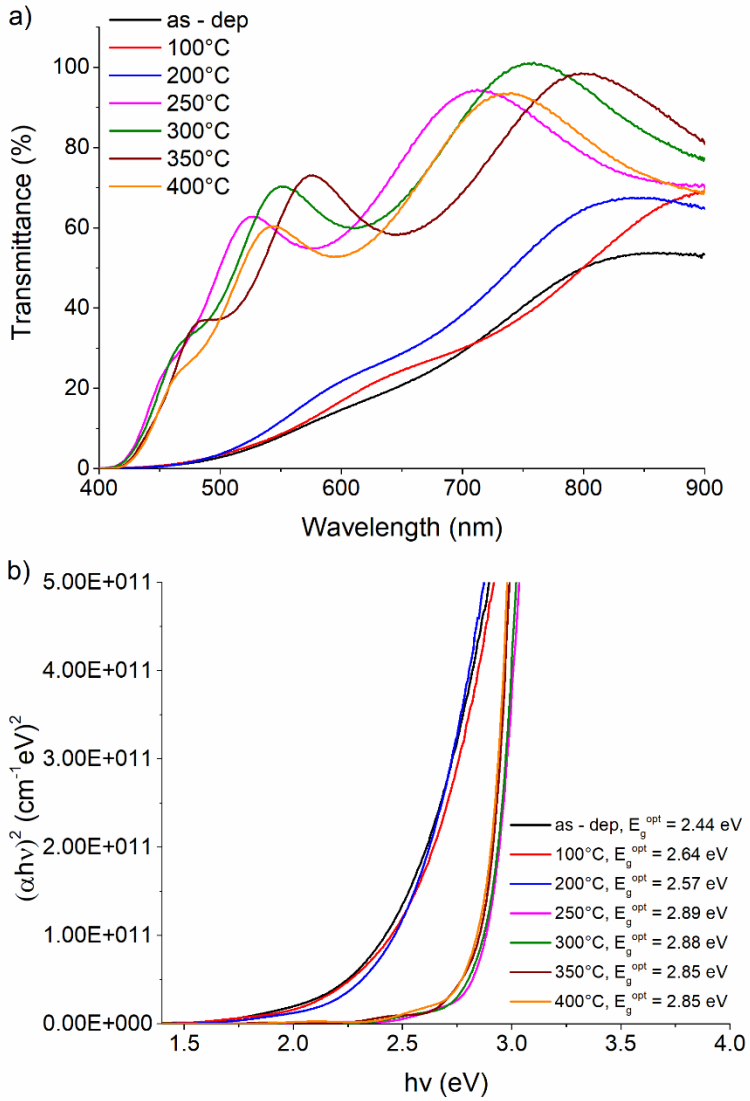

Figure V. 12 : *UV-Vis result of of SnO fabricated on DC mode and after annealing from 100°C to 400°C: a) Transmittance vs. wavelength spectra, b) Optical gap calculated using Tauc's equation.*

Figure V. 12 shows transmittance results and corresponding optical bandgap of SnO thin films deposited in DC mode. The change in properties due to the amorphous-crystalline

transition appearing around 200°C is clearer than observed on RF mode-deposited samples. The largest optical band gap is obtained at annealing of 250°C and is equal to 2.89 eV. It should correspond to the crystallization of the film before phase modification occurs at higher temperature.

The electrical properties (**Figure V. 13**) have rather the same behavior as obtained in RF mode except that whatever the case, p-type polarity is always recorded.

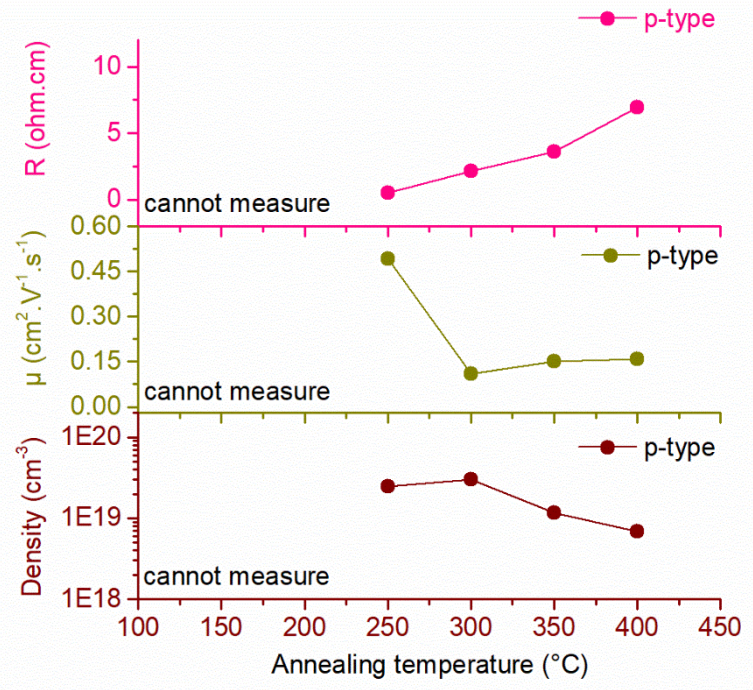

Figure V. 13 : *Resistivity (R), carrier mobility (μ) and carrier density of SnO films fabricated under DC mode versus annealing temperature.*

V.3 **Discussions and partial conclusions:**

- *AZO thin film*

The deposition process of AZO was previously set in IEMN, so we did not go into details the factors affecting the properties of AZO thin film in this study. The AZO thin film fabricated by DC magnetron sputtering shows a very high optical transmittance (approx. 97%) and good crystallinity. In addition, the electrical properties are promising ones for the potential use of AZO thin film as a n-type transparent conductive electrode for a solar cell. We will use in the next chapter, AZO films made in DC mode (80W applied power) without any post-annealing treatment and exhibiting a bandgap value of 3.3 eV.

- *SnO thin film*

The SnO thin films were fabricated in RF and DC mode, the as-deposition samples and those annealed at low temperature (< 250°C) show amorphous nature. At high annealing temperatures, cracks appear and the surface of the thin film is no longer homogenous (see **Figure V. 4** and **V. 9**), but the XRD shows only the crystalline phase of SnO, according to JCPDS # 06-0395 (see **Figures V. 5** and **V. 10**).

- In RF mode: When the annealing temperature increases, the transmittance and the optical bandgap increase (see **Figure V. 7**), the maximum transmittance (96%) and optical bandgap 2.90 eV are obtained for post-annealing temperature of 300°C. The majority charge carriers change from holes to electrons as the annealing temperature reaches 400°C (see **Figure V. 8**).
- In DC mode: Almost the same trend concerning the optical properties versus annealing temperature (see **Figure V. 12**) is obtained with a maximum transmittance (100%) for post-annealing temperature of 300°C. The highest optical bandgap value is obtained for sample annealed at 250°C and the majority charge carriers is always recorded as p-type (see **Figure V.13**).

There are very few reports on the selection of p-type layer to create p-n junction with $ZnSnN_2$. n-$ZnSnN_2$/p-SnO heterojunction has been published by K. Javiad *et al* [49], [83] but no detailed information was given on the used SnO material. Based on above results we selected a process in DC mode (50W applied power) with a post-annealing treatment at 250°C and exhibiting a bandgap value of 2.9 eV.

In this chapter, we will examine the photoelectric properties of $ZnSnN_2$ by constructing 2 photodetection structures such as reported by Dharmadasa *et al* [164] (**Figure V. 1)**. In the hereafter denominated *Structure1*, aluminum doped zinc oxide (AZO) was used as wide bandgap n-type layer and transparent electrode and Ti/Au as backside metallic electrode. Such a configuration amounts to a photoconductor design. In *Structure2* , a p-n junction structure is made using a p-type tin oxide (p-SnO) or p-doped silicon (p-Si), as done by Javaid *et al* [49], [83] and Quin *et al* [48], respectively. This structure corresponds to a photodiode design.

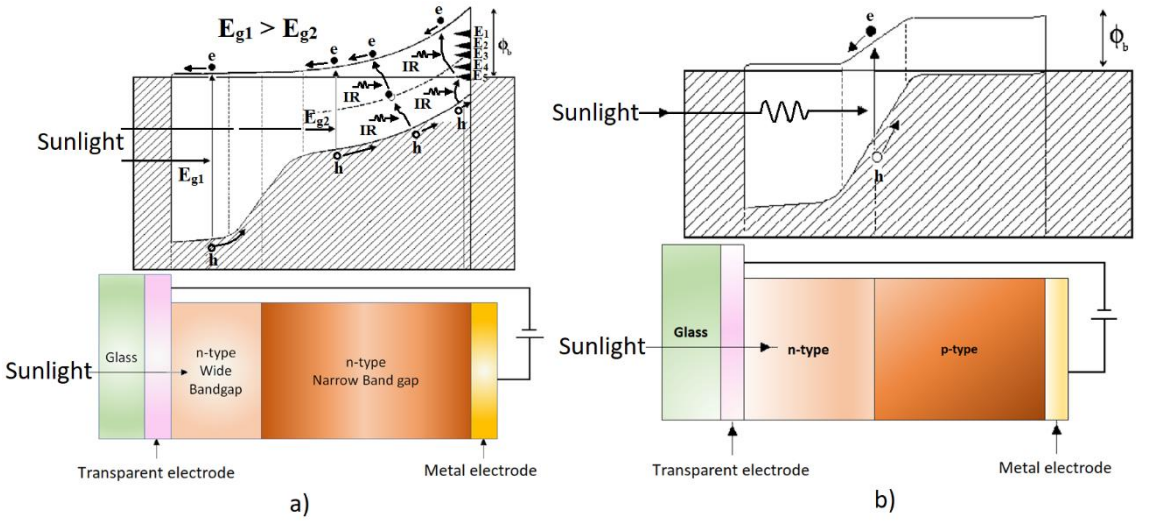

Figure VI. 1: *The energy band diagram (on top) and device structure (on bottom) of: a) photoconductor (Structure1) and b) photodiode (Structure2)* [164].

The optoelectronic properties were determined using a 2 probes Oriel Sol3A Solar Simulator under AM1.5 illumination conditions.

VI.1 Structure 1 - Photoconductor

VI.1.1 First attempt: overview of the fabrication process

All samples have been fabricated on Eagle XG substrate (1 inch x 1 inch). The 20nm-Ti/300nm-Au back contact was deposited by evaporation on a cleaned substrate. Following, the 300 nm-thick $ZnSnN_2$ film was deposited at room temperature, working pressure of 0.02 mbar, N_2/Ar ratio of 2.0, power feeding of 25W-DC and 40W-RF for Zn and Sn targets respectively ($Zn_{DC}Sn_{RF}$ series, see Section IV.1.1) and sputtering time of 30 minutes. EDS measurement shows the obtained thin film was slightly Sn-rich, x was equal to 0.47. Obtaining stoichiometry (x = 0.5) is always touchy by the change in effective surface area of target after using it for a while (mentioned in Section II.3.1) although regular calibration tests are conducted. Finally, the 300 nm of AZO layer was deposited on top using the deposition process presented in Section V.1.2. The main steps of the fabrication process are presented in **Figure VI. 2**.

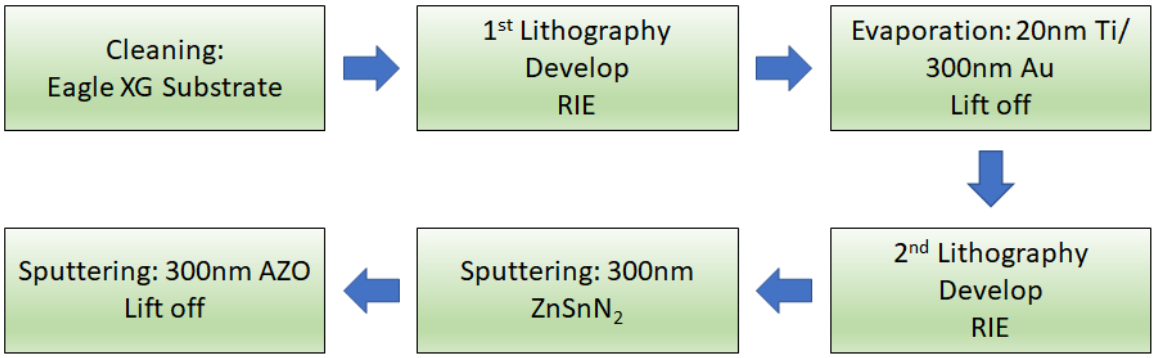

***Figure VI. 2**: Schematic process flow for the fabrication of $ZnSnN_2$ Structure1 device*

Figure VI. 3a describes a schematic cross-section of Structure1 device. The probe positions of solar simulator are on Au and AZO layers. **Figure VI. 3b** shows the top view of *Structure1.1* samples (first fabrication run of *Structure1* devices): the active area of cells is varied from 0.05 to 0.25 cm^2. The SEM cross-sectional view of the structure and particularly the $Zn_{0.47}Sn_{0.53}N_2$/AZO bi-layer is shown in **Figure VI. 3c**. The columnar structure seems to be continuous between the two films. The AZO film appears dense and previously observed voids can be seen into the $ZnSnN_2$ film. The slight lattice mismatch, smaller than 5% [110]–[112], and the columnar growth of both films could explain this

phenomenon. In this study, c parameter of $Zn_{0.47}Sn_{0.53}N_2$ is approx. 5.50 Å (see Figure IV. 3), it is close to c parameter of AZO (5.20 Å), according to the result in Section V.1.2. The evaluated lattice mismatch Δc/c equals to 5.4%. It has to be noted that the AZO layer was deposited immediately after the $Zn_{0.47}Sn_{0.53}N_2$ film, in the same deposition chamber without any exposure to ambient atmosphere.

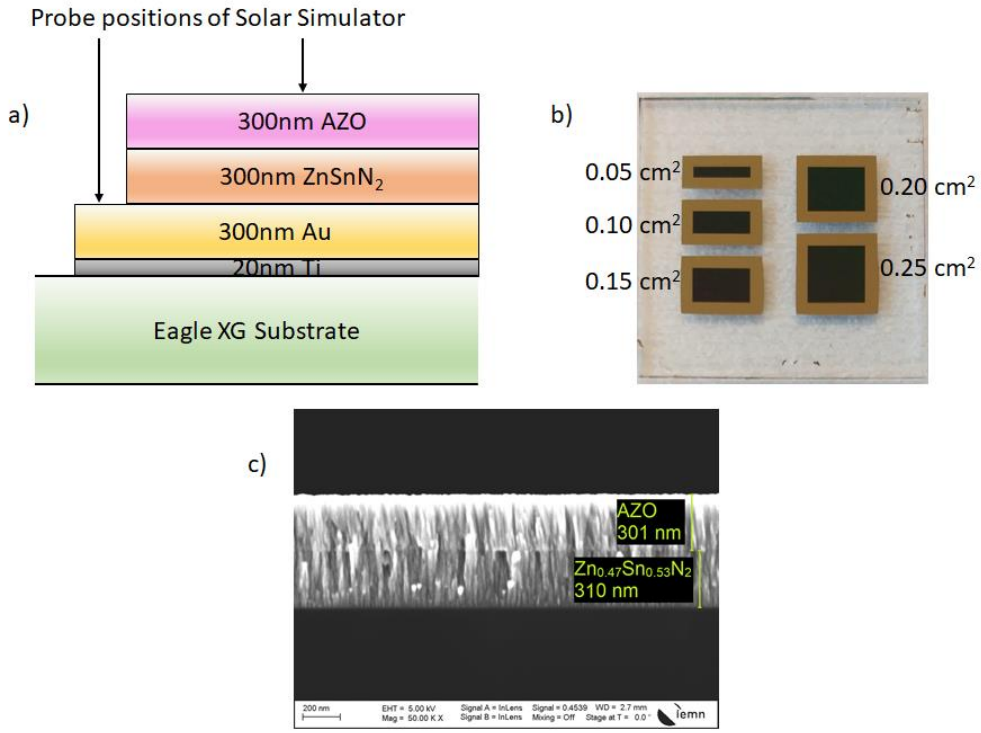

Figure VI. 3*: Structure1.1 (first fabrication run): a) Schematic cross-section b) Top view of fabricated devices with surface areas from 0.05 cm² to 0.25cm² and c) Cross-sectional SEM view*

The electrical characterization of *Structure1.1* samples is showed in **Figure VI. 4**; as this device reacts as a photoconductor, no sign of a rectifier behavior is awaited. Nevertheless, the dark J-V curve is asymmetric due to the two different materials that are used as electrical contacts. A particular behavior is observed since the current density is not constant, it decreases as increasing the cell surface area. In other words, the dark current only varies slightly with the surface area.

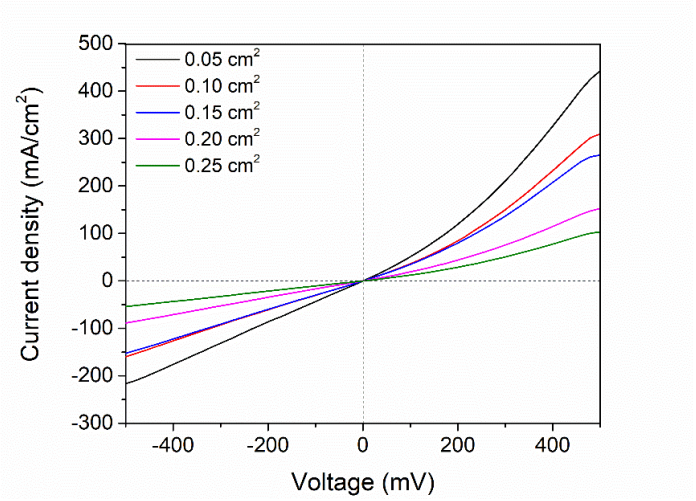

Figure VI. 4*: Dark J-V curves of Structure1.1 devices versus their active surface area, from 0.05 cm^2 to 0.25 cm^2*

The *Structure1.1* samples were illuminated under 1-sun AM 1.5 (100mW/cm^2) during 20s at room temperature. The obtained J-V curves are shown in **Figure VI. 5a**. The photocurrent density obtained after illumination can be defined by equation (6.1):

$$J_{Ph} = J_{AM1.5} - J_D \qquad (6.1)$$

where J_{Ph} is the photocurrent density, J_D is the dark current density (**Figure VI.4**) and $J_{AM1.5}$ is the current density under illumination (**Figure VI.5a**).

The current under 1 Sun illumination as the photocurrent values obtained following Eq. 6.1 versus cell area are illustrated in **Figure VI. 5**. When the cell area increases, the photocurrent density at 500 mV reduces from 218 to 2.9 mA/cm^2, approx. two orders of magnitude. The qualitative behavior is so the same that for the dark current density but the quantitative behavior is strongly different (roughly one order of magnitude higher). Beside that the J_{Ph}/J_D ratio decrease from 0.58 to 0.036.

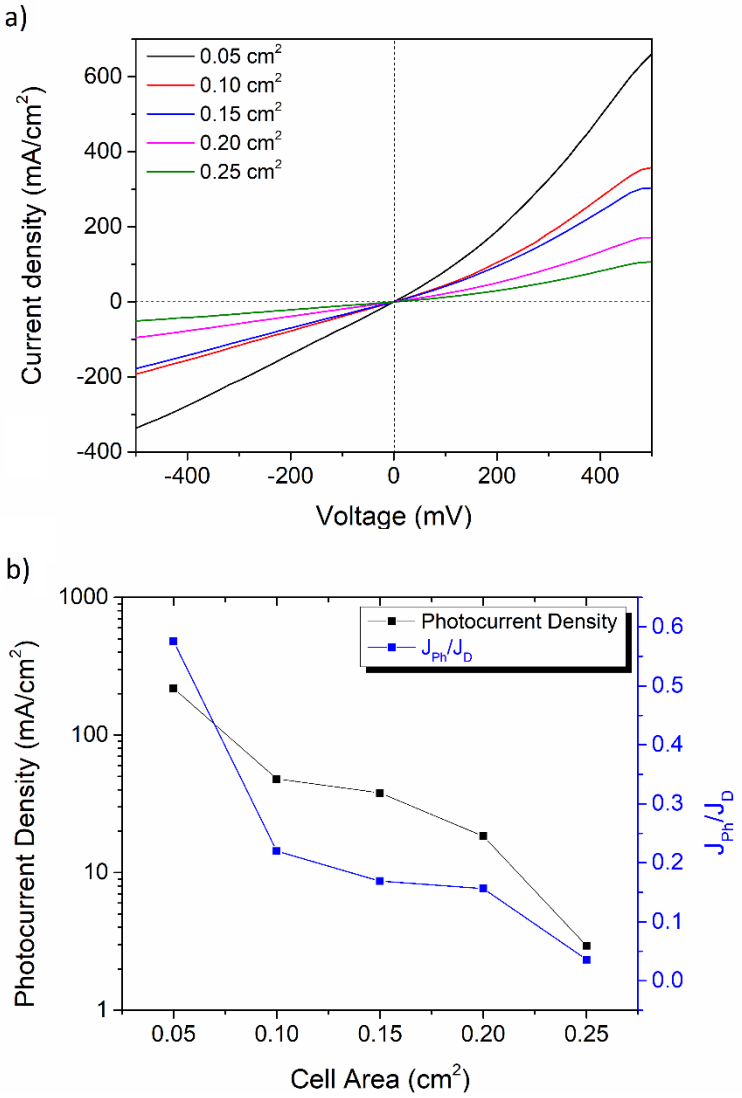

Figure VI. 5: *Structure1.1 samples a) J-V curve under 1-sunAM1.5 solar spectra illumination (100 mW/cm^2) at room temperature, b) J_{Ph}/J_D average and photocurrent obtained at 500mV versus cell area*

According to these results, 0.05 cm^2 surface area allows achieving the highest photocurrent values, so we will use this size for the next fabrication run (*Structure1.2*).

VI.1.2 Second fabrication run

VI.1.2.1 Effect of x value

So, for this second fabrication run, only 0.05 cm^2 surface area samples have been fabricated, the overall fabrication process is the same than for *Structure1.1* devices (see section VI.1.1), except the power supplied to the target Sn that has been varied in order to achieve the different compositions (see **Table VI. 1**). We are so still in a $Zn_{DC}Sn_{RF}$ series sweeping from Zn rich (x> 0.5) to Sn rich (x< 0.5) samples. Each sample consists of 9 elementary cells of same composition, 5 samples have been so made in order achieving the different compositions.

Table VI. 1: Change in x value by adjusting the plasma power of Sn target (x value is obtained from EDS measurements)

Sn Power (W)	Time (min)	Thickness (nm)	x
25	40	290	0.58
35	33	305	0.50
40	30	310	0.47
55	23	301	0.34
70	19	298	0.26

Figure VI. 6 shows a schematic cross-section of *Structure1.2* samples as the result of their fabrication on Eagle XG substrate, the active area of each cell is 0.05 cm^2.

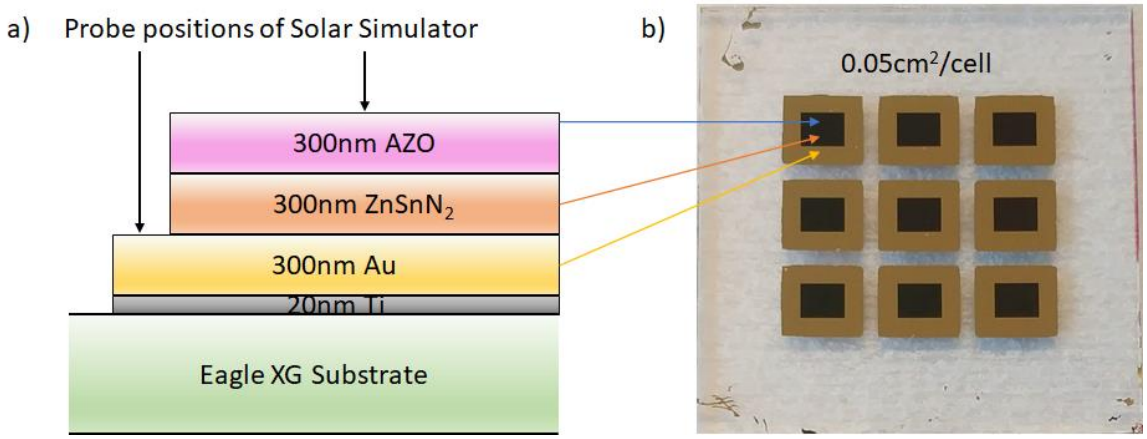

***Figure VI. 6**: a) Cross-section and b) Final view of Structure1.2 devices (0.05cm^2 cells).*

The dark J-V curves are shown in **Figure VI. 7a**: comparing to results presented in **Figure IV. 4**, the trend of dark current density seems to follow the resistivity values that were determined by Hall effect, i.e. as x value equals to 0.58, 0.34 and 0.26, the dark current density at 500mV ranges in the order of 10^{-1} mA/cm^2, whereas when x equals to 0.50 and 0.47, it reaches 15 and 257 mA/cm^2, respectively. Those ranges correspond respectively to high and low resistivity ranges presented on **Figure IV.4**, nevertheless, comparison stops there and only this qualitative observation can be made since one order of magnitude on resistivity value was recorded for longitudinal transport devices (**Figure IV. 4**) and almost two are recorded here for these transverse transport devices. Besides that, the dark current density obtained on *Structure1.1* samples is twice higher than on *Structure1.2* samples (for x = 0.47). No particular explanation for that change can be given except the variability of material properties between different fabrication runs.

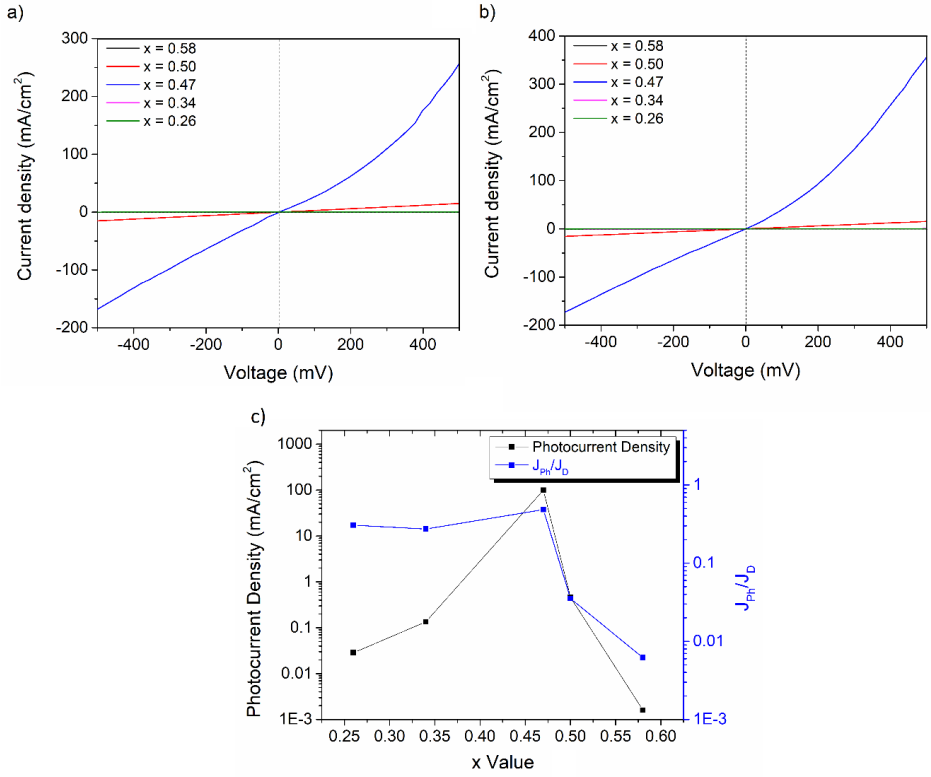

Figure VI. 7: *Structure1.2 samples a) dark J-V curves, b) J-V curves under 1-sun illumination and c) photocurrent density and J_{Ph}/J_D values (averaged values other the 9 devices of same x composition @ 500mV bias)*

After illumination (**Figure VI. 7b,c**), the J-V does not significantly change for x = 0.58. For x = 0.50, the photocurrent density is 0.46 mA/cm^2 and the J_{Ph}/J_D ratio is low, approximately 0.03. The value for x=0.47 is indisputably better since photocurrent density reaches more than 100 mA/cm^2 with a J_{Ph}/J_D ratio close to 0.6: those two values being very similar to those of 0.05 cm² *Structure1.1* cells (see **Figure IV. 5**). The photocurrent density decreases from 98.9 to 0.029 mA/cm^2 when x value reduces from 0.47 to 0.26. Jointly the J_D values follow almost the same decrease and the J_{Ph}/J_D ratio does not change dramatically and ranges between 0.30 and 0.48.

VI.1.2.2 Effect of rapid thermal annealing:

The *Structure1.2* samples ($0.26 < x < 0.47$) were then annealed at 300°C in pure N_2 atmosphere (300 sccm) during 15 minutes. The electrical contact can no more be achieved for x = 0.26 and 0.34 samples, so the photoelectrical characterization has not been carried out. For x = 0.47, dark J-V curves (**Figure VI. 8a**) exhibits more than one order of magnitude higher values than as-deposited samples. Otherwise, the photocurrent density increases only 2 times after annealing. The same trend than observed in previous paragraph when varying the x parameter can be made: if we refer to results presented in **Figure III. 18**, the resistivity of the film is one order of magnitude lower after a 300°C anneal that corresponds to the observed increase of the dark current density. On the contrary, this order of magnitude is lost on the photoelectric properties since the J_{Ph}/J_D is equal to 0.06 for the annealed sample (it was 0.6 for the as-deposited sample).

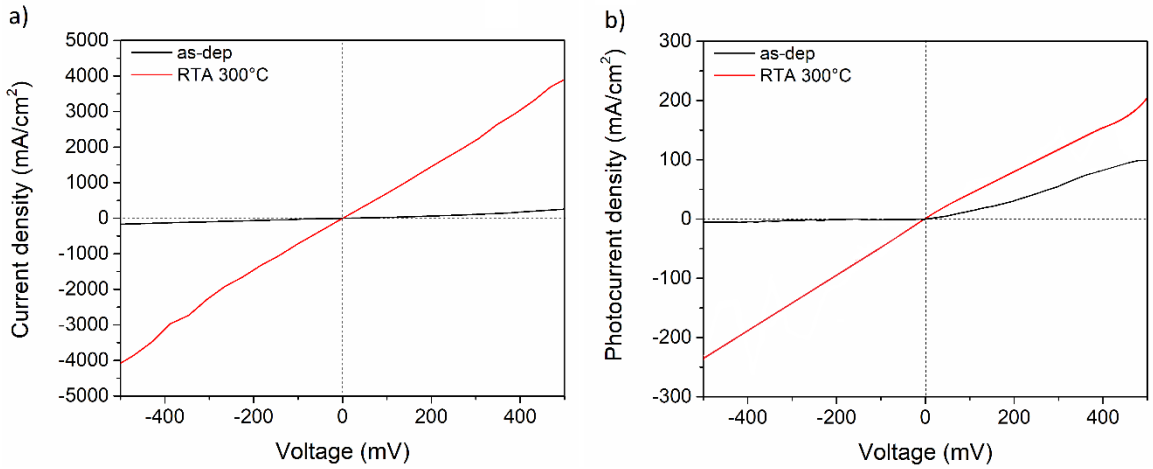

Figure VI. 8: *Structure 1.2 (x= 0.47). a) Dark J-V curve, b) J_{Ph}-V curve under 1-sun illumination after annealing at 300°C in N_2 atmosphere during 15 minutes.*

VI.1.3 Symmetric AZO/ZnSnN$_2$/AZO structure

The high dark current density obtained, on which the band diagram arrangement or interface behaviors can possibly affect, is not really compatible with photovoltaic applications. Material deposition scheme can also be different depending on which substrate it is deposited, especially if base material is also a PVD deposited material with a columnar structure. In this *Structure1.3*, we replaced the back Ti/Au metallic contact by another AZO layer deposited the same way the top AZO layer. The follow-up of the fabrication process flow is identical to Structure 1.2 devices.

Figure VI. 9 shows a schematic cross-sectional view of *Structure1.3* and final view of fabricated samples on Eagle XG substrate. The active area of elementary cells is 0.05 cm^2. Therefore, except the bottom electrode deposition process, all other fabrication and deposition steps were conducted in the same conditions that in Section VI.1.2. Samples were post-annealed at 300°C in N_2 atmosphere during 15 minutes.

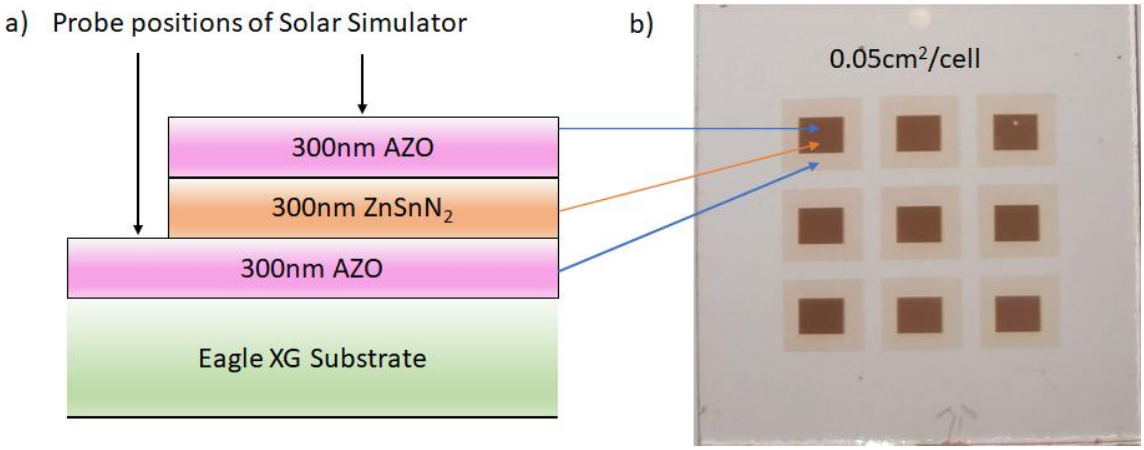

Figure VI. 9: *Structure1.3 a) Schematic cross-section and b) Final view of the 0.05cm^2 surface area samples.*

The dark J-V curve of *Structure1.3* samples (for x = 0.47) is shown in **Figure VI. 10a**. At 500mV, the dark current density is approximately 5 times lower than *Structure1.2* (at same composition). After annealing, the dark current density reduced 2 times in opposition to the result obtained when using Ti/Au as bottom electrode. It can also be observed that using two identical contacts, the J-V curve is now almost symmetric. Under solar illumination, the obtained J_{Ph}-V curve (**Figure VI. 10b**), the J_{Ph}/J_D ratio is equal to 0.5 and 0.64 for the as-deposited and annealed samples, respectively. Contrary to *Structure1.2* devices, the post-anneal does not destroy the J_{Ph}/J_D ratio and even improves it by roughly 30% by a larger decrease of dark current density

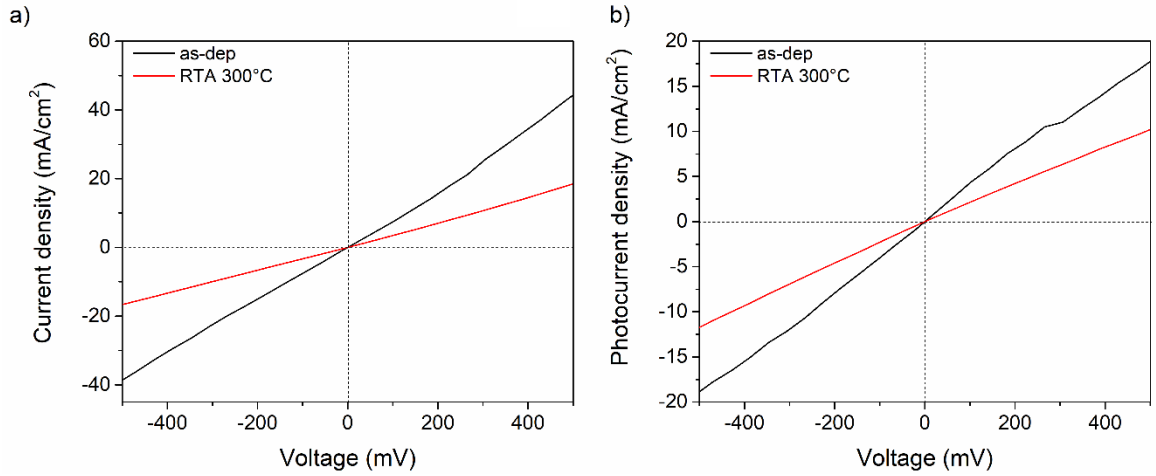

Figure VI. 10: *a) J-V characterization of Structure1.3 samples (x=0.47) dark conditions and b) J_{Ph} -V curve under 1-sun AM1.5 solar spectra illumination for as-deposited and post-annealed-samples.*

From those results, we can conclude that the annealing process does not affect the AZO/ZTN/AZO structure and even helps to improve the photoelectrical properties of the device. The opposite phenomenon that was observed after annealing in section VI.1.2.2 may originate from the Ti/Au electrode. According A. Hiraki [165], [166], at low temperature or even at room temperature, gold can diffuse into semiconductors that have a bandgap smaller than 2.5 eV and dielectric constant higher than 8. By experiment result (see **Figure IV. 5**), obtained optical bandgap is approx. 2.0 eV, and dielectric constant of $ZnSnN_2$ was reported higher than 11 by T. Paudel *et al* [19]. In addition, in the temperature range 135 – 225°C, gold diffuses in tin by an interstitial mechanism, published by B. Dyson [167]. So, we can reasonably hypothesize that gold diffused into the $ZnSnN_2$ layer during the annealing process.

VI.1.4 Effect of device structure and electrode distance

All along the parametric studies that are reported in Chapters II to IV, the photoelectric characterization was made on "simple" devices, i.e., the ones used for Hall measurements (see **Figure II. 8**). No particular electrodes were used, no technology steps used, only the material layer with some indium balls for contacting. This photoelectric characterization is not reported in those chapters since we never succeeded collecting the least photocurrent!

Almost all devices reported in this chapter have a completely different structure since by using the above-mentioned technological processes, the carrier transport is now in the transverse direction (direction of material deposition) instead of a longitudinal one:

- 1) it corresponds to the configuration that would be used in a potential PV application,

- 2) it is done, along the film thickness, i.e., 300 nm and no more between two surface contacts that were distant by at least 1 cm in previous chapters.

To check the effect of carrier transport direction, *Structure1.4* was fabricated. It consists of a device structure with two top AZO contacts separated by 100µm. This distance is still far away from the 300nm corresponding to the layer thickness but is much closer than the 1 cm of previous longitudinal configurations. Deposition processes of $ZnSnN_2$ and AZO layers were unchanged as compared to *Structure1.3* samples. A schematic cross-sectional structure and final view of *Structure1.4* on Eagle XG substrate are illustrated on **Figure VI. 11**

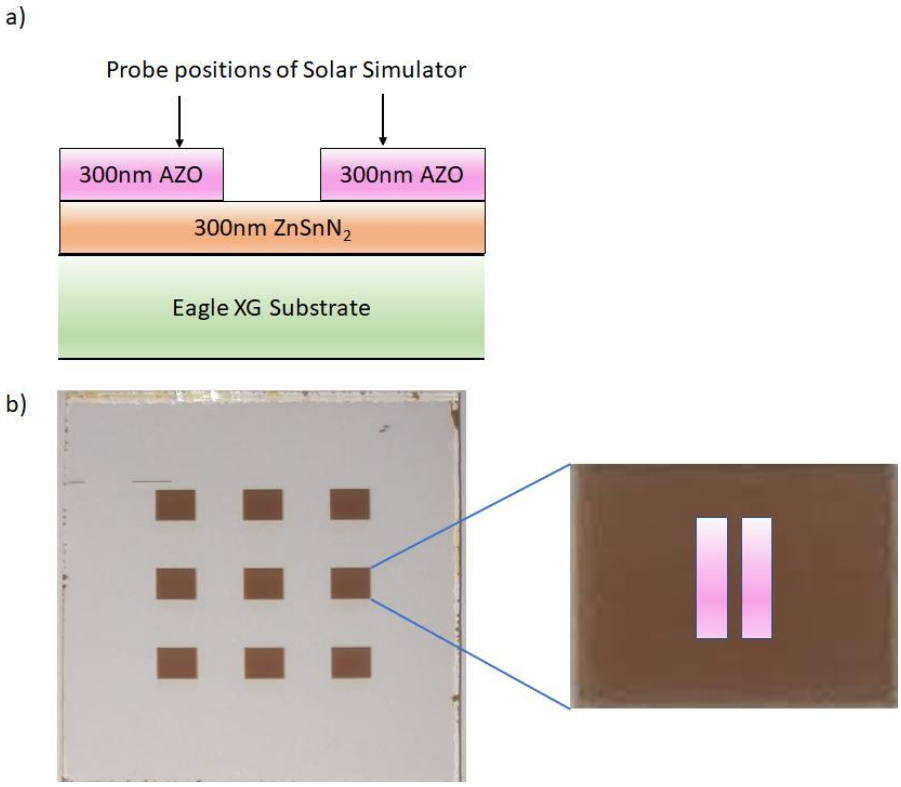

Figure VI. 11*: Structure1.4: a) Schematic cross-section and b) final view of 0.05cm² surface area samples.*

The dark J-V curve of *Structure1.4* (x = 0.47) is shown in **Figure VI. 12a**. At 500mV, the dark current density of as-deposited sample is more than one order of magnitude higher than corresponding (at same composition) *Structure1.3* sample. After annealing, the dark current density reduced, i.e., same overall behavior than for *Structure1.3,* but here by almost one order of magnitude. The J_{Ph}-V curves obtained under illumination (**Figure VI. 12b**) exhibit the same behavior than for *Structure1.3:* an increase close to 30% is observed for the post-annealed devices with a J_{Ph}/J_D ratio equal to 0.15 versus 0.12 for the as-deposited samples. Comparing *Structure1.3* and *Structure1.4* samples, the J_{Ph}/J_D ratio decreases 4 time for both as-deposited and annealed-samples. However, the carrier transport distance increases from 300nm to 100µm and the carrier transport direction modifies from transverse to parallel.

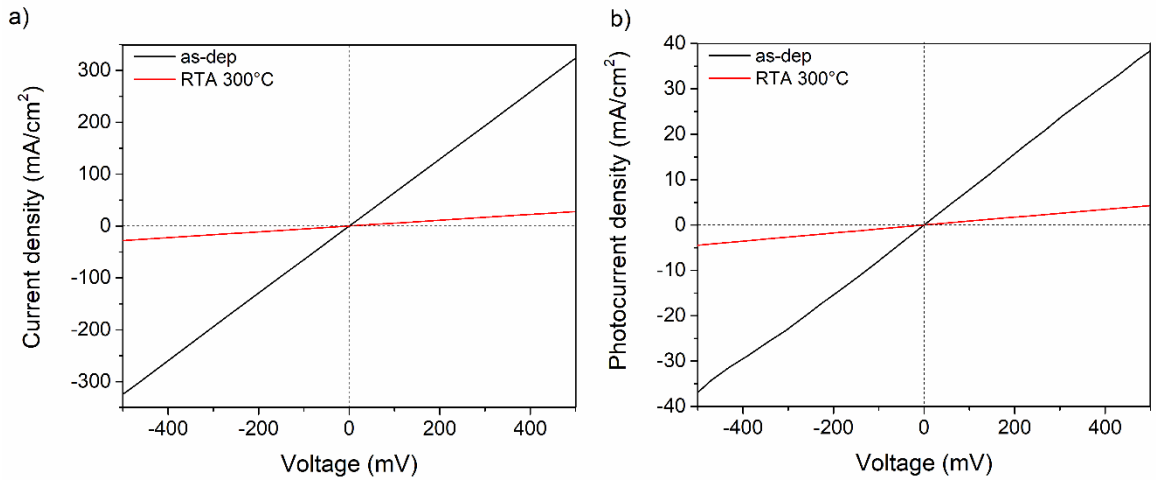

Figure VI. 12: *a) Dark J-V characterization of Structure1.4 samples, b) J_{Ph} – V curve under 1-sun illumination for as-deposited and post-annealed-samples.*

Right now, it is difficult to discern the influence of the distance and direction of carrier transport on the modification of the electric and photoelectric properties of the films. So, specific samples have been fabricated and sent to one partner of the OPERA project, the Laboratoire de génie électrique de Paris (GeePs), for characterization. This will be discussed in the next section.

VI.1.5 Conductivity measurements in transverse and longitudinal electrode configurations

All samples have been fabricated on Eagle XG substrate (1 inch x 1 inch). The 300 nm of $ZnSnN_2$ was deposited in $Zn_{RF}Sn_{DC}$ mode at room temperature, the working pressure was 0.02 mbar, the N_2/Ar ratio was fixed at 2.0, 30W-RF and 50W-DC were used for Zn and Sn target power feeding. The thin film composition was measured by EDS and exhibited an x value of 0.48. AZO and Ti/Au were fabricated in the same parameters as in Section VI.1.1, the main steps of fabrication process are presented in **Figure VI. 13**.

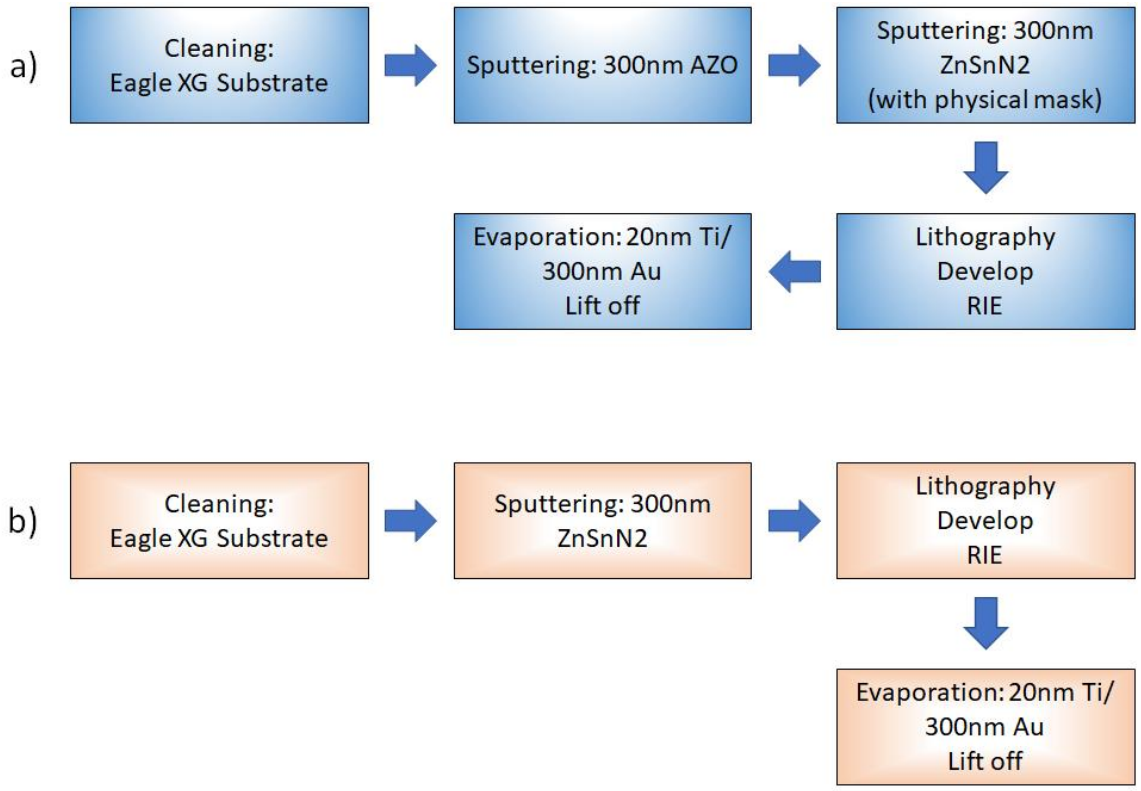

***Figure VI. 13**: Schematic process flow of samples a) Structure1.M1 and b) Structure1.M2*

The top and cross-sectional views of *Structure1.M1* and *Structure1.M2* samples are described in **Figure VI. 14**. It can be noticed that, contrary to the *Structure1.1*, the metallic electrode composed of Ti/Au allows in this configuration to prevent Au diffusion in the $ZnSnN_2$ layer using the Ti layer. The configuration of the *Structure1.M1* samples allows conductivity measurement in the transverse direction, using the bottom AZO layer

meanwhile *Structure1.M2* sample configuration allows measurements in parallel transport across different lengths.

Different Structure1.M1 samples were fabricated, under N_2/Ar atmosphere (labelled RT on **Figure VI. 15a**), under N_2-H_2/Ar atmosphere (labelled 2% on **Figure VI. 15a**) and under N_2/Ar atmosphere at 300°C (labelled 300°C on **Figure VI. 15a**) but material of both configurations were deposited in the same fabrication run. Structure 1.M2 samples are mentioned as "coplanaire" on **Figure VI. 15b**.

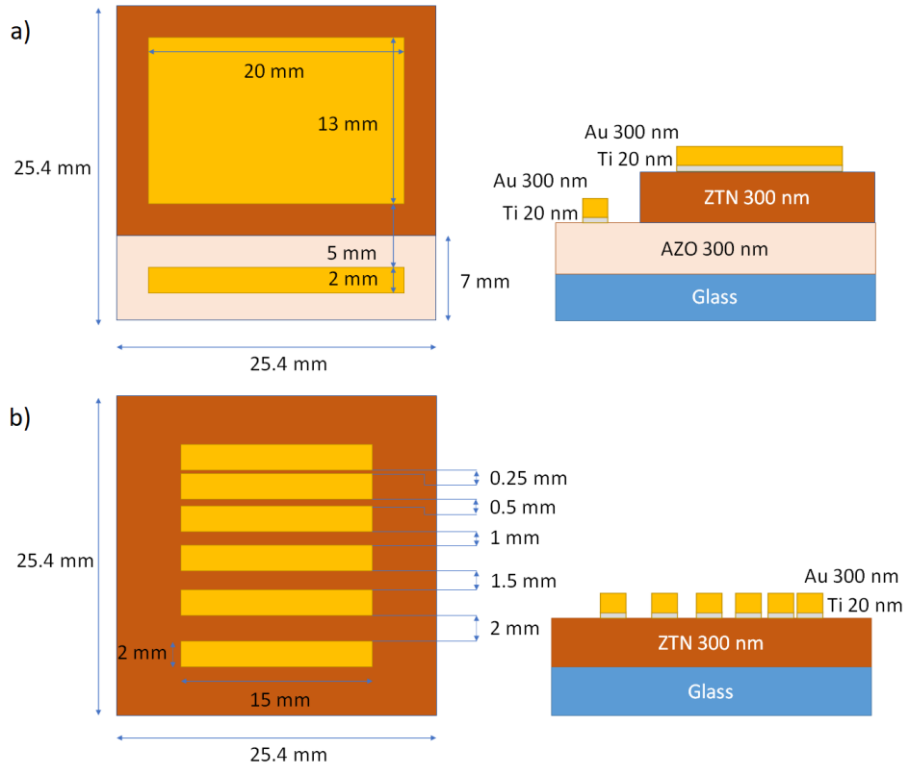

Figure VI. 14: *Top (left) and cross-sectional (right) views of a) Structure1.M1 and b) Structure1.M2 samples.*

GeePs colleagues have measured the variations of the dark conductivity of samples under vacuum and temperature varying between ambient up to 245°C and back to 25 °C (**Figure VI. 15**). Regardless the material deposition conditions are, the conductivity of transverse transport samples (*Structure1.M1*) is almost constant with temperature and is between 2 and 3 x10^{-6} S/cm. The conductivity obtained on the return way to ambient temperature is

slightly higher indicating that material conductivity has been slightly modified by the temperature increase (even for the one that was deposited at 300°C). The main difference is observed by comparison to the measurements carried out on the lateral transport samples (*Structure1.M2*) that exhibit a conductivity value 10^6 order of magnitude higher. The large difference in conductivity value that is measured on transverse and lateral configurations shows that the electrical properties of $ZnSnN_2$ strongly depends how the carrier transport is.

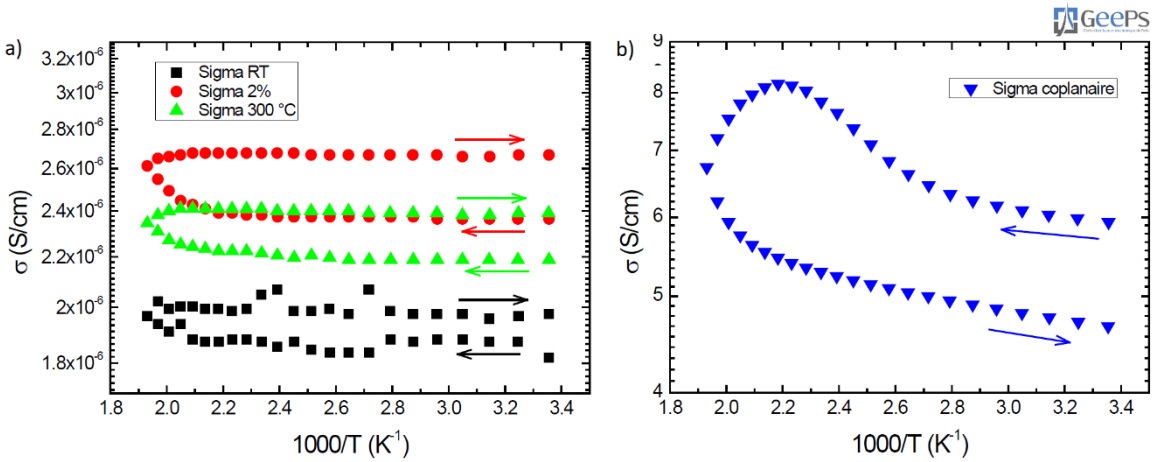

Figure VI. 15: *Conductivity versus temperatures varying between 25°C up to 245°C of a) transverse conduction samples (Structure1.M1) and b) longitudinal conduction (Structure1.M2) samples (2mm electrode spacing). (data obtained by GeePs researchers)*

Figure VI. 16 shows the conductivity value measured on longitudinal transport samples (*Structure1.M2*) for the different electrode spacings that were made 0.25, 0.5, 1, 1.5, and 2 mm. No significant, at least in comparison with values obtained for the *Structure1.M1* samples, was pointed out for the different electrode spacings.

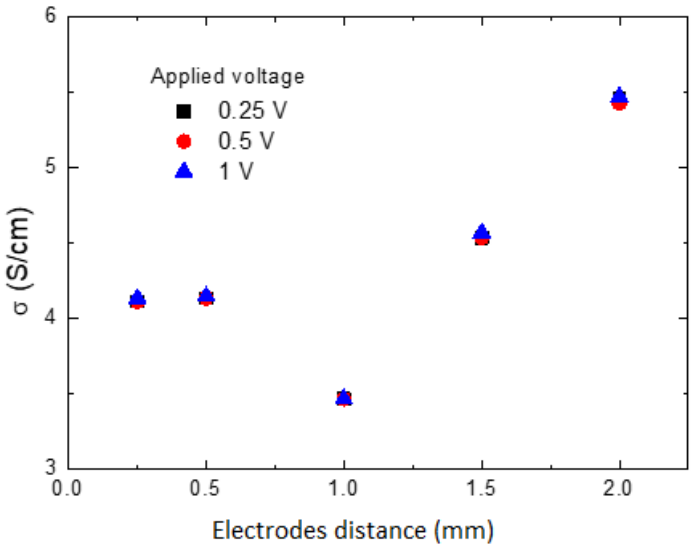

Figure VI. 16: *Conductivity versus electrode spacing for lateral transport samples (distance of Structure1.M2). (data obtained by GeePs researchers)*

From all results obtained on *Structure1* samples, it appears that:

- lateral and transverse conduction properties are completely different. Up to now, the presence of a thin film of conductive oxide, linked to oxygen incorporation during deposition might be an explanation for the high conductivity values reported in longitudinal transport devices,

- only transverse transport samples exhibited photodetection capabilities.

It appears then that material characterization shall also be conducted on transverse conduction devices that compels technology to be done to get the right electrode configuration. So, a longer study would be required comparing to just depositing a thin film.

VI.2 **Structure2: Photodiode**

VI.2.1 p-SnO/ZnSnN$_2$ hetero junction

VI.2.1.1 Fabrication of ZnSnN$_2$ in Zn$_{DC}$Sn$_{RF}$ mode:

In this section, SnO thin film was deposited on Eagle XG first following the fabrication process described in Section V.2.2.2. Deposition time was 18 minutes and the sample was post-annealed at 250°C in N_2 atmosphere during 30 minutes. Then $ZnSnN_2$ thin film was deposited at room temperature during 12.5 minutes, the working pressure was 0.02 mbar, the N_2/Ar ratio was fixed at 2.0, 24W-DC and 80W-RF were used for Zn and Sn target, respectively. The EDS measurement of only the $ZnSnN_2$ layer deposited on glass displayed slightly a Sn-rich material with a x value of 0.48. Next step consisted in the sputtering deposition of 300 nm of AZO which deposition process was presented in Section V.1.2. Finally, 20 nm of Ti and 300 nm of Au were evaporated as electrode contacts. The main steps of fabrication process are presented in **Figure VI. 17**.

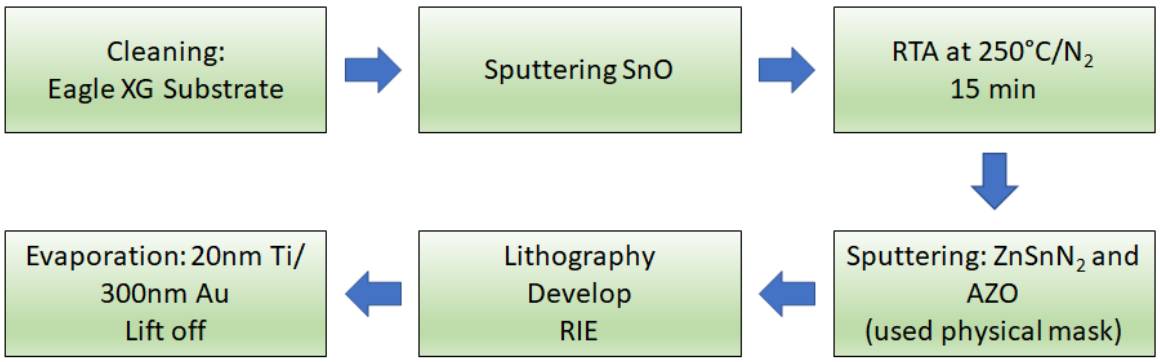

Figure VI. 17: *Schematic process flow of p-SnO/ZnSnN$_2$ heterojunction structure.*

The design parameters of fabricated samples are shown in **Figure VI. 18a, b**. According to cross-sectional SEM image (**Figure VI. 18c**), the thickness of SnO, $ZnSnN_2$ and AZO layers are 610 nm, 290 nm and 285 nm, respectively. These three layers are tightly arranged, with no signs of peeling.

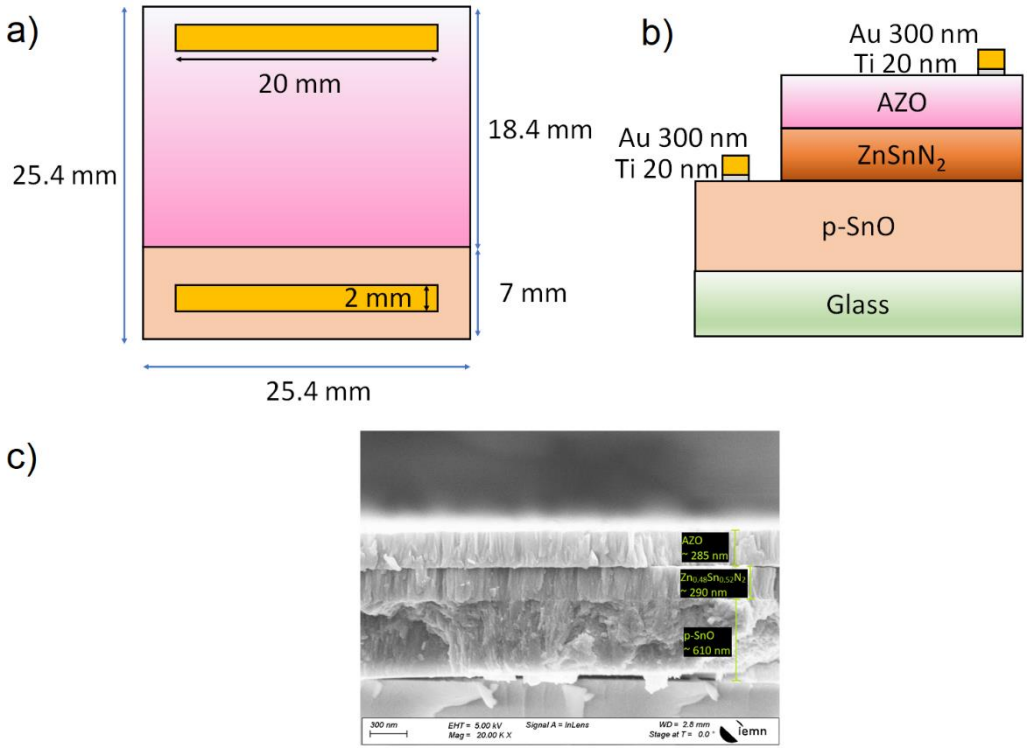

Figure VI. 18: *Structure2.1 sample with $Zn_{0.48}Sn_{0.52}N_2$ fabricated in $Zn_{DC}Sn_{RF}$ mode: a) Top design b) Cross-section design and c) Cross-sectional SEM image of p-SnO/$Zn_{0.48}Sn_{0.52}N_2$/AZO*

In the table below, $TiAu_1$ corresponds to the Ti/Au contact deposited on bottom SnO layer and $TiAu_2$ to the Ti/Au contact deposited on top AZO layer. For the J-V characteristics measurements, the probes can be located either on Ti/Au contact, SnO or AZO. The different configurations mentioned in **Figure VI. 19** are defined in the following table:

Table VI. 2: Probe positioning for the different measurements shown in **Figure IV. 19**

Sample symbol	Probe position of Solar Simulator	
	1st	2nd
pSnO.$TiAu_1$-$Zn_{DC}Sn_{RF}$-AZO-$TiAu_2$	$TiAu_1$	$TiAu_2$
pSnO.$TiAu_1$-$Zn_{DC}Sn_{RF}$-AZO	$TiAu_1$	AZO
pSnO-$Zn_{DC}Sn_{RF}$-AZO-$TiAu_2$	SnO	$TiAu_2$
pSnO-$Zn_{DC}Sn_{RF}$-AZO	SnO	AZO

The dark J-V curve (**Figure VI. 19a**) does not relate to a diode functionality and is similar to a conductive behavior. In addition, when the probe was located on $TiAu_1$, the obtained

dark current density is higher almost one order of magnitude than when located on SnO indicating that direct probe contact on SnO is highly resistive. Whereas there is no significant difference when placed on $TiAu_2$ or AZO.

Under 1-sun illumination, a small photocurrent is obtained for all configurations. As can be awaited from dark measurements, the J_{Ph}/J_D ratio as probe is located on $TiAu_1$ is higher than on SnO. The best result is obtained when the two probes are connected to $TiAu_1$ and $TiAu_2$ contacts, then the J_{Ph}/J_D ratio at 5V equals to 0.32. On the contrary, the worst case is obtained when the two probes are connected directly to SnO and AZO layer, the J_{Ph}/J_D ratio at 5V equals to 0.08, mainly due to the direct contact on SnO.

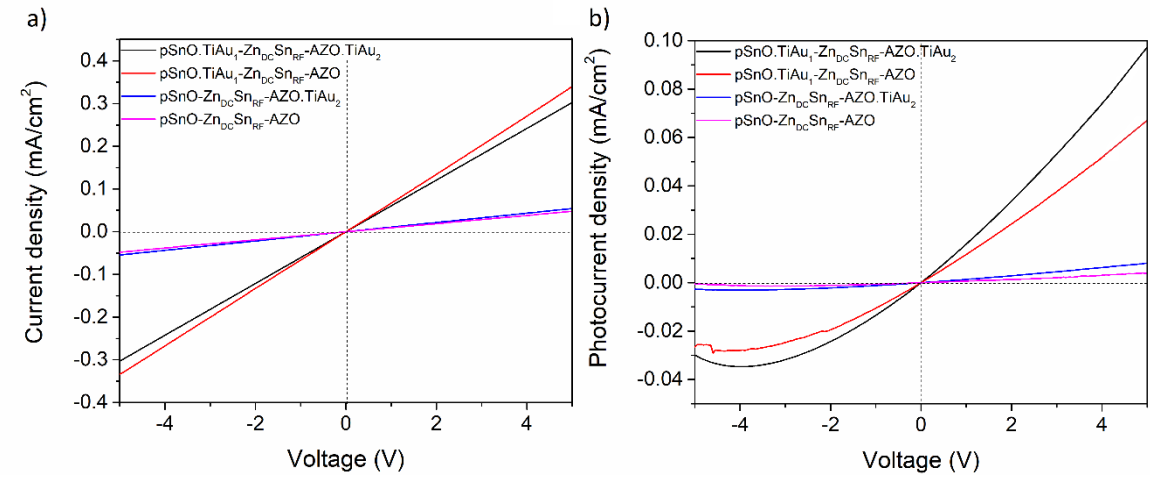

***Figure VI. 19**: a) J-V characterization of Structure2.1 samples with $Zn_{0.48}Sn_{0.52}N_2$ fabricated in $Zn_{DC}Sn_{RF}$ mode in dark and b) $J_{Ph} - V$ curve under 1-sun AM1.5 solar spectra illumination (100 mW/cm^2) at room temperature*

In a next trial (*Structure2.2)*, the thickness of SnO layer has been increased in order to check its effect on the properties of the device. Except the sputtering time of SnO that was increased from 18 to 27 min, all fabrication parameters were kept identical to *Structure2.1* device (**Figure VI. 17)**. The SEM observation of the device cross-section (**Figure VI. 20**) allowed determining the thickness of SnO, $ZnSnN_2$ and AZO layers to 870 nm, 290 nm and 320 nm, respectively.

Figure VI. 21 illustrates the J-V characterization in dark and the J_{Ph} -V characterization under 1-sun AM1.5 solar spectra illumination. The overall behavior, ether in dark or under

illumination, is the same that of *Structure2.1*. The decrease in resistivity of p-SnO, linked to its increased thickness, can be clearly observed by the 5-times increase of the dark current density. Otherwise, an overall ohmic behavior is still observed. An increase is also observed on the photocurrent but with no real relationship with that of dark current (a ratio around 2 is noticed).

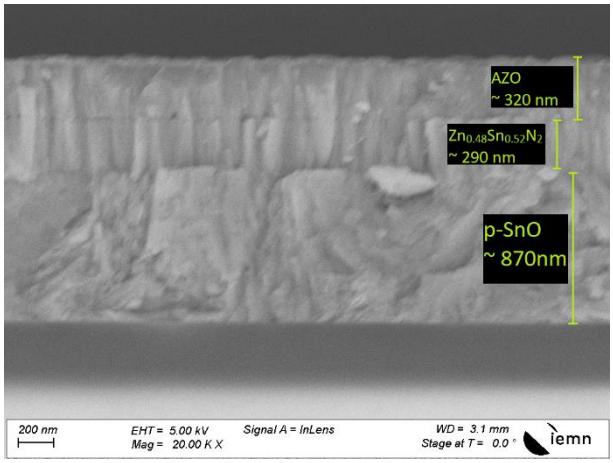

Figure VI. 20: *Cross-section SEM image of Structure2.2 (identical to Structure2.1 except an increased SnO bottom contact layer thickness).*

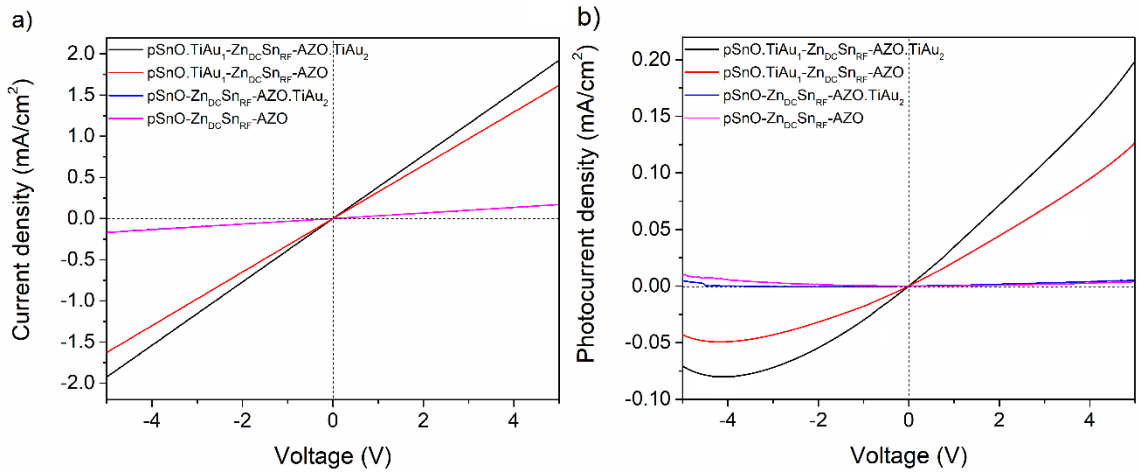

Figure VI. 21: *a) J-V characterization of Structure2.2 sample in dark and b) J_{Ph} – V curve under 1-sun AM1.5 solar spectra illumination (100 mW/cm^2) at room temperature*

VI.2.1.2 Fabrication of $ZnSnN_2$ in $Zn_{RF}Sn_{DC}$ mode:

The main steps of fabrication process of this *Structure2.3* sample are identical to those used for the $Zn_{DC}Sn_{RF}$ mode sample presented in Section V.2.1.1 and in **Figure VI. 17**. The only difference concerns obviously the parameters used for the $ZnSnN_2$ layer deposition that are here: 30W-RF and 50W-DC power biasing for the Zn and Sn targets, respectively (to get an x value of 0.48), and a deposition time of 11.5 minutes.

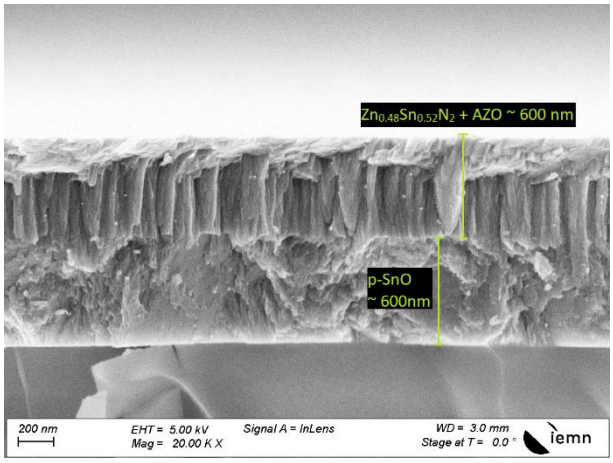

Figure VI. 22: *Cross-section SEM image of Structure2.3: p-SnO/$Zn_{0.48}Sn_{0.52}N_2$/AZO with $ZnSnN_2$ layer deposited in $Zn_{RF}Sn_{DC}$ mode*

Figure VI. 22 shows the cross-section of the tri-layer p-SnO/$Zn_{0.48}Sn_{0.52}N_2$/AZO structure. The thickness of p-SnO is approximately 600 nm so except the deposition mode of the $ZnSnN_2$ layer, this device is almost identical to *Structure2.1* sample.

The J-V characterization of *Structure2.3* is reported in **Figure VI. 23**. The global current density values are the same that for the *Structure2.1* sample (**Figure IV. 19**). The J_{Ph}/J_D ratio at 5V when two probes were connected to $TiAu_1$ and $TiAu_2$ obtains the best value, equal to 0.36, so almost the same value than in $Zn_{DC}Sn_{RF}$ mode. This confirms the previous observations in Chapter II and IV that there is no significant influence of the DC or RF biasing of targets.

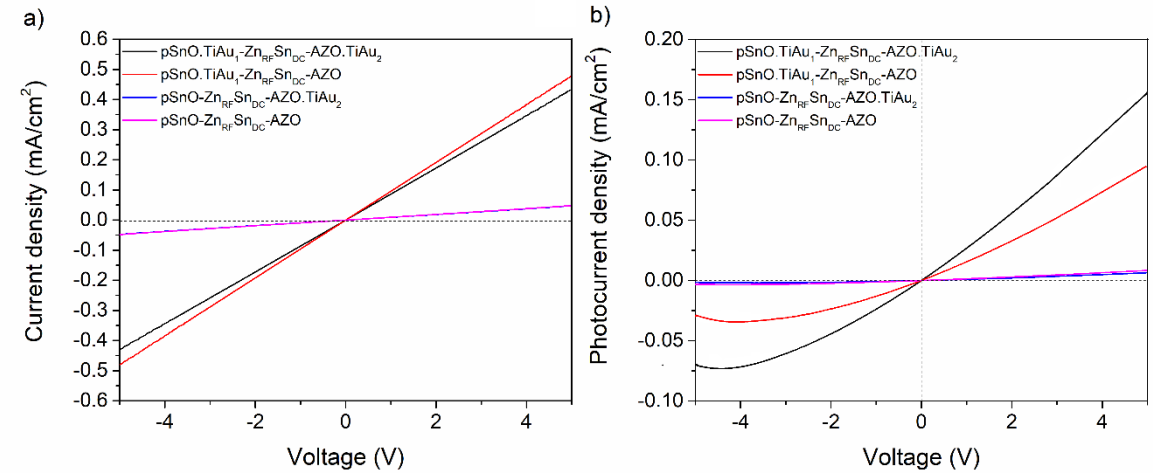

Figure VI. 23: *a) J-V characterization of Structure2.3 in dark and b) $J_{Ph} - V$ curve under 1-sun AM1.5 solar spectra illumination (100 mW/cm^2) at room temperature*

Following the same idea that previously used for the $Zn_{DC}Sn_{RF}$ mode, the thickness of the SnO layer was increased the same way (increase of the sputtering time from 18 to 27 min). The so-obtained *Structure2.4* sample is represented in **Figure VI. 24**. The thickness of SnO layer is here of 790 nm and the thickness $ZnSnN_2$ and AZO are approximately 300 nm.

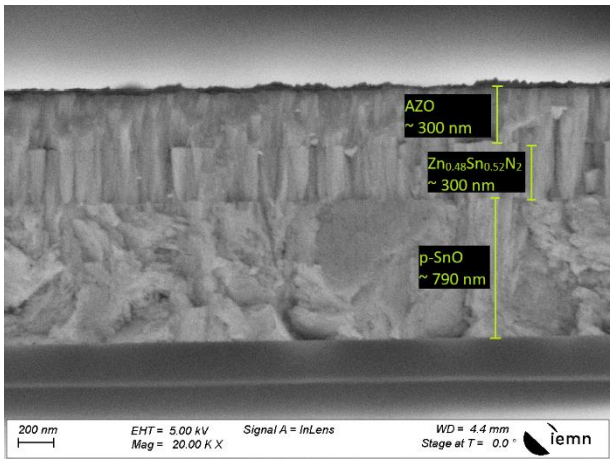

Figure VI. 24*: Cross-section SEM image of p-SnO/$Zn_{0.48}Sn_{0.52}N_2$/AZO with sputtering time of SnO increased to 27 min, and $ZnSnN_2$ was deposited in $Zn_{DC}Sn_{RF}$ mode (Structure2.4).*

Figure VI. 25 reports the J-V measurements. By comparison with identical structure in $Zn_{DC}Sn_{RF}$ mode (*Structure2.2*), this *Structure2.4* ($Zn_{RF}Sn_{DC}$ mode) does not display

fiercely different results and reinforces the conclusion made comparing Structures 2.3 and 2.1.

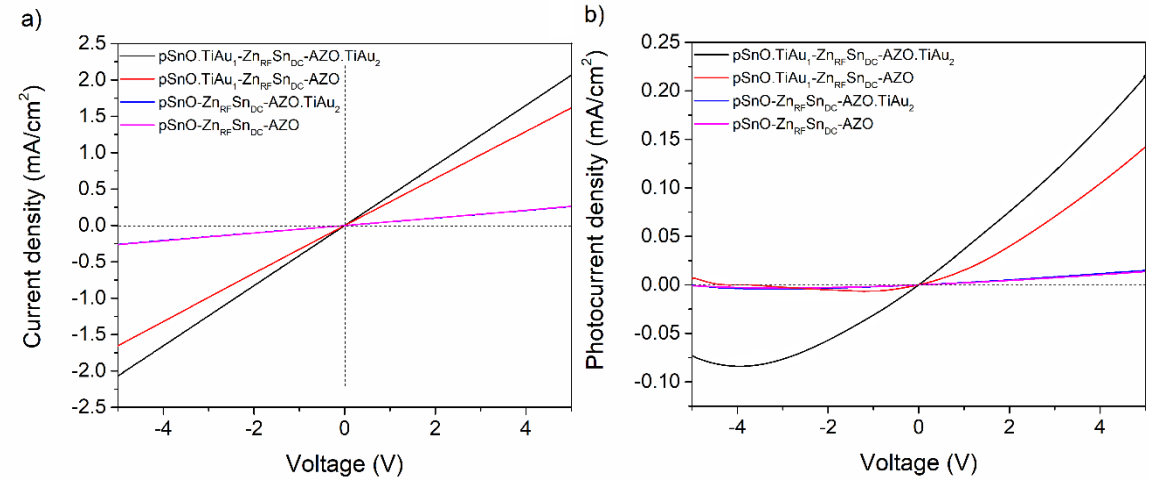

Figure VI. 25: *a) J-V characterization of Structure2.4 sample in dark and b) $J_{Ph} - V$ under 1-sun AM1.5 solar spectra illumination (100 maw/cm^2) at room temperature*

VI.2.2 p-Si/ZnSnN$_2$ heterojunction

In this section, $ZnSnN_2$ was deposited on p-type boron-doped silicon wafer at room temperature, the working pressure was 0.02 mbar, the N_2/Are ratio was fixed at 2.0, and the applied power scheme is described in **Table VI. 3**. It was replicated from previous experiments and chosen in order to obtain an x value close to 0.48. AZO and electrode deposition steps are the same that used in Section V.1.2. The main steps of fabrication process are presented in **Figure VI. 26**.

Table VI. 3: Bias applied power of $ZnSnN_2$ layer to fabricate *Structure2.5* samples

	Applied Power		**Sputtering time**
	Zn target	Sn target	**(min)**
pSi-Zn$_{DC}$Sn$_{RF}$	DC – 24 W	RF – 80W	12.5
pSi-Zn$_{RF}$Sn$_{DC}$	RF – 30 W	DC – 50 W	11.5

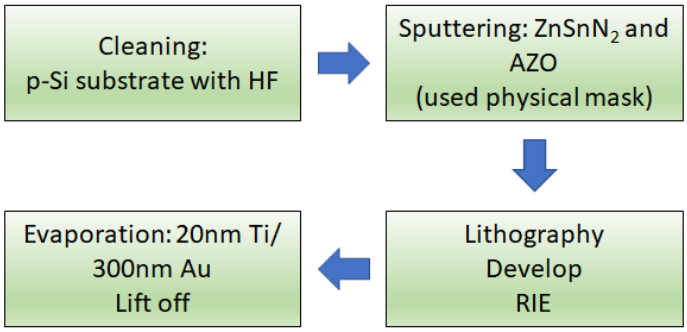

Figure VI. 26: *Main steps of the process flow of p-Si/$ZnSnN_2$ heterojunction sample (Structure2.5).*

The top and cross-sectional designs are shown in **Figure VI. 27a, b**. The deposition has been made on a full 2" silicon wafer. The p-Si contact pad is located in the center. The cross-sectional SEM images of fabricated sample are shown in **Figure VI. 27c, d** for the $Zn_{DC}Sn_{RF}$ and $Zn_{RF}Sn_{DC}$ modes, respectively. The thickness of $ZnSnN_2$ and AZO layer is approximately 300 nm.

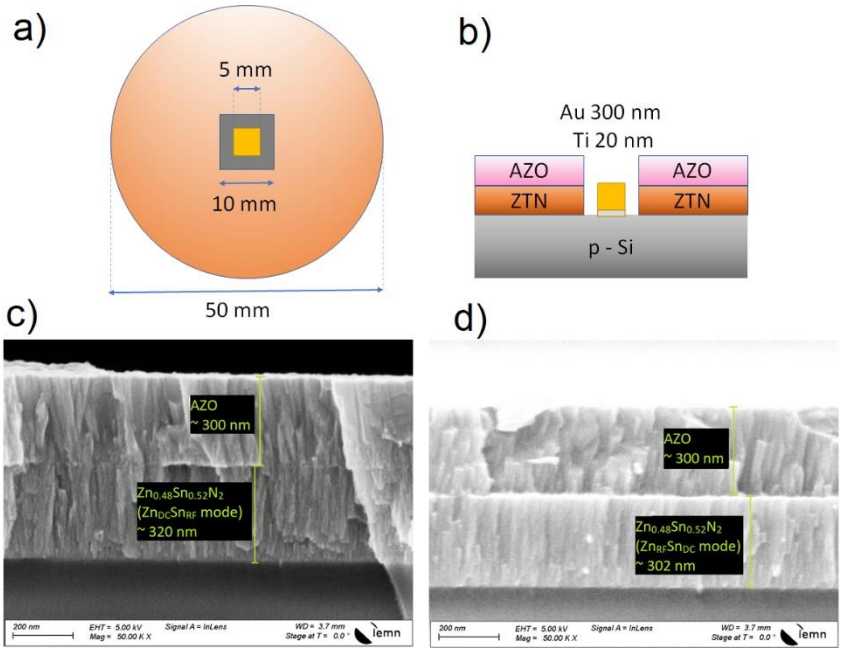

Figure VI. 27: *Structure2.5 sample with of p-Si/$Zn_{0.48}Sn_{0.52}N_2$/AZO: a) top design, b) cross-section design structure, c) cross-section SEM image with $ZnSnN_2$ fabricated in $Zn_{DC}Sn_{RF}$ mode and d) in $Zn_{RF}Sn_{DC}$*

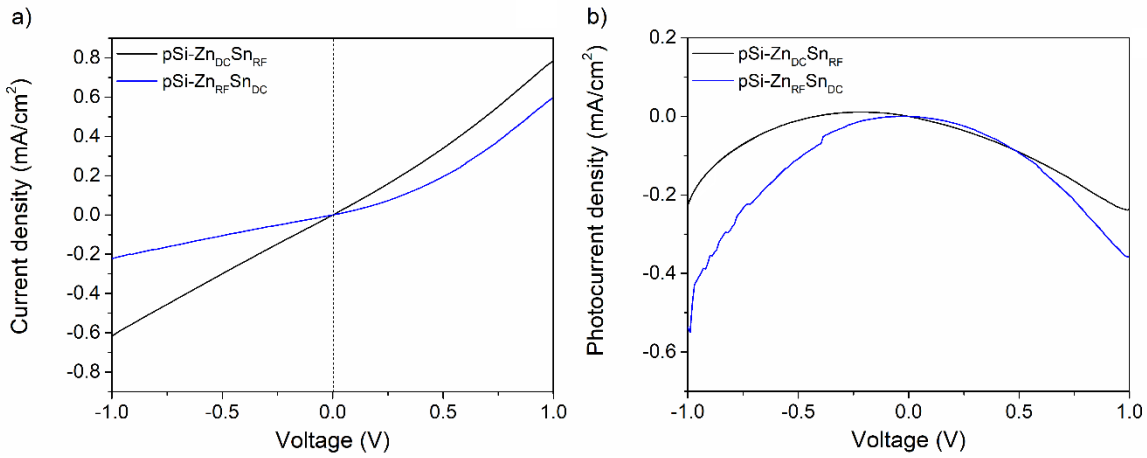

Figure VI. 28: *a) J-V characterization of Structure2.5 sample (p-Si/$Zn_{0.48}Sn_{0.52}N_2$/AZO) in dark and b) J_{Ph} – V curve under 1-sun AM1.5 solar spectra illumination (100 mW/cm^2) at room temperature, the probes of solar simulator are located on Ti/Au and AZO*

The positive probe of simulator was located on Ti/Au and the negative one was located on AZO, the dark J-V curves (**Figure VI. 28**) almost describe an ohmic behavior for the $Zn_{DC}Sn_{RF}$ mode deposited sample while some rectifying behavior could be perceived for the $Zn_{RF}Sn_{DC}$ mode deposited sample. After illumination under 1-sun, negative photocurrent is obtained when applied voltage is positive. At 1V, the J_{ph}/J_D ratio are -0.30 and -0.60 for sample fabricated in $Zn_{DC}Sn_{RF}$ and $Zn_{RF}Sn_{DC}$ mode, respectively. At -1V, the obtained photocurrent is positive, equals to 0.37 and 2.42 for sample fabricated in $Zn_{DC}Sn_{RF}$ and $Zn_{RF}Sn_{DC}$ mode, respectively. At this stage, since absorption in ZTN has not been clearly proven, silicon photoresponse can interfere and modify the overall photoresponse of the device. Even if some rectifying look-like response can be observed, it does not reflect a rectifying behavior of the device since the curve still runs through the 0,0 point.

VI.3 **Discussions and partial conclusions**

In this chapter, $ZnSnN_2$ films are no more considered as "simple" thin films but are inserted in device structures requiring technological steps to be fabricated. These device topologies allowed characterizing the $ZnSnN_2$ films in transverse carrier transport conditions, i.e. along the columnar structure of the material. In previous chapters, the material electrical characterization (e.g., by Hall effect measurements) was made using only top electrodes with a longitudinal carrier transport condition, i.e., across the columnar structure of the material.

First devices (*Structure1*) were fabricated as a photoconductor design. From preliminary observations on transverse conduction samples (*Structure1.1*), it appeared that the surface area of samples reacts on their electrical behavior (**Figure VI. 5**). Making so small surface area samples (*Structure1.2*) pointed out that gold can pollute the $ZnSnN_2$ layer. AZO electrodes were then used for contacting the $ZnSnN_2$ layer both ends (*Structures1.3* -transverse conduction- and *Structure1.4* -longitudinal conduction-). Different electrical behaviors were observed on those two series (**Figures VI. 10** and **VI. 12**) motivating us to investigate transverse and longitudinal conduction conditions. Specific devices were so fabricated (*Structure1.M1* and *Structure1.M2)* and more deeply characterized by GeePs partner of the OPERA project. Their results (**Figure VI. 15**) showed that transverse and longitudinal conductivity values are strongly different (around 6 orders of magnitude). The oxygen contamination of $ZnSnN_2$ films, also strongly suspected by the IJL partner of the OPERA project, can create some highly conductive oxide within the $ZnSnN_2$ film that completely shadows the real properties of the material. Those results have been obtained at the end of my work and shall deserve further investigation in future work.

In parallel, the parametric study on the composition of the $ZnSnN_2$ layer pointed out that slightly Sn rich materials (x = 0.47-0.48) exhibit the highest photoresponse (**Figure VI. 7**). This composition was then fixed for the remaining studies.

A 300°C post-anneal under N_2 atmosphere during 15 minutes has also been seen as beneficial for the electrical properties. Such a behavior was not observed during the parametric study of chapters II to IV in longitudinal carrier transport conditions.

Structure2 topologies aimed achieving a junction device. Whatever the materials used, p-SnO or p-Si, all fabricated samples react as photoconductors and a photodiode behavior cannot be observed. Target biasing conditions (DC or RF feeding of Zn and Sn targets)

have also been reiterated and results do not exhibit significant modifications of electrical properties as it was observed in the parametric study in longitudinal conduction conditions.

Table VI. 4: Main results of n-$ZnSnN_2$/n-AZO, p-SnO/n-$ZnSnN_2$ and p-Si/n-$ZnSnN_2$ heterojunction

	Action	Voltage (V)	J_d (mA/cm^2)	J_{ph} (mA/cm^2)	J_{ph}/J_d
Structure 1.1	Surface area (cm^2)				
TiAu/$ZnSnN_2$/AZO	0.05	0.5	442.8	256.8	0.58
	0.10	0.5	310.1	68.2	0.22
	0.15	0.5	265.6	45.2	0.17
	0.20	0.5	152.6	24.4	0.16
	0.25	0.5	103.4	3.7	0.036
Structure 1.2	Zn/(Zn+Sn)				
TiAu/$ZnSnN_2$/AZO	x = 0.58	0.5	0.26	0.0016	0.0062
Area = 0.05 cm^2	x = 0.5	0.5	13.1	0.46	0.035
	x = 0.47	0.5	206.0	98.9	0.48
	x = 0.34	0.5	0.48	0.13	0.27
	x = 0.26	0.5	0.09	0.029	0.31
	RTA 300°C/15min/N_2				
	x = 0.47	0.5	3975	240	0.060
	x = 0.34	0.5	The electrical contact cannot be accessed		
	x = 0.26	0.5			
Structure 1.3	As-dep	0.5	36.2	18.1	0.50
AZO/$Zn_{0.47}Sn_{0.53}N_2$/AZO **Area = 0.05 cm^2**	RTA 300°C/15min/N_2	0.5	16.2	10.4	0.64
Structure 1.4	As-dep	0.5	330	39.2	0.12
$Zn_{0.47}Sn_{0.53}N_2$/AZO **Area = 0.05 cm^2**	RTA 300°C/15min/N_2	0.5	24.5	4.36	0.15
Structure 2.1&2.2	SnO thickness (nm)				
p-SnO/$Zn_{DC}Sn_{RF}N_2$/AZO	610	5	0.30	0.097	0.32
x = 0.58	870	5	1.92	0.19	0.1
Structure 2.3&2.4	SnO thickness (nm)				
p-SnO/$Zn_{RF}Sn_{DC}N_2$/AZO	600	5	0.43	0.16	0.36
x = 0.58	790	5	2.07	0.22	0.1
Structure 2.5	$Zn_{DC}Sn_{RF}$	-1	-0.62	-0.23	0.37
p-Si/$ZnSnN_2$		1	0.78	-0.24	-0.30
	$Zn_{RF}Sn_{DC}$	-1	-0.22	-0.54	2.42
		1	0.60	-0.36	-0.60

SUMMARY

The first and major part of this work has been dedicated to a parametric study of the deposition conditions of $ZnSnN_2$ material, using sputtering technique, on its electrical and optical properties. The main tools that have been used are XRD for the crystallography monitoring, SEM for the surface topology observation, Hall Effect measurements for the electrical characterization, and UV-Vis spectroscopy for the optical properties assessment. Except the material deposition, no particular technological steps were made and all characterization were made on thin films; in particular, electrical characterization was conducted in a longitudinal carrier transport scheme, i.e., in a direction perpendicular to the film deposition. The second part aimed at evaluating the optoelectronic properties. I mean that technology was deployed, first for the fabrication of transparent conductive oxides, and second for fabricating photodetectors. Device structure included then bottom and top electrodes, closer to that of a real solar cell implementation. Thus, the main difference with all previous studies was that carrier transport was then in transverse direction, i.e., in the direction of film growth.

Parametric study

- *Deposition atmosphere:*

Starting by sputtering metallic targets in a pure argon atmosphere, the power supply of each target was determined in order achieving a stoichiometric compound. However, the deposited films shift to a Zn-rich composition when nitrogen is inserted into the sputtering chamber. Additionally, for all sputtering atmospheres containing argon, the increase in nitrogen concentration leads to decrease the deposition rate. In H_2/N_2 atmosphere, the lighter mass of hydrogen (1 u) does not modify the sputtering process that is governed by the nitrogen ions.

The XRD patterns of samples that were fabricated in N_2/Ar atmosphere show all the characteristic peaks of $ZnSnN_2$, reported in literature from simulated or experimental

results; nevertheless, the crystal structure of the material cannot be clearly concluded between orthorhombic and wurtzite. Without argon in deposition atmosphere, there are only 2 main diffraction peaks obtained for materials deposited in pure N_2, and 4 for those fabricated in H_2/N_2 atmosphere.

Top views of films show a cauliflower-like structure for almost all cases. Only sputtering in pure N_2 atmosphere exhibits a completely different structure with large triangular/pyramidal shape.

The electrical characterization of materials deposited in H_2-free atmosphere shows that they are almost degenerated with a very high electron density, around some 10^{20} cm^{-3}. The carrier mobility is very low ranging from 0.15 to 0.42 $cm^2V^{-1}s^{-1}$ and the resistivity is then also very low, in the order of 0.1 - 1 Ω.cm. Insertion of hydrogen in the deposition atmosphere leads to decrease the carrier concentration by at least two decades, some 10^{17} cm^{-3} can even be achieved, the carrier mobility and resistivity are also reported at slightly higher values than without hydrogen.

The optical bandgap deduced from UV-Vis spectroscopy measurements show a very huge large range, from 1.6 eV up to 2.2 eV depending on the different sputtering conditions.

- *Deposition pressure:*

The increase in sputtering pressure leads to increase the Sn content, the optical band gap, and the carrier mobility as to decrease the carrier density. However, at high pressure, the crystallinity is reduced, voids exist on the surface and the strain of thin films increases. Those two can affect material stability.

- *Temperature*

    - *during deposition, by heating the substrate:*

Heating the substrate during deposition does not really impact the sputtering rate as well as the film composition. The crystallite size is also not really modified. However, the number and size of voids increase with the increase of temperature.

- *after deposition using Rapid thermal annealing treatment:*

Using a post-anneal using an RTA under N_2 has no significant effect on $ZnSnN_2$ crystallography and its electrical properties as long as temperature stays below 400°C. At higher temperatures, the films disaggregate and Sn balls can be observed at their surface. Cracks in the films appear approximately above 300°C for material deposited on glass since none can be observed when on silicon. Using a hydrogenated argon-free deposition atmosphere, cracks appear on both those substrates, but at higher temperatures (300°C) on Si than on glass (150°C).

Whatever the way temperature was applied, during or after deposition, no significant effect on electrical and optical properties of $ZnSnN_2$ thin films were recorded.

- *Material composition and target biasing:*

The characteristics XRD peaks of $ZnSnN_2$ are rather always observed for near stoichiometric or moderately Zn rich material ($0.45 < x < 0.6$). Highly Zn rich films seem amorphous and moderately to highly Sn rich films do not show all diffraction peaks. For $0.45 < x < 0.6$, the optical bandgap ranges from roughly 2 eV down to 1.85 eV. This has been observed in the two main deposition modes that have been tested by swapping DC and RF bias conditions on Zn and Sn targets. The electrical parameters exhibit also almost the same behavior versus the Zn composition whatever the deposition mode is. It can be noticed that electron concentration decreases by two orders of magnitude, from 10^{20} down to 10^{18} cm^{-3} for highly Zn rich films.

Optoelectronic properties

Finally, the optoelectronic characteristics of $ZnSnN_2$ have been examined by fabricating two device structures that were originally intended to constitute n-n and p-n device structures.

- Photoconductor (*Structure 1*): no junction exists in this structure and the device using a slightly Sn rich material, $Zn_{0.47}Sn_{0.53}N_2$, exhibited the highest photocurrent density and

J_{Ph}/J_D ratio. When Ti/Au is used as bottom electrode, the obtained dark current density is very high. It is mainly attributed to gold diffusion inside the material. In addition, since technology was used on those samples, several electrode spacings were fabricated of which the electrical characterization revealed that a spacing-dependent conductivity value.

- Photodiode (*Structure2*):

- p-SnO/n-$ZnSnN_2$/AZO structure: the J-V characteristics did not relate a rectifying behavior and is rather similar to that of a resistance. The J_{Ph}/J_D ratio equals to 0.36 (at 5V bias) for samples with a 600nm-thick SnO layer.

- p-Si/n-$ZnSnN_2$/AZO structure: on this structure that involves transverse carrier transport, some difference was observed depending the target bias that was used. The behavior is almost ohmic in $Zn_{DC}Sn_{RF}$ mode while it looks like exhibiting some rectifying behavior in $Zn_{RF}Sn_{DC}$ mode. Nevertheless, curves always pass through the 0,0 point and no particular photovoltaic effect can be pointed out.

OPENING

The rather exhaustive parametric study of $ZnSnN_2$ electrical properties versus the deposition conditions did not show obvious drastic behavior modifications except on carrier density that can sometimes be significantly reduced.

The measurement of the photoelectric behavior cannot, right now, be correlated to the electrical parameters obtained during this parametric study. Such measurements involved the development of technological steps in order to build photodetector devices. Contrary to the parametric study that was carried out on as deposited films and so using longitudinal carrier transport conditions, those structures implied transverse carrier transport designs. The results obtained on those latter, by my own characterizations but also by a deeper study at one OPERA project partner (GeePs), showed a completely different electrical behavior: transverse carrier conduction exhibits several orders of magnitude higher in resistivity values than longitudinal one. Other material studies conducted in another OPERA project partner (IJL) [XX] showed that oxygen atoms are present in the film. They can be included

during deposition or absorbed in the film after deposition. The low resistivity values that are measured can then express the existence of a parallel conductive oxide film that short-cuts the $ZnSnN_2$ material in longitudinal transport devices. IJL partner has the possibility implementing the sputtering deposition technique using a substrate bias and showed that using such a technique reduces significantly the porosity of the film avoiding post deposition oxygen absorption. Next step will be then to coupe such a deposition technique with the technology developed her to build transverse carrier transport structures.

The measurement of the photoelectric properties of $ZnSnN_2$ is at the very beginning. In this work, we cannot succeed obtaining a diode functionality, although some photocurrent was recorded.

Realizing a junction is still a challenge using this material. The high carrier density levels that have been observed seem to kill any hope achieving an homojunction, p-type material being difficult to fabricate (some amphoteric behavior has been recorded in longitudinal transport devices but this has not been clarified right now). If any junction could potentially be made, it might most probably be a heterojunction. The preliminary results we obtained using p-Si could be a route. The use of hydrogen in deposition atmosphere that seems hindering the formation of donor defects, such as nitrogen vacancies VN and unintentional ON impurities has not been tested in transverse carrier transport devices yet. It can also constitute a route achieving higher photoelectric performance and, may be, allow some promise to reverse doping polarity. Post-deposition implantation of species, particularly of group III elements (such as B, Al, Ga), has also shown some potentiality to decrease the free carrier density.

In the OPERA project, and in collaboration with another partner of the project (CEA-INES), owing to its high carrier concentration and wide bandgap, $ZnSnN_2$ has been investigated as selective electrode for silicon heterojunction (SHJ) solar cells. First preliminary experiments have been made that way depositing $ZnSnN_2$ on top of a Si cell. Right now, sputtering damage on the Si cell passivation layer is prohibitive but such experiments are in their infancy.

REFERENCES

Photovoltaics

[1] International Energy Agency, "Global Energy Review 2020," 2020. [Online]. Available: https://www.iea.org/reports/global-energy-review-2020.

[2] "Best Research-Cell Efficiency Chart | Photovoltaic Research 2020| NREL." [Online]. Available: https://www.nrel.gov/pv/cell-efficiency.html.

[3] "Alta Devices Sets 29.1% Solar Efficiency Record; NASA Selects Alta Devices for International Space Station Test." [Online]. Available: https://www.businesswire.com/news/home/20181212005060/en.

[4] J. F. Geisz *et al.*, "Six-junction III–V solar cells with 47.1% conversion efficiency under 143 Suns concentration," *Nat. Energy*, vol. 5, pp. 326–335, 2020.

[5] "Photovoltaic Roadmap (ITRPV): Eleventh Edition Online," 2020. [Online]. Available: https://itrpv.vdma.org/viewer/-/v2article/render/48393879.

[6] A. Richter, M. Hermle, and S. W. Glunz, "Reassessment of the limiting efficiency for crystalline silicon solar cells," *IEEE J. Photovoltaics*, vol. 3, no. 4, pp. 1184–1191, 2013.

[7] A. Slade and V. Garboushian, "27.6% Efficient Silicon Concentrator Solar Cells for Mass Production," *Tech. Dig. 15th Int. ...*, no. January 2005, pp. 1–2, 2005.

[8] K. Yamamoto *et al.*, "High-efficiency heterojunction crystalline Si solar cell and optical splitting structure fabricated by applying thin-film Si technology," *Jpn. J. Appl. Phys.*, vol. 54, no. 8, pp. 6–11, 2015.

[9] H. Sai, T. Matsui, and K. Matsubara, "Stabilized 14.0%-efficient triple-junction thin-film silicon solar cell," *Appl. Phys. Lett.*, vol. 109, no. 18, pp. 1–6, 2016.

[10] "Solar Frontier Achieves World Record Thin-Film Solar Cell Efficiency of 23.35%." [Online]. Available: https://www.solar-frontier.com/eng/news/2019/0117_press.html.

[11] First Solar, "Leading the World's Sustainable Energy Future," 2019.

[12] T. P. White, N. N. Lal, and K. R. Catchpole, "Tandem solar cells based on high-efficiency c-Si bottom cells: Top cell requirements for >30% efficiency," *IEEE J. Photovoltaics*, vol. 4, no. 1, pp. 208–214, 2014.

[13] R. Cariou *et al.*, "III-V-on-silicon solar cells reaching 33% photoconversion efficiency in two-terminal configuration," *Nat. Energy*, vol. 3, no. 4, pp. 326–333,

2018.

[14] B. M. Kayes *et al.*, “27.6% Conversion efficiency, a new record for single-junction solar cells under 1 sun illumination,” in *37th IEEE Photovoltaic Specialists Conference*, 2011, pp. 000004–000008.

[15] M. A. Green, E. D. Dunlop, D. H. Levi, J. Hohl-Ebinger, M. Yoshita, and A. W. Y. Ho-Baillie, “Solar cell efficiency tables (version 54),” *Prog. Photovoltaics Res. Appl.*, vol. 27, no. 7, pp. 565–575, Jul. 2019.

[16] M. Hu *et al.*, “Sub-1.4eV bandgap inorganic perovskite solar cells with long-term stability,” *Nat. Commun.*, vol. 11, no. 1, pp. 1–10, 2020.

[17] B. Ehrler, E. Alarcón-Lladó, S. W. Tabernig, T. Veeken, E. C. Garnett, and A. Polman, “Photovoltaics reaching for the shockley-queisser limit,” *ACS Energy Lett.*, vol. 5, no. 9, pp. 3029–3033, 2020.

[18] Y. Hinuma *et al.*, “Discovery of earth-abundant nitride semiconductors by computational screening and high-pressure synthesis,” *Nat. Commun.*, vol. 7, no. May, pp. 1–2, 2016.

[19] T. R. Paudel and W. R. L. Lambrecht, “First-principles study of phonons and related ground-state properties and spectra in Zn-IV-N2 compounds,” *Phys. Rev. B - Condens. Matter Mater. Phys.*, vol. 78, no. 11, 2008.

[20] T. R. Paudel and W. R. L. Lambrecht, “First-principles calculations of elasticity, polarization-related properties, and nonlinear optical coefficients in Zn-IV- N2 compounds,” *Phys. Rev. B - Condens. Matter Mater. Phys.*, vol. 79, no. 24, pp. 1–6, 2009.

[21] A. Punya., T. R. Paudel, and W. R. L. Lambrecht, “Electronic and lattice dynamical properties of II-IV-N2 semiconductors,” *Phys. Status Solidi C*, vol. 8, no. 7, pp. 2492–2499, 2011.

[22] P. C. Quayle, K. He, J. Shan, and K. Kash, “Synthesis, lattice structure, and band gap of ZnSnN2,” *MRS Commun.*, vol. 3, no. 3, pp. 135–138, 2013.

[23] A. Punya, W. R. L. Lambrecht, and M. Van Schilfgaarde, “Quasiparticle band structure of Zn-IV-N2 compounds,” *Phys. Rev. B - Condens. Matter Mater. Phys.*, vol. 84, no. 16, pp. 1–10, 2011.

[24] L. Lahourcade, N. C. Coronel, K. T. Delaney, S. K. Shukla, N. A. Spaldin, and H. A. Atwater, “Structural and optoelectronic characterization of RF sputtered ZnSnN 2,” *Adv. Mater.*, vol. 25, no. 18, pp. 2562–2566, 2013.

[25] P. C. Quayle *et al.*, “Charge-neutral disorder and polytypes in heterovalent wurtzite-based ternary semiconductors: The importance of the octet rule,” *Phys. Rev. B - Condens. Matter Mater. Phys.*, vol. 91, no. 20, pp. 1–14, 2015.

[26] S. Chen, P. Narang, H. A. Atwater, and L. W. Wang, “Phase stability and defect physics of a ternary ZnSnN2 semiconductor: First principles insights,” *Adv. Mater.*, vol. 26, no. 2, pp. 311–315, 2014.

[27] V. Stevanovic, X. Zhang, and A. Zunger, “Correcting density functional theory for accurate predictions of compound enthalpies of formation : Fitted elemental-phase reference energies Fitted elemental-phase reference energies,” *Phys. Rev. B*, vol. 85, no. March, p. 115104, 2012.

[28] T. D. Veal *et al.*, “Band Gap Dependence on Cation Disorder in ZnSnN 2 Solar Absorber,” *Adv. Energy Mater.*, vol. 5, no. 24, pp. 1–5, 2015.

[29] R. A. Makin *et al.*, “Growth of ordered and disordered ZnSnN2,” *J. Vac. Sci. Technol. B, Nanotechnol. Microelectron. Mater. Process. Meas. Phenom.*, vol. 35, no. 2, p. 02B116, 2017.

[30] S. Lany *et al.*, “Monte Carlo simulations of disorder in ZnSn N2 and the effects on the electronic structure,” *Phys. Rev. Mater.*, vol. 1, no. 3, pp. 1–7, 2017.

[31] F. Kawamura, N. Yamada, M. Imai, and T. Taniguchi, “Synthesis of ZnSnN2 crystals via a high-pressure metathesis reaction,” *Cryst. Res. Technol.*, vol. 51, no. 3, pp. 220–224, 2016.

[32] E. Arca *et al.*, “Band edge positions and their impact on the simulated device performance of ZnSnN2-based solar cells,” *IEEE J. Photovoltaics*, vol. 8, no. 1, pp. 110–117, 2018.

[33] X. M. Cai *et al.*, “Tuning the photoluminescence, conduction mechanism and scattering mechanism of ZnSnN 2,” *J. Alloys Compd.*, vol. 779, pp. 237–243, 2019.

[34] R. Qin *et al.*, “Effects of surface condition on the work function and valence-band position of ZnSnN2,” *Appl. Phys. A Mater. Sci. Process.*, vol. 123, no. 12, p. 0, 2017.

[35] N. C. Coronel, L. Lahourcade, K. T. Delaney, A. M. Shing, and H. A. Atwater, “Earth-abundant ZnSnxGe1-xN2 alloys as potential photovoltaic absorber materials,” *Conf. Rec. IEEE Photovolt. Spec. Conf.*, pp. 3204–3207, 2012.

[36] N. Feldberg *et al.*, “ZnSnN2: A new earth-abundant element semiconductor for solar cells,” *Conf. Rec. IEEE Photovolt. Spec. Conf.*, pp. 2524–2527, 2012.

[37] N. Feldberg *et al.*, “Growth, disorder, and physical properties of ZnSnN2,” *Appl.*

Phys. Lett., vol. 103, no. 4, 2013.

[38] N. Feldberg, J. D. Aldous, P. A. Stampe, R. J. Kennedy, T. D. Veal, and S. M. Durbin, "Growth of ZnSnN2 by molecular beam epitaxy," *J. Electron. Mater.*, vol. 43, no. 4, pp. 884–888, 2014.

[39] S. Swann, "Magnetron sputtering," *Phys. Technol.*, vol. 19, no. 6, pp. 67–75, 1988.

[40] A. N. Fioretti *et al.*, "Effects of Hydrogen on Acceptor Activation in Ternary Nitride Semiconductors," *Adv. Electron. Mater.*, vol. 3, no. 3, pp. 3–7, 2017.

[41] H. A. Atwater, N. Coronel, and L. Lahourcade, "Photovoltaic Semiconductive Materials," US 2013/0240026 A1, 2013.

[42] D. Q. Fang, X. Chen, P. F. Gao, Y. Zhang, and S. L. Zhang, "Mono- and Bilayer ZnSnN 2 Sheets for Visible-Light Photocatalysis: First-Principles Predictions," *J. Phys. Chem. C*, vol. 121, no. 46, pp. 26063–26068, 2017.

[43] X. Cao, F. Kawamura, Y. Ninomiya, T. Taniguchi, and N. Yamada, "Conduction-band effective mass and bandgap of ZnSnN2 earth-abundant solar absorber," *Sci. Rep.*, vol. 7, no. 1, pp. 1–10, 2017.

[44] A. N. Fioretti *et al.*, "Combinatorial insights into doping control and transport properties of zinc tin nitride," *J. Mater. Chem. C*, vol. 3, pp. 11017–11028, 2015.

[45] K. kumar Chinnakutti, V. Panneerselvam, and S. Thankaraj Salammal, "Tailoring optoelectronic properties of earth abundant ZnSnN2 by combinatorial RF magnetron sputtering," *J. Alloys Compd.*, vol. 772, pp. 348–358, 2019.

[46] K. K. Chinnakutti, V. Panneerselvam, and S. Thankaraj Salammal, "Investigation on structural and optoelectronic properties of in-situ post growth annealed ZnSnN2 thin films," *Mater. Sci. Semicond. Process.*, vol. 89, no. September 2018, pp. 234–239, 2019.

[47] F. Deng *et al.*, "Determination of the basic optical parameters of ZnSnN2," *Opt. Lett.*, vol. 40, no. 7, p. 1282, 2015.

[48] R. Qin *et al.*, "Semiconducting ZnSnN2 thin films for Si/ZnSnN2 p-n junctions," *Appl. Phys. Lett.*, vol. 108, no. 14, pp. 0–5, 2016.

[49] K. Javaid *et al.*, "Thin Film Solar Cell Based on ZnSnN2/SnO Heterojunction," *Phys. Status Solidi - Rapid Res. Lett.*, vol. 12, no. 1, pp. 1–7, 2017.

[50] F. Alnjiman *et al.*, "Chemical environment and functional properties of highly crystalline ZnSnN2 thin films deposited by reactive sputtering at room temperature," *Sol. Energy Mater. Sol. Cells*, vol. 182, no. March, pp. 30–36, 2018.

[51] F. Ye *et al.*, “Improving the chemical potential of nitrogen to tune the electron density and mobility of ZnSnN2,” *J. Mater. Chem. C*, vol. 8, no. 13, pp. 4314–4320, 2020.

[52] D. M. Mattox, “Physical Sputtering and Sputter Deposition (Sputtering),” in *Handbook of Physical Vapor Deposition (PVD) Processing*, 2nd ed., Elsevier, 2010, pp. 237–286.

[53] A. H. Simon, *Sputter Processing*, Third Edit. Elsevier Inc., 2012.

[54] D. M. Mattox, “Substrate (‘Real’) Surfaces and Surface Modification,” in *Handbook of Physical Vapor Deposition (PVD) Processing*, 2nd ed., Elsevier, 2010, pp. 25–72.

[55] A. N. Fioretti *et al.*, “Effects of Hydrogen on Acceptor Activation in Ternary Nitride Semiconductors,” pp. 3–7, 2017.

[56] A. Nyaiesh and L. Holland, “The dependence of deposition rate on power input for dc and rf magnetron sputtering,” *Vacuum*, vol. 31, no. 7, pp. 315–317, Jan. 1981.

[57] G. Samuel and L. Holland, “No Title,” in *Le Vide-les couches minces*, 1980, pp. 34–37.

[58] Semicore, “Material sputtering yield table.” .

[59] Shenglin Ye., “Preparation, Characterization, and Device Applications of Zinc Tin Nitride and Zinc Tin Oxynitride Materials,” University of California, 2015.

[60] A. T. D. Agostmo, “Determination of thin metal film thickness by x-ray diffractometry using the Scherrer equation , atomic absorption analysis and transmission / reflection visible spectroscopy,” *Anal. Chim.*, vol. 262, pp. 269–275, 1992.

[61] A. M. Shing, N. C. Coronel, N. S. Lewis, and H. A. Atwater, “Semiconducting ZnSnxGe1−xN2 alloys prepared by reactive radio-frequency sputtering,” *AIP Publ.*, vol. 3, no. 076104, 2015.

[62] A. Virfeu *et al.*, “Approaching Theoretical Band Gap of ZnSnN 2 Films via Bias Magnetron Cosputtering at Room Temperature,” *ACS Appl. Electron. Mater.*, Aug. 2021.

[63] N. C. Coronel, “Earth-Abundant Zinc-IV-Nitride Semiconductors,” California Institute of Technology Pasadena, 2016.

[64] S. J. Pearton, J. W. Corbett, and M. Stavola, *Hydrogen in Crystalline Semiconductors*. 1992.

[65] S. J. Pearton, J. C. Zolper, R. J. Shul, and F. Ren, “GaN: Processing, defects, and devices,” *J. Appl. Phys.*, vol. 86, no. 1, pp. 1–78, Jul. 1999.

[66] N. Tsunoda, Y. Kumagai, A. Takahashi, and F. Oba, “Electrically Benign Defect Behavior in Zinc Tin Nitride Revealed from First Principles,” *Phys. Rev. Appl.*, vol. 10, no. 1, p. 1, 2018.

[67] K. Wasa, I. Kanno, and H. Kotera, *Handbook of Sputtering Technology*. Elsevier, 2012.

[68] X. Cao, F. Kawamura, T. Taniguchi, and N. Yamada, “Electron-transport properties of degenerate ZnSnN2 doped with oxygen,” *BMC Mater.*, vol. 2, no. 1, pp. 1–7, 2020.

[69] J. A. Thornton, “Influence of apparatus geometry and deposition conditions on the structure and topography of thick sputtered coatings,” *J. Vac. Sci. Technol.*, vol. 11, no. 4, pp. 666–670, 1974.

[70] J. A. Thornton and D. W. Hoffman, “Internal stresses in titanium, nickel, molybdenum, and tantalum films deposited by cylindrical magnetron sputtering,” *J. Vac. Sci. Technol.*, vol. 14, no. 1, pp. 164–168, 1977.

[71] G. . Williamson and W. . Hall, “X-ray line broadening from filed aluminium and wolfram,” *Acta Metall.*, vol. 1, no. 1, pp. 22–31, 1953.

[72] D. M. Mattox, *Film Characterization and Some Basic Film Properties*. 2010.

[73] L. J. Meng and M. P. Dos Santos, “Properties of indium tin oxide films prepared by rf reactive magnetron sputtering at different substrate temperature,” *Thin Solid Films*, vol. 322, no. 1–2, pp. 56–62, 1998.

[74] F. Chaabouni, M. Abaab, and B. Rezig, “Effect of the substrate temperature on the properties of ZnO films grown by RF magnetron sputtering,” *Mater. Sci. Eng. B Solid-State Mater. Adv. Technol.*, vol. 109, no. 1–3, pp. 236–240, 2004.

[75] L. Ai *et al.*, “Influence of substrate temperature on electrical and optical properties of p-type semitransparent conductive nickel oxide thin films deposited by radio frequency sputtering,” *Appl. Surf. Sci.*, vol. 254, no. 8, pp. 2401–2405, 2008.

[76] L. Lahourcade, N. C. Coronel, K. T. Delaney, S. K. Shukla, N. A. Spaldin, and H. A. Atwater, “Structural and optoelectronic characterization of RF sputtered ZnSnN2,” *Adv. Mater.*, vol. 25, no. 18, pp. 2562–2566, 2013.

[77] Z. C. Xia and J. W. Hutchinson, “Crack patterns in thin films,” *J. Mech. Phys. Solids*, vol. 48, no. 6, pp. 1107–1131, 2000.

[78] H. A. Atwater, N. Coronel, and L. Lahourcade, “US 2013/0240026 A1 Photovoltaic semiconductive materials,” 2013.

[79] R. Hu, W. Sun, M. Zeng, and M. Zhu, “Dispersing SnO2 nanocrystals in amorphous carbon as a cyclic durable anode material for lithium ion batteries,” *J. Energy Chem.*, vol. 23, no. 3, pp. 338–345, 2014.

[80] P. Wang, L. Yang, J. Li, and B. Sadeh, “Zn/ZnO Heterostructure for the Application of MO Degradation and NO Removal,” *Catal. Letters*, vol. 150, no. 7, pp. 1985–1992, 2020.

[81] Y. Okada and Y. Tokumaru, “Precise determination of lattice parameter and thermal expansion coefficient of silicon between 300 and 1500 K,” *J. Appl. Phys.*, vol. 56, no. 2, pp. 314–320, 1984.

[82] A. Laidouci, A. Aissat, and J. P. Vilcot, “Numerical study of solar cells based on ZnSnN2 structure,” *Sol. Energy*, vol. 211, no. April, pp. 237–243, 2020.

[83] K. Javaid *et al.*, “Band Offset Engineering in ZnSnN2-Based Heterojunction for Low-Cost Solar Cells,” *ACS Photonics*, vol. 5, no. 6, pp. 2094–2099, 2018.

[84] M. Khuili, N. Fazouan, H. Abou, E. Makarim, G. El, and E. Houssine, “Comparative first principles study of ZnO doped with group III elements,” *J. Alloys Compd.*, vol. 688, pp. 368–375, 2016.

[85] J. E. Jaffe, J. A. Snyder, Z. Lin, and A. C. Hess, “LDA and GGA calculations for high-pressure phase transitions in ZnO and MgO,” vol. 62, no. 3, pp. 1660–1665, 2000.

[86] Ü. Özgür *et al.*, “A comprehensive review of ZnO materials and devices,” *J. Appl. Phys.*, vol. 98, no. 0, p. 041301, 2005.

[87] M. Ruth, J. Tuttle, J. Goral, and R. Noufi, “Aluminum doped zinc oxide thin films deposited by ion beam sputtering,” *J. Cryst. Growth*, vol. 96, no. 2, pp. 363–368, 1989.

[88] K.-C. Park, D.-Y. Ma, and K.-H. Kim, “The physical properties of Al-doped zinc oxide films prepared by RF magnetron sputtering,” vol. 305, pp. 201–209, 1997.

[89] K.-H. Kim, K.-C. Park, and D.-Y. Ma, “Structural, electrical and optical properties of zirconium-doped zinc oxide films prepared by radio frequency magnetron sputtering,” *J. Appl. Phys.*, vol. 81, p. 7764, 1997.

[90] T. L. Yang, D. H. Zhang, J. Ma, H. L. Ma, and Y. Chen, “Transparent conducting ZnO:Al films deposited on organic substrates deposited by r.f. magnetron-

sputtering," *Thin Solid Films*, vol. 326, no. 1–2, pp. 60–62, 1998.

[91] T. Schuler and M. A. Aegerter, "Optical, electrical and structural properties of sol gel ZnO:Al coatings," *Thin Solid Films*, vol. 351, no. 1–2, pp. 125–131, 1999.

[92] M. Chen, Z. L. Pei, C. Sun, L. S. Wen, and X. Wang, "Surface characterization of transparent conductive oxide Al-doped ZnO films," *J. Cryst. Growth*, vol. 220, no. 3, pp. 254–262, 2000.

[93] D. Song, A. G. Aberle, and J. Xia, "Optimisation of ZnO:Al films by change of sputter gas pressure for solar cell application," *Appl. Surf. Sci.*, vol. 195, no. 1–4, pp. 291–296, 2002.

[94] S. . Jeong, J. . Lee, S. . Lee, and J. . Boo, "Deposition of aluminum-doped zincoxide films by RF magnetron sputtering and study of their structural, electrical and optical properties," *Thin Solid Films*, vol. 435, no. 1–2, pp. 78–82, 2003.

[95] B. Y. Oh, M. C. Jeong, D. S. Kim, W. Lee, and J. M. Myoung, "Post-annealing of Al-doped ZnO films in hydrogen atmosphere," *J. Cryst. Growth*, vol. 281, no. 2–4, pp. 475–480, 2005.

[96] J. Yoo *et al.*, "High transmittance and low resistive ZnO:Al films for thin film solar cells," *Thin Solid Films*, vol. 480–481, pp. 213–217, 2005.

[97] H. ming Zhou, D. qing Yi, Z. ming Yu, L. rong Xiao, and J. Li, "Preparation of aluminum doped zinc oxide films and the study of their microstructure, electrical and optical properties," *Thin Solid Films*, vol. 515, no. 17, pp. 6909–6914, 2007.

[98] J. G. Lu *et al.*, "Carrier concentration dependence of band gap shift in n-type ZnO:Al films," *J. Appl. Phys.*, vol. 101, no. 8, p. 083705, Apr. 2007.

[99] M. L. Grilli, A. Sytchkova, S. Boycheva, and A. Piegari, "Transparent and conductive Al-doped ZnO films for solar cells applications," *Phys. Status Solidi A*, no. 4, pp. 748–754, 2013.

[100] A. Henni, A. Merrouche, L. Telli, and A. Karar, "Studies on the structural , morphological , optical and electrical properties of Al-doped ZnO nanorods prepared by electrochemical deposition," *J. Electroanal. Chem. J.*, vol. 763, pp. 149–154, 2016.

[101] S. Ghosh, A. Mallick, B. Dou, M. F. A. M. Van Hest, and S. M. Garner, "A novel blanket annealing process to achieve highly transparent and conducting Al doped ZnO thin films: Its mechanism and application in perovskite solar cells," *Sol. Energy*, vol. 174, pp. 815–825, 2018.

[102] K. N. Tonny, R. Rafique, A. Sharmin, M. S. Bashar, and Z. H. Mahmood, “Electrical, optical and structural properties of transparent conducting Al doped ZnO (AZO) deposited by sol-gel spin coating,” *AIP Adv.*, vol. 8, p. 065307, 2018.

[103] M. D. Tyona, S. B. Jambure, C. D. Lokhande, A. G. Banpurkar, R. U. Osuji, and F. I. Ezema, “Dye-sensitized solar cells based on Al-doped ZnO photoelectrodes sensitized with rhodamine,” *Mater. Lett.*, vol. 220, no. 036, pp. 281–284, 2018.

[104] A. Sharmin, S. Tabassum, M. S. B. Zahid, and H. Mahmood, “Depositions and characterization of sol – gel processed Al - doped ZnO (AZO) as transparent conducting oxide (TCO) for solar cell application,” *J. Theor. Appl. Phys.*, vol. 13, no. 2, pp. 123–132, 2019.

[105] I. Jellal, H. Ahmoum, Y. Khaaissa, K. Nouneh, M. Boughrara, and M. Fahoume, “Experimental and ab-initio investigation of the microstructure and optoelectronic properties of FCM–CVD-prepared Al-doped ZnO thin films,” *Appl. Phys. A*, pp. 1–8, 2019.

[106] M. Murugesan, D. Arjunraj, J. Mayandi, V. Venkatachalapathy, and J. M. Pearce, “Properties of Al-doped zinc oxide and In-doped zinc oxide bilayer transparent conducting oxides for solar cell applications,” *Mater. Lett.*, vol. 222, pp. 50–53, 2018.

[107] J. Mass, P. Bhattacharya, and R. S. Katiyar, “Effect of high substrate temperature on Al-doped ZnO thin films grown by pulsed laser deposition,” *Mater. Sci. Eng.*, vol. 103, pp. 9–15, 2003.

[108] T. Pauporté, O. Lupan, V. Postica, M. Hoppe, L. Chow, and R. Adelung, “Al-Doped ZnO Nanowires by Electrochemical Deposition for Selective VOC Nanosensor and Nanophotodetector,” *Phys. Status Solidi A*, vol. 215, p. 1700824, 2018.

[109] N. P. Dasgupta, S. Neubert, W. Lee, O. Trejo, J. Lee, and F. B. Prinz, “Atomic Layer Deposition of Al-doped ZnO Films : Effect of Grain Orientation on Conductivity,” *Chem. Mater.*, vol. 22, pp. 4769–4775, 2010.

[110] D. Q. Fang, Y. Zhang, and S. L. Zhang, “Band gap engineering of ZnSnN2/ZnO (001) short-period superlattices via built-in electric field,” *J. Appl. Phys.*, vol. 120, no. 21, p. 215703, 2016.

[111] D. Gogova *et al.*, “High electron mobility single-crystalline ZnSnN2on ZnO (0001) substrates,” *CrystEngComm*, vol. 22, no. 38, pp. 6268–6274, 2020.

[112] A. Punya and W. R. L. Lambrecht, “Band offsets between ZnGeN2, GaN, ZnO, and

ZnSnN2 and their potential impact for solar cells," *Phys. Rev. B*, vol. 88, no. 7, p. 075302, 2013.

[113] O. Kluth *et al.*, "Texture etched ZnO:Al coated glass substrates for silicon based thin film solar cells," *Thin Solid Films*, vol. 351, no. 1–2, pp. 247–253, 1999.

[114] M. Jin, J. Feng, Z. De-Heng, M. Hong-Lei, and L. Shu-Ying, "Optical and electronic properties of transparent conducting ZnO and ZnO:Al films prepared by evaporating method," *Thin Solid Films*, vol. 357, no. 2, pp. 98–101, 1999.

[115] X. Jiang, F. L. Wong, M. K. Fung, and S. T. Lee, "Aluminum-doped zinc oxide films as transparent conductive electrode for organic light-emitting devices," *Appl. Phys. Lett.*, vol. 83, no. 9, pp. 1875–1877, 2003.

[116] J. Nomoto, T. Hirano, T. Miyata, and T. Minami, "Preparation of Al-doped ZnO transparent electrodes suitable for thin- film solar cell applications by various types of magnetron sputtering depositions," *Thin Solid Films*, vol. 520, no. 5, pp. 1400–1406, 2011.

[117] A. Crossay *et al.*, "Solar Energy Materials & Solar Cells Spray-deposited Al-doped ZnO transparent contacts for CdTe solar cells," *Sol. Energy Mater. Sol. Cells*, vol. 101, pp. 283–288, 2012.

[118] S. Neubert *et al.*, "Improved conversion ef fi ciency of a-Si : H / m c-Si : H thin- fi lm solar cells by using annealed Al-doped zinc oxide as front electrode material," *Prog. Photovoltaics Res. Appl.*, no. 22, pp. 1285–1291, 2014.

[119] M. Asemi, M. Ahmadi, and M. Ghanaatshoar, "Preparation of highly conducting Al-doped ZnO target by vacuum heat- treatment for thin film solar cell applications," *Ceram. Int.*, vol. 44, no. 11, pp. 12862–12868, 2018.

[120] Z. C. Jin, I. Hamberg, and C. G. Granqvist, "Optical properties of sputter-deposited ZnO:Al thin films," *J. Appl. Phys.*, vol. 64, no. 10, pp. 5117–5131, 1988.

[121] T. Tynell, H. Yamauchi, M. Karppinen, R. Okazaki, and I. Terasaki, "Atomic layer deposition of Al-doped ZnO thin films," *J. Vac. Sci. Technol. A Vacuum, Surfaces, Film.*, vol. 31, p. 01A109, 2013.

[122] H. Yang *et al.*, "Energy Level-Graded Al-Doped ZnO Protection Layers for Copper Nanowire-Based Window Electrodes for Efficient Flexible Perovskite Solar Cells," *ACS Appl. Mater. Interfaces*, vol. 12, pp. 13824–13835, 2020.

[123] A. Kuroyanagi, "Crystallographic characteristics and electrical properties of Al-doped ZnO thin films prepared by ionized deposition," *J. Appl. Phys.*, vol. 66, p.

5492, 1989.

[124] K. Mahmood, B. S. Swain, and H. S. Jung, “Controlling the surface nanostructure of ZnO and Al-doped ZnO thin films using electrostatic spraying for their application in 12% efficient perovskite solar cells,” *R. Soc. Chem.*, pp. 9127–9138, 2014.

[125] I. Volintiru, M. Creatore, B. J. Kniknie, C. I. M. A. Spee, and M. C. M. van de Sanden, “Evolution of the electrical and structural properties during the growth of Al doped ZnO films by remote plasma-enhanced metalorganic chemical vapor deposition,” *J. Appl. Phys.*, vol. 102, no. 043709, 2007.

[126] H. Kim, J. S. Horwitz, S. B. Qadri, and D. B. Chrisey, “Epitaxial growth of Al-doped ZnO thin films grown by pulsed laser deposition,” *Thin Solid Films*, vol. 420–421, pp. 107–111, 2002.

[127] G. Kaur, A. Mitra, and K. L. Yadav, “Pulsed laser deposited Al-doped ZnO thin films for optical applications,” *Prog. Nat. Sci. Mater. Int.*, vol. 25, no. 1, pp. 12–21, 2015.

[128] N. Srinatha, P. Raghu, H. M. Mahesh, and B. Angadi, “Spin-coated Al-doped ZnO thin films for optical applications: Structural, micro-structural, optical and luminescence studies,” *J. Alloys Compd.*, vol. 722, pp. 888–895, 2017.

[129] M. N. Islam, T. B. Ghosh, K. L. Chopra, and H. N. Acharya, “XPS and X-ray diffraction studies of aluminum-doped zinc oxide transparent conducting films,” *Thin Solid Films*, vol. 280, no. 1–2, pp. 20–25, 1996.

[130] O. Gençyılmaz, F. Atay, and I. Akyü, “Deposition and Ellipsometric Characterization of Transparent Conductive Al-doped ZnO for Solar Cell Application,” *J. Clean Energy Technol.*, vol. 4, no. 2, 2016.

[131] Z. L. Pei *et al.*, “Optical and electrical properties of direct-current magnetron sputtered ZnO:Al films,” *J. Appl. Phys.*, vol. 90, no. 7, pp. 3432–3436, 2001.

[132] A. N. Tiwari, A. Romeo, D. Baetzner, and H. Zogg, “Flexible CdTe Solar Cells on Polymer Films,” *Prog. Photovoltaics Res. Appl.*, vol. 9, no. December 2000, pp. 211–215, 2001.

[133] A. Gupta and A. D. Compaan, “All-sputtered 14% CdS/CdTe thin-film solar cell with ZnO: Al transparent conducting oxide,” *Appl. Phys. Lett.*, vol. 85, no. 4, pp. 684–686, 2004.

[134] J. Perrenoud, L. Kranz, S. Buecheler, F. Pianezzi, and A. N. Tiwari, “The use of

aluminium doped ZnO as transparent conductive oxide for CdS / CdTe solar cells," *Thin Solid Films*, vol. 519, no. 21, pp. 7444–7448, 2011.

[135] G. Drewelow, A. Reed, C. Stone, K. Roh, and Z. Jiang, "Work function investigations of Al-doped ZnO for band-alignment in electronic and optoelectronic applications," *Appl. Surf. Sci.*, vol. 484, no. December 2018, pp. 990–998, 2019.

[136] E. Leja, J. Korecki, K. Krop, and K. Toll, "Phase composition of SnOx thin films obtained by reactive d.c. sputtering," *Thin Solid Films*, vol. 59, no. 2, pp. 147–155, 1979.

[137] E. Leja, T. Pisarkiewicz, and A. Kołodziej, "Electrical properties of non-stoichiometric tin oxide films obtained by the d.c. reactive sputtering method," *Thin Solid Films*, vol. 67, no. 1, pp. 45–48, 1980.

[138] C. Kim, S. Kim, and S. E. Kim, "Transparent SnOx thin films fabricated by radio frequency reactive sputtering with a SnO/Sn composite target," *Thin Solid Films*, vol. 634, pp. 175–180, 2017.

[139] A. Garzon-Fontecha *et al.*, "SnOx thin films with tunable conductivity for fabrication of p–n homo-junction," *Surf. Interface Anal.*, vol. 53, no. 1, pp. 68–75, 2021.

[140] S. S. Lin, Y. S. Tsai, and K. R. Bai, "Structural and physical properties of tin oxide thin films for optoelectronic applications," *Appl. Surf. Sci.*, vol. 380, pp. 203–209, 2016.

[141] S. J. Lee *et al.*, "Composition, Microstructure, and Electrical Performance of Sputtered SnO Thin Films for p-Type Oxide Semiconductor," *ACS Appl. Mater. Interfaces*, vol. 10, no. 4, pp. 3810–3821, 2018.

[142] L. Y. Liang *et al.*, "Phase and Optical Characterizations of Annealed SnO Thin Films and Their p-Type TFT Application," *J. Electrochem. Soc.*, vol. 157, no. 6, p. H598, 2010.

[143] M. Moreno, A. Varela, and L. Otero-Díaz, "Cation nonstoichiometry in tin-monoxide-phase with tweed microstructure," *Phys. Rev. B - Condens. Matter Mater. Phys.*, vol. 56, no. 9, pp. 5186–5192, 1997.

[144] E. Fortunato *et al.*, "Transparent p-type SnOx thin film transistors produced by reactive rf magnetron sputtering followed by low temperature annealing," *Appl. Phys. Lett.*, vol. 97, no. 5, pp. 1–4, 2010.

[145] P. C. Hsu *et al.*, "Sputtering deposition of P-type SnO films with SnO2 target in

hydrogen-containing atmosphere," *ACS Appl. Mater. Interfaces*, vol. 6, no. 16, pp. 13724–13729, 2014.

[146] W. Guo *et al.*, "Microstructure, optical, and electrical properties of p -type SnO thin films," *Appl. Phys. Lett.*, vol. 96, no. 4, pp. 1–4, 2010.

[147] X. Q. Pan and L. Fu, "Tin oxide thin films grown on the (1̄012) sapphire substrate," *J. Electroceramics*, vol. 7, no. 1, pp. 35–46, 2001.

[148] A. Togo, F. Oba, I. Tanaka, and K. Tatsumi, "First-principles calculations of native defects in tin monoxide," *Phys. Rev. B - Condens. Matter Mater. Phys.*, vol. 74, no. 19, pp. 1–8, 2006.

[149] H. Hayashi, S. Katayama, R. Huang, K. Kurushima, and I. Tanaka, "Selective fabrication of n- and p-type SnO films without doping," *Phys. Status Solidi - Rapid Res. Lett.*, vol. 9, no. 3, pp. 192–196, 2015.

[150] H. Luo, L. Y. Liang, H. T. Cao, Z. M. Liu, and F. Zhuge, "Structural, chemical, optical, and electrical evolution of SnO x films deposited by reactive rf magnetron sputtering," *ACS Appl. Mater. Interfaces*, vol. 4, no. 10, pp. 5673–5677, 2012.

[151] R. Barros *et al.*, "Role of structure and composition on the performances of P-type tin oxide thin-film transistors processed at low-temperatures," *Nanomaterials*, vol. 9, no. 3, 2019.

[152] S. H. Kim *et al.*, "Fabrication of high-performance p-type thin film transistors using atomic-layer-deposited SnO films," *J. Mater. Chem. C*, vol. 5, no. 12, pp. 3139–3145, 2017.

[153] Y. Ogo *et al.*, "P -channel thin-film transistor using p -type oxide semiconductor, SnO," *Appl. Phys. Lett.*, vol. 93, no. 3, pp. 1–4, 2008.

[154] K. Nomura, T. Kamiya, and H. Hosono, "Ambipolar oxide thin-film transistor," *Adv. Mater.*, vol. 23, no. 30, pp. 3431–3434, 2011.

[155] H. Yabuta *et al.*, "Sputtering formation of p-type SnO thin-film transistors on glass toward oxide complimentary circuits," *Appl. Phys. Lett.*, vol. 97, no. 7, 2010.

[156] Y. Kim, J. H. Jang, J. S. Kim, S. D. Kim, and S. E. Kim, "Nitrogen doped p-type SnO thin films deposited via sputtering," *Mater. Sci. Eng. B Solid-State Mater. Adv. Technol.*, vol. 177, no. 16, pp. 1470–1475, 2012.

[157] J. Um, B. M. Roh, S. Kim, and S. Eunkyung Kim, "Effect of radio frequency power on the properties of p-type SnO deposited via sputtering," *Mater. Sci. Semicond. Process.*, vol. 16, no. 6, pp. 1679–1683, 2013.

[158] H. Luo, L. Y. Liang, Q. Liu, and H. T. Cao, “Magnetron-Sputtered SnO Thin Films for p-Type and Ambipolar TFT Applications,” *ECS J. Solid State Sci. Technol.*, vol. 3, no. 9, pp. Q3091–Q3094, 2014.

[159] I. C. Chiu and I. C. Cheng, “Gate-bias stress stability of P-type SnO thin-film transistors fabricated by RF-sputtering,” *IEEE Electron Device Lett.*, vol. 35, no. 1, pp. 90–92, 2014.

[160] F. Izumi, “Pattern-fitting structure refinement of tin(II) oxide,” *J. Solid State Chem.*, vol. 38, no. 3, pp. 381–385, 1981.

[161] C. Y. Jeong, D. Lee, Y. J. Han, Y. J. Choi, and H. I. Kwon, “Subgap states in p-channel tin monoxide thin-film transistors from temperature-dependent field-effect characteristics,” *Semicond. Sci. Technol.*, vol. 30, no. 8, 2015.

[162] J. A. Caraveo-Frescas, P. K. Nayak, H. A. Al-Jawhari, D. B. Granato, U. Schwingenschlögl, and H. N. Alshareef, “Record mobility in transparent p-type tin monoxide films and devices by phase engineering,” *ACS Nano*, vol. 7, no. 6, pp. 5160–5167, 2013.

[163] J. Huo, X. Wang, X. Wu, W. J. Liu, and S. J. Ding, “Preparation and characterization of SnO films via reactive sputtering for ambipolar thin-film transistor applications,” *Semicond. Sci. Technol.*, vol. 36, no. 2, 2020.

[164] I. M. Dharmadasa, A. P. Samantilleke, N. B. Chaure, and J. Young, “New ways of developing glass/conducting glass/CdS/CdTe/metal thin-film solar cells based on a new model,” *Semicond. Sci. Technol.*, vol. 17, no. 12, pp. 1238–1248, 2002.

[165] A. Hiraki, K. Shuto, S. Kim, W. Kammura, and M. Iwami, “Room-temperature interfacial reaction in Au-semiconductor systems,” *Appl. Phys. Lett.*, vol. 31, no. 9, pp. 611–612, Nov. 1977.

[166] A. Hiraki, “Low temperature reactions at Si/metal interfaces; What is going on at the interfaces?,” *Surf. Sci. Rep.*, vol. 3, no. 7, pp. 357–412, 1983.

[167] B. F. Dyson, “Diffusion of gold and silver in tin single crystals,” *J. Appl. Phys.*, vol. 37, no. 6, pp. 2375–2377, 1966.

List of Abbreviations

AZO	Aluminum doped zinc oxide
CIGS	Copper indium gallium di-selenide
CSP	Concentrated solar power
DC	Direct current
ECR	Electron cyclotron resonance
EDS or EDX	Energy-dispersive X-ray spectroscopy
FP-LMTO	Full–potential linearized muffin-tin orbital
FWHM	Full width at half maximum
GGA	Generalized gradient approximation
KPFM	Kelvin Probe Force Microscopy
LDA	Local density approximation
MBE	Molecular beam epitaxy
PES	Photoelectron spectroscopy
PV	Photovoltaic
QSGW	Quasiparticle self-consistent GW
RF	Radio frequency
RTA	Rapid thermal annealing
sccm	Standard cubic centimetres per minute
SEM	Scanning electron microscope
TEC	Thermal expansion coefficient
UPS	Ultraviolet photoelectron spectroscopy
XPS	X-ray photoelectron spectroscopy
XRD	X-ray Powder Diffraction
m_e^*	Effective mass of electron
m_0	Free electron mass
E_F	Fermi level
E_C	Minimum energy of the conduction band
N_C	Concentration coefficient
k	Boltzmann's constant
ħ	Planck’s constant
v	Velocity
μ	Carrier mobility
n	Carrier density
e	Electron charge
$\vec{E}$	Electric field
$\bar{\tau}$	Average scattering time
Y	Sputtering yield
M_t	Target particle mass

M_i	Incident particle mass
E_i	Initial energy of the incident atom
E_{th}	Threshold energy
γ	Energy transfer mass factor
θ	Angle of impact
E_t	Energy transferred by the physical collision between hard spheres
d	Thickness
ρ	Density
D	Average crystallite size
K	Shape factor (~ 0.93)
λ	Wavelength
β	Full width at half maximum
α	Absorption coefficient
E_g^{opt}	Optical bandgap energy
T	Transmittance
R	Reflection
n_{air}	Refractive index of air
n_{glass}	Refractive index of glass
n_{ZnSnN2}	Refractive index of $ZnSnN_2$
E_g	Intrinsic bandgap energy
ΔE_{ee}	Bandgap narrowing based on electron-electron
ΔE_{ei}	Bandgap narrowing based on electron-impurity interactions
ΔE_g^{BM}	Band gap widening induced by the Burstein-Moss effect
m_{vc}^*	Reduced effective mass
m_c^*	Conduction-band effective mass
m_v^*	Valence-band effective mass
u_s	Stored energy at unit area of the deposited film
u_v	Elastic energy
σ	Internal stress
Y	Young's modulus
ε	Strain
ν	Poisson's ratio of the films
β_{tot}	Total broadening
β_D	Broadening due to crystalline size
β_ε	Broadening due to strain
J_{Ph}	Photocurrent density
J_D	Dark current density
$J_{AM1.5}$	Current density after illuminated under 1-sun AM 1.5

List of Figures

List of Tables

- T. Bui, M. Halbwax and J-P. Vilcot, **Effect of Sputtering Atmosphere on $ZnSnN_2$ Thin Films Electrical and Optoelectronic Properties**, *ECS Transactions*, 97 (4) 47-55 (2020)
- J-P. Vilcot., T. Bui, B. Ayachi, P. Miska, J-F. Pierson, C. Longeaud, S. Le Gall, W. Favre, V.S. Nguyen, **$ZnSnN_2$: material investigations for photovoltaic applications**, *37th European Materials Research Society Spring Meeting, E-MRS Spring 2019,* Nice, France, may 27-31, 2019, Symposium E - Earth-abundant next generation materials for solar energy - III, invited paper E 9.1
- T. Bui, M. Halbwax and J-P. Vilcot, **Effect of sputtering atmosphere on $ZnSnN_2$ thin films electrical and optoelectronic properties**, accepted for oral presentation in 237th Meeting of the Electrochemical Society, Montréal, Canada, may 10-14, 2020, but conference cancelled by organizers (sanitary crisis)
- T. Bui, M. Halbwax, J-P. Vilcot, **Effects of sputtering environment on the optical, electrical and optoelectronic properties of $ZnSnN_2$**, oral presentation in JNPV (December 2019, Dourdan)
- B. Ayachi, T. Bui, C. Sion, J-P Vilcot, **Reactively co-sputtered $ZnSnN_2$ thin films: a promising material/process for low cost/high efficiency sustainable tandem cells**, poster presentation in JNPV (December 2017, Dourdan)
- S. Le Gall, B. Ayachi, N. Beddelem, T. Bui, C. Longeaud, A. Goldani, J. Alvarez, A. Jaffres, J-P. Kleider, J-P. Vilcot, P. Miska, **Etude des propriétés de photoconductivité de couches minces de $ZnSnN_2$ par implantation de dopants et selon différentes conditions de croissance**, poster presentation in JNPV (December 2018, Dourdan)
- V.S. Nguyen, T. Bui, J-P. Vilcot, A. Valla, A. Chabli, W. Favre, **Influence of growing conditions on optical and electrical properties of $ZnSnN_2$ thin films for PV applications**, poster presentation in JNPV (December 2018, Dourdan)
- L. Kopprio, S. Le Gall, C. Longeaud, T. Bui, B. Ayachi, J-P Vilcot, A. Virfeu, J-F. Pierson, **Evaluation of the optoelectronic properties of $ZnSnN_2$ thin films under different growth conditions and doping implantation of As and P at different concentrations**, poster presentation in JNPV (December 2019, Dourdan)
- T. Bui, M. Halbwax, J-P. Vilcot, **Comparison of DC and RF Sputtering: Effect on Structural and Optical Properties of $ZnSnN_2$**, poster presentation in JNPV (December 2020, Dourdan)

ABSTRACT

By literature reports, $ZnSnN_2$ has been pointed out as a potential high bandgap semiconductor material. We particularly investigated on it as an earth abundant and low environmental footprint material for photovoltaic application, and more specifically as a thin film inorganic top absorber for tandem cells based on silicon bottom cell. In this work, $ZnSnN_2$ has been deposited using magnetron sputtering and a parametric study of the influence of its deposition parameters on the material properties has been carried out. The effect of sputtering atmosphere, pressure, temperature and composition were so investigated. The crystal structure of the films has been characterized by X-ray diffraction (XRD) and their composition by energy-dispersive X-ray spectroscopy (EDS). Electrical characterization has been made using Hall Effect measurements and optical properties determined from UV-Vis spectroscopy. Wide variations of carrier density and optical bandgap have been experimentally observed, from 10^{17} to of 10^{20} cm^{-3} and from 1.6 to 2.3 eV, respectively. The photoelectric characteristics of $ZnSnN_2$ have been assessed by fabricating photoconductor and photodiode structures. Although some photocurrent could have been retrieved under 1 sun solar illumination, no photodiode behavior has been obtained.

Key words: $ZnSnN_2$, earth abundant II-IV-N_2 material, magnetron sputtering, parametric study, photovoltaics

RESUME

Les résultats théoriques publiés sur le matériau $ZnSnN_2$ le font apparaitre comme un matériau semiconducteur à grand gap. Dans ce travail, ses qualités de matériau abondant et à faible empreinte écologique nous ont particulièrement intéressés, en particulier, pour son utilisation en tant que matériau inorganique en film mince pour la réalisation de l'absorbeur de la cellule supérieure d'une cellule tandem dont la cellule inférieure serait en silicium. Nous avons réalisé une étude paramétrique de l'influence des conditions de dépôt, atmosphère, pression, température par pulvérisation cathodique et de la composition ainsi obtenue sur les propriétés cristallines, électriques et optiques des films. La cristallographie a été analysée par diffraction de rayons X (DRX) et la composition par spectroscopie de rayons X à dispersion d'énergie (EDX). Des mesures par Effet Hall ont permis d'obtenir les caractéristiques électriques et la spectroscopie UV-Visible l'évaluation du gap optique. En fonctions des paramètres de dépôt, de grandes variations à la fois sur la densité de porteurs, de 10^{17} to of 10^{20} cm^{-3}, et sur la valeur du gap optique, de 1.6 to 2.3 eV ont été obtenues. Des structures de type photoconducteur et photodiode ont été fabriquées pour évaluer les propriétés photoélectriques. Bien qu'un photocourant ait pu être mesuré, aucune fonctionnalité de type "photodiode" n'a pour l'instant pu être mise en évidence.

Mots clefs: $ZnSnN_2$, matériau abondant II-IV-N_2, pulvérisation cathodique, étude paramétrique, photovoltaïque